ISBN 978-82-326-7956-0 (printed ver.)
ISBN 978-82-326-7955-3 (electronic ver.)
ISSN 1503-8181 (printed ver.)
ISSN 2703-8084 (electronic ver.)

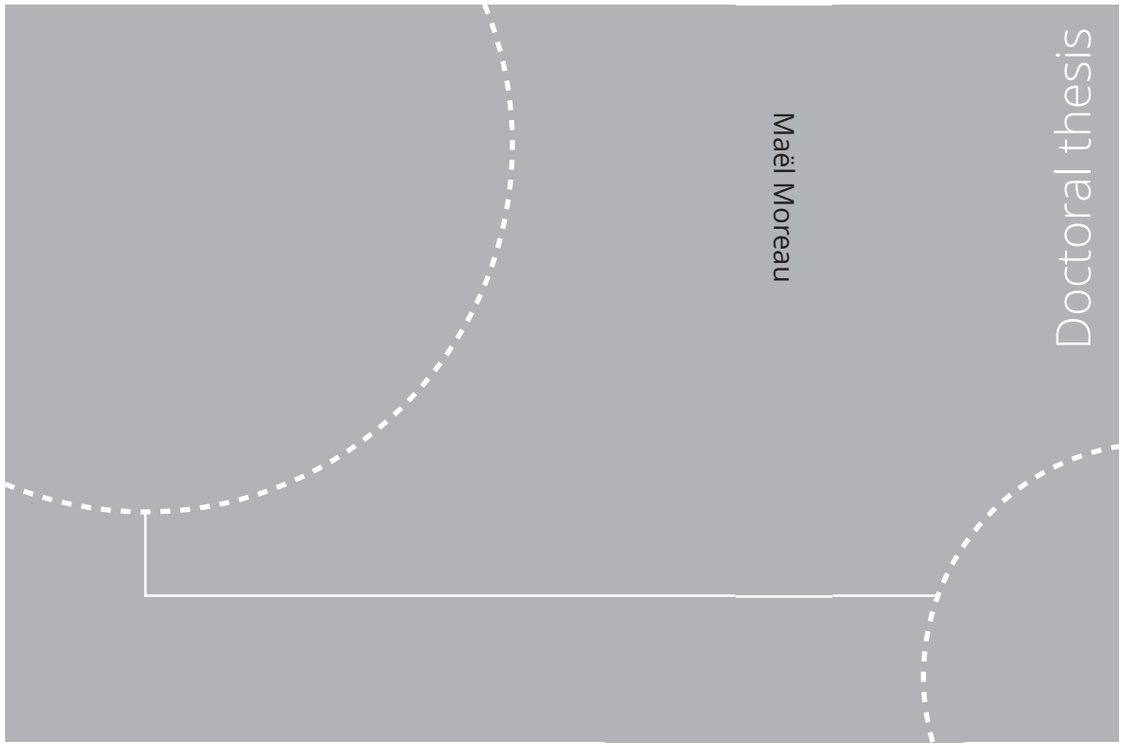

Doctoral theses at NTNU, 2024:182

Maël Moreau

Numerical and experimental hydrodynamic study of a vertical circular floating dock in waves

NTNU
Norwegian University of
Science and Technology

Doctoral theses at NTNU, 2024:182

NTNU
Norwegian University of Science and Technology
Thesis for the degree of Philosophiae Doctor
Faculty of Engineering
Department of Marine Technology

NTNU
Norwegian University of
Science and Technology

Maël Moreau

Numerical and experimental hydrodynamic study of a vertical circular floating dock in waves

Thesis for the degree of Philosophiae Doctor

Trondheim, May 2024

Norwegian University of Science and Technology
Faculty of Engineering
Department of Marine Technology

NTNU
Norwegian University of
Science and Technology

NTNU
Norwegian University of Science and Technology

Thesis for the degree of Philosophiae Doctor

Faculty of Engineering
Department of Marine Technology

ISBN 978-82-326-7956-0 (printed ver.)
ISBN 978-82-326-7955-3 (electronic ver.)
ISSN 1503-8181 (printed ver.)
ISSN 2703-8084 (electronic ver.)

Doctoral theses at NTNU, 2024:182

PRINTED IN NORWAY
NO - 1598

NORDIC SWAN ECOLABEL
Printed matter
2041 0731

Printed by Skipnes Kommunikasjon AS

Acknowledgements

This thesis concludes a PhD program in Marine Technology achieved at NTNU (Norwegian University of Science and Technology). It would never have seen the light of day without the support and contribution of many people in all facets that constitute research work.

First, I am thankful to my supervisor Professor Trygve Kristiansen for his enlightened guidance and the time dedicated to my work through numerous meetings. I am also grateful for the in-depth proofreading of many parts of the current thesis, and more generally his constant patience and support.

I have enjoyed the many discussions with my co-supervisor Babak Ommani and with Professor Bernard Molin. Those meetings undeniably enriched the content of this work, for which I am grateful. I also have a special thought for Zhyiu Jiang and Professor Odd M. Faltinsen, who both pointed me in the right direction at the beginning of my thesis, as well as for Professor Marilena Greco as I enjoyed being teacher assistant at her side, even in the tumultuous period of the Covid lockdown.

I would like to thank Terje Rosten, Trond Innset and Torgeir Wahl for their invaluable contribution to the model tests achieved both in 2018 and 2019, and more generally to all the staff working at Sintef Ocean for their availability and precious help with the use of the various software and instrumentation.

My last thanks go to my friends overseas, who always remained by my side despite the long distances that separate us.

Abstract

A hydrodynamic analysis of a free-floating bottom-less upright circular dock in waves conceived for the installation of spar-type floating offshore wind turbines (FOWT) is carried out in this work for incident wave frequencies near the first lateral sloshing resonance. The motions of the circular dock as well as the sloshing-induced motions of a FOWT's spar floating inside the dock are studied through both semi-analytical and experimental methods in the frequency domain.

The diffraction and radiation problems in heave surge and pitch are tackled by a domain decomposition approach under linear potential flow assumptions. In addition, known theories used to describe sloshing waves in closed containers and based on a decomposition of the velocity potential into sloshing eigenmodes are here adapted for the open-bottom structure. This semi-analytical model is extended to include the effects of solid and perforated annular baffles installed on the internal wall of the dock. A reduced natural sloshing frequency as well as a damping ratio estimated from the energy dissipated by the flow separation at the sharp edge of the baffles are introduced in the free-surface boundary conditions to model the effects of the baffles on the sloshing eigenmodes. The equations of motions are solved, and both a sensitivity and eigenvalue analyses are carried out to assess the differences between the numerical and experimental models, emphasising in particular uncertainties related to the numerical modelling of the inertial matrix.
Model tests were performed at the scale 1:100 on a 0.80m diameter model in regular waves with wave periods near the highest sloshing natural period. The internal free-surface elevation and model's rigid body motions were measured, both for the case without and with a FOWT's spar. Perforated and solid annular baffles of width-to-dock's internal radius ratio 0.17 were installed inside the dock at various submergences. Few model tests included polystyrene foam balls of various sizes and quantities covering the entire internal water surface, which is shown to be a relatively inefficient way to damp sloshing waves unless an excessively large amount of them is placed in the dock. In addition, few tests in irregular waves were performed, generated from JONSWAP spectra with peak periods near sloshing resonance.
The amplitudes and phases of the bodies' motions and of the free-surface elevation inside the dock are compared with those obtained with the semi-analytical model. The results present a good agreement for the highest ratio between the submergence of the baffle d_B and the internal radius of the dock a that was considered (i.e. $d_B/a = 0.27$), while numerical results tend to under-predict the damping ratio for lower baffle's submergences, most likely due to free-surface interactions. The resonant peak amplitudes of the spar's surge and pitch motions are reduced by almost half when a solid baffle is installed, with a strong dependency on the

incident wave height due to viscous dissipation caused by the baffle. A significant reduction of the motions' amplitudes is also observed for perforated baffles with resonant periods closer to the case without baffle.

Nomenclature

The main symbols and abbreviations encountered in this work are given below. This list is not exhaustive and few symbols represent different variables or constants. Definitions are further clarified in the text wherever necessary.

Abreviations

BB	Bilge boxes
BC	Boundary condition
BEM	Boundary Element Method
BVP	Boundary value problem
DoF	Degree of freedom
FOWT	Floating offshore wind turbine
WP	Wave probe

Greek symbols

$\bar{\eta}_j^{(k)}$	[m] or [rad] Motion's complex amplitude
$\beta_{p,q}$	[m^2] Modal coefficient
$\boldsymbol{n}^{(k)}$	[-] Unit vector pointing outward the body (k)
$\boldsymbol{r}$	[m] Position vector
ϵ	[-] Wave steepness
ϵ_p	[-] Neuman's notation
$\eta_j^{(k)}$	[m] or [rad] Generalized body motions
$\iota_{p,q}$	[-] Root of Bessel functions or of their first derivative
λ	[m] Wave length
ν	[m^2/s] Water kinematic viscosity
Ω	[m^3] Fluid domain or [m^2] Stokes-Joukowski potential
ω	[rad/s] Wave frequency
Φ	[m^2/s] Potential flow

ρ	[kg/m^3] Water density
Σ_0	[m^2] Mean internal free surface
$\sigma_{p,q}$	[rad/s] Sloshing eigenfrequencies
$\sigma'_{p,q}$	[rad/s] Shifted sloshing eigenfrequency
τ	[-] Perforation ratio of the baffles
$\varphi_{p,q}$	[-] Sloshing eigenfunction
ξ_1	[-] Damping ratio
ζ	[m] Instantaneous wave elevation
ζ_A	[m] Incident waves' amplitude
$k_{p,q}$	[rad/s] Sloshing wave number eigenvalues
v_r	[m/s] Relative flow velocity on the baffle

Latin symbols

a	[m] Dock's inner radius
a_0	[m] Spar's radius
a_B	[m] Baffle's width
$a_{i,j}^{(k)}$, $d_{i,j}^{(k)}$	[kg], [kg·m] or [kg·m^2] Added mass coefficients
b	[m] Dock's outer radius
$b_{i,j}^{(k)}$, $e_{i,j}^{(k)}$	[kg/s], [kg·m/s] or [kg·m^2/s] Radiation damping coefficients
$c - b$	[m] Bilge box's width
C_D	[-] Drag coefficient
C_M	[-] Mass coefficient
$c_{i,j}^{(k)}$, $f_{i,j}^{(k)}$	[kg/s^2] Restoring coefficients
$d + s$	[m] Dock's draught
d_0	[m] Spar's draught
d_B	[m] Baffle's submergence
E_M	[J] Mechanical energy

F^D	[N] Heuristic drag load in surge
$F^{S,(k)}$	[N] or [N·m] Exciting force or moment
F_5^M	[N·m] Pitch moment on the baffle
g	[m/s^2] Gravitational acceleration
h	[m] Water depth
H_s	[m] Significant wave height
I_p	[-] Modified Bessel function of the first kind
$I_{5,5}^{(k)}$	[kg·m^2] Body's moment of inertia in pitch
J_p	[-] Bessel function of the first kind
k	[rad/m] Wave number
K_p	[-] Modified Bessel function of the second kind
$M^{(k)}$	[kg] Body's mass
N_I to N_V	Number of eigenfunctions kept in each subdomain I to V
O, r, θ, z	Cylindrical coordinates
O, x, y, z	Cartesian coordinates
Q_0	[m^3] Internal fluid domain of closed body
$R_{p,q}$	[m^2/s] Modal coefficient
s	[m] Bilge boxes' height
$S_0^{(k)}$	[m^2] Body's mean wetted surface
S_x	[m^2·s] or [rad^2·s] Power spectral density
T	[s] Wave period
t	[s] Time
T_p	[s] Peak period
$T_{p,q}$	[s] Lateral sloshing natural period
T_{piston}	[s] Piston mode's natural period
Y_p	[-] Bessel function of the second kind
$z_G^{(k)}$	[m] Body's vertical location of the centre of gravity
KC	[-] Keulegan Carpenter number

Contents

1 | Introduction

1.1 Installation of floating offshore wind turbines

Renewable energies are playing a key role in the framework of the COP21 objective to reduce global warming. The offshore wind turbine (OWT) industry is one of the fastest growing and one of the most promising, with high technical potential that could provide several times the national needs in electricity for a large number of countries (Cozzi et al., 2019). The cumulative installed capacity of OWTs has hence known a significant increase over the last 20 years, from 45MW of installed power in 2000, 8750MW in 2014, to more than 23GW in 2019 (Breeze, 2016). This growth is expected to continue in the years to come, with projected installed power higher than 200GW for 2030 (Cozzi et al., 2019). About 80% of the current world-wide installed power is located in Europe, mostly on fixed foundations for low water depths (<45m). Among them, monopile foundations are the most common (80%), even though jacket (10%) or gravitational (5%) foundations are also encountered (Ramírez et al., 2021).
The capacity of OWT's units has also increased, from less than 500kW for the very first units installed in Denmark in the early 90s, to around 6.5MW in average nowadays (Lee and Zhao, 2020). The power produced by a wind turbine is function of the square of the blades' length, such that it is advantageous for the industry to increase the size of individual units. Floating offshore wind turbines (FOWT) of 12MW with blades measuring around 100m long each are for instance currently under development. With FOWT technologies, it also becomes possible to install the turbines further from the coast, where stronger and more regular winds are available. Since the first full-scale pilot FOWT Hywind developed by Equinor in 2009 in Norway, several technologies have emerged. Three types of floating hulls can be distinguished: semi-submersibles, spar types, or tension-leg platforms. The spar-type Hywind FOWTs and the semi-submersible WindFloat FOWTs are currently the only two models that have been installed in large scale projects.

In 2017 the first farm of FOWTs was installed along the coast of Scotland at water depths around 100m. Five Hywind spar-type FOWTs were assembled in a protected area near Stavanger, Norway, and then towed to site at 25km from the coast of Peterhead (Skaare, 2017). The installation and assembly of FOWTs represent today around 5-6% of the total capital expenditures (Stehly and Duffy, 2021). While fixed foundations as the monopiles are typically installed from jack-up based cranes, or directly from floating vessels, the installation on-site of FOWTs is particularly costly due to the technical challenges that arise from the severe weather conditions far from the coast. To overcome these challenges and reduce the installation costs, the concept of a 80m-diameter cylindrical and bottom-less

floating dock (cf. Fig. 1.1) was proposed by Equinor in order to create a protected water area inside, and facilitate the assembly on site of the tower, nacelle, rotor and blades of the FOWT onto its floating spar foundation. This cylindrical platform, referred to in this work as "the dock", is intended to be anchored the time of the operation, then lifted up and towed to the next emplacement thanks to an adequate ballast system. The top of the dock is a 20m width annular section allowing the deployment of cranes and storage facilities. The spar being introduced inside the cylinder through opening gates still to be defined. A parametric study was achieved by Jiang et al. (2020) who provided first estimations of the dock's dimensions, based on a minimum weight optimisation. Their work points out the importance of hydrodynamic resonance (sloshing) inside the cylindrical dock, which might undermine its original purpose: create a calm water area. Their conclusions are the starting point of the current thesis, which aims to carry out an hydrodynamic study of the project at operational weather condition.

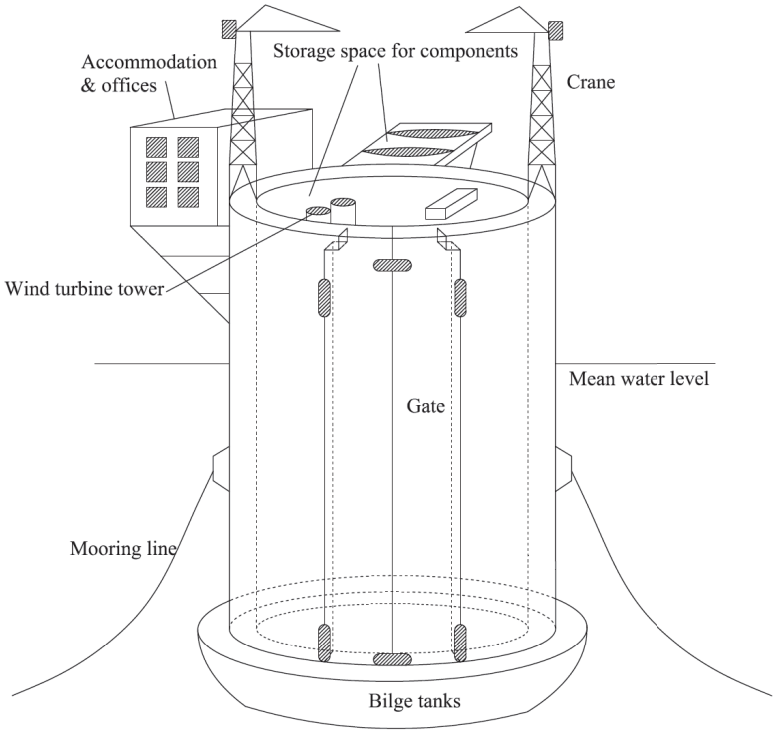

Figure 1.1: *Artist view of the floating dock used for the assembly on-site of spar-type Hywind floating wind turbines. Sketch from Jiang et al. (2020).*

1.2 Scope of the present work

The response of the dock in regular and irregular waves are studied in the frequency domain under linear potential flow assumptions. The dock is in operational condition, i.e. ballasted and moored as if a FOWT was to be assembled inside. Waves are assumed to be long crested with low steepnesses. A special focus is made on incident wave periods near the highest natural period of the lateral sloshing modes. For the dock designed by Jiang et al. (2020), this natural period is around $T_{1,1} = 8$s. It is most likely to be excited by the dock's motions in waves, as typical wave periods far from the coast range between 5s and 25s. We mostly limit our study to wave periods below 15s. For higher periods, the vertical resonant mode of the water column, called piston mode, would have to be considered, and is only briefly mentioned here (cf. Secs. 6.1.3 and 6.1.4). The natural period of the piston mode was integrated by Jiang et al. (2020) in their design optimisation study in order to keep it higher than typical wave periods encountered at operational conditions. For the main draught consider in this work (80m), this piston mode natural period is near $T_{piston} = 20$s. Natural periods of the dock's motions were also found higher than 20s by Jiang et al. (2020). In consequence, the heave motions are negligible at operational conditions, as they are not linearly coupled with lateral sloshing modes. We will therefore mostly focus on the surge and pitch motions.
We propose in this work to damp the sloshing waves thanks to annular baffles rigidly fixed to the internal wall of the tank. The baffle are either solid or perforated, and their effects investigated both through experiments and rational methods. The non-linear viscous effects introduced by the baffles are treated locally in Sec. 3.5, while the rest of the flow is assumed to remain linear and inviscid. The damping effects of free-floating polystyrene foam balls are also tested through experiments only. The case where a FOWT's spar is moored inside the dock is then considered to investigate its sloshing-induced motions.

1.3 Background

1.3.1 Cylindrical structures in waves

Analytical studies of the behaviour of cylindrical bodies of revolution in waves in the frequency domain and under the classical linear potential flow assumptions have been extensively treated in the literature. The loads caused by the scattering of waves on a circular cylinder fixed to the sea bottom were derived by MacCamy and Fuchs (1954) by decomposing the velocity potential of incident waves as a series of solutions of the Laplace equation in cylindrical coordinates. A similar method was used by Miles and Gilbert (1968), who first solved the diffraction problem for an upright circular cylinder with a finite draught using a domain decomposition (DD) approach based on matched eigenfunction expansions. Their

work contained an error in the expression of the dynamic pressure below the structure, resulting in wrong vertical forces. This mistake was pointed out and corrected by Garrett (1971). Garrett (1970) also derived semi-analytical solutions for the scattering loads on a hollow circular cylinder without bottom, making a special focus on sloshing resonance. Later, both Yeung (1980) and Sabuncu and Calisal (1981) solved the radiation problems for a closed-bottom circular cylinder, also using a domain decomposition method to determine the velocity potential under forced motions in order to derive added mass and damping coefficients. The special case of a bottomless cylinder with finite wall thickness, which geometry is very close to the one of the floating dock considered in the present study, was treated by Mavrakos (1985) for the diffraction problem. Ilkişik and K. Kafali (1986) solved analytically the radiation problem in surge for the same geometry, later completed by Mavrakos (1988) for the radiation problems in all the degrees of freedom. The geometry of the dock only differs from their studies due to that it includes bilge boxes at the bottom of the structure.
Attempts to generalise such domain decomposition methods for any body of revolutions were made. Kokkinowracho et al. (1986) showed that the solutions of the radiation and diffraction problems of any body of revolution could be obtained using known solutions for circular cylindrical bodies by discretising the body's surface into small circular or annular elements. Exhaustive lists of eigenfunctions, solutions of the Laplace equation in any type of circular cylindrical domains were for instance provided by Chatjigeorgiou (2018).
When the velocity potential is singular along the geometry, typically at sharp corners, the domain decomposition approach often fails to represent correctly the flow around the singularity. The consequence is that the convergence of the results is poor, requiring a high number of eigenmodes in each subdomain around the corner. This is for instance treated by Faltinsen et al. (2007) who studied forced heave motions of a two-dimensional rectangular moonpool. In order to establish a better description of the flow at the entrance of the moonpool, they express the velocity potential as series of solutions of the Laplace equation for a flow on a 90-degrees infinite corner in infinite fluid. These eigenfunctions do not intrinsically satisfy the other boundary conditions in the fluid domain, and a Galerkin scheme must therefore be applied to enforce these boundary conditions.

Similar DD approaches were extended to more complex problems in recent works. Analytical studies of porous cylindrical structures in waves were for instance carried out by Molin and Legras (1990); Mackay et al. (2021); Konispoliatis et al. (2021); Park and Koo (2015), in which the viscous dissipation through the porous media is modelled as either a linear or quadratic pressure drop. Mavrakos (2004) and Mavrakos et al. (2023) solved the radiation problem of a cylinder body inside an annular cylinder, i.e. a geometry similar to the case of a FOWT's spar inside the dock (without the bilge boxes). Han et al. (2022) considered the radiation problems in surge and heave for the same geometry as Mavrakos (1988), with a fluid of

lighter density inside the moonpool. Nokob and Yeung (2014a,b, 2015) solved the diffraction problem on cylindrical moonpools with a constant angular opening, using Green functions to deal with the absence of thickness of the moopools' wall. In particular, their results suggest that the wave loads can be reduced for an optimum orientation of the moonpool's opening with respect to incident waves.

1.3.2 Moonpools

Moonpools in waves have received a special focus since the early 2000s. Molin (2001) derived analytical formulas to express eigenfrequencies of resonant modes in both two- dimensional and three-dimensional rectangular moonpools. The piston mode in his work is represented as a single degree of freedom oscillating water column generated by a source distribution at the entrance of the moonpool. The radiated waves are modelled by two sinks at the external edges of the ship. His model assumes in particular that the dimensions of the moonpool are small with respect to the vessel's width. The piston mode natural frequency in a circular moonpool was also investigated by Molin et al. (2018) in similar ways, both for finite and infinite water depths. The coupling between piston mode resonance and the motions of the ship in regular waves were further studied by Ravinthrakumar et al. (2018, 2019) for a moonpool with recess. The importance of the viscous dissipation caused by the flow separation at the entrance of the moonpool is particularly emphasised in their work. When the ship is free to move, large motions of the water column do not necessarily occur at the piston mode natural frequency. Studying the coupling between the motions of a free-floating two-dimensional moonpool in waves, Fredriksen et al. (2015) thus showed that little water motions was observed at the natural piston-mode frequency, but high motions would occur at the natural frequency in heave. In their work, the water motion is determined thanks to a hybrid code which combines a viscous CFD solver around the moonpool, and an inviscid linear potential solver in the far field. This approach was already used by the same authors (Fredriksen et al., 2014) to study a two-dimensional moonpool at low forward speed subjected to forced heave motions, with good agreement with experimental results. As the floating dock is also expected to be towed, it can be interesting to note from their results that a slight reduction of the piston mode amplitude is observed for increasing forward speeds. If high water motions in moonpools are most generally undesired, Reiersen et al. (2021) showed that it could also be used as a pitch reduction device, taking advantage of the high increase of added mass at the piston mode natural frequency.

A floating platform (MONOBR) with similar dimensions of the dock and intended for the exploitation of deep-water oil fields was described by Barreira et al. (2005) and Isaias Quaresma Masetti et al. (2012). In their work, the width of the opening at the bottom could vary, and model tests were performed with a relatively low draught - near half the internal diameter - focusing on the heave and piston

mode responses to high incident wave periods. Their numerical model includes an empirical viscous damping based on their experiments. In their results, heave's amplitude at resonance is reduced by more than 50% for a 30% closed bottom compared to a fully open bottom. Jiang et al. (2020) integrated the piston mode resonance as a constraint in their optimization study, considering a dock with a draught about twice higher than the model of Isaias Quaresma Masetti et al. (2012) in order to shift the piston resonance to higher periods. They also showed that the first lateral sloshing resonance however would occur at typical operational sea-states, and would inducing high motions of Hywind FOWT's spars.

1.3.3 Lateral sloshing

In addition to piston mode resonance, lateral sloshing modes are also linearly excited in moonpools, and are similar to sloshing modes in closed containers. For large marine structures, the lateral sloshing response is generally dominated by the lowest natural frequency. This resonant mode could not be shifted away from typical incident wave length at operational condition by Jiang et al. (2020) and is of primary interest in our work.
Sloshing resonance in a circular public water pool was first studied by Ostrogradsky (1832), who already solved the spectral problem for the velocity potential in cylindrical coordinates by separating the variables. Nowadays, generalised methods to study both linear and non-linear sloshing responses to arbitrary excitations in a closed tank have been established, which are for instance summarised by Faltinsen and Timokha (2009). The velocity potential is expressed in their work as an expansion of sloshing natural eigenmodes, solutions of the spectral problem. By inserting this modal representation of the flow into the free-surface boundary conditions, the so-called modal equations are established. An equivalent formulation was proposed by Molin et al. (2002), which slightly differ from Faltinsen and Timokha (2009)'s approach as they introduce an infinite-frequency potential in their formulation. Non-linear formulations are not considered in this thesis, but it can be mentioned that similar methods exist to describe weakly non-linear sloshing problems, which are also presented by Faltinsen and Timokha (2009). These are referred to as multimodal analyses, derived thanks to a Lagrangian method based on the minimisation of the work of pressure forces in the fluid domain.
For the specific cases of circular cylindrical tanks and annular tanks, analytical linear solutions have been derived (Timokha, 2015; Faltinsen et al., 2016; Lukovsky et al., 1984; Lukovsky, 2015; Takahara and Kimura, 2012; Yue et al., 2018). These can be compared to the geometry of the dock without and with a FOWT's spar. In particular, the presence of the spar inside the dock affects the sloshing natural eigenmodes and eigenfrequencies, which is discussed in more details in Chapter 3.

1.3.4 Ring baffles

Sloshing resonance can cause severe structural damages, and numerous attempts to damp sloshing waves have been made. Extensive experimental and analytical works were for instance carried out by the NASA in the 60s in order to reduce fuel motions in cylindrical rocket reservoirs. Different damping devices were tested, including ring baffles of various shapes, or even floating lids. The conclusions of these studies have been summarised by Abramson (1966), later by Dodge (2000), who both point out the superior efficiency of baffles over other types of damping devices. A semi-analytical method was developed by Miles (1958) to estimate the damping ratio caused by horizontal annular baffles in a cylindrical tank, which compares well with the NASA's experimental results.
Mathematical models were developed in more recent publications to study specifically flows in circular tanks with annular baffles. For examples Gnitko et al. (2016), Wang and Zhou (2010), or Gavrilyuk et al. (2006) used domain decomposition approaches, with inviscid and irrotational flow assumptions. Wang et al. (2012) later generalised this method for multiple ring baffles, also extended to non-linear flows by Wang et al. (2019) through a multimodal analysis. Choudhary and Bora (2017) considered a rigid lid covering partially the free surface of the annular tank, pointing out a sharp increase of the first natural sloshing frequency as a function of increasing width of the lid. Their work, however, did not include in-and-out water motions over the lid.
Other studies tried to include the viscous effects caused by the flow separation at the edge of the baffle, essential to estimate the damping of sloshing waves. Violent sloshing in two-dimensional tanks with baffle was for instance treated by Jin et al. (2022) through CFD simulations. Isaacson and Premasiri (2001) established a purely analytical method to estimate the damping ratio caused by a baffle in a 2D rectangular tank, and used this coefficient through linear modal sloshing theory to describe the damped internal waves. Their method is based on the calculation of the dissipated energy over one wave period, using Morison equation (Morison et al., 1950). The baffle is locally considered as a 2D flat plate mirrored through the tank. Then, the estimation of the drag coefficient for such 2D plates can be found in many studies (Keulegan and Carpenter, 1958; Graham, 1980; Mentzoni, 2020). Maleki and Mansour (2008) presented a similar method for circular cylindrical tanks with annular baffle.
Another important effect of ring baffles reported by Abramson (1966) or Gavrilyuk et al. (2006) is the shift of the natural sloshing frequencies compared to the case without baffle. Estimations of the shifted frequencies caused by small internal bodies in closed-tanks were derived by Faltinsen and Timokha (2009) based on variational formulations. They showed in particular that the shift of the natural frequency can be expressed as a function of the baffle's added mass.

In the current work, the viscous damping and shifted natural sloshing frequency

caused by ring baffles are estimated based on results derived for two-dimensional flat plates. The plates are mirrored through the wall, and the results summed in the angular direction. Graham (1980) presented explicit expressions of the inertial and drag coefficients for oscillatory flows around bodies with sharp corners, valid for low Keulegan-Carpenter (KC) numbers, typically KC<2, and provided empirical coefficients for simple geometries, including flat plates. Mentzoni et al. (2018); Mentzoni and Kristiansen (2019, 2020) studied extensively solid and perforated plates under forced oscillations in infinite fluid through both experiments and CFD simulations. In particular, they proposed empirical added mass and damping coefficients based on their numerical simulations for perforated baffles, assuming a similar dependency on the KC number as developed by Graham (1980) for non-perforated plates. When the plates oscillates near the free surface, the viscous damping is generally higher than in infinite fluid, which was documented by Molin et al. (2007) or Song and Faltinsen (2013). More in-depth and exhaustive reviews of the literature on oscillating solid and perforated plates have been gathered by Ezoji et al. (2022).

Results based on the model presented in this work for a free-floating open-bottom dock with annular baffles were also published by Moreau et al. (2022), (2023a) and (2023b).

1.4 Structure of the thesis

In Chapter 2 the diffraction and radiation problems are solved in surge, pitch and heave through a domain decomposition method, both for the dock with and without a FOWT's spar. A linear system of equations is derived from matched eigenfunction expansions in order to solve the velocity potential in the whole fluid domain. Scattering loads, as well as added mass and damping coefficients are obtained by pressure integration on the bodies' surface, and the convergence of the results as a function of the number of eigenmodes is verified with simulations run with the software WAMIT.
A simplified representation of the dock with a closed bottom is considered in Chapter 3 to describe sloshing resonance. In this chapter, the internal flow is represented as an expansion of sloshing eigenmodes, and the effects of annular solid and perforated baffles expressed through modal equations.
Model tests were performed at scale 1:100 in the towing tank at SINTEF Ocean, which are described in Chapter 4.
The equations of motion are set in Chapter 5, defining our numerical model as closely as possible to the experimental one. Solutions of the radiation velocity potentials for the case of an open-bottom dock with baffle are proposed, inspired by the theories developed in Chapters 2 and 3. Hydrodynamic loads that account

for the effects of the baffles are derived, and included in the equations of motion through the added mass and damping coefficients.
Results in regular waves are presented in Chapter 6, and in irregular waves in Chapter 7. The main conclusions and thoughts for further works are drawn in Chapter 8.

2 | Diffraction and radiation

We present in this Chapter a semi-analytical model based on a linear potential flow theory and using a domain-decomposition approach to solve the radiation and diffraction problems for the floating dock, both without and with the spar of a FOWT. The results in term of added mass and damping coefficients, as well as exciting forces and moments caused by incident waves are compared to the ones obtained for the same geometries with the commercial software WAMIT based on boundary element methods (BEM). The semi-analytical model described in this Chapter will in particular be completed in the later Chapter 5 to include the effects of annular baffles.
The semi-analytical models are first presented in Sec. 2.1, and the radiation and diffraction problems treated in the Secs. 2.3 and 2.2, respectively. Convergence studies are carried out and the results are presented in Sec. 2.4.

2.1 Governing equations

2.1.1 Linear potential flow theory

Fluid motions in hydrodynamics are generally described by the incompressible Navier-Stokes (NS) equations (2.1) and (2.2) for a Newtonian fluid, respectively derived from Newton's *2nd* law, and the conservation of mass:

$$\left(\frac{\partial \mathbf{V}}{\partial t} + \mathbf{V}\cdot\nabla\mathbf{V}\right) = -\nabla\left(\frac{p}{\rho} + gz\right) + \nabla\cdot\left[\nu\left(\nabla\mathbf{V} + (\nabla\mathbf{V})^T\right)\right], \tag{2.1}$$

$$\nabla\cdot\mathbf{V} = 0, \tag{2.2}$$

where the three-dimensional fluid velocity $\mathbf{V}$ and fluid pressure p are unknown. $g = 9.81$ m/s^2 is the gravitational acceleration, z the Cartesian coordinate in the vertical upward direction, ρ the fluid density and ν the kinematic viscosity. Typically, the sea water has the density $\rho = 1025$ kg/m^3. In this current work however, we use the density of fresh water $\rho = 1000$ kg/m^3 to stay in agreement with the model tests that were made in unsalted water.
We assume that the flow is irrotational, i.e. $\nabla\times\mathbf{V} = 0$. The flow velocity can then be expressed as the gradient of a scalar potential:

$$\mathbf{V} = \nabla\Phi \tag{2.3}$$

Furthermore, the fluid is assumed to be inviscid. Inserting Eq. (2.3) in (2.1) and (2.2), the vector NS equation (2.1) becomes after integration the scalar equation

(2.4), also called Bernoulli equation, and Eq. (2.2) becomes the Laplace equation (2.5), both written as:

$$\frac{\partial \Phi}{\partial t} + \frac{1}{2}(\nabla\Phi \cdot \nabla\Phi) = -\frac{1}{\rho}p - gz + \mathrm{C}, \tag{2.4}$$

$$\nabla^2\Phi = 0. \tag{2.5}$$

For fluids with an interface with atmospheric air, the constant C is found by imposing the atmospheric pressure at the free surface boundary.
In the present work, we consider operational weather conditions, which in particular means that the steepness of incident waves are relatively low (see more details in Sec. 4.3.1). Water motions are thus assumed to be linear, and the quadratic term in the left-hand side of Eq. (2.4) is neglected. This linearity assumption should generally be made with caution for the internal flow inside the dock due to sloshing resonance. This last point is discussed in more details in Sec. 6.1.2.

2.1.2 Semi-analytical models

In this work, we model the floating dock as illustrated in Fig. 2.1. Its geometry is similar to the circular cylinder with thick wall studied by Mavrakos (1985, 1988), with the addition of bilge boxes at the bottom of the dock. The hydrodynamic loads due to pitching and heaving are generally higher with the bilge boxes, such that they can not be neglected in our analysis. We also consider the case where the spar of a FOWT is floating inside the dock, as illustrated in Fig. 2.2, where the spar has a circular cross-section with constant radius a_0. All the geometrical parameters are defined in these two figures. Variables related to the spar are denoted with the upper index $^{(1)}$, and the ones related to the dock with the upper index $^{(2)}$. A Cartesian coordinate system is defined with its origin at the mean free surface. The bodies' mean wetted surface is denoted S_0. We generally use complex notations to simplify the calculations, where the physical quantities correspond to the real parts of the given variables.

Long-crested incident regular waves of amplitudes ζ_A travel in the positive x-direction at the frequency ω. The instantaneous free-surface elevation of incident waves is expressed with cylindrical coordinates by:

$$\zeta_0 = \zeta_A e^{i(kr\cos(\theta)-\omega t)}, \tag{2.6}$$

where $k = 2\pi/\lambda$ is the wave number, and λ the wave length. The velocity potential of the undisturbed incident waves is then written (Faltinsen, 1990):

$$\Phi_0 = \frac{\zeta_A g \cosh(k(z+h))}{\omega \cosh(kh)} e^{i(kr\cos(\theta)-\omega t)}, \tag{2.7}$$

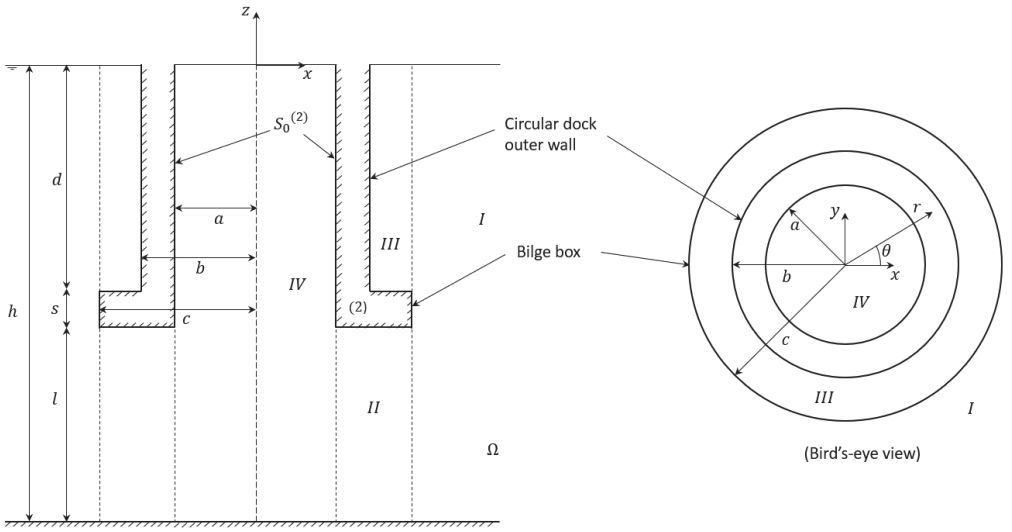

Figure 2.1: *Sketch of the upright, circular, bottomless floating dock with bilge boxes. Explanation of parameters and the division of the domain* Ω *into the four subdomains denoted I–IV used for the present analysis. A Cartesian Earth-fixed coordinate system* $Oxyz$ *is adopted with the origin at the mean free-surface and the z-axis positive upwards.*

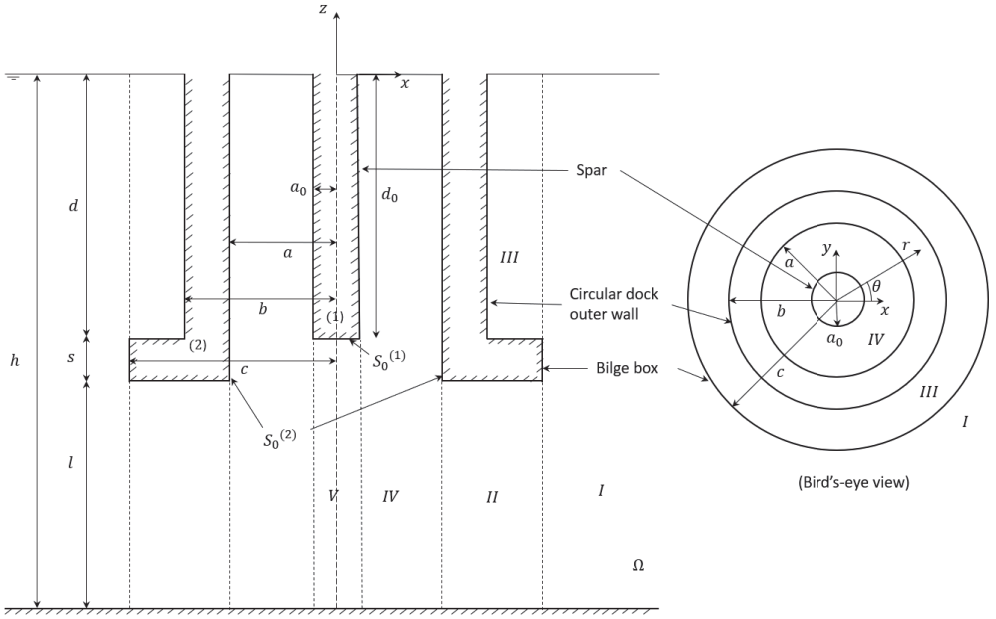

Figure 2.2: *Sketch of the spar of a floating wind turbine (body* $^{(1)}$*) inside the upright cylindrical dock with bilge boxes (body* $^{(2)}$*). The domain* Ω *is divided into five subdomains denoted I to V. The mean wetted surface of the bodies are denoted* S_0*.*

where h the water depth. Due to symmetry, only the bodies' motions in surge, heave and pitch are excited by incident waves. The motions of both bodies are generally expressed by:

$$\eta_j^{(k)} = \overline{\eta}_j^{(k)} e^{-i\omega t}, \quad j \in \{1,3,5\}, \quad k \in \{1,2\}, \tag{2.8}$$

where $\overline{\eta}_j^{(k)}$ is the complex amplitude of the j^{th} degree of freedom (DoF) of the body (k).
As the incident waves, the total linear potential flow Φ must also be harmonic in ω due to linearity of the problem. Φ is defined in the domain Ω as the solution of the standard boundary value problem (BVP):

$$\nabla^2\Phi = 0, \quad \text{in}\,\Omega, \tag{2.9}$$

$$\frac{\partial\Phi}{\partial z} = \frac{\omega^2}{g}\Phi \ \text{ on}\, z = 0, \tag{2.10}$$

$$\frac{\partial\Phi}{\partial z} = 0 \ \text{ on}\, z = -h, \tag{2.11}$$

$$\frac{\partial\Phi}{\partial n} = -i\omega\boldsymbol{\eta}^{(k)} \cdot \boldsymbol{n}^{(k)} \ \text{ on } \ S_0^{(k)}, k \in \{1,2\}. \tag{2.12}$$

$\boldsymbol{\eta}^{(k)}$ is the 6-dimensional generalised motion vector of the body (k), $\boldsymbol{n}^{(k)} = [n_1^{(k)}\ n_2^{(k)}\ n_3^{(k)}]^T$ is the unit vector pointing outwards from the body (k), $\boldsymbol{r} = [r\cos(\theta)\ r\sin(\theta)\ z]^T$ is the position vector, and $[n_4^{(k)}\ n_5^{(k)}\ n_6^{(k)}]^T = \boldsymbol{r} \times \boldsymbol{n}^{(k)}$. Φ is commonly linearly decomposed as a scattered potential Φ_S, which satisfies (2.9)-(2.11) and the body-boundary conditions $\partial\Phi_S/\partial n = 0$ on $S_0^{(k)}$, and radiation potentials $\Phi_j^{(k)}$ which satisfy the body-boundary conditions $\partial\Phi_j^{(k)}/\partial n = -i\omega\eta_j^{(k)} n_j^{(k)}$ on $S_0^{(k)}$ when there is no incident waves:

$$\Phi(r,\theta,z,t) = \Phi_S + \sum_{k\in\{1,2\}} \sum_{j\in\{1,3,5\}} \Phi_j^{(k)}. \tag{2.13}$$

The free surface elevation is obtained from the kinematic free surface boundary condition:

$$\frac{\partial\zeta}{\partial t} = \frac{\partial\Phi}{\partial z} \ \text{in}\ z = 0. \tag{2.14}$$

The radiated potentials can more conveniently be written:

$$\Phi_j^{(k)} = -i\omega\phi_j^{(k)}(r,z)\eta_j^{(k)} \begin{cases} 1 & \text{for} \quad j = 3 \\ \cos(\theta) & \text{for}\, j = 1,5 \end{cases} . \tag{2.15}$$

$\phi_j^{(k)}(r,z)$ describes the velocity potential caused by a forced motion with unit velocity of the body $^{(k)}$ in the j^{th} DoF when there is no incident waves. In addition to the boundary conditions (2.10) to (2.12), both the diffracted potential $(\Phi_S - \Phi_0)$ and the radiated potentials $\Phi_j^{(k)}$ are local flow perturbations which must vanish far away from the bodies. Both these potentials must therefore also satisfy a radiation condition, which can be expressed as (Sommerfeld, 1948):

$$\lim_{r\to\infty} \sqrt{kr}\left(\frac{\partial(\phi)}{\partial r} - ik(\phi)\right) = 0. \tag{2.16}$$

For most marine structures, it is generally not possible to obtain analytical solutions of the Laplace equation due to the complexity of the bodies' geometry. Hence, both the radiation and diffraction problems are typically solved by software based on boundary element methods. In such methods, the potential flow in the whole domain is expressed through astute mathematical transformations as generated by combined source and dipole distributions on the body's surface along with a free-surface Green function. Thanks to these formulations, it is not necessary to spatially discretise the whole domain, but only the body's mean surface S_0. A linear matrical equation of order N_{panels} must be solved, where N_{panels} is the number of panels forming the body's mesh. The computational time associated to these methods is typically of the order $O\left(N_{\text{panels}}^3\right)$, even though this time can be reduced by iterative schemes.

In the present work, both the geometries of the dock and the FOWT's spar have a symmetry of revolution, allowing us to establish semi-analytical solutions of the radiated and scattered potentials using a domain decomposition approach. The fluid domain Ω is divided in four subdomains of revolution I-IV, similar as in Mavrakos' papers with an additional domain above the bilge boxes (cf. Fig 2.1). A fifth subdomain is defined below the spar when the one is introduced in the dock (cf. Fig. 2.2). In each subdomain, the Laplace equation is solved into an infinite number of eigenmodes. The potential Φ_S and $\phi_j^{(k)}$ are expressed as the summation of these eigenmodes, weighted by unknown modal coefficients. The matching of normal velocities and dynamic pressures are averaged by integrations over each vertical boundary common to two adjacent subdomains or by integration over the body boundaries, resulting in a linear system of equations whose solution gives the desired modal coefficients.

The choice of eigenmodes and the derivation of the hydrodynamic loads resulting from the radiation and diffraction problems are presented in the two next sections for the dock with and without the spar. In addition, the radiation and diffraction problems for a circular cylinder as shown in Fig. 2.3 with the radius and draught of the dock have also been solved. This simplified representation of the dock is used in Chapters 3 and 5 as an ingredient in handling the sloshing problem, along with sloshing theories in closed containers. The solutions of the diffraction and radiation problems of a circular cylinder are for instance treated in details by Garrett

(1971) and Yeung (1980), respectively, both using a similar domain decomposition approach. The derivation of semi-analytical solutions for this geometry is therefore not repeated in this work.

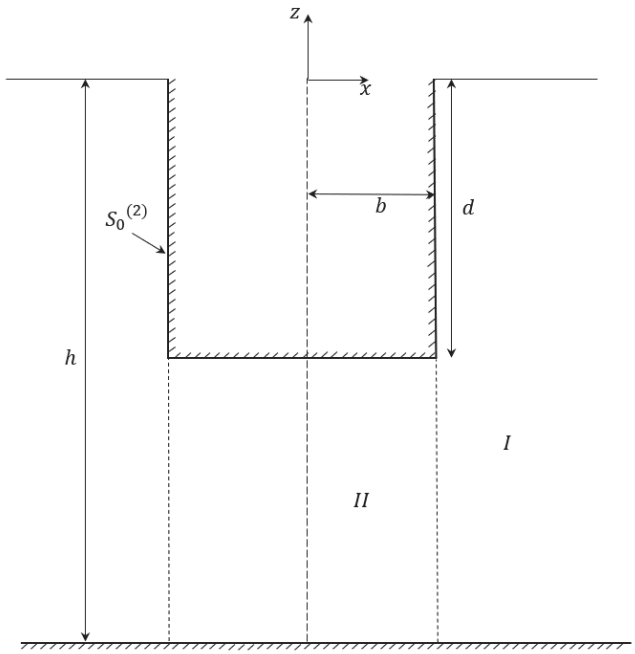

Figure 2.3: *Sketch of the middle cross section of an imagined dock without bilge boxes and with a closed bottom. Radiation and diffraction problems are solved by decomposing the domain* Ω *into two subdomains, similar to Garrett (1971) and Yeung (1980).*

2.2 Diffraction problem

2.2.1 Polar harmonics

In this section, the scattered potential Φ_S caused by the scattering of incident waves on the motionless dock is solved through a domain decomposition method. First, we express ζ_0 and Φ_0 in Eqs.(2.6) and (2.7) as Jacobi-Anger expansions (Olver et al., 2010):

$$\zeta_0 = \zeta_A \sum_{p=0}^{\infty} \epsilon_p i^p J_p(kr)\cos(p\theta)e^{-i\omega t}, \tag{2.17}$$

$$\Phi_0 = \frac{g\zeta_A}{\omega}\frac{\cosh(k(z+h))}{\cosh(kh)} \sum_{p=0}^{\infty} \epsilon_p i^p J_p(kr)\cos(p\theta)e^{-i\omega t}, \tag{2.18}$$

where $\epsilon_0 = 1$, $\epsilon_p = 2$ for $p \in \mathbb{N}^*$, and $J_p,\ p \in \mathbb{N}$ are the Bessel functions of the first kind (see Appendix B.1). The total scattered free-surface elevation and velocity potential can be expressed under the same form:

$$\zeta_S(r,\theta,t) = \zeta_A \sum_{p=0}^{\infty} \epsilon_p i^p \zeta_p(r)\cos(p\theta)e^{-i\omega t}, \tag{2.19}$$

$$\Phi_S(r,\theta,z,t) = -i\omega\zeta_A \sum_{p=0}^{\infty} \epsilon_p i^p \phi_p(r,z)\cos(p\theta)e^{-i\omega t}. \tag{2.20}$$

The expansion (2.20) follows the convention first proposed by Miles and Gilbert (1968) and mostly used in the literature (Garrett, 1970, 1971; Mavrakos, 1985), which introduces the displacement potentials ϕ_p (corresponding to the potentials $-i\omega\phi_p$). Inserting Φ_S into Eqs.(2.9)-(2.11) and the non-penetration condition on $S_0^{(2)}$, and using the orthogonal properties of the cosine function, the boundary value problem for each displacement potential ϕ_p is expressed as:

$$\frac{\partial^2\phi_p}{\partial z^2} + \frac{1}{r}\frac{\partial}{\partial r}\left(r\frac{\partial\phi_p}{\partial r}\right) - \frac{p^2}{r^2}\phi_p = 0 \ \text{ in } \Omega, \tag{2.21}$$

$$\frac{\partial\phi_p}{\partial z} = \frac{\omega^2}{g}\phi_p \ \text{ on } z = 0, \tag{2.22}$$

$$\frac{\partial\phi_p}{\partial z} = 0 \ \text{ on } z = -h, \tag{2.23}$$

$$\frac{\partial\phi_p}{\partial n} = 0 \ \text{ on } S_0^{(2)}. \tag{2.24}$$

The kinematic free-surface boundary condition $\dfrac{\partial\zeta_S}{\partial t} = \dfrac{\partial\Phi_S}{\partial z}$ in $z = 0$ gives the relationship between the functions ζ_p and ϕ_p:

$$\zeta_p(r) = \frac{\partial\phi_p}{\partial z}(r,0),\ p \in \mathbb{N}. \tag{2.25}$$

2.2.2 Floating dock with bilge boxes

Solutions of Eq. (2.21) are established in each subdomain I-IV by separating the variables. We insert the decomposition $\phi_p(r,z) = W_{p,q}(r)Z_{p,q}(z)$ in Eq. (2.21), where the index q is introduced to distinguish the different solutions of the Laplace equation. Dividing by $W_{p,q}Z_{p,q}$, we get:

$$\underbrace{\frac{Z''_{p,q}}{Z_{p,q}}}_{=-C^2_{p,q}} + \frac{1}{rW_{p,q}}\frac{d}{dr}\left(r\frac{dW_{p,q}}{dr}\right) - \frac{p^2}{r^2} = 0. \tag{2.26}$$

Since $W_{p,q}$ and $Z_{p,q}$ are independent, $Z''_{p,q}/Z_{p,q} = -C^2_{p,q}$ must be constant. The solutions for $Z_{p,q}$ are therefore trigonometric functions, for which the constants of integration are imposed by horizontal boundary conditions. In the subdomains with a free surface, we write either $C_{p,q} = \alpha_q$ in the subdomains I and IV or $C_{p,q} = \beta_q$ in the subdomain III above the bilge boxes. The free-surface boundary condition (2.22) and either the condition (2.23) on the sea bottom in I and IV or (2.24) on the top of the bilge boxes in III impose the following relationships:

$$\frac{\omega^2}{g} + \alpha_q \tan(\alpha_q h) = 0, \tag{2.27}$$

$$\frac{\omega^2}{g} + \beta_q \tan(\beta_q d) = 0, \tag{2.28}$$

where h is the water depth and d the distance from the bilge boxes to the mean free surface. The Eqs. (2.27) and (2.28) admit only one imaginary solution (Chatjigeorgiou, 2018), respectively $\alpha_0 = -ik$ and $\beta_0 = -i\tilde{k}$, and an infinity of real solutions, respectively α_q and β_q, $q \in \mathbb{N}^*$, ordered by increasing values. The wave numbers k and $\tilde{k}$ are real and satisfy the dispersion relationships:

$$\frac{\omega^2}{g} = k \tanh(kh) \tag{2.29}$$

$$\frac{\omega^2}{g} = \tilde{k} \tanh(\tilde{k}d). \tag{2.30}$$

$Z_{p,q}$ are then given by:

$$Z_q(z) = N_q^{-\frac{1}{2}} \cos(\alpha_q(z+h)),\ q \in \mathbb{N},\ \text{in I and IV}, \tag{2.31}$$

$$\tilde{Z}_q(z) = \tilde{N}_q^{-\frac{1}{2}} \cos(\beta_q(z+d)),\ q \in \mathbb{N},\ \text{in III}. \tag{2.32}$$

The normalised coefficients

$$N_q = \frac{1}{2}\left[1 + \frac{\sin(2\alpha_q h)}{2\alpha_q h}\right], \tag{2.33}$$

$$\tilde{N}_q = \frac{1}{2}\left[1 + \frac{\sin(2\beta_q d)}{2\beta_q d}\right], \tag{2.34}$$

were introduced similar to Miles and Gilbert (1968), such that Z_q and $\tilde{Z}_q$ satisfy the orthonormal conditions:

$$\frac{1}{h}\int_{-h}^{0} Z_i(z)Z_j(z)dz = \delta_{i,j},\ (i,j) \in \mathbb{N}^2, \tag{2.35}$$

$$\frac{1}{d}\int_{-d}^{0} \tilde{Z}_i(z)\tilde{Z}_j(z)dz = \delta_{i,j},\ (i,j) \in \mathbb{N}^2. \tag{2.36}$$

δ is the Kronecker delta symbol.

When the constant $C^2_{p,q}$ is strictly negative, Eq. (2.26) for $W_{p,q}$ is called the Bessel equation. Solutions are Bessel functions of the first and second kinds, respectively J_p and Y_p. For strictly positive $C^2_{p,q}$, Eq. (2.26) becomes the modified Bessel equations whose solutions are the modified Bessel functions I_p and K_p. More details about the definitions and properties of Bessel functions are given in Appendix B.1. The displacement potentials ϕ_p are then expressed as the summation of all the solutions of the Laplace equations.

In the external subdomain I, they are written as:

$$\phi^I_p(r,z) = \left[J_p(kr) - \frac{J_p(kc)}{H_p(kc)}H_p(kr)\right]\frac{Z_0(z)}{Z'_0(0)} + b\sum_{q=0}^{\infty} A^I_{p,q}\frac{K_p(\alpha_q r)}{K_p(\alpha_q c)}Z_q(z). \tag{2.37}$$

H_p is the Hankel function of the first kind, and we have the relationship $K_p(-ikr) = \frac{1}{2}\pi i^{p+1}H_p(kr)$ and $I_p(\alpha_0 r) = J_p(kr)$. The first term inside the bracket in Eq. (2.37) accounts for incident waves, and is written to be null in $r = c$ in order to simplify the matching conditions. Only the Bessel functions of the second kind K_p are solutions since I_p diverge for large r, which contradicts the radiation condition in the subdomain I. We note that the modes $p \geq 1$ are evanescent waves exponentially decaying at large r (Mavrakos, 1988). The eigenmodes in Eq. (2.37) are multiplied by the dock's external radius b to keep the unknown $A^I_{p,q}$ coefficients non-dimensional.
The potentials in the subdomains II and III are next given by:

$$\phi^{II}_p(r,z) = b\sum_{q=0}^{\infty}\epsilon_q\left[A^{II}_{1,p,q}P^{II}_{p,q}(r) + A^{II}_{2,p,q}Q^{II}_{p,q}(r)\right]\cos\left(\frac{q\pi(z+h)}{l}\right), \tag{2.38}$$

$$\phi_p^{III}(r,z) = b\sum_{q=0}^{\infty}[A_{1,p,q}^{III}P_{p,q}^{III}(r) + A_{2,p,q}^{III}Q_{p,q}^{III}(r)]\tilde{Z}_q(z), \tag{2.39}$$

where the functions $P_{p,q}(r)$ and $Q_{p,q}(r)$ have been defined similar to Garrett (1970) in order to simplify the matching conditions for the potential at the boundaries with adjacent domains, and to lighten the notations:

$$\begin{cases} P_{0,0}^{II}(r) = \dfrac{\ln(\frac{r}{a})}{\ln(\frac{c}{a})} \\ \\ Q_{0,0}^{II}(r) = \dfrac{\ln(\frac{c}{r})}{\ln(\frac{c}{a})} \end{cases} \quad \text{for } q = 0,\ p = 0, \tag{2.40}$$

$$\begin{cases} P_{p,0}^{II}(r) = \dfrac{(\frac{r}{a})^p - (\frac{a}{r})^p}{(\frac{c}{a})^p - (\frac{a}{c})^p} \\ \\ Q_{p,0}^{II}(r) = \dfrac{(\frac{c}{r})^p - (\frac{r}{c})^p}{(\frac{c}{a})^p - (\frac{a}{c})^p} \end{cases} \quad \text{for } q = 0,\ p \in \mathbb{N}^*, \tag{2.41}$$

$$\begin{cases} P_{p,q}^{II}(r) = \dfrac{K_p(\frac{q\pi a}{l})I_p(\frac{q\pi r}{l}) - I_p(\frac{q\pi a}{l})K_p(\frac{q\pi r}{l})}{K_p(\frac{q\pi a}{l})I_p(\frac{q\pi c}{l}) - I_p(\frac{q\pi a}{l})K_p(\frac{q\pi c}{l})} \\ \\ Q_{p,q}^{II}(r) = \dfrac{K_p(\frac{q\pi r}{l})I_p(\frac{q\pi c}{l}) - I_p(\frac{q\pi r}{l})K_p(\frac{q\pi c}{l})}{K_p(\frac{q\pi a}{l})I_p(\frac{q\pi c}{l}) - I_p(\frac{q\pi a}{l})K_p(\frac{q\pi c}{l})} \end{cases} \quad \text{for } q \in \mathbb{N}^*,\ p \in \mathbb{N}^*, \tag{2.42}$$

$$\begin{cases} P_{p,q}^{III}(r) = \dfrac{K_p(\beta_q b)I_p(\beta_q r) - I_p(\beta_q b)K_p(\beta_q r)}{K_p(\beta_q b)I_p(\beta_q c) - I_p(\beta_q b)K_p(\beta_q c)} \\ \\ Q_{p,q}^{III}(r) = \dfrac{K_p(\beta_q r)I_p(\beta_q c) - I_p(\beta_q r)K_p(\beta_q c)}{K_p(\beta_q b)I_p(\beta_q c) - I_p(\beta_q b)K_p(\beta_q c)} \end{cases} \quad \text{for } q \in \mathbb{N},\ p \in \mathbb{N}, \tag{2.43}$$

In subdomain IV, only the modified Bessel functions of the first kind I_p are physical since K_p diverge for $r = 0$. The potential in this subdomain is written:

$$\phi_p^{IV}(r,z) = b\sum_{q=0}^{\infty}A_{p,q}^{IV}\frac{I_p(\alpha_q r)}{I_p(\alpha_q a)}Z_q(z). \tag{2.44}$$

For each mode $p \in \mathbb{N}$, we have introduced an infinite number of unknown coefficients $A_{p,q}$, $q \in \mathbb{N}$, which remain to be determined by establishing the matching conditions on all the vertical boundaries. First, the averaged continuity

of the dynamic pressure between two consecutive subdomains is enforced over the corresponding boundary, in the way of Miles and Gilbert (1968):

$$\int_{-h}^{-(d+s)} \phi_p^{II}(a,z)\cos\left(\frac{q\pi(z+h)}{l}\right)dz = \int_{-h}^{-(d+s)} \phi_p^{IV}(a,z)\cos\left(\frac{q\pi(z+h)}{l}\right)dz, \tag{2.45}$$

$$\int_{-h}^{-(d+s)} \phi_p^{II}(c,z)\cos\left(\frac{q\pi(z+h)}{l}\right)dz = \int_{-h}^{-(d+s)} \phi_p^{I}(c,z)\cos\left(\frac{q\pi(z+h)}{l}\right)dz, \tag{2.46}$$

$$\int_{-d}^{0} \phi_p^{III}(c,z)\tilde{Z}_q(z)dz = \int_{-d}^{0} \phi_p^{I}(c,z)\tilde{Z}_q(z)dz. \tag{2.47}$$

Then the averaged continuity of the normal velocity, as well as the non-penetration condition on the vertical walls are assured by integration over the whole water depth:

$$\int_{-d}^{0} \frac{\partial \phi_p^{III}}{\partial r}(b,z)\tilde{Z}_q(z)dz = 0, \tag{2.48}$$

$$\int_{-h}^{0} \frac{\partial \phi_p^{I}}{\partial r}(c,z)Z_q(z)dz = \int_{-h}^{-(d+s)} \frac{\partial \phi_p^{II}}{\partial r}(c,z)Z_q(z)dz + \int_{-d}^{0} \frac{\partial \phi_p^{III}}{\partial r}(c,z)Z_q(z)dz, \tag{2.49}$$

$$\int_{-h}^{0} \frac{\partial \phi_p^{IV}}{\partial r}(a,z)Z_q(z)dz = \int_{-h}^{-(d+s)} \frac{\partial \phi_p^{II}}{\partial r}(a,z)Z_q(z)dz. \tag{2.50}$$

Because of the orthogonality properties of the functions Z_q, $\tilde{Z}_q$, and cos, respectively, these equations result in a linear system for the coefficients $A_{p,q}$, $q \in \mathbb{N}$, independently for each $p \in \mathbb{N}$. In practice, the sums from the potential expansions must be truncated. We write N_S the total number of polar harmonics in Eq. (2.20), and N_I, N_{II}, N_{III} and N_{IV} the numbers of modes kept in the subdomains I, II, III and IV, i.e. in the expansions (2.37), (2.38), (2.39) and (2.44) for the potential ϕ_p. The same number of modes in the domains I to IV are chosen for each $p \in \left[0, N_S\right]$ for the sake of simplicity. Eqs (2.45) to (2.48) give a relationship between each unknown coefficients A^{II} and A^{III} as a function of the coefficients A^{I} and A^{IV}, which can be substituted in the right hand side of Eqs (2.49) and (2.50). The order of the linear systems resulting from the matching conditions is then reduced to $N_I + N_{IV}$ for all fixed $p \in \left[0, N_S\right]$. This system is condensed by the matricial equation

$$\mathbb{B}^S \boldsymbol{A}^S = \boldsymbol{C}^S \tag{2.51}$$

for the variable $\boldsymbol{A}^S = \left[A^I_{p,1} \cdots A^I_{p,N_I}\, A^{IV}_{p,1} \cdots A^{IV}_{p,N_{IV}}\right]^T$. The upper index S stands here for "Scattering". The coefficients of the matrices $\mathbb{B}^S$, $\boldsymbol{C}^S$ and the relation to the remaining coefficients $A_{p,q}$ are given in Appendix A.
The hydrodynamic exciting forces and moments are derived by integrating the dynamic pressure on the walls of the structure:

$$F^S_j = \rho \int\int_{S_0^{(2)}} \frac{\partial \Phi_S}{\partial t}\, n_j dS = -\omega^2 \zeta_A \rho \sum_{p=0}^{\infty} \epsilon_p i^p \left[\int\int_{S_0^{(2)}} \phi_p(r,z)\cos(p\theta)\, n_j^{(2)} dS\right] e^{-i\omega t}, \tag{2.52}$$

for $j \in \{1,3,5\}$. Because of the orthogonal properties of cosine, only the mode $p = 1$ gives a non-zero term for the force in surge, and moment in pitch. In heave, the only contribution comes from the symmetric mode $p = 0$.

2.2.3 Floating dock with a FOWT's spar

When the spar is introduced in the dock (cf. Fig. 2.2), displacement potentials in the domain IV between the dock and the spar now include modified Bessel functions of the first kind I_p as the singularity in $r = 0$ disappear. Similarly to domain III, we write:

$$\phi^{IV}_p(r,z) = b\sum_{p=0}^{\infty}[A^{IV}_{1,p,q} P^{IV}_{p,q}(r) + A^{IV}_{2,p,q} Q^{IV}_{p,q}(r)] Z_q(z), \tag{2.53}$$

where we introduced the functions:

$$\begin{cases} P^{IV}_{p,q}(r) = \dfrac{K_p(\alpha_q a_0) I_p(\alpha_q r) - I_p(\alpha_q a_0) K_p(\alpha_q r)}{K_p(\alpha_q a_0) I_p(\alpha_q a) - I_p(\alpha_q a_0) K_p(\alpha_q a)}, \ (p,q) \in \mathbb{N}^2, \\ \\ Q^{IV}_{p,q}(r) = \dfrac{K_p(\alpha_q r) I_p(\alpha_q a) - I_p(\alpha_q r) K_p(\alpha_q a)}{K_p(\alpha_q a_0) I_p(\alpha_q a) - I_p(\alpha_q a_0) K_p(\alpha_q a)}, \ (p,q) \in \mathbb{N}^2. \end{cases} \tag{2.54}$$

The expansion of ϕ_p in the domain V below the spar is written similar to Garrett (1971):

$$\phi^V_p(r,z) = bA^V_{p,0}(\frac{r}{a_0})^p + 2b\sum_{q=1}^{\infty} A^V_{p,q} \frac{I_p(\frac{q\pi}{h-d_0} r)}{I_p(\frac{q\pi}{h-d_0} a_0)} \cos\left(\frac{q\pi(z+h)}{h-d_0}\right). \tag{2.55}$$

We note that the first term is constant for $p = 0$, which matters to estimate the loads in heave. This term was pointed out by Garrett (1971) to be incorrectly dismissed in the work of Miles and Gilbert (1968). The same constant appear implicitly for the mode $q = 0$ and $p = 0$ in the subdomain II below the bilge boxes (cf. Eqs. (2.38) and (2.40)), together with a logarithmic term. In the subdomain V, there is no such term in "$\log(r)$", as it is nonphysical in $r = 0$.

The potentials ϕ_p in the subdomains I, II and III have the same expressions as for the dock without spar (cf. Eqs. (2.37), (2.38) and (2.39)). In addition to the matching conditions (2.45)-(2.50), averaged continuous pressure and normal velocity are imposed in $r = a_0$ by integration over the boundary:

$$\int_{-h}^{d_0} \phi_p^{IV}(a_0, z) \cos(\frac{q\pi(z+h)}{h-d_0}) dz = \int_{-h}^{d_0} \phi_p^{V}(a_0, z) \cos(\frac{q\pi(z+h)}{h-d_0}) dz, \tag{2.56}$$

$$\int_{-h}^{0} \frac{\partial \phi_p^{IV}}{\partial r}(a_0, z) Z_q(z) dz = \int_{-h}^{0} \frac{\partial \phi_p^{V}}{\partial r}(a_0, z) Z_q(z) dz. \tag{2.57}$$

Conserving the notations introduced for the dock without spar, we write N_I-N_V the number of modes, indexed by q, kept in the subdomain I-V. For each polar mode $p \in \mathbb{N}$, the matching conditions result in a linear system of equations for the unknown coefficients $A_{p,q}^I$ to $A_{p,q}^V$. As in the previous section, the size of this system is reduced to $N_I + N_{IV}$ through astute substitutions. The matricial equation (2.51) is then solved for the variable $\boldsymbol{A}^S = \left[A_{p,1}^I \cdots A_{p,N_I}^I A_{2,p,1}^{IV} \cdots A_{2,p,N_{IV}}^{IV}\right]^T$. The coefficients of the matrices are given in Appendix A. Finally, the hydrodynamic loads on each body caused the scattering problem are:

$$F_j^{(k),S} = -\omega^2 \zeta_A \rho \sum_{p=0}^{\infty} \epsilon_p i^p \left[\int \int_{S_0^{(k)}} \phi_p(r, z) \cos(p\theta)\, n_j^{(k)} dS \right] e^{-i\omega t}, \;\; j \in \{1, 3, 5\}, k \in \{1, 2\}, \tag{2.58}$$

where the only difference from Eq. (2.52) is that the integration is made over each body's surface $S_0^{(k)}$, instead of $S_0^{(2)}$ only.

2.2.4 MacCamy and Fuchs (1954)

Because the draught of the dock is high compared to wave lengths ($\lambda/(d+s) < 2$), the exciting force in surge and moment in pitch on the dock can be verified thanks to MacCamy and Fuchs (1954)'s formula, which is exact for an upright cylinder extended to the sea bottom under the assumption of linear potential flow theory, as in our work. In their work, the scattered potential is also expressed as an expansion of polar harmonics, which have a much simpler form due to the absence of evanescent waves (i.e. the modes $q \geq 1$). Only the first polar mode $p = 1$ contributes to the loads in surge and pitch. From the dynamic pressure, the horizontal force per unit length in z is given by:

$$f_x(z) = \frac{4\rho g \zeta_A \cosh(k(h+z))}{k \cosh(kh)} A(kb) e^{-i\omega t + \alpha}, \tag{2.59}$$

where

$$A(kb) = \frac{1}{\sqrt{J_1'^2(kb) + Y_1'^2(kb)}}, \tag{2.60}$$

$$\alpha = -\tan^{-1}\frac{Y_1'(kb)}{J_1'(kb)}. \tag{2.61}$$

The force in surge and moment in pitch are obtained by integration over the draught of the dock:

$$F_1 = \int_{-(d+s)}^{0} f_x(z)dz, \tag{2.62}$$

$$F_5 = \int_{-(d+s)}^{0} z f_x(z)dz, \tag{2.63}$$

which gives:

$$F_1^S = 4\rho g \zeta_A \frac{\sinh(kh) - \sinh(k(h-(d+s)))}{k^2\cosh(kh)} A(kb) e^{-i\omega t+\alpha}, \tag{2.64}$$

$$F_5^S = 4g\rho\zeta_A A(kb)\left[\frac{(d+s)k\sinh(k(h-(d+s))) + \cosh(k(h-(d+s))) - \cosh(kh)}{k^3\cosh(kh)}\right] e^{-i\omega t+\alpha}. \tag{2.65}$$

The derivation of Eq. (2.59) follows the one by MacCamy and Fuchs (1954) and is not detailed here. We can however note that the definition of the phase α in Eq.(2.61) differs from their work, introducing a difference of phase of π in the loads. This is due to that MacCamy and Fuchs (1954) define the incident potential Φ_0 with a difference of phase of π compared to one defined in this thesis (cf. Eq. 2.7).

2.3 Radiation problem

2.3.1 Floating dock with bilge boxes

The radiation potentials $\phi_j^{(2)}$ defined in Eq. (2.15) for the three degrees of freedom $j = 1, 3$ and 5 are solved in this section for the dock without spar (cf. Fig 2.1), through a similar domain decomposition method as for the diffraction problem. $p = 0$ corresponds here to the symmetric DoF, heave, and $p = 1$ to the anti-symmetric DoFs, surge and pitch. The potentials $\phi_j^{(2)}$ satisfy the Laplace equation (2.21), the

free-surface and bottom-boundary conditions (2.22) and (2.23), the body-boundary condition

$$\frac{\partial \phi_j^{(2)}}{\partial n} = n_j^{(2)}, \tag{2.66}$$

as well as the radiation condition for outgoing radiated waves

$$\lim_{r\to\infty} \sqrt{kr}\left(\frac{\partial \phi_j^{(2)}}{\partial r} - ik\phi_j^{(2)}\right) = 0. \tag{2.67}$$

The potentials in the subdomains I and IV correspond to the symmetric and anti-symmetric modes of the diffraction problem, with the difference that there is no incident waves and all the radiated potentials have to vanish for large r in subdomain I. They are given by

$$\phi_j^{(2),I}(r,z) = \psi \sum_{q=0}^{\infty} A_q^I \frac{K_p(\alpha_q r)}{K_p(\alpha_q c)} Z_q(z), \tag{2.68}$$

$$\phi_j^{(2),IV}(r,z) = \psi \sum_{q=0}^{\infty} A_q^{IV} \frac{I_p(\alpha_q r)}{I_p(\alpha_q a)} Z_q(z), \tag{2.69}$$

where $\psi = b$ for the problems in heave and surge, and $\psi = b^2$ for the problem in pitch.

The expansions are chosen to satisfy exactly all the horizontal boundary conditions in their corresponding subdomain. In the subdomains II and III, where a horizontal body-boundary condition is present, and similar to Yeung (1980), the potential is decomposed in:

- A particular solution $\phi_{j,m}^{(2)}$ that satisfies the Laplace equation, and all the horizontal boundary conditions when the forced motion is applied, but without any condition on the vertical boundaries (taken care of by $\phi_{j,h}^{(2)}$).

- A homogeneous solution $\phi_{j,h}^{(2)}$ that satisfies the Laplace equation when the structure is fixed, and which assures that the vertical matching with adjacent subdomains or body-boundary conditions are satisfied.

The potentials in the domain II and III are thus expressed as $\phi_j^{(2),II} = \phi_{j,h}^{(2),II} + \phi_{j,m}^{(2),II}$ and $\phi_j^{(2),III} = \phi_{j,h}^{(2),III} + \phi_{j,m}^{(2),III}$. The functions (2.70)-(2.73) are proposed for the particular solutions, and the homogeneous parts are given by (2.74) and (2.75):

$$\phi_{3,m}^{(2),II}(r,z) = \frac{(z+h)^2 - \dfrac{r^2}{2}}{2(h-(d+s))}, \tag{2.70}$$

$$\phi_{5,m}^{(2),II}(r,z) = -\frac{r(z+h)^2 - \dfrac{r^3}{4}}{2(h-(d+s))}, \tag{2.71}$$

$$\phi_{3,m}^{(2),III}(r,z) = z + \frac{g}{\omega^2}, \tag{2.72}$$

$$\phi_{5,m}^{(2),III}(r,z) = -\left(z + \frac{g}{\omega^2}\right) r, \tag{2.73}$$

$$\phi_{j,h}^{(2),II}(r,z) = \psi \sum_{q=0}^{\infty} \epsilon_q \left[A_{1,q}^{II} P_{m,q}^{II}(r) + A_{2,q}^{II} Q_{m,q}^{II}(r)\right] \cos\left(\frac{q\pi(z+h)}{l}\right), \tag{2.74}$$

$$\phi_{j,h}^{(2),III}(r,z) = \psi \sum_{q=0}^{\infty} \left[A_{1,q}^{III} P_{m,q}^{III}(r) + A_{2,q}^{III} Q_{m,q}^{III}(r)\right] \tilde{Z}_q(z). \tag{2.75}$$

We note that for the problem in surge, $\phi_{1,m}^{(2),II} = \phi_{1,m}^{(2),III} = 0$.

As for the diffraction problem, the averaged continuity of the dynamic pressure between two subdomains is assured by integration over the subdomains' common boundary:

$$\begin{aligned}
&\int_{-h}^{-(d+s)} \phi_{j,h}^{(2),II}(a,z) \cos\left(\frac{q\pi(z+h)}{l}\right) dz \\
&\quad = \int_{-h}^{-(d+s)} \left[\phi_j^{(2),IV}(a,z) - \phi_{j,m}^{(2),II}(a,z)\right] \cos\left(\frac{q\pi(z+h)}{l}\right) dz,
\end{aligned} \tag{2.76}$$

$$\begin{aligned}
&\int_{-h}^{-(d+s)} \phi_{j,h}^{(2),II}(c,z) \cos\left(\frac{q\pi(z+h)}{l}\right) dz \\
&\quad = \int_{-h}^{-(d+s)} \left[\phi_j^{(2),I}(c,z) - \phi_{j,m}^{(2),II}(c,z)\right] \cos\left(\frac{q\pi(z+h)}{l}\right) dz,
\end{aligned} \tag{2.77}$$

$$\int_{-d}^{0} \phi_{j,h}^{(2),III}(c,z) \tilde{Z}_q dz = \int_{-d}^{0} \left[\phi_j^{(2),I}(c,z) - \phi_{j,m}^{(2),III}(c,z)\right] \cos\left(\frac{q\pi(z+h)}{l}\right) dz, \tag{2.78}$$

while the conditions on the normal velocity for the problems in $\left|\begin{array}{l}\text{surge}\\ \text{heave}\\ \text{pitch}\end{array}\right.$, respectively, are imposed over the whole water depth:

$$\int_{-d}^{0} \frac{\partial \phi_{j,h}^{(2),III}}{\partial r}(b,z)\tilde{Z}_q(z)dz = \int_{-d}^{0} \left[\left|\begin{array}{l}1\\0\\z\end{array}\right| - \frac{\partial \phi_{j,m}^{(2),III}}{\partial r}(b,z)\right]\tilde{Z}_q(z)dz, \tag{2.79}$$

$$\int_{-h}^{0} \frac{\partial \phi_j^{(2),I}}{\partial r}(c,z)Z_q(z)dz = \int_{-h}^{-(d+s)} \frac{\partial \phi_j^{(2),II}}{\partial r}(c,z)Z_q(z)dz + \int_{-(d+s)}^{-d} \left|\begin{array}{l}1\\0\\z\end{array}\right| Z_q(z)dz + \int_{-d}^{0} \frac{\partial \phi_j^{(2),III}}{\partial r}(c,z)Z_q(z)dz, \tag{2.80}$$

$$\int_{-h}^{0} \frac{\partial \phi_j^{(2),IV}}{\partial r}(a,z)Z_q(z)dz = \int_{-h}^{-(d+s)} \frac{\partial \phi_j^{(2),II}}{\partial r}(a,z)Z_q(z)dz + \int_{-(d+s)}^{0} \left|\begin{array}{l}1\\0\\z\end{array}\right| Z_q(z)dz. \tag{2.81}$$

The sums are once again truncated, and the modes kept in the four subdomains for each DoF denoted N_I, N_{II}, N_{III} and N_{IV}. Similar to the diffraction problem, the matching equations are expressed by the matrical equation

$$\mathbb{B}^R \boldsymbol{A}^R = \boldsymbol{C}^R \tag{2.82}$$

of order $N_I + N_{IV}$ for each DoF, and for the unknown vector $\boldsymbol{A}^R = \left[A_1^I \cdots A_q^I\, A_1^{IV} \cdots A_q^{IV}\right]^T$. The upper index R stands here for "Radiation". The analytical expressions of the matrices $\mathbb{B}^R$ and $\boldsymbol{C}^R$, and the relation to the remaining coefficient A_q are given in Appendix A.2.3.

Once the potential is known in each domain, the hydrodynamic coefficients are determined by Newman (1977):

$$a_{s,j} + i\frac{b_{s,j}}{\omega} = -\rho \int\int_{S_0^{(2)}} \phi_j^{(2)} \cos(p\theta) n_s dS, \quad (s,j) \in \{1,3,5\}^2. \tag{2.83}$$

The added mass and damping matrices are symmetric, such that $a_{1,5} = a_{5,1}$ and $b_{1,5} = b_{5,1}$ since there is no current nor forward speed. Yeung (1980) advises for instance to only calculate the coupled coefficients $a_{1,5}$ and $b_{1,5}$ from the solution of the problem in pitch ϕ_5: the calculations are indeed simplified by that n_1 is null on the horizontal boundaries. The analytical expressions of the added mass and

damping coefficients in Eq. (2.83) are given in Appendix A.4.1.
We can note that Newman (1962) established very simple relationships for axi-symmetrical bodies giving the amplitudes - but not the phases - of the loads F_j^S caused by scattered waves as functions of the damping coefficients $b_{s,j}$ (cf. Appendix A.4.1). It is more generally possible to estimate the loads of scattered waves on marine structures from the solution of the radiation problem using Haskind (1954)'s formula. In our case, Haskind (1954)'s formula comes with heavy calculations and has not been used to verify exciting forces and moments in Sec. 2.2. Furthermore, with such method, the pressure field of the scattered flow remains unknown, as well as the scattered free-surface elevation ζ_S.

2.3.2 Floating dock with a FOWT's spar

Six radiation problems in surge, heave and pitch for both the dock and the spar are considered in this section for the geometry presented in Fig. 2.2.
The homogeneous solutions (2.68), (2.74) and (2.75) of the potentials in the subdomains I, II and III are identical as for the dock without spar, as well as the matching conditions (2.76)-(2.81), replacing the upper index $^{(2)}$ by $^{(1)}$ for the problems corresponding to the spar's motions. The particular solutions $\phi_{j,m}^{(2),II}$ and $\phi_{j,m}^{(2),III}$ for the dock in the subdomains II and III - respectively below and above the bilge boxes - conserve the same expressions (2.70)-(2.73) as for the case without spar. In these two subdomains, the particular solutions for the three radiation problems of the spar are $\phi_{j,m}^{(1),II} = \phi_{j,m}^{(1),II} = 0$ since the dock is then fixed. In the subdomain IV, similar to the diffraction problem for the dock with spar (cf. Sec. 2.2.3), the potential is written:

$$\phi_j^{(k),IV}(r,z) = \psi \sum_{q=0}^{\infty} \left[A_{1,q}^{IV} P_{p,q}^{IV}(r) + A_{2,q}^{IV} Q_{p,q}^{IV}(r) \right] Z_q(z), \tag{2.84}$$

where $p = 0$ in heave, and $p = 1$ in surge and pitch for both bodies. In the subdomain V below the spar, the potential is again decomposed into a homogeneous and a particular solutions $\phi_j^{(k),V} = \phi_{j,h}^{(k),V} + \phi_{j,m}^{(k),V}$, given by:

$$\phi_{1,m}^{(1),V}(r,z) = \phi_{j,m}^{(2),V}(r,z) = 0 \tag{2.85}$$

$$\phi_{3,m}^{(1),V}(r,z) = \frac{(z+h)^2 - \dfrac{r^2}{2}}{2(h-d_0)}, \tag{2.86}$$

$$\phi_{5,m}^{(1),V}(r,z) = -\frac{r(z+h)^2 - \dfrac{r^3}{4}}{2(h-d_0)}, \tag{2.87}$$

$$\phi_{j,h}^{(k),V}(r,z) = \psi A_0^V \left(\frac{r}{a_0}\right)^p + 2\psi \sum_{q=1}^{\infty} A_q^V \frac{I_p\left(\frac{q\pi}{h-d_0}r\right)}{I_p\left(\frac{q\pi}{h-d_0}a_0\right)} \cos\left(\frac{q\pi(z+h)}{h-d_0}\right), \tag{2.88}$$

Finally, the matching conditions must be imposed in $r = a_0$ for the potentials $\left|\begin{matrix}\phi_1^{(1)}\\ \phi_3^{(1)} \text{ and } \phi_j^{(2)}\\ \phi_5^{(1)}\end{matrix}\right.$ respectively:

$$\int_{-h}^{-d_0} \phi_{j,h}^{(k),V}(a_0,z)\cos(\frac{p\pi(z+h)}{h-d_0})dz$$

$$= \int_{-h}^{-d_0} \left[\phi_j^{(k),IV}(a_0,z) - \phi_{j,m}^{(k),V}(a_0,z)\right]\cos(\frac{p\pi(z+h)}{h-d_0})dz \tag{2.89}$$

$$\int_{-h}^{0} \frac{\partial \phi_j^{(k),IV}}{\partial r}(a_0,z)Z_p(z)dz = \int_{-h}^{-d_0} \frac{\partial \phi_j^{(k),V}}{\partial r}(a_0,z)Z_p(z)dz + \int_{-d_0}^{0} \left|\begin{matrix}1\\0\\z\end{matrix}\right. Z_p(z)dz, \ p \in \mathbb{N} \tag{2.90}$$

The linear matricial equation of order N_I+N_{IV}, similar to (2.82) but now established for six radiation problems for the unknown vector $\boldsymbol{A}^S = \left[A_1^I \cdots A_{N_I}^I \, A_{2,1}^{IV} \cdots A_{2,N_{IV}}^{IV}\right]^T$ is given in Appendix A.2.3. The added mass and damping coefficients on both bodies are obtained from the radiation potentials by:

$$a_{s,j}^{(k)} + i\frac{b_{s,j}^{(k)}}{\omega} = -\rho \int\int_{S_0^{(k)}} \phi_j^{(k)} \cos(p\theta) n_s dS, \tag{2.91}$$

$$d_{s,j}^{(k)} + i\frac{e_{s,j}^{(k)}}{\omega} = -\rho \int\int_{S_0^{(k)}} \phi_j^{(k')} \cos(p\theta) n_s dS, \tag{2.92}$$

for $(s,j) \in \{1,3,5\}^2$ and $(k,k') \in \{1,2\}^2$. In particular, these coefficients have the symmetrical properties: $a_{s,j}^{(k)} = a_{j,s}^{(k)}$, $b_{s,j}^{(k)} = b_{j,s}^{(k)}$, $d_{s,j}^{(k)} = d_{j,s}^{(k')}$, $e_{s,j}^{(k)} = e_{j,s}^{(k')}$. Their semi-analytical expressions are given in Appendix A.4.1.

2.4 Convergence and results

2.4.1 Simulations in WAMIT

In parallel of the loads calculated by the domain decomposition method, simulations were run with the commercial software WAMIT to verify the convergence of the semi-analytically results. In WAMIT, the radiation and diffraction problems are solved in the frequency domain assuming linear potential flow assumptions. The solutions are obtained through a boundary element method, which require to discretise the surface of the bodies. Because of the symmetry of revolution and the linearity of the problems, it is sufficient to mesh only one quarter of the dock and spar (Lee and Newman, 2006). Examples of home-made meshes are shown in Fig 2.4. The distribution of panels (or cells) is evenly distributed over the bodies, except for the dock which has a higher concentration of panels near the bilge boxes. Convergence of the meshes is presented in Appendix A.5. The lowest irregular frequencies for the dock were in the range of incident wave periods, and were therefore removed using the corresponding option provided by the software (see more details in Appendix B.2).

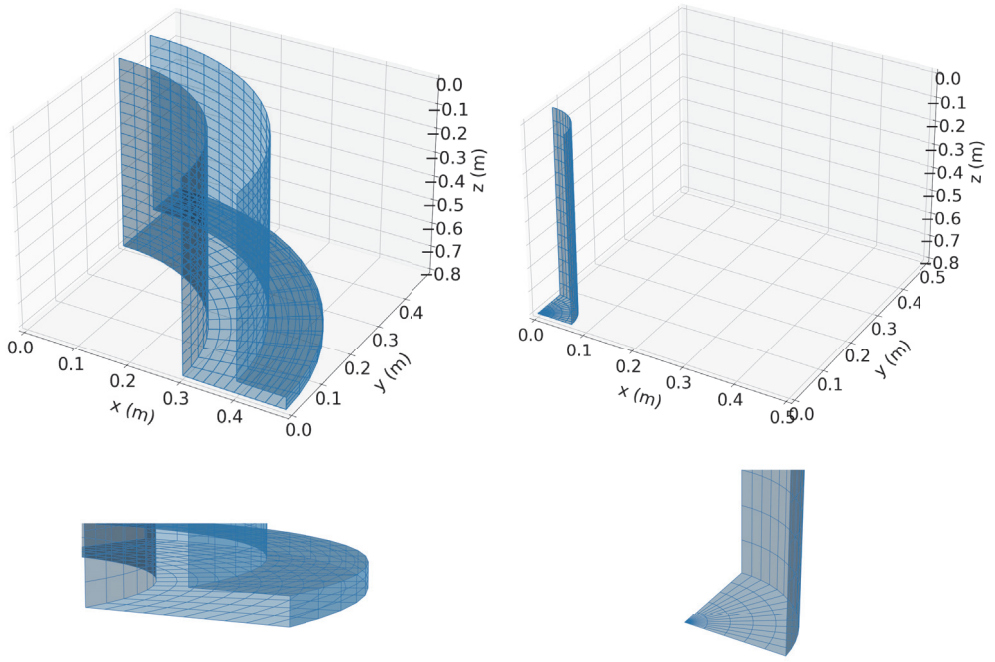

Figure 2.4: *Example of meshes of the spar (left, 490 panels) and the dock (right, 907 panels) in model scale (1:100). Top: full meshes. Bottom: zoom on the lower body parts.*

2.4.2 Results - Scattering forces

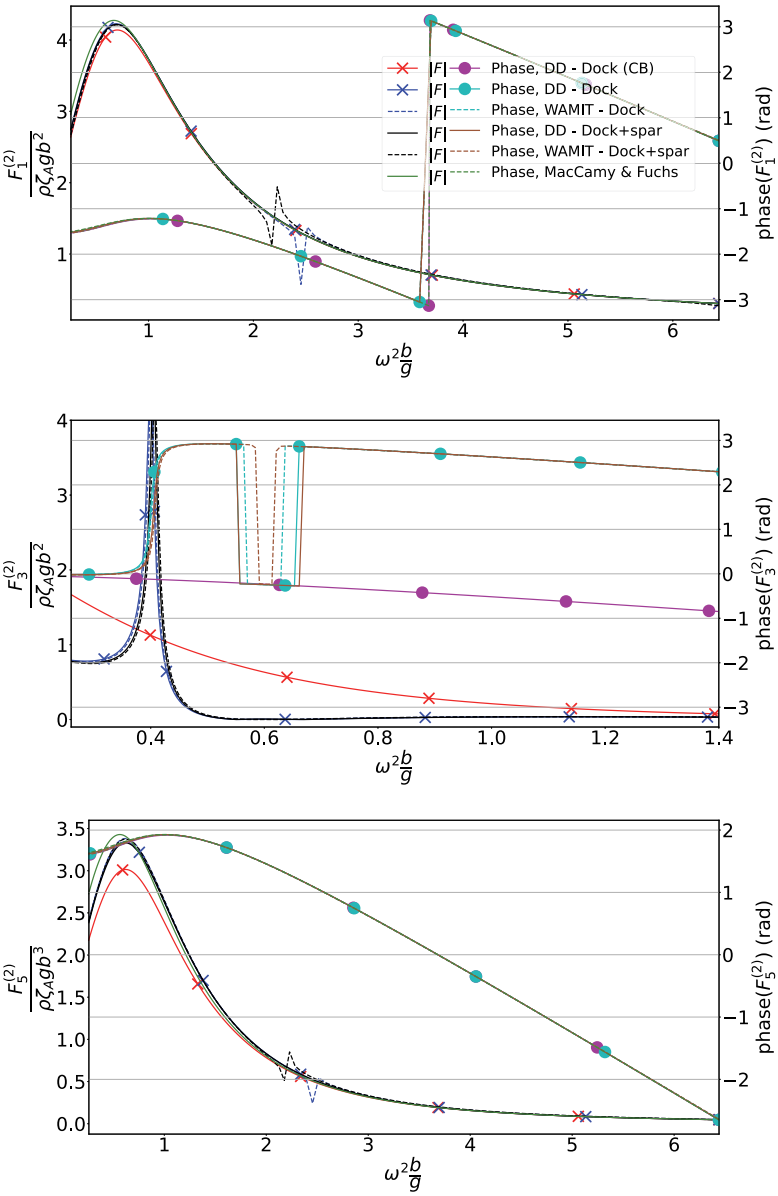

Figure 2.5: *Non-dimensional amplitude of exciting forces and moments (left axis) and their phases (right axis) computed by the present DD method (cf. Secs. 2.2.2 and 2.2.3) and the BEM software WAMIT. In addition, scattering loads in surge and pitch from MacCamy and Fuchs (1954)'s model (cf. Sec. 2.2.4), as well as the scattering loads on a closed-bottom (CB) dock (cf. Garrett (1971)) are also indicated. Top: force in surge. Middle: force in heave. Bottom: moment in pitch.*

The scattering loads in surge, have and pitch on the dock derived in this chapter are compared from results from WAMIT in Fig. 2.5. The present DD method was coded in python. The following dimensions were used to run the numerical simulations: $a/b = 0.75$, $c/b = 1.22$, $s/b = 0.13$, $(d+s)/b = 2$, $a_0/b = 0.18$, $d_0/b = 2$, and $h/b = 5$. Scattering loads on a closed-bottom dock (cf. Garrett (1971)) are also indicated on the figure, as well as the force in surge and moment in pitch estimated from MacCamy and Fuchs (1954)'s model (cf. Sec. 2.2.4). Their model provide good estimations of the loads on the dock as long $\omega^2 b/g \gtrsim 1$. Because the dock's draught is high in our model, scattering loads on the spar are negligible. Loads on the dock for the case with and without spar are very similar for the same reason. Convergence of the loads from the DD method was found to be achieved for a number of modes in each subdomain as low as $N_I = N_{II} = N_{III} = N_{IV} = 10$, at the exception of the phases of the loads in heave, which are not converged in Fig. 2.5. These last are very numerically sensitive due to that the waves are short compared to the dock's draught, and the pressures are very small at the bottom of the dock. Only the first two polar harmonics are needed to determine the scattering loads in surge and pitch (mode $p = 1$) and in heave (mode $p = 0$). On the other hand, $N_S = 12$ was found to be sufficient for the dynamic pressure field to converge, which was estimated at several locations in $z = 0$m and $z = -(d + s)$. More details about the convergence studies are given in Appendix A.5 for the case without spar.
The loads in surge and pitch for the case without spar are also compared to results from Mavrakos (1985) in Fig. 2.6 with good agreement, where very small dimensions of the bilge boxes were defined in our model for these simulations.

2.4.3 Results - Added mass and damping coefficients

The added mass and damping coefficients derived in Secs. 2.3.1 and 2.3.2 are presented in Fig 2.7 for the dock, in Fig. 2.8 for the spar, and in Fig. 2.9 for the cross added mass coefficients d between the dock and the spar. The case of a spar alone in open water, and of the dock without spar and with a closed bottom are also indicated. In both of these cases, the radiation problems are the one of circular cylinder of finite draught, and solved similar to Yeung (1980). For the case of the dock with closed bottom, the internal domain is filled with water which also contributes to the added mass coefficients (see more details in the later Sec. 3.3.2). The same dimensions of the bodies as in Sec. 2.4.2 were uses to run the numerical simulations. The number of modes $N_I = 50$, $N_{II} = 33$, $N_{III} = 15$, $N_{IV} = 50$, and $N_V = 33$ were found to give a good convergence between the DD method and WAMIT. Convergence of the problems in heave in pitch generally required higher number of eigenmodes due lower convergence of the flow near the sharp corners at the bottom of the dock. The spar's added mass in heave in Fig. 2.9 is for instance not fully converged for these number of modes and in the range of frequencies presented on this figure. A convergence study for the case without

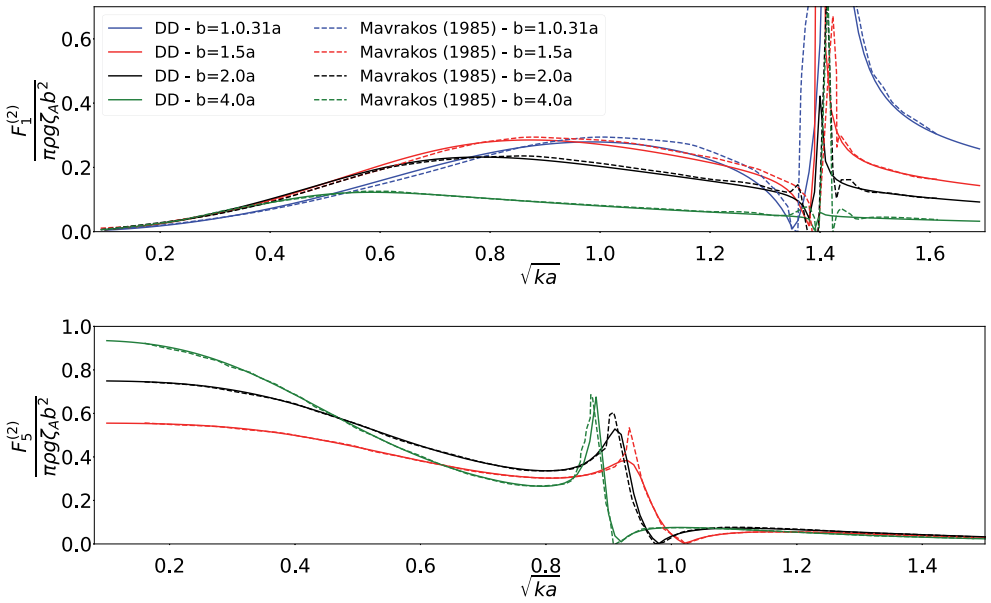

Figure 2.6: *Non-dimensional amplitude of exciting force in surge and moments from Mavrakos (1985), compared with the current DD model for the case without spar and for small dimensions of the bilge boxes:* $(c-b)/a = 0.01$ *and* $s/a = 0.01$.

spar is presented in more details in Appendix A.5.

The sloshing resonance occurs at $\omega^2 b/g = 2.45$ for the dock alone, and is shifted to $\omega^2 b/g = 2.2$ when the spar is inserted. This can be see from $a_{1,1}^{(2)}$ or $a_{5,5}^{(2)}$ for instance. The same resonant frequency is observed from the added mass coefficients in surge and pitch for the spar. The damping coefficients on the spar were negligible because of the large draught of the dock. The "excitation" of the spar hence entirely came from the cross added-mass coefficients $d_{i,j}^{(1)}$, $(i,j) \in \{1,5\}^2$ caused by the dock's motions, or in other words by sloshing waves.
The peak at $\omega^2 b/g = 0.40$ observed from the added mass coefficients in heave corresponds to the piston-mode frequency described by Molin (2001), which was also observed from the scattering load $F_3^{(2)}$ in Fig. 2.5. The piston mode natural frequency does not seem affected by the presence of the spar.
Similar to the diffraction problem, added mass and damping coefficients for the case without spar converge to the coefficients given by Mavrakos (1988) when the dimensions of the bilge boxes go to 0 (see Appendix A.5), which provide additional validation to our method.

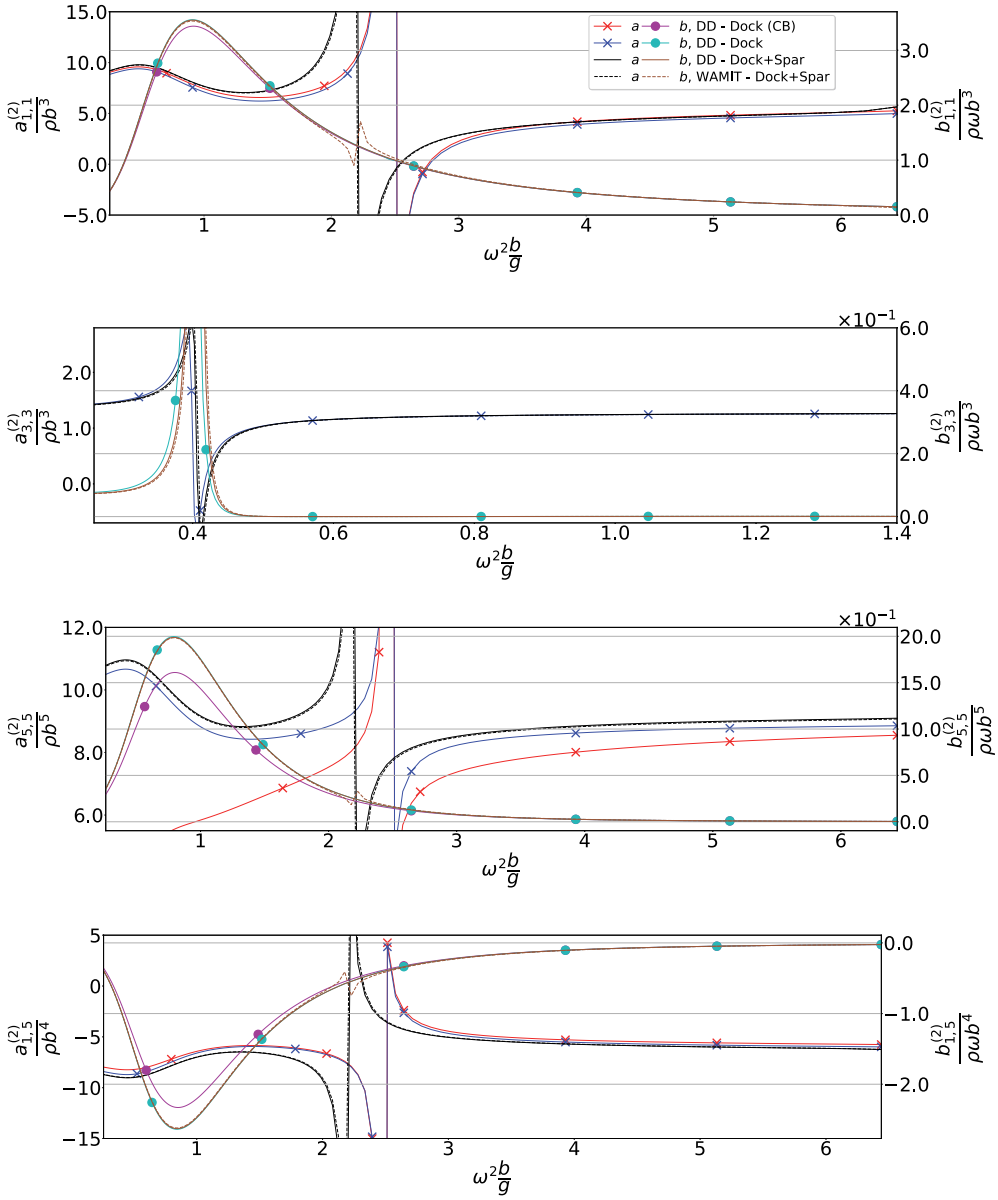

Figure 2.7: *Non-dimensional added mass (left axis) and damping coefficients (right axis) of the dock with and without spar computed by the present DD method and the BEM software WAMIT. The case of a closed-bottom (CB) dock filled with water is also indicated. In the legend, a and b stand for the added mass and damping coefficients, respectively.* $N_I = 50$, $N_{II} = 33$, $N_{III} = 15$, $N_{IV} = 50$, *and* $N_V = 33$.

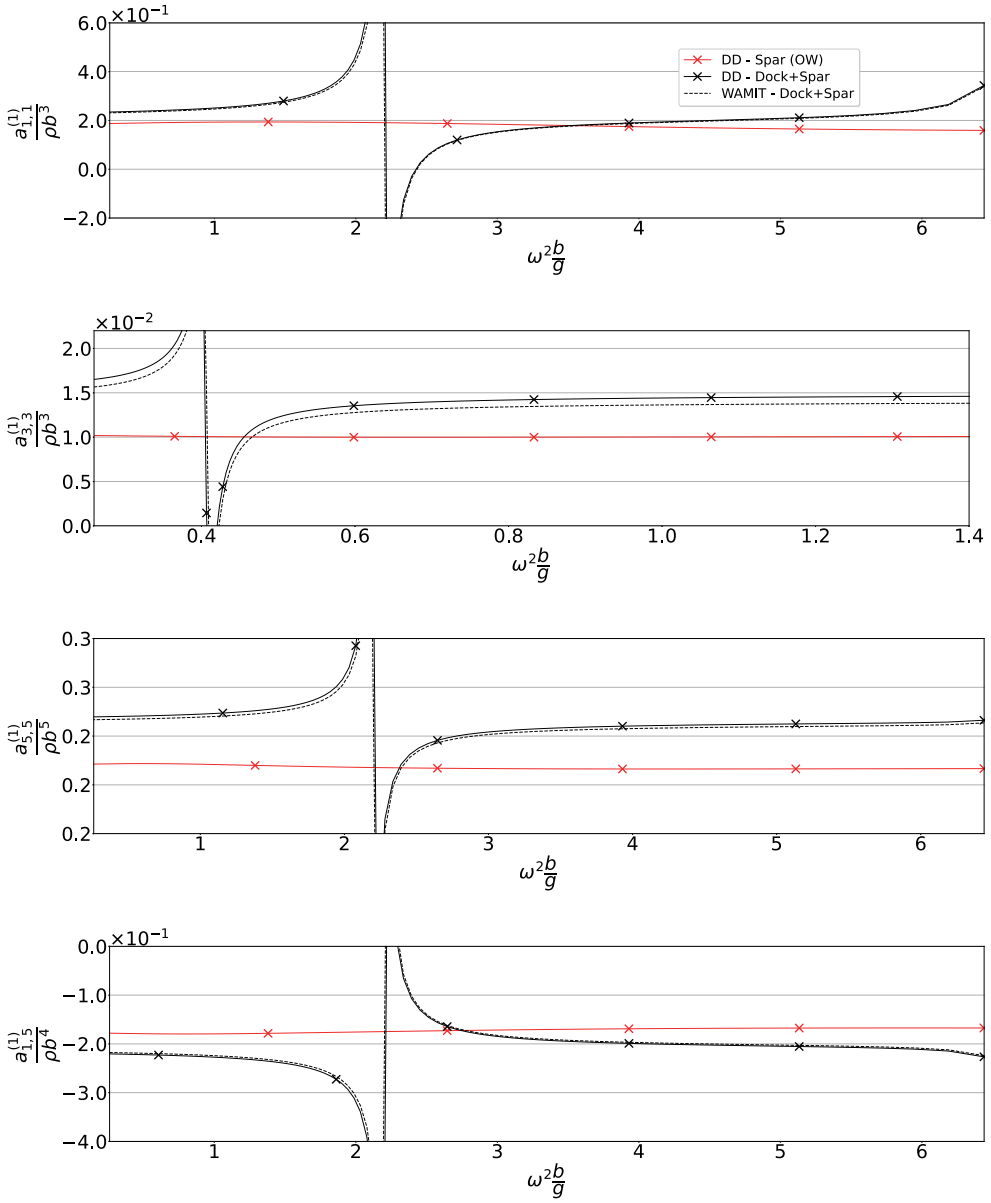

Figure 2.8: *Non-dimensional added mass of the spar computed by the present DD method and the BEM software WAMIT. The case of the spar in open water (OW) without the dock is also indicated. In the legend, a and b stand for the added mass and damping coefficients, respectively. $N_I = 50$, $N_{II} = 33$, $N_{III} = 15$, $N_{IV} = 50$, and $N_V = 33$.*

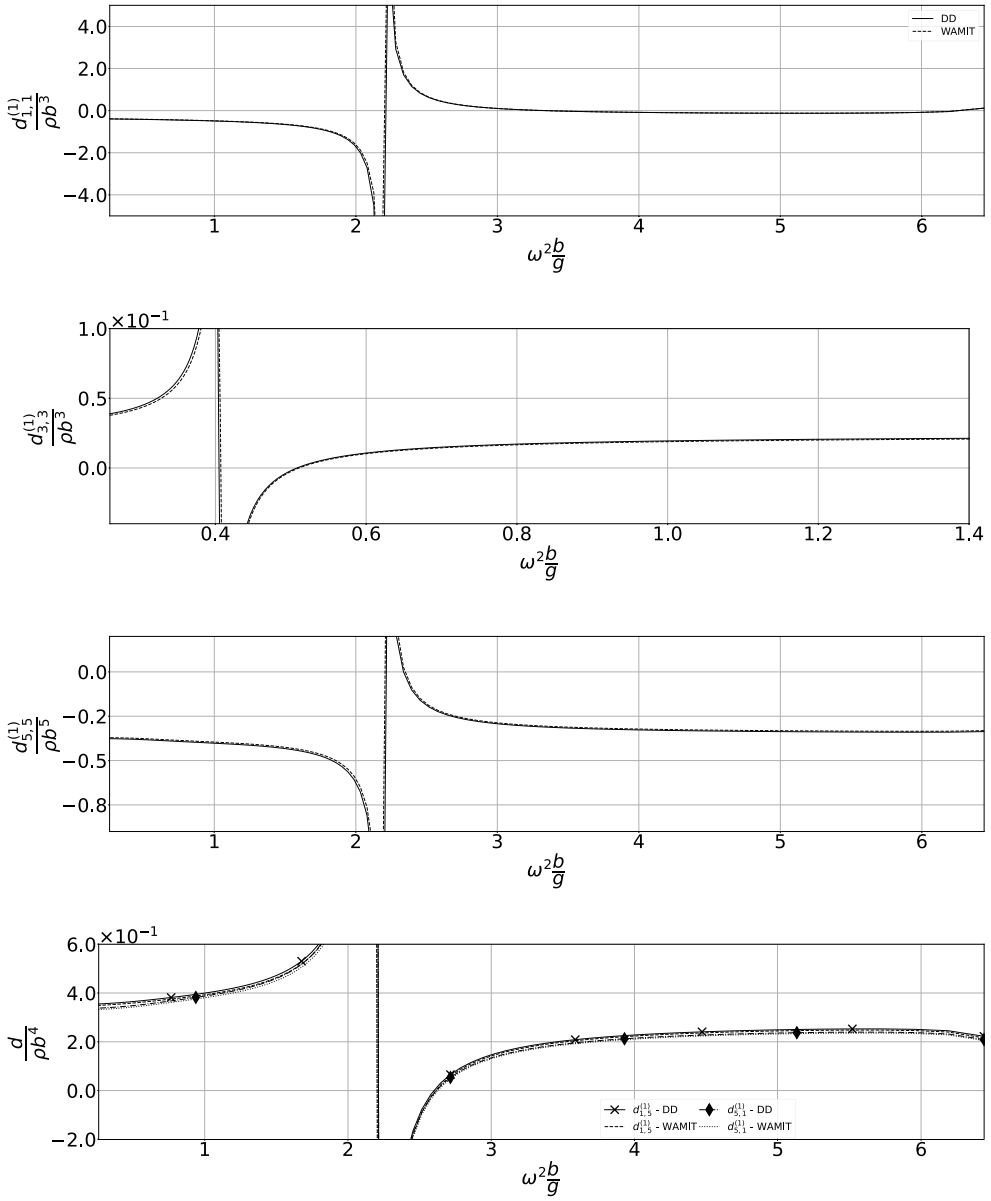

Figure 2.9: *Non-dimensional added mass cross-coefficients of the two bodies system dock+spar (see Eq.* (2.92)*).* $N_I = 50$*,* $N_{II} = 33$*,* $N_{III} = 15$*,* $N_{IV} = 50$*, and* $N_V = 33$*.*

3 | Sloshing

The approach described by Faltinsen and Timokha (2009) has mainly been used in this current work to model near-resonance sloshing flows. Analytical works for closed vertical cylinder provide good estimations of the sloshing response to given dock's motions, since this last is designed with a high draught compared to incident wave lengths ($\lambda/(d+s) < 2$) near the highest natural sloshing period. In addition, natural periods in pitch and heave are distinctly higher than the considered incident wave periods (see more details in Sec. 5.4). It results that the fluid motion at the bottom of the dock is negligible at operational weather conditions. For instance, the dynamic pressure calculated with the DD model developed in the previous chapter for the free-floating dock in regular incident waves with frequencies near sloshing resonance reaches less than 1% of its maximal value at the free surface, and is mainly caused by pitch motions.
In this chapter only, we consider that the dock has a closed bottom, and we focus on the internal flow, both with and without the spar as shown in Fig. 3.1, and under linear potential flow assumptions. From Sec. 3.1 to Sec. 3.3, sloshing eigenmodes are discussed, and the so-called "modal equations" describing sloshing waves for given surge and pitch motions of the dock are established. Known theories which model the effects - and in particular the viscous effects - of horizontal baffles on sloshing in closed tanks are then considered in Secs. 3.4 and Sec. 3.5, extended in the present work to perforated baffles. The total draught of the dock is renamed d instead of $d+s$ in this chapter only in order to simplify the notations. The coupling between internal and external flows for the open-bottom dock, especially in the case where baffles are installed, will be discussed in the dedicated Chapter 5.

3.1 Spectral problems

3.1.1 Upright cylinder

The potential flow is assumed to be harmonic, and is expressed as: $\phi(x,y,z,t) = \varphi(x,y,z)e^{-i\sigma t}$. The sloshing eigenfrequencies $\sigma_{p,q}$ and eigenmodes $\varphi_{p,q}$ are found by solving the following linear boundary-value problem when the dock is fixed, also called spectral problem:

$$\begin{cases} \nabla^2\varphi = 0 \quad \text{in } Q_0, \\ \dfrac{\partial\varphi}{\partial n} = 0 \quad \text{on } S_0, \\ \dfrac{\partial\varphi}{\partial z} = \kappa\varphi \quad \text{on } \Sigma_0, \end{cases} \tag{3.1}$$

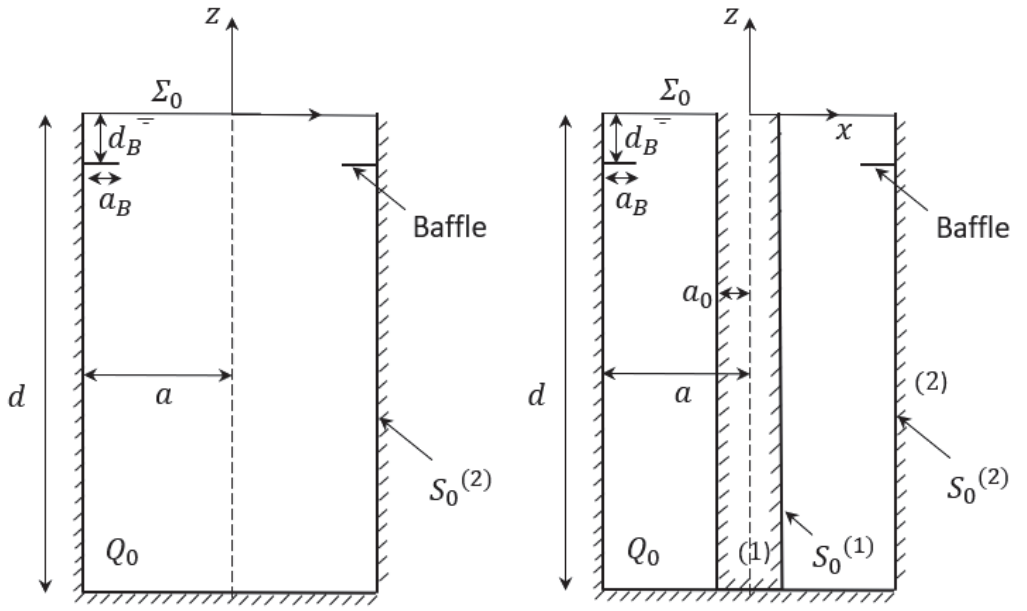

Figure 3.1: *Sketch of the floating dock's internal domain centre-plane, represented in this Chapter with a closed bottom, both without (left) and with (right) the spar. The baffle draught d_B and width a_B are illustrated. The draft $d + s$ is re-written d in this chapter only for lighter notations.*

where $\kappa = \sigma^2/g$. For the particular cases of upright circular and annular cylinder, as here for the dock without and with the spar, analytical solutions of the BVP (3.1) can be established. $\varphi_{p,q}(r,\theta,z) = \Theta(\theta)W(r)Z(z)$ are found by separating the variables, similar to what we did in the previous chapter (cf. Sec. 2.2.2). However, for this problem, the functions $Z(z)$ only admit real wave numbers. Indeed, the radial solution W corresponding to imaginary wave number are the modified Bessel functions, which never satisfy the body-boundary condition since both $I'_p(r) = 0$ and $K'_p(r) = 0$ do not have solutions (cf. Appendix B.1). Solutions for $W(r)$ are thus generally the Bessel functions J_p and Y_p.

In this section, we first consider the dock without spar. The internal domain is an upright cylinder of radius a and draught d (see left part of Fig. 3.1). Without the spar, only the Bessel functions of the first kind are physical since the Bessel functions of the second kind diverge in $r = 0$. Eigenfunctions can then be written (Faltinsen and Timokha, 2009):

$$\varphi_{p,q}(r,\theta,z) = \frac{J_p\left(\iota_{p,q}\frac{r}{a}\right)}{J_p(\iota_{p,q})} \frac{\cosh\left(\frac{\iota_{p,q}(z+d)}{a}\right)}{\cosh\left(\frac{\iota_{p,q}d}{a}\right)} \times \begin{cases} \cos(p\theta) \\ \sin(p\theta) \end{cases}, \tag{3.2}$$

where $(p,q) \in \mathbb{N} \times \mathbb{N}^*$ and $\iota_{p,q}$ are the roots by increasing order of $J'_p(\iota_{p,q}) = 0$. The free surface's shape for several eigenmodes are shown in Fig. 3.2. Eigenmodes are orthogonal due to the orthogonal properties of the trigonometric and Bessel functions (cf. Appendix B.1). They are defined up to a multiplying constant, chosen arbitrarily here such that $\varphi_{p,q}(a,0,0) = 1$. $k_{p,q} = \iota_{p,q}/a$ are the eigen wave numbers, and the wave frequencies are determined from the dispersion relationship,

$$\sigma_{p,q}^2 = \frac{g\iota_{p,q}}{a} \tanh\left(\frac{\iota_{p,q} d}{a}\right). \tag{3.3}$$

Eigenperiods are defined as $T_{p,q} = 2\pi/\sigma_{p,q}$. Only the modes proportional to $\cos(\theta)$ are linearly excited by surge and pitch motions, while the modes proportional to $\sin(\theta)$ are excited by sway and roll. It can also be noted that heave does not linearly excite any sloshing modes in closed tanks.
The five lowest natural frequencies for two different values of the draught, chosen within the range considered by Jiang et al. (2020) for the dock in operational conditions, are given in Table 3.1. Typical incident wave frequencies range from $\omega^2 b/g = 0.26$ to $\omega^2 b/g = 6.44$ (or $T = 5$s to $T = 25$s in full scale), such that resonance of the lowest natural frequency $\sigma_{1,1}^2 b/g = 2.45$ ($T_{1,1} = 8$s in full scale) is most likely to occur. We note that it corresponds exactly to the value of sloshing resonance found from the added masses in surge and added moment in inertia in Sec. 2.4 for the open-bottom dock with $d/b = 2$, supporting our closed-tank approach. Jiang et al. (2020) imposed constraint on the draught in order to keep the spar inside the dock protected from incident waves. In particular, $d/b = 1.25$ is the minimum draught that he considered. We see in Table 3.1 that the natural frequencies are almost identical for $d/b = 1.25$ and $d/b = 2$, such that it is not possible to shift natural sloshing frequencies away from the range of excitations by playing with the vertical dimensions of the dock, as it was done for the piston mode (Jiang et al., 2020). Variations of the lowest natural frequency with the draught for various radii are presented in Fig, 3.3 for the lowest natural frequency, showing that for draught-to-radius ratios higher than $d/a > 1.6$, $\omega^2 b/g$ is practically constant.

3.1.2 Annular cylinder

A cylindrical spar of radius a_0 and draught d is now installed inside the dock (cf. right part of Fig. 3.1). The spectral problem 3.1 is solved in the annular domain between the spar and the dock. The solution of the Laplace equation in z and θ are identical to those for the dock alone. However, the singularity in $r = 0$ does not appear anymore since r is bounded: $a \geq r \geq a_0$. Thus, both Bessel functions of the first and second kind are solution for W, which can be written under the form:

$$W_p(r) = A_p J_p(k_{p,q} r) + B_p Y_p(k_{p,q} r), \qquad (p,q) \in \mathbb{N} \times \mathbb{N}^*, \tag{3.4}$$

where A_p and B_p are unknown coefficients. The boundary condition on S_0 impose that $W'_p(r) = 0$ in $r = a$ and $r = a_0$, which leads to the system:

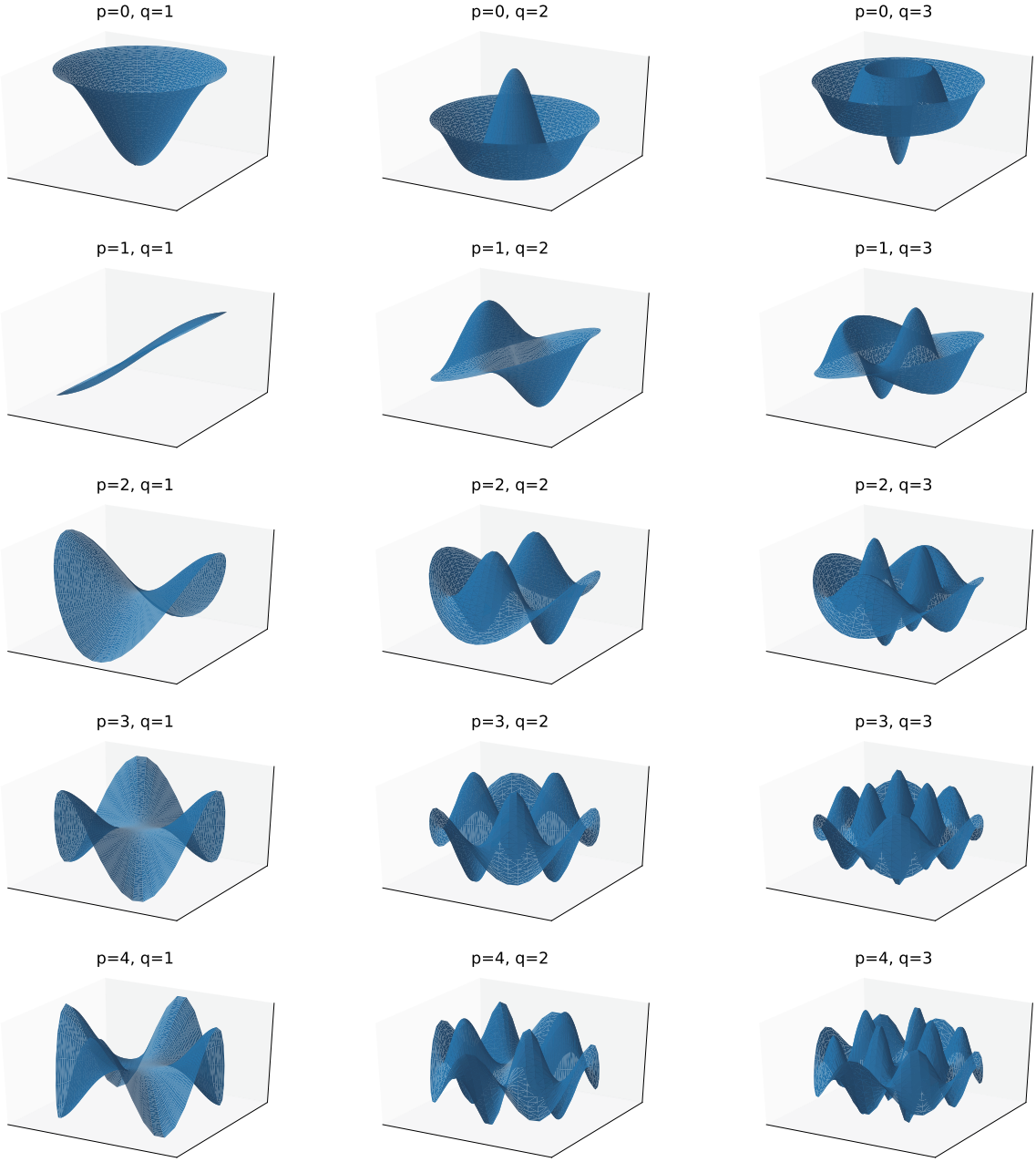

Figure 3.2: *Visualisation of sloshing eigenmodes in an upright vertical cylinder with a radius to draught ratio $a/d = 0.37$. Each row represents the first three modes proportional to $\cos(p\theta)$, for $p = 0$ to $p = 4$ (cf. Eq. (3.2)).*

Table 3.1: *First five lowest natural sloshing frequencies for two different dock's draughts. Only the modes $p = 1$ are excited by surge and pitch. b corresponds to the external diameter in the previous chapter, and is only used here for a non-dimensionalisation purpose. $a/b = 0.75$.*

Modes	$\sigma^2 b/g$ $(d/b = 1.25)$	$\sigma^2 b/g$ $(d/b = 2)$
$p = 1,\ q = 1$	2.44	2.45
$p = 2,\ q = 1$	4.07	4.07
$p = 0,\ q = 1$	5.11	5.11
$p = 3,\ q = 1$	5.60	5.60
$p = 4,\ q = 1$	7.09	7.09

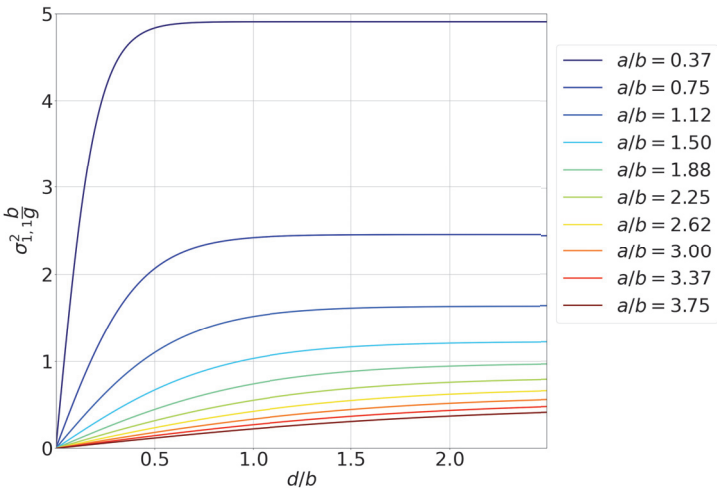

Figure 3.3: *Lowest anti-symmetric natural sloshing frequency as a function of the non-dimensional draught, and for several radius of the dock. For the dock: $a/b = 0.75$.*

$$\begin{bmatrix} J'_p(k_{p,q}a) & Y'_p(k_{p,q}a) \\ J'_p(k_{p,q}a_0) & Y'_p(k_{p,q}a_0) \end{bmatrix} \begin{bmatrix} A_p \\ B_p \end{bmatrix} = \begin{bmatrix} 0 \\ 0 \end{bmatrix}. \tag{3.5}$$

Non-zeros solutions are found only if the determinant of the matrix in Eq. (3.5) is null. We define then $\iota_{p,q} = a_0 k_{p,q}$ $(p,q) \in \mathbb{N} \times \mathbb{N}^*$ as the roots in increasing order of:

$$J'_p\left(\iota_{p,q}\frac{a}{a_0}\right) Y'_p(\iota_{p,q}) - J'_p(\iota_{p,q}) Y'_p\left(\iota_{p,q}\frac{a}{a_0}\right) = 0. \tag{3.6}$$

$\iota_{p,q}$ are estimated in this current work by the algorithm proposed by Sorolla et al. (2013) (see Fig. 3.4), which uses in an efficient manner the interlacing properties

of the Bessel functions (see more details in Appendix B.1). Eigenfunctions in the annular domain are finally given by:

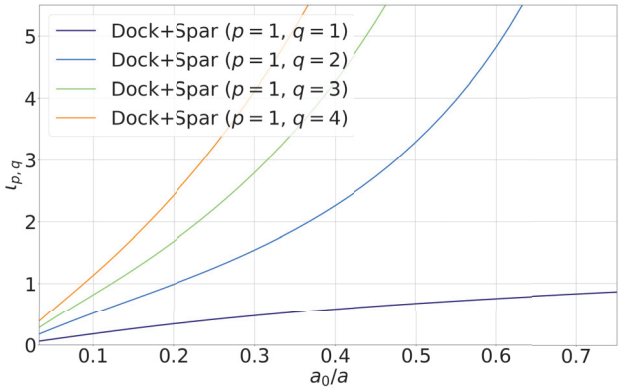

Figure 3.4: *Selected roots of the cross-products* (3.6).

$$\varphi_{p,q}(r,\theta,z) = \frac{b\Psi_{p,q}(r)}{\sqrt{\upsilon_{p,q}}} \frac{\cosh\left(k_{p,q}(z+d)\right)}{\cosh\left(k_{p,q}d\right)} \times \begin{cases} \cos(p\theta) \\ \sin(p\theta) \end{cases}, \tag{3.7}$$

where the functions $\Psi_{p,q}$ and the normalising coefficient $\upsilon_{p,q}$ are defined as:

$$\Psi_{p,q}(r) = Y'_p(k_{p,q}a)J_p(k_{p,q}r) - J'_p(k_{p,q}a)Y_p(k_{p,q}r), \tag{3.8}$$

$$\upsilon_{p,q} = \left[\frac{r^2}{2}\Psi^2_{p,q}(r)\right]_{a_0}^{a}. \tag{3.9}$$

The coefficient b in Eq. (3.7) is a fixed length used to make $\varphi_{p,q}$ non-dimensional, and corresponding to the external radius of the dock in the previous chapter. These eigenmodes are also orthogonal (cf. Appendix B.1), their shape for selected (p,q) are shown in Fig. 3.5. The eigenfrequencies are determined from the dispersion relationship:

$$\sigma^2_{p,q} = g\frac{\iota_{p,q}}{a_0}\tanh\left(\frac{\iota_{p,q}}{a_0}d\right). \tag{3.10}$$

As for the dock alone, only the modes $p = 1$ interact with the surge and pitch motions of the bodies. The frequencies of the first mode $\sigma_{1,q}$ are presented in Fig. 3.6 both as functions of the dock and spar's radii, and compared to the eigenfrequencies for the dock without spar. As one should expect, the frequencies converge to the case without spar when a_0/a goes to 0. It is observed that for $a_0/a \geq 0.37$, the eigenfrequencies for modes $q \geq 2$ are increased compared to the case of the dock without spar, while it is reduced for the first mode $q = 1$. This

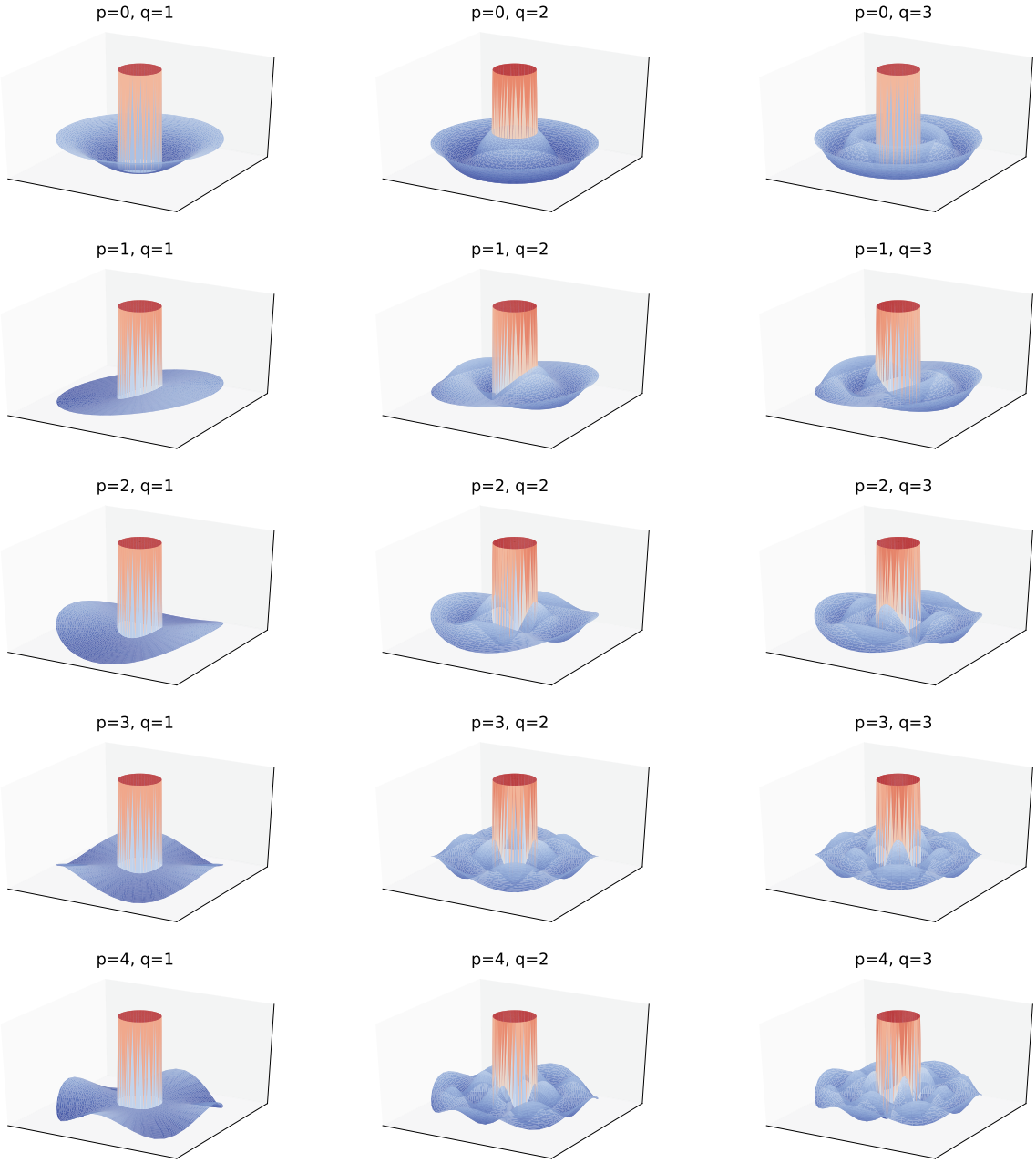

Figure 3.5: *Visualisation of sloshing eigenmodes in the annular domain between the dock and the spar. Each line represents the first three modes proportional to* $\cos(p\theta)$*, for* $p = 0$ *to* $p = 4$ *(cf. Eq.* (3.7)*). Dock's radius-to-draught ratio used to generate the plots:* $a/d = 0.37$*. Spar's radius:* $a_0/a = 0.23$*.*

is due to that $\sigma_{1,q}$ is an increasing function of $\iota_{1,q}/(a_0/a)$, and to that the ratio $\iota_{1,q}/(a_0/a)$ only decreases with a_0/a for the first mode $q = 1$, while it increases for higher modes and for $a_0/a \geq 0.37$. For the actual radius of the dock (square points on the figure), $\sigma_{1,1}^2 b/g$ is around 10% lower with the spar than for the dock alone, meaning that the natural period is about 5% higher with the spar installed in the dock.

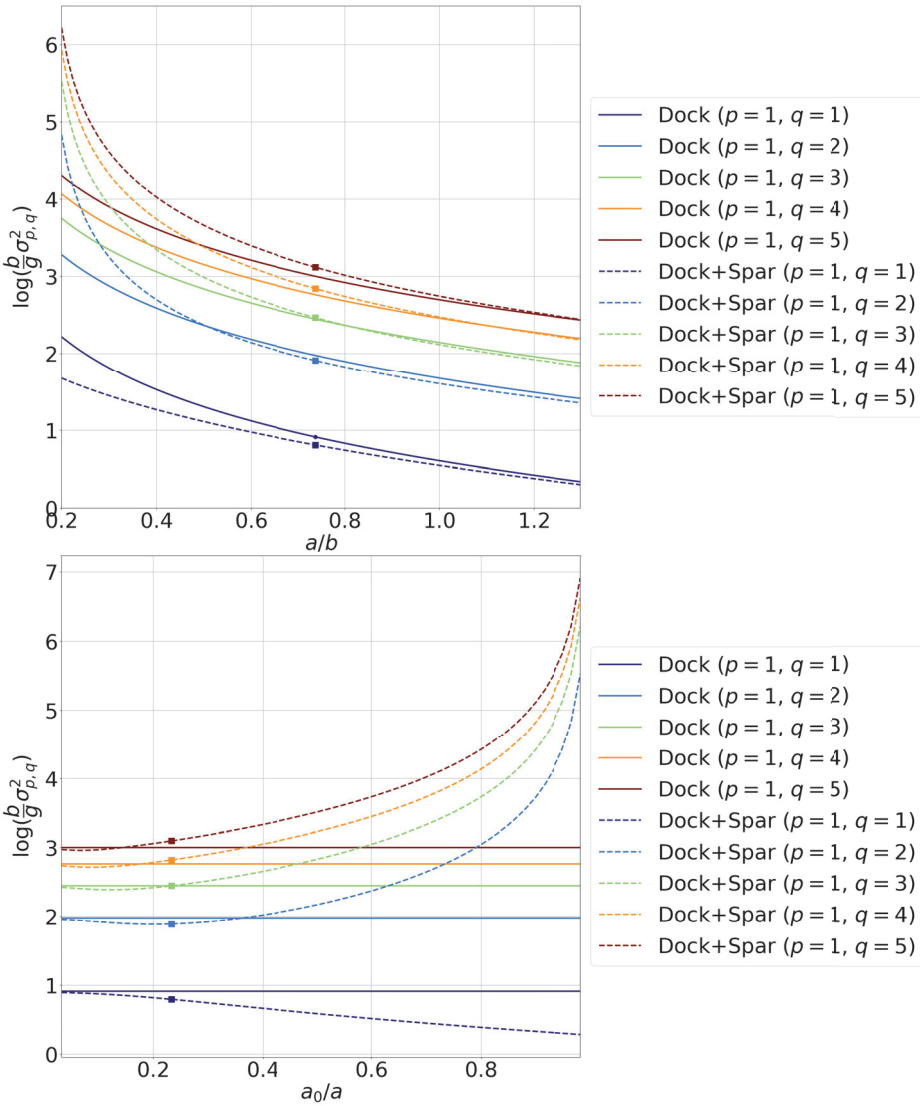

Figure 3.6: *Comparison of the non-dimensional logarithmic natural sloshing frequencies of the five first modes in $p = 1$ for the dock alone and with spar. Top: as a function of the dock's internal radius a/b. Bottom: as a function of the spar's radius a_0/a for the case with spar, the dock radius being fixed to $a/b = 0.75$. $d/b = 2$, frequencies corresponding to actual dimensions of the dock are indicated by square points.*

3.2 Stokes-Joukowski potentials

Linear Stokes-Joukowski potentials were introduced by Joukowski (1885) for flows in closed cavities without free surface, and typically associated with forcing angular motions. It is commonly used in sloshing problems in order to express the free-surface boundary problems in a tank fixed referential. Analytical solution of Stokes-Joukowski potentials for both circular (Faltinsen and Timokha, 2009; Lukovsky et al., 1984) and co-axial (Timokha, 2015; Faltinsen et al., 2016) cylinders are well-known.
In this section, we first treat in a detail the case of circular cylinder to present the method, based on separation of variables and decomposition of the body-boundary condition. We note that other methods based on Lagrange variational formulations can also be found in the literature (Lukovsky, 2015). Then, we consider the system composed by both the dock and the spar, which differs from co-axial cylinders found in the literature due to that both bodies can rotate independently. We propose in the present work to solve the problem by introducing two Stokes-Joukowski potentials, each associated to either the pitch motions of the dock or the spar. This simplified approach works because the linear solution is calculated from the mean positions of the bodies. For higher orders, the problem would become nonphysical at the bottom of the spar, and a better model would be required. We note that for the case where the spar can move freely inside the dock, stokes-Joukowski potentials associated to the surge motions of both bodies must also be determined, which we only treat in later Sec. 3.3.3.

3.2.1 $\boldsymbol{\Omega}$ for the dock

The Stokes-Joukowski potential $\boldsymbol{\Omega}$ is defined by the BVP (Faltinsen and Timokha, 2009):

$$\begin{cases} \nabla^2 \boldsymbol{\Omega} = \mathbf{0} \quad \text{in } Q_0, \\ \dfrac{\partial \boldsymbol{\Omega}}{\partial n} = \boldsymbol{r} \times \boldsymbol{n} \quad \text{on } S_0^{(2)} \cup \Sigma_0, \end{cases} \tag{3.11}$$

$\boldsymbol{\Omega}_i$ for $i \in [1, 2, 3]$ being the velocity potential of the fluid when the tank has a unit angular motion in the $(i+3)$th DoF. Because of the symmetry of revolution, $\boldsymbol{\Omega}$ can always be expressed as

$$\boldsymbol{\Omega} = F(r, z) \begin{bmatrix} -\sin(\theta) \\ \cos(\theta) \\ 0 \end{bmatrix}. \tag{3.12}$$

The problem is hence reduced in determining the function $F(r, z)$. The BVP (3.11) then becomes:

$$\frac{\partial^2 F}{\partial z^2} + \frac{\partial^2 F}{\partial r^2} + \frac{1}{r}\frac{\partial F}{\partial r} - \frac{1}{r^2}F = 0 \quad \text{in } Q_0, \tag{3.13}$$

$$\left.\frac{\partial F}{\partial z}\right|_{\substack{0\le r\le a \\ z=0,-d}} = -r, \tag{3.14}$$

$$\left.\frac{\partial F}{\partial r}\right|_{\substack{r=a \\ -d\le z\le 0}} = z. \tag{3.15}$$

We introduce the decomposition

$$F(r,z) = F_p(r,z) + F_1(r,z) \tag{3.16}$$

such that the particular solution $F_p = rz$ satisfies both the vertical boundary conditions on the wall, and the Laplace equation (3.13) in the internal domain. Then, by replacing F into the system, F_1 satisfies the same Laplace equation, as well as the following BCs

$$\left.\frac{\partial F_1}{\partial z}\right|_{\substack{0\le r\le a \\ z=0,-d}} = -2r \tag{3.17}$$

$$\left.\frac{\partial F_1}{\partial r}\right|_{\substack{r=a \\ -d\le z\le 0}} = 0 \tag{3.18}$$

We can now use the separation of variable $F_1(r,z) = A(r)B(z)$, and replace this expression in Eq. (3.13). The solutions in z takes the form $B(z) = C_1 e^{k_{1,j}z} + C_2 e^{-k_{1,j}z}$ where the wave parameters $k_{1,j}$ have already been defined in Section 3.1.1 and follow the condition (3.18). Because F is bounded in the cylinder, the solution for A are the Bessel functions of the first kind, i.e. $A_j(r) = C_{3,j} J_1(k_{1,j} r)$. The BC (3.17) becomes then:

$$A_j(r)\Big|_{0\le r\le a} \cdot \left.\frac{\partial B_j(z)}{\partial z}\right|_{z=0,d} = -2r \cdot 1, \tag{3.19}$$

which implies $B_j(z) = \dfrac{\sinh\left(k_{1,j}(z+\frac{d}{2})\right)}{k_{1,j}\cosh\left(k_{1,j}\frac{d}{2}\right)}$. At this stage we have determined $F_1 = \sum_{j=1}^{\infty} C_{3,j} J_1\left(k_{1,j}, r\right) B_j(z)$ and still have to find the coefficients $C_{3,j}$ from the

BC (3.19) for $A(r)$. This is achieved by multiplying F_1 by $rJ_1(k_{1,j}r)$ and averaging this last condition over the radius of the cylinder:

$$\int_0^a F_1(r,z)J_1\left(k_{1,j}r\right) \times r dr = \int_0^a (-2r)J_1\left(k_{1,j},r\right) r dr. \tag{3.20}$$

By this operation we take advantage of the orthogonal properties of the Bessel functions (cf. Appendix B.1), and the remaining coefficients can easily be calculated. It results that $C_{3,j} = -\dfrac{4a}{\left(\iota_{1,j}^2 - 1\right) J_1\left(\iota_{1,j}\right)}$. Finally, the solution for the dock without spar is:

$$F(r,z) = rz - 4a^2 \sum_{j=1}^{\infty} \frac{J_1\left(\iota_{1,j}\dfrac{r}{a}\right)}{J_1\left(\iota_{1,j}\right)\iota_{1,j}\left(\iota_{1,j}^2 - 1\right)} \frac{\sinh(k_{1,j}(z+\dfrac{d}{2}))}{\cosh(k_{1,j}\dfrac{d}{2})}. \tag{3.21}$$

3.2.2 $\boldsymbol{\Omega}$ for the two-body system dock and spar

We define $\boldsymbol{\Omega^{(1)}}$ and $\boldsymbol{\Omega^{(2)}}$ the Stokes Joukowski potentials associated to the motions of the spar and the dock, respectively. We also write $S_0^{(2)} = {S_0^{(2)}}^V + {S_0^{(2)}}^H$ the internal surface of the dock including the bottom, where the upper indices V and H stand for Vertical and Horizontal boundaries, and $S_0^{(1)}$ the surface of the spar. The BVPs for the two potentials are then:

$$\begin{cases} \nabla^2\boldsymbol{\Omega^{(1)}} = \mathbf{0} \quad \text{in } Q_0, \\ \dfrac{\partial \boldsymbol{\Omega^{(1)}}}{\partial n} = \mathbf{0} \quad \text{on } S_0^{(2)} \cup \Sigma_0, \\ \dfrac{\partial \boldsymbol{\Omega^{(1)}}}{\partial n} = \boldsymbol{r} \times \boldsymbol{n} \quad \text{on } S_0^{(1)}, \end{cases} \tag{3.22}$$

$$\begin{cases} \nabla^2\boldsymbol{\Omega^{(2)}} = 0 \quad \text{in } Q_0, \\ \dfrac{\partial \boldsymbol{\Omega^{(2)}}}{\partial n} = \boldsymbol{r} \times \boldsymbol{n} \quad \text{on } S_0^{(2)} \cup \Sigma_0, \\ \dfrac{\partial \boldsymbol{\Omega^{(2)}}}{\partial n} = \mathbf{0} \quad \text{on } S_0^{(1)}. \end{cases} \tag{3.23}$$

As Eq. (3.12) for the dock alone, we can introduce $F^{(1)}$ and $F^{(2)}$ which both satisfy Eq. (3.13) where Q_0 is now the annular domain. The previous BCs can thus be written:

$$\begin{cases} \dfrac{\partial F^{(1)}}{\partial r} = z \quad \text{on } S_0^{(1)}, \\ \dfrac{\partial F^{(1)}}{\partial z} = 0 \quad \text{on } {S_0^{(2)}}^H \cup \Sigma_0, \\ \dfrac{\partial F^{(1)}}{\partial r} = 0 \quad \text{on } {S_0^{(2)}}^H \cup \Sigma_0, \end{cases} \tag{3.24}$$

$$\begin{cases} \dfrac{\partial F^{(2)}}{\partial r} = z \quad \text{on } {S_0^{(2)}}^V, \\ \dfrac{\partial F^{(2)}}{\partial z} = -r \quad \text{on } {S_0^{(2)}}^H \cup \Sigma_0, \\ \dfrac{\partial F^{(2)}}{\partial r} = 0 \quad \text{on } S_0^{(1)}. \end{cases} \tag{3.25}$$

Both functions F are decomposed as in Eq. (3.16) such that the particular solution $F_p^{(1)}$ and $F_p^{(2)}$ satisfy the BCs on the vertical walls and the Laplace Equation. The following functions are for instance candidates:

$$F_p^{(1)}(r,z) = -\frac{a_0^2 z r}{a^2 - a_0^2} - \frac{a_0^2 a^2 z}{\left(a^2 - a_0^2\right) r}, \qquad F_p^{(2)}(r,z) = \frac{a^2 r z}{a^2 - a_0^2} + \frac{a^2 a_0^2 z}{\left(a^2 - a_0^2\right) r} \tag{3.26}$$

The system is now set for $F_1^{(1)}$ and $F_1^{(2)}$, which are also solutions of the Laplace equation and satisfy the BCs:

$$\begin{cases} \dfrac{\partial F_1^{(1)}}{\partial r} = 0 \ \text{ on } \ {S_0^{(2)}}^V \cup S_0^{(1)}, \\ \dfrac{\partial F_1^{(1)}}{\partial z} = -\dfrac{a_0^2 r}{a^2 - a_0^2} + \dfrac{a^2 a_0^2}{\left(a^2 - a_0^2\right) r} \\ \qquad\qquad \text{on } {S_0^{(2)}}^H \cup \Sigma_0, \end{cases} \tag{3.28}$$

$$\begin{cases} \dfrac{\partial F_1^{(2)}}{\partial r} = 0 \ \text{ on } \ {S_0^{(2)}}^V \cup S_0^{(1)}, \\ \dfrac{\partial F_1^{(2)}}{\partial z} = r - \dfrac{a^2 r}{a^2 - a_0^2} - \dfrac{a^2 a_0^2}{\left(a^2 - a_0^2\right) r} \\ \qquad\qquad \text{on } {S_0^{(2)}}^H \cup \Sigma_0. \end{cases} \tag{3.29}$$

Using separation of variables, the functions in z are exactly the same as the function $B(z)$ for the dock alone defined in the previous section. $F_1^{(1)}$ and $F_1^{(2)}$ are written as expansions of the functions $\Psi_{1,q}$, $q \in \mathbb{N}^*$ defined from the spectral problem. Thus, the zero normal velocity on all the vertical walls is satisfied. The second conditions of Eqs. (3.28) and (3.29) are now multiplied by $r\Psi_{1,j}$ and integrated over the radius in the annular domain. Using the orthonormal properties of $r\Psi_{1,j}$, the unknown coefficients for each term of the expansions can be calculated individually, similar to the dock alone. It results:

$$F^{(k)}(r,z) = F_p^{(k)}(r,z) + \sum_{j=1}^{\infty} \mathscr{G}_j^{(k)}(a,a_0) \frac{\Psi_{1,j}(r)}{\upsilon_{1,j} k_{1,j}} \frac{\sinh\left(k_{1,j}(z+\frac{d}{2})\right)}{\cosh\left(k_{1,j}\frac{d}{2}\right)} \qquad k \in \{1,2\}, \tag{3.30}$$

where we have defined:

$$\mathscr{G}_j^{(1)}(a, a_0) = \frac{a_0^2 a^2}{a^2 - a_0^2} I_{2,p} + \frac{a_0^2}{a^2 - a_0^2} I_{1,p}, \tag{3.31}$$

$$\mathscr{G}_j^{(2)}(a, a_0) = -\frac{2a^2 - a_0^2}{a^2 - a_0^2} I_{1,p} - \frac{a^2 a_0^2}{a^2 - a_0^2} I_{2,p}. \tag{3.32}$$

The integral $I_{1,p}$ and $I_{2,p}$ are given in Appendix B.3.

3.3 Linear modal theory

3.3.1 Modal equations for the dock

We consider now the motions of the dock. The absolute potential of the internal domain is expressed in a tank-fixed coordinate system (Faltinsen and Timokha, 2009):

$$\Phi(x, y, z, t) = \dot{\boldsymbol{\eta}}^{(2)}(t) \cdot \boldsymbol{r} + \boldsymbol{\omega}^{(2)}(t) \cdot \boldsymbol{\Omega} + \sum_{p=0}^{\infty} \sum_{q=1}^{\infty} R_{p,q}(t) \varphi_{p,q}(r, \theta, z), \tag{3.33}$$

where $\boldsymbol{\eta}^{(2)}$ and $\boldsymbol{\omega}^{(2)}$ are three-dimensional vectors describing respectively the rigid dock's translational and rotational motions, and the $\boldsymbol{r}$ position vector:

$$\boldsymbol{r} = \begin{bmatrix} r\cos(\theta) \\ r\sin(\theta) \\ z \end{bmatrix}, \qquad \boldsymbol{\eta}^{(2)} = \begin{bmatrix} \eta_1^{(2)} \\ \eta_2^{(2)} \\ \eta_3^{(2)} \end{bmatrix}, \qquad \boldsymbol{\omega}^{(2)} = \begin{bmatrix} \dot{\eta}_4^{(2)} \\ \dot{\eta}_5^{(2)} \\ \dot{\eta}_6^{(2)} \end{bmatrix}. \tag{3.34}$$

$\boldsymbol{\Omega}$ is the Joukowski potential established for the dock alone in Eq. (3.21), and $\varphi_{p,q}$ the eigenfunctions (3.2) in the dock alone. The first two terms of Eq. (3.33) correspond to the particular solutions of Φ satisfying the body-boundary conditions when the dock is moving and the free surface is rigid, while the last term satisfies the free-surface boundary condition in dock-fixed coordinate system. This last term is written as a summation of eigenmodes, weighted by unknown time-dependent modal coefficients $R_{p,q}(t)$, which remain to be determined from the Earth-fixed kinematic and dynamic free-surface boundary conditions. The same eigenfunction expansion is used to express the free-surface elevation in a dock-fixed coordinate system:

$$\zeta(x, y, t) = \sum_{p=0}^{\infty} \sum_{q=1}^{\infty} \beta_{p,q}(t) \varphi_{p,q}(x, y, 0), \tag{3.35}$$

where $\beta_{p,q}(t)$ are new unknown modal coefficients. The linear kinematic and dynamic free-surface boundary conditions are then written:

$$\begin{cases} \dfrac{\partial \Phi}{\partial z} = \dfrac{\partial \zeta}{\partial t} - r\cos(\theta)\dot{\eta}_5^{(2)} \text{ on } z = 0, \\ \\ \dfrac{\partial \Phi}{\partial t} = xg\eta_5^{(2)} - g\zeta \text{ on } z = 0. \end{cases} \tag{3.36}$$

Making use of the orthogonal properties of the Bessel functions J_p for $p \in \mathbb{N}$, we replace Φ and ζ by their expressions in Eq. (3.33) and (3.35), respectively, multiply these free surface conditions by J_p, and integrate over the free surface in the dock. It results modal equations for the unknown coefficients $R_{p,q}$ and $\beta_{p,q}$, independent for each pair (p, q):

$$\begin{cases} \dot{\beta}_{p,q} = \kappa_{p,q} R_{p,q}, \\ \\ \ddot{\beta}_{p,q} + \sigma_{p,q}^2 \beta_{p,q} = K_{p,q}(t), \end{cases} \tag{3.37}$$

where $K_{p,q}$ are the excitation introduced by the dock's motions, and $\kappa_{p,q} = \sigma_{p,q}^2/g$. In our model, the body is excited in surge and pitch only, and thus only the eigenfunctions in $\cos(p\theta)$ are considered. The exciting coefficients are then written:

$$K_{p,q}(t) = -\frac{\lambda_{1,p,q}}{\mu_{p,q}}\left(\ddot{\eta}_1^{(2)}(t) - g\eta_5^{(2)}(t)\right) - \frac{\ddot{\eta}_5(t)\lambda_{2,p,q}}{\mu_{p,q}}, \tag{3.38}$$

where we defined the following coefficients:

$$\mu_{p,q} = \frac{\rho}{\kappa_{p,q}} \int_{\Sigma_0} \varphi_{p,q}(r,\theta,0)^2 r d\theta dr = \frac{\rho\pi a^3\left(\iota_{p,q}^2 - p^2\right)}{2\iota_{p,q}^3 \tanh\left(\iota_{p,q} d/a\right)}, \tag{3.39}$$

$$\lambda_{1,p,q} = \rho \int_{\Sigma_0} \varphi_{p,q}(r,\theta,0) r^2 \cos(\theta) d\theta dr = \begin{cases} \rho\pi a^3/\iota_{1,q}^2 \text{ if } p = 1 \\ \\ 0 \text{ if } p \neq 1 \end{cases}, \tag{3.40}$$

$$\lambda_{2,p,q} = \rho \int_{\Sigma_0} \varphi_{p,q}(r,\theta,0)\Omega_2 r d\theta dr = \begin{cases} -2\pi\rho a^4/\iota_{1,q}^3 \tanh\left(\iota_{1,q} d/(2a)\right) \text{ if } p = 1 \\ \\ 0 \text{ if } p \neq 1 \end{cases}. \tag{3.41}$$

We note that only the anti-symmetric modes $p = 1$ are non-zero for the closed-bottom dock. As discussed in Sec. 3.1.1, this is because the anti-symmetric surge and pitch motions are the only excitation. We can note that for an open-bottom structure in waves, higher modes $p > 1$ would also be excited by incident waves for lower draughts. Finally the modal equations (3.37) can be re-written under the simplified form:

$$\ddot{\beta}_{1,q} + \sigma_{1,q}^2 \beta_{1,q} = -P_q \left[\ddot{\eta}_1^{(2)}(t) - g\eta_5(t) - S_q \ddot{\eta}_5^{(2)}(t) \right] \quad \text{for } q \in \mathbb{N}, \tag{3.42}$$

with:

$$\begin{cases} P_q = \dfrac{2\iota_{1,q} \tanh\left(\iota_{1,q} d/a\right)}{\iota_{1,q}^2 - 1}, \\ S_q = \dfrac{2a \tanh\left(\iota_{1,q} d/(2a)\right)}{\iota_{1,q}} \end{cases}. \tag{3.43}$$

Eq. (3.42) can generally be solved in time domain for instance by a 4th order Runge-Kutta numerical scheme for arbitrary motions of the dock. When the motions of the dock are harmonic at the frequency ω, as it is for example the case in regular waves, the exciting term in the right hand side of Equation (3.42) can be simplified under the form $K_{1,q} = C_q \cos(\alpha_q - \omega t)$ for $q \in \mathbb{N}$, where C_q and α_q are the real amplitude and phase of the excitation. An analytical solution of $\beta_{1,q}$ can thus easily be determined. If we assume the fluid initially at rest, i.e. $\beta_{1,q} = 0$ and $\dot{\beta}_{1,q} = 0$, it comes:

$$\beta_{1,q} = C_q \frac{\cos(\alpha_q)\cos(\sigma_{1,q}t)\sigma_{1,q} + \sin(\alpha_q)\sin(\sigma_{1,q}t)\omega - \sigma_{1,q}\cos(-\omega t + \alpha_q)}{\sigma_{1,q}(\omega^2 - \sigma_{1,q}^2)}. \tag{3.44}$$

ζ can now be reconstructed by summing the modes q in Eq. (3.35), Faltinsen and Timokha (2009) recommend for example seven to twelve modes. The two first terms of Eq. (3.44) oscillate at the natural sloshing frequency, while the last term is harmonic in the forcing frequency ω imposed by the motions of the dock. Within linear assumptions, and without any additional damping, we observe that the wave elevation will diverge at the sloshing natural frequency. In practice, viscous damping from the boundary layers and non-linear energy dissipation would introduce additional damping. If in addition we define a time-line such that the exciting phase $\alpha_q = 0$, the modal coefficients can be expressed as:

$$\beta_{1,q} = \frac{C_q}{\omega^2 - \sigma_{1,q}^2}[\cos(\sigma_{1,q}t) - \cos(\omega t)] = \frac{2C_q}{\omega^2 - \sigma_{1,q}^2}[\sin(\frac{\sigma_{1,q} - \omega}{2}t)\sin(\frac{\sigma_{1,q} + \omega}{2}t)]. \tag{3.45}$$

The wave elevation is thus oscillating at the frequency $(\sigma_{1,q} + \omega)/2$ inside an envelope oscillating at the frequency $(\sigma_{1,q} - \omega)/2$. This phenomenon is known as beating, and is characterized by the beating frequency:

$$\omega_{beating} = \sigma_{1,q} - \omega. \tag{3.46}$$

In absence of heave motion, the wave elevation in an Earth-fixed referential can simply be expressed as follow:

$$\zeta^{\text{Earth fixed}} = \zeta^{\text{body fixed}} - x\eta_5. \tag{3.47}$$

3.3.2 Hydrodynamic loads in frequency domain

We assume now a steady-state problem, i.e. we neglect the transient part of Eq. (3.44). Eq. (3.38) can be written

$$K_{1,q} = -\omega^2 \tilde{P}_{q,1} \overline{\eta}_1^{(2)} e^{-i\omega t} - \omega^2 \tilde{P}_{q,5} \overline{\eta}_5^{(2)} e^{-i\omega t}, \tag{3.48}$$

where $\tilde{P}_{q,1}$ and $\tilde{P}_{q,5}$ are the real coefficients

$$\begin{cases} \tilde{P}_{q,1} = -\lambda_{1,1,q}/\mu_{1,q}, \\ \tilde{P}_{q,5} = -(g\lambda_{1,1,q}\omega^{-2} + \lambda_{2,1,q})/\mu_{1,q}. \end{cases} \tag{3.49}$$

These expressions make in evidence accelerating terms in surge and pitch. Each mode of the potential flow is then also proportional to the motion's accelerations. The same conclusion can be made for the dynamic pressure, and exciting forces on the internal walls of the dock. It results that the hydrodynamic loads caused by the sloshing waves can be written in an Earth-fixed coordinate system as $-A_{i,j}^{\text{slosh}} \ddot{\eta}_j^{(2)}$, $(i,j) \in \{1,5\}^2$, where $A_{i,j}^{\text{slosh}}$ represent added mass coefficients. We can note that they could alternatively be considered as restoring forces, associated to the restoring coefficients $A_{i,j}^{\text{slosh}}/\omega^2$. In additions to these forces, the inertia of the water mass itself when there is no flow motions, also named "frozen water" by Faltinsen and Timokha (2009), has to be taken into account in the equations of motions of the dock. They are expressed here as added mass coefficients $A_{i,j}^F$, where the upper-script F stands for "frozen water". Both $A_{i,j}^F$ and $A_{i,j}^{\text{slosh}}$ coefficients can be written:

$$\begin{cases} A_{1,1}^F = A_{3,3}^F = M_l, \\ A_{5,5}^F = \omega^{-2} M_l g z_{lC_0} + I_{2,2}, \\ A_{1,5}^F = A_{5,1}^F = M_l z_{lC_0}, \\ A_{5,3}^F = -A_{3,5}^F = M_l x_{lC_0}, \end{cases} \tag{3.50}$$

$$\begin{cases} A_{1,k}^{\text{slosh}} = \sum_{m=1}^{\infty} \lambda_{1m} \frac{\tilde{P}_{m,k}\omega^2}{\sigma_m^2 - \omega^2}, \\ A_{5,1}^{\text{slosh}} = \sum_{m=1}^{\infty} \left(\frac{g\lambda_{1m}}{\omega^2} + \lambda_{02m} \right) \frac{\tilde{P}_{m,1}\omega^2}{\sigma_m^2 - \omega^2}, \\ A_{5,5}^{\text{slosh}} = \sum_{m=1}^{\infty} \left(\frac{g\lambda_{1m}}{\omega^2} + \lambda_{02m} \right) \frac{\tilde{P}_{m,5}\omega^2}{\sigma_m^2 - \omega^2}, \\ A_{5,3}^{\text{slosh}} = A_{3,5}^{\text{slosh}} = 0, \end{cases} \tag{3.51}$$

where $(x_{lC_0}, y_{lC_0}, z_{lC_0}) = \left(0, 0, -\frac{d}{2}\right)$ is the geometric centre of the water mass, M_l is the mass of the water, and $I_{2,2}$ is defined from the inertia matrix of the "frozen water" mass:

$$\mathbf{I} = \rho \begin{bmatrix} \int_{Q_0} (y^2+z^2)\, dQ & -\int_{Q_0} xy dQ & -\int_{Q_0} xz dQ \\ -\int_{Q_0} xy dQ & \int_{Q_0} (x^2+z^2)\, dQ & -\int_{Q_0} yz dQ \\ -\int_{Q_0} xz dQ & -\int_{Q_0} zy dQ & \int_{Q_0} (y^2+x^2)\, dQ \end{bmatrix} = \begin{bmatrix} I_{1,1} & 0 & 0 \\ 0 & I_{2,2} & 0 \\ 0 & 0 & I_{3,3} \end{bmatrix} \tag{3.52}$$

where

$$I_{1,1} = I_{2,2} = \frac{1}{12} M_l \left(3a^2 + d^2\right) + M_l \left(\frac{d}{2}\right)^2. \tag{3.53}$$

Furthermore, the internal flow will also have global rotational motions, corresponding with the second term of Φ in Eq. (3.33). These will affect the moment of inertia in pitch of the water volume, which is then defined by

$$J_{2,2} = \rho \int_{S_0 \cup \Sigma_0} \Omega_2 \frac{\partial \Omega_2}{\partial n} dS = \rho \pi a^2 \left(\frac{1}{3} d^3 - \frac{3}{4} d a^2 + 16 a^2 \sum_{p=1}^{\infty} \frac{\tanh(\frac{\iota_{1,p} d}{2a})}{\iota_{1,p}^3 (\iota_{1,p}^2 - 1)} \right). \tag{3.54}$$

Finally, the total hydrodynamic loads inside the dock can be included in the equations of the motions in the frequency domain thanks to the following added mass coefficients:

$$A_{i,j} = A_{i,j}^{\text{filled}} + A_{i,j}^{\text{slosh}}, \tag{3.55}$$

where

$$A_{i,j}^{\text{filled}} = \begin{cases} A_{5,5}^F + \left(J_{2,2} - I_{2,2}\right) & \text{if } \; i = j = 5, \\ A_{i,j}^F & \text{otherwise.} \end{cases} \tag{3.56}$$

3.3.3 Modal equations for the dock with spar

We propose in the present work similar modal equations for the dock with the spar. Sloshing eigenmodes are now excited by the surge and pitch motions of both the dock and the spar. The absolute potential flow in the annular domain can be written:

$$\Phi(x,y,z,t) = \dot{\boldsymbol{\eta}}^{(1)}(t) \cdot \boldsymbol{\Gamma}^{(1)} + \dot{\boldsymbol{\eta}}^{(2)}(t) \cdot \boldsymbol{\Gamma}^{(2)} + \boldsymbol{\omega}^{(1)}(t) \cdot \boldsymbol{\Omega}^{(1)} + \boldsymbol{\omega}^{(2)}(t) \cdot \boldsymbol{\Omega}^{(2)} + \sum_{p=0}^{\infty} \sum_{q=1}^{\infty} R_{p,q}(t) \varphi_{p,q}(r,\theta,z) \tag{3.57}$$

where $\varphi_{p,q}$ are the eigenfunctions (3.7) in the annular domain, $\boldsymbol{\Omega}^{(1)}$ and $\boldsymbol{\Omega}^{(2)}$ the Stokes-Joukowski potential defined in Sec. 3.2.2, and $\boldsymbol{\eta}^{(1)}$ and $\boldsymbol{\omega}^{(1)}$ are the

three-dimensional vectors describing respectively the spar's translational and rotational motions:

$$\boldsymbol{\eta}^{(1)} = \begin{bmatrix} \eta_1^{(1)} \\ \eta_2^{(1)} \\ \eta_3^{(1)} \end{bmatrix}, \qquad \boldsymbol{\omega}^{(1)} = \begin{bmatrix} \dot{\eta}_4^{(1)} \\ \dot{\eta}_5^{(1)} \\ \dot{\eta}_6^{(1)} \end{bmatrix}. \tag{3.58}$$

Because the spar remains fixed when the dock is moving in surge and vice versa, we now have to consider an internal potential flow associated to surge motions when the free surface is rigid. It is the equivalent in surge to the Stokes-Joukowski problems that we solved for the pitch motions. The potential $\boldsymbol{\Gamma}^{(1)}$ and $\boldsymbol{\Gamma}^{(2)}$ in Eq. (3.57) are thus defined as the solutions of the boundary-value problems (3.59) and (3.60) associated with the translational motions $\boldsymbol{\eta}^{(1)}$ and $\boldsymbol{\eta}^{(2)}$, respectively:

$$\begin{cases} \nabla^2 \boldsymbol{\Gamma}^{(1)} = \mathbf{0} & \text{in } Q_0, \\ \dfrac{\partial \boldsymbol{\Gamma}^{(1)}}{\partial n} = \mathbf{0} & \text{on } S_0^{(2)} \cup \Sigma_0, \\ \dfrac{\partial \boldsymbol{\Gamma}^{(1)}}{\partial n} = \boldsymbol{n} & \text{on } S_0^{(1)}, \end{cases} \tag{3.59}$$

$$\begin{cases} \nabla^2 \boldsymbol{\Gamma}^{(2)} = 0 & \text{in } Q_0, \\ \dfrac{\partial \boldsymbol{\Gamma}^{(2)}}{\partial n} = \boldsymbol{n} & \text{on } S_0^{(2)} \cup \Sigma_0, \\ \dfrac{\partial \boldsymbol{\Gamma}^{(2)}}{\partial n} = \mathbf{0} & \text{on } S_0^{(1)}. \end{cases} \tag{3.60}$$

These two systems are solved by separation of variables, noting that the potential caused by surge motions must be anti-symmetrical, i.e. proportional to $\cos(\theta)$, and independent of z. The Laplace equation imposes solutions in r of the form $[r, 1/r]$, fully determined thanks to the body-boundary conditions. The general expressions of the vectors $\boldsymbol{\Gamma}^{(1)}$ and $\boldsymbol{\Gamma}^{(2)}$ are given below for the three translational motions:

$$\boldsymbol{\Gamma}^{(1)} = \left(-\frac{a_0^2}{a^2 - a_0^2} r - \frac{a^2 a_0^2}{\left(a^2 - a_0^2\right) r} \right) \begin{bmatrix} \cos(\theta) \\ -\sin(\theta) \\ 0 \end{bmatrix}, \tag{3.61}$$

$$\boldsymbol{\Gamma}^{(2)} = \left(\frac{a^2}{a^2 - a_0^2} r + \frac{a^2 a_0^2}{\left(a^2 - a_0^2\right) r} \right) \begin{bmatrix} \cos(\theta) \\ -\sin(\theta) \\ 0 \end{bmatrix} + \begin{bmatrix} 0 \\ 0 \\ z \end{bmatrix}. \tag{3.62}$$

As for the dock alone, surge and pitch motions only excite the first mode $p = 1$. We express the free-surface elevation in a dock-fixed coordinate system:

$$\zeta(x, y, t) = \sum_{q=1}^{\infty} \beta_{1,q}(t) \varphi_{1,q}(x, y, 0). \tag{3.63}$$

We now insert the expressions of Φ and ζ in Eqs. (3.57) and (3.63) in the free-surface boundary condition (3.36) for the two-body system. Both the kinematic and dynamic boundary conditions are multiplied by the orthogonal eigenfunctions

$\varphi_{1,q}$ and integrated over the free surface, resulting in the same modal equations as for the dock alone:

$$\begin{cases} \dot{\beta}_{1,q} = \kappa_{1,q} R_{1,q}, \\ \ddot{\beta}_{1,q} + \sigma_{1,q}^2 \beta_{1,q} = K_{1,q}(t). \end{cases} \tag{3.64}$$

but where $K_{1,q}(t)$ is now defined as

$$K_{1,q}(t) = -\frac{1}{\mu_{1,q}} \left[\lambda_{1,1,q} \ddot{\eta}_1^{(1)} + \lambda_{2,1,q} \ddot{\eta}_1^{(2)} + \lambda_{3,1,q} \ddot{\eta}_5^{(1)} + \lambda_{4,1,q} \ddot{\eta}_5^{(2)} - \lambda_{5,1,q} g \eta_5^{(2)} \right]. \tag{3.65}$$

The hydrodynamic coefficients μ and λ in Eq. (3.65) are given in Appendix B.3. It should be emphasised that the λ coefficients associated to the dock motions differ from the case of the dock without spar. The solutions are expressed under the same form as for the dock alone (cf. Eq (3.44)), replacing the natural sloshing frequencies by those of the annular domain between the dock and the spar, and with additional exciting terms caused by the spar's surge and pitch motions.

3.4 Variational methods

We consider now that a thin annular baffle is installed inside the dock. The baffle has a width a_B and is submerged at the distance d_B from the mean free surface, mounted as shown in Fig. 3.1. Its thickness is assumed to be small compared to a_B. The spectral problem (3.1) can not be solved analytically for the case with a baffle. Variational approaches, which are based on the conservation of mechanical energy, present alternative methods to estimate eigenmodes and eigenfrequencies for small variations of the volume Q_0.
The potential and kinetic energies of an arbitrary flow in the domain Q_0 can generally be expressed as:

$$E_p = \rho g \int_{\Sigma_0} \int_0^{\zeta(r,\theta)} z \mathrm{d}z \mathrm{d}S, \tag{3.66}$$

$$E_k = \frac{1}{2} \rho \int_{Q_0} (\nabla \Phi)^2 \, \mathrm{d}Q. \tag{3.67}$$

For a free standing wave periodic in time $\Phi(x, y, z, t) = \varphi_{p,q}(x, y, z) \cos(\sigma_{p,q} t)$ associated to the mode $(p, q) \in \mathbb{N} \times \mathbb{N}^*$, Eqs. (3.66) and (3.67) becomes:

$$E_p = \frac{\rho \sigma_{p,q}^2}{2g} \sin^2\left(\sigma_{p,q} t\right) \int_{\Sigma_0} \varphi_{p,q}^2 dS, \tag{3.68}$$

$$E_k = \frac{1}{2} \rho \cos^2\left(\sigma_{p,q} t\right) \int_{Q_0} \left(\nabla \varphi_{p,q}\right)^2 \mathrm{d}Q. \tag{3.69}$$

The kinematic free-surface boundary condition was used in (3.68) to express the instantaneous free-surface elevation as a function of the eigenmode $\varphi_{p,q}$. The conservation of energy $dE_M/dt = d\left(E_k + E_p\right)/dt = 0$ results in the relationship:

$$\kappa_{p,q} = \frac{\sigma_{p,q}^2}{g} = \frac{\int_{Q_0} \left(\nabla \varphi_{p,q}\right)^2 \mathrm{d}Q}{\int_{\Sigma_0} \varphi_{p,q}^2 \mathrm{d}S}, \tag{3.70}$$

from which is defined the functional, also called Rayleigh quotient:

$$K_{Q_0,\Sigma_0}(\varphi) = \frac{\int_{Q_0} (\nabla \varphi)^2 \mathrm{d}Q}{\int_{\Sigma_0} \varphi^2 \mathrm{d}S}. \tag{3.71}$$

Its argument φ is a spatial function which does not necessarily satisfy the boundary value problem (3.1). Local minima of the Rayleigh quotient are reached at the eigenmodes $\varphi = \varphi_{p,q}$, and in particular, the functions for which these minima are reached always satisfy all the equations of the spectral problem. This latest assertion is demonstrated in detail by Faltinsen and Timokha (2009), and is only true for Neumann's type of BCs on the body surface: the spectral problem is then called "natural".
It is interesting to note that for two volumes $Q_0^{(1)}$ and $Q_0^{(2)}$ that have an identical free surface Σ_0, and such that $Q_0^{(2)} \subsetneq Q_0^{(1)}$, then the eigen frequencies verify $\sigma_p^{(2)} < \sigma_p^{(1)}$. Thus, even if it is generally not possible to determine the eigenfunctions for most problems, we can often estimate bounds of the natural frequencies by bounding the domain Q_0 with geometries for which the eigenmodes and frequencies are known.

Faltinsen and Timokha (2009) present asymptotic methods to estimate shifted natural frequencies for small variations of the water volume, adapted to the case when a thin annular baffle is installed inside the dock. We write respectively $\varphi_{p,q}$ and $\varphi'_{p,q}$ the sloshing eigenfunctions in the dock without and with the baffle. We also denote by Q'_0 the water volume with the baffle. Because of the singularity at the sharp edge of the baffle, $\varphi'_{p,q}$ does not converge to $\varphi_{p,q}$ when the baffle's width a_B converges to 0. It is therefore not possible to estimate the kinetic energy in the reduced volume from the velocity caused by undisturbed eigenmodes: $K_{Q'_0,\Sigma_0}(\varphi'_{p,q}) \neq K_{Q'_0,\Sigma'_0}(\varphi_{p,q})$, as it is commonly the usage for chamfered tanks. To overcome this difficulty, Faltinsen and Timokha (2009) propose an estimation of the reduced sloshing eigenfrequencies based on Green's second identity and

assuming that the baffle's width is small compared to both the eigenmode wave length and the submergence d_B. The main steps of their derivations, including the main assumptions made in the case of the dock with baffle are presented below.

We denote C the surface of the baffle. Since both $\varphi_{p,q}$ and $\varphi'_{p,q}$ satisfies the non-penetration boundary condition on S_0, Green's second identity for both potential in the domain delimited by $S_0 + C + \Sigma_0$ is given by:

$$\int_{\Sigma_0} \left(\varphi'_{p,q} \frac{\partial \varphi_{p,q}}{\partial n} - \varphi_{p,q} \frac{\partial \varphi'_{p,q}}{\partial n} \right) \mathrm{d}S + \int_C \varphi'_{p,q} \frac{\partial \varphi_{p,q}}{\partial n} \mathrm{d}S = 0. \tag{3.72}$$

Inserting the body-boundary condition $\partial \varphi'_{p,q}/\partial n = 0$ on C, and the free-surface boundary conditions $\partial \varphi_{p,q}/\partial z = \kappa_{p,q} \varphi_{p,q}$ on Σ_0 and $\partial \varphi'_{p,q}/\partial z = \kappa_{p,q} \varphi'_{p,q}$ on Σ_0, Eq. (3.72) is simplified to:

$$\kappa'_{p,q} = \kappa_{p,q} + \frac{\int_C \varphi'_{p,q} \dfrac{\partial \varphi_{p,q}}{\partial n} \mathrm{d}S}{\int_{\Sigma_0} \varphi_{p,q} \varphi'_{p,q} \mathrm{d}S} \tag{3.73}$$

We introduce the perturbation $\varphi^d_{p,q}$ of the potential flow caused by the baffle:

$$\varphi^d_{p,q} = \varphi'_{p,q} - \varphi_{p,q}. \tag{3.74}$$

The body-boundary condition on the baffle can be written $\partial \varphi^d_{p,q}/\partial z = -\partial \varphi_{p,q}/\partial z$ on C. We assume that the baffle's width is small compared to the wave length of the sloshing eigenmode, such that

$$\frac{\partial \varphi^d_{p,q}}{\partial z} = -\frac{\partial \varphi_{p,q}}{\partial z} \simeq -\frac{\partial \varphi_{p,q}}{\partial z}\Big|_{\substack{r=a \\ z=-d_B}} + O\left(a_B/a\right) \text{ on } C \tag{3.75}$$

We define the potential $\tilde{\varphi}^d_{p,q}$, related to $\varphi^d_{p,q}$ by

$$\varphi^d_{p,q} \simeq -\tilde{\varphi}^d_{p,q} \frac{\partial \varphi^d_{p,q}}{\partial z}\Big|_{\substack{r=a \\ z=-d_B}} + O\left(a_B/a\right) \text{ on } C, \tag{3.76}$$

and where $\partial \tilde{\varphi}^d_{p,q}/\partial z = 1$ on C in order to satisfy Eq. (3.75). From Eq. (3.76), $\tilde{\varphi}^d_{p,q}$ can be seen as the radiation potential created by the baffle when this one oscillates along the wall of the dock at the velocity $-\partial \varphi^d_{p,q}/\partial z$. The added mass of the baffle associated to this radiation problem is then given by:

$$A^{\text{baffle}} = -\rho \int_C \tilde{\varphi}^d_{p,q} \mathrm{d}S. \tag{3.77}$$

With the decomposition (3.74), the numerator of Eq. (3.73) becomes:

$$\int_C \varphi'_{p,q} \frac{\partial \varphi_{p,q}}{\partial n} \mathrm{d}S = \int_C \varphi_{p,q} \frac{\partial \varphi_{p,q}}{\partial n} \mathrm{d}S + \int_C \varphi^d_{p,q} \frac{\partial \varphi_{p,q}}{\partial n} \mathrm{d}S. \tag{3.78}$$

As in Eqs. (3.75)-(3.76), we assume that the flow velocity of the undisturbed potential varies slowly along the baffle, and can be expressed by its value at the fixation point on the dock on C. We replace then $\varphi^d_{p,q}$ by its expression in Eq. (3.76) in Eq. (3.78):

$$\int_C \varphi'_{p,q} \frac{\partial \varphi_{p,q}}{\partial n} \mathrm{d}S = \left[\frac{\partial \varphi_{p,q}}{\partial z}\Big|_{\substack{r=a \\ z=-d_B}} + O\left(a_B/a\right) \right] \int_C \varphi_{p,q} \mathrm{d}S + \left[\frac{\partial \varphi_{p,q}}{\partial z}\Big|_{\substack{r=a \\ z=-d_B}} + O\left(a_B/a\right) \right] \times \left[-\frac{\partial \varphi_{p,q}}{\partial z}\Big|_{\substack{r=a \\ z=-d_B}} + O\left(a_B/a\right) \right] \int_C \tilde{\varphi}^d_{p,q} \mathrm{d}S \tag{3.79}$$

We see that the second integral in the left hand side of Eq. (3.79) can be expressed as an added mass term as in Eq.(3.77). The first integral in the left hand side of Eq. (3.79) can be approximated applying Gauss theorem:

$$\int_C \varphi_{p,q} \mathrm{d}S = \int_{\delta Q_0} \frac{\partial \varphi_{p,q}}{\partial n} \mathrm{d}Q \simeq \left[\frac{\partial \varphi_{p,q}}{\partial z}\Big|_{\substack{r=a \\ z=-d_B}} + O\left(a_B/a\right) \right] \times \mathrm{Vol}(\delta Q_0) \tag{3.80}$$

where $\delta Q_0 = Q_0 - Q'_0$ and $\mathrm{Vol}(\delta Q_0)$ is the volume of the baffle, which is of higher order with respect to a_B. The integral Eq. (3.80) is thus negligible in our approach. The denominator of Eq. (3.73) is now simplified by making the assumption that d_B/a_B is high enough, such that $\varphi^d_{p,q}$ does not affect the free surface. Then we can write:

$$\int_{\Sigma_0} \varphi_{p,q} \varphi'_{p,q} \mathrm{d}S \simeq \int_{\Sigma_0} \varphi^2_{p,q} \mathrm{d}S \tag{3.81}$$

Including all the simplifications made from Eqs. (3.79) to (3.81), Eq. (3.73) can be expressed as:

$$\kappa'_{p,q}/\kappa_{p,q} = \frac{\sigma'^2_{p,q}}{\sigma^2_{p,q}} = 1 - \frac{\left.\frac{\partial \varphi_{p,q}}{\partial z}\right|^2_{\substack{r=a \\ z=-d_B}} A^{\mathrm{baffle}}}{\rho \kappa_{p,q} \int_{\Sigma_0} \varphi^2_{p,q} \mathrm{d}S} \tag{3.82}$$

The added mass of the baffle A^{baffle} is not known, but can be estimated from the two-dimensional added mass A_0^{plate} of a flat plate perpendicular to a wall, then integrated along θ. A_0^{plate} is given analytically by Eq. (3.83) as half of the added mass of a flat plate of length $2a_B$ in infinite fluidNewman (1977):

$$A_0^{\mathrm{plate}} = \frac{1}{2} \pi \rho a_B^2. \tag{3.83}$$

The reduced eigenfrequencies $\sigma'^2_{p,q}$ when the baffle is installed are hence given by:

$$\frac{\sigma'^2_{p,q}}{\sigma^2_{p,q}} = 1 - \frac{\int_0^{2\pi} \left.\frac{\partial \varphi_{p,q}}{\partial z}\right|^2_{\substack{r=a \\ z=-d_B}} A_0^{\text{plate}} a \mathrm{d}\theta}{\rho \kappa_{p,q} \int_{\Sigma_0} \varphi^2_{p,q} \mathrm{d}S}. \tag{3.84}$$

It is important to emphasise that the formula (3.84) is based on the assumption that the flow is irrotational, and does not account for the viscous eddies created by the flow separation at the edge of the baffle. A corrective term will be brought to the added mass of the baffle in a later section to account for these viscous effects. In our model, the width of the baffle $a_B/a = 0.17$ is low compared to the the wave length associated to the lowest sloshing eigenfrequencies $\lambda_{1,1}/a = 3.4$. It is therefore reasonable to assume that the flow velocity $\partial\varphi_{p,q}/\partial z$ does not vary much along C. However, a_B and d_B have similar dimensions in our work, and the assumption (3.81) is more questionable.

This last point is for example discussed by Gavrilyuk et al. (2006). In their work, they solve the spectral problem for a cylinder with an annular solid baffle thanks to a domain decomposition approach. In particular, they consider several values of a_B and d_B in the same range as in the present work. Fig. 3.7 shows the radial profile of the first sloshing eigenmode $\varphi_{1,1}$ at the free surface from their results, both for $d_B/a = 0.1$ and $d_B/a = 0.3$, and for several baffle's widths. As expected, the larger deviations from the case without baffle are obtained for the smallest submergence $d_B/a = 0.1$. Interestingly, larger deviations from the case without baffle are also observed for the lowest a_B/a ratios. Gavrilyuk et al. (2006) emphasise that both $\varphi'_{1,1}(r, 0, 0)$ and $\sigma'_{1,1}$ vary less than 1% as long as $a_B/a \lesssim 0.05$. It is however not true when comparing with the case without baffle, i.e. $a_B/a = 0$. As discussed at the beginning of the section, there is indeed no analytical continuation from $\varphi'_{1,1}$ to $\varphi_{1,1}$ when the baffle's width goes to 0 due to the singularity at the sharp corner. In our work, we consider $a_B/a = 0.17$ and the three submergences $d_B/a = 0.10$, $d_B/a = 0.17$ and $d_B/a = 0.27$. For the lowest submergence $d_B/a = 0.10$, significant deviation is observed from Gavrilyuk et al. (2006)'s results between the eigenmodes with and without baffles at the free surface and over the width of the baffle near $r/a = 1$. However, the natural frequency of the first sloshing mode for the dock with baffle and estimated from Eq. (3.84) remains very close to the ones calculated by Gavrilyuk et al. (2006) for all submergences d_B, as long as $a_B/a \lesssim 0.25$ (cf. Fig. 3.8).

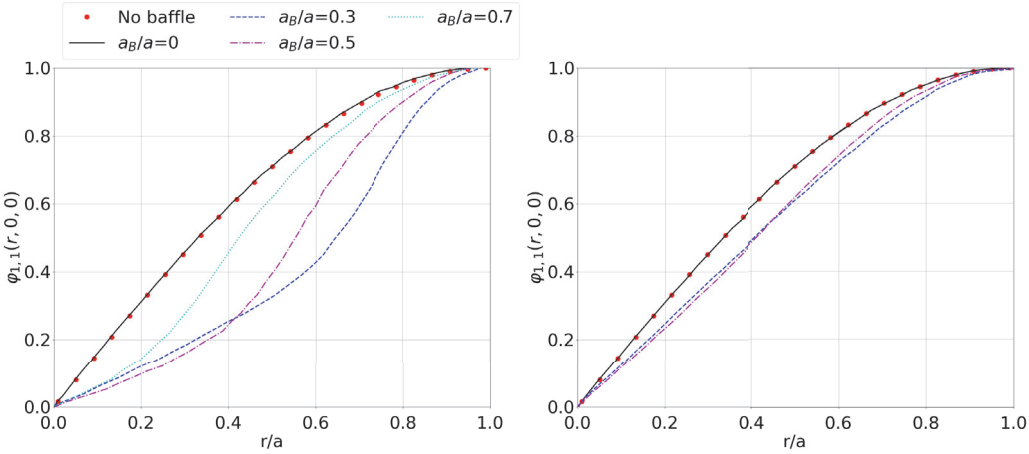

Figure 3.7: *Radial profile of the first sloshing eigenmode* $\varphi_{1,1}$ *in* $\theta = 0°$ *and* $z = 0m$ *from Gavrilyuk et al. (2006) for a cylinder with a solid annular baffle. In their work, the radius-to-draught ratio is* $a/d = 1$*. For the case without baffle, i.e.* $a_B/a = 0$*, personal computations made from Eq.* (3.2) *are indicated by red dots. Left:* $d_B/a = 0.1$*, right:* $d_B/a = 0.3$*. For comparison, the following dimensions are used in our experimental model (not in the figure):* $a/d = 0.38$*,* $a_B/a = 0.17$*, and either* $d_B/a = 0.10$*,* $d_B/a = 0.17$ *or* $d_B/a = 0.27$*.*

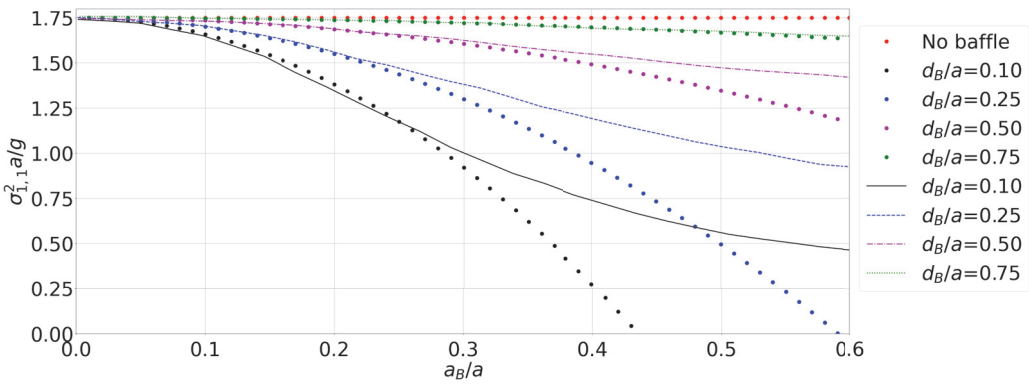

Figure 3.8: *Dots: first eigenfrequencies calculated from either Eq.* (3.84) *when a baffle is installed or Eq.* (3.3) *when there is no baffle. Solid and dashed lines:* $\sigma'_{1,1}$ *from Gavrilyuk et al. (2006) for a cylinder with a solid annular baffle. Radius-to-draught ratio:* $a/d = 1$*.*

3.5 Viscous effects of annular baffles

The viscous eddies formed by the flow separation at the sharp edge of the baffles, and through the perforated holes for perforated baffles, dissipate the energy of the sloshing waves. Similar to Faltinsen and Timokha (2009), we model these viscous effects through the modal equations (3.37) by introducing a linear equivalent damping ratio ξ_1:

$$\begin{cases} \dot{\beta}_{1,1} = \kappa_{1,1} R_{1,1}, \\ \\ \ddot{\beta}_{1,1} + 2\xi_1 \sigma'_{1,1} \dot{\beta}_{1,1} + \sigma'^2_{1,1} \beta_{1,1} = K_{1,1}(t). \end{cases} \tag{3.85}$$

In this approach, we consider that viscous effects only affect the first sloshing mode, as this is the one that is excited mainly, and it will therefore dominate the internal flow entirely. It is assumed that the shape of the sloshing eigenmodes is unchanged compared to the case without baffle. This last assumption is best for high baffle's submergences d_B/a, as discussed in the previous section, and represents an error source in our model. $\sigma_{1,1}$ was replaced by $\sigma'_{1,1}$ in Eq. (3.85) to include the effects of the baffle on the first eigenfrequency. The viscous effects will also affect the added mass of the baffle, and so the reduced natural frequency (cf. Eq (3.84)). Isaacson and Premasiri (2001) gave estimations of the damping ratio caused by a horizontal solid baffle in a two-dimensional rectangular tank, relating the work produced by a non-linear Morison-type force on the baffle to the average rate of energy dissipated during one period of oscillation. In this section, we adapt their approach for a three-dimensional circular cylinder with either solid or perforated annular baffle.

We will mostly use complex notations. $K_{1,1}(t) = C_1 e^{-i\omega t}$ is assumed to be harmonic at the frequency ω, where C_1 is here a complex amplitude containing information on the phase of the excitation. The modal equations (3.85) represent a damped harmonic oscillator. The solutions $\beta_{1,1}(t)$ and $R_{1,1}(t)$ are composed of both a transient part and a steady-state part. The steady-state part is the response to the forcing frequency ω, while the transient part is dominated by the sloshing response, oscillating at the reduced frequency $\sqrt{1-\xi_1^2}\sigma'_{1,1}$, and vanishing exponentially for high t because of viscous damping. Typical damping ratios in our work range between 1% to 3.5% (see more details in Sec. 6.2.1), such that typical relaxation times $\tau_r = 1/(\sigma'_{1,1}\xi_1)$ range between 3.6s to 12.7s, which are high compared to the sloshing period $T_{1,1} = 0.80$s. We will assume that $t >> \tau_r$, and only consider the steady-state part of the modal coefficients, given by;

$$\beta_{1,1}(t) = \frac{-C_1 e^{-i\omega t}}{2i\omega\sigma_{1,1}\xi_1 + \omega^2 - \sigma_{1,1}^2} \tag{3.86}$$

$$R_{1,1}(t) = \frac{g}{\sigma_{1,1}'^2} \frac{i\omega C_1 e^{-i\omega t}}{2i\omega\sigma_{1,1}'\xi_1 + \omega^2 - \sigma_{1,1}'^2} = f_1(\omega) C_1 e^{-i\omega t} \tag{3.87}$$

3.5.1 Average time rate of energy dissipation

The mechanical energy in the dock when there is no baffle is estimated by the energy of the first sloshing mode, corresponding to a standing wave of amplitude $|\beta_{1,1}|$ and frequency $\sigma_{1,1}$. From Eqs. (3.66) and (3.67), the potential and kinetic energies become:

$$E_p = \frac{1}{2}\rho g \int_0^{2\pi} \int_{r=0}^{a} \left(\beta_{1,1}\varphi_{1,1}(r,\theta,0)\right)^2 r\mathrm{d}r\mathrm{d}\theta, \tag{3.88}$$

$$E_k = \frac{1}{2}\rho \int_0^{2\pi} \int_{z=-d}^{0} \int_{r=0}^{a} R_{1,1}^2 \left[\left(\frac{\partial\varphi_{1,1}}{\partial r}\right)^2 + \left(\frac{\partial\varphi_{1,1}}{\partial z'}\right)^2 + \left(\frac{1}{r}\frac{\partial\varphi_{1,1}}{\partial\theta}\right)^2 \right] r\mathrm{d}r\mathrm{d}z\mathrm{d}\theta. \tag{3.89}$$

The total mechanical energy is then defined by:

$$E_M = E_p(t) + E_k(t), \tag{3.90}$$

which remains constant in the absence of the baffle since there is no dissipative forces. Time series of E_k, E_p and E_M are illustrated in Fig. 3.9 for the dock without spar. As expected, E_p and E_k are harmonic at the frequency $2\sigma_{1,1}$ due their dependency in $\beta_{1,1}^2(t)$ and $R_{1,1}^2(t)$, respectively. In this figure, it is shown that E_M is bounded by the mechanical energies of standing waves in three-dimensional rectangular tanks either contained in the dock (lower bound), or containing the dock (higher bound), as defined in Fig. 3.10. It can be noted that in rectangular tanks, the local energy is the same over the whole length of the tank in the direction perpendicular to the eigenmode, while for a circular tank, the local energy decreases with $\cos^2\theta$ in the angular direction.

Both E_p and E_k in Eqs. (3.88) and (3.89) have analytical solutions. However, because the kinetic energy is maximum when the potential energy is null, and vice versa, it is sufficient to calculate E_M either from E_k or E_p. The latter leads to much simpler calculation and has been used in the present work. Their amplitudes are given for the cases with and without spar:

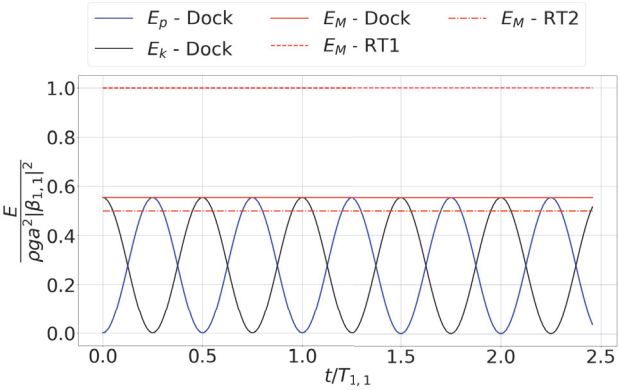

Figure 3.9: *Potential, kinetic, and mechanical energies of a standing wave $\beta_{1,1}(t) = |\beta_{1,1}|\sin(\sigma_{1,1}t)$ in the dock without spar nor baffle, compared with the mechanical energies of standing waves with the same amplitude in the rectangular tanks RT1 and RT2 (cf. Fig. 3.10). The mechanical energy of a standing wave of amplitude $|\beta_{1,1}|$ in a rectangular tank with a square section is given by (Newman, 1977): $\frac{1}{4}\rho g s^2 |\beta_{1,1}|^2$. The analytical expression of E_k used in this figure is given in Appendix B.4.*

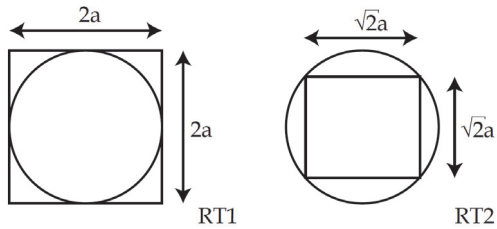

Figure 3.10: *Sketch of the two rectangular tanks compared with the dock (circular), bird's-eye view. Left: rectangular tank RT1 of side's length $s = 2a$. Right: rectangular tank RT2 of side's length $s = \sqrt{2}a$.*

$$E_{p,\max}^{\text{dock}} = \rho g \pi a^2 \frac{\iota_{1,1}^2 - 1}{4\iota_{1,1}^2} |\beta_{1,1}|^2, \tag{3.91}$$

$$E_{p,\max}^{\text{dock+spar}} = \frac{1}{2}\rho g b^2 \pi |\beta_{1,1}|^2. \tag{3.92}$$

When dissipative forces play a role, the mechanical energy is no longer conserved. Studying the energy of a standing wave in a rectangular tank dissipated by boundary layer viscous effects, Keulegan (1959) introduced a formalism that is now most commonly used to relate the damping ratio to the average time rate of energy dissipation. We denote $\epsilon_D(t)$ the energy dissipated by viscous forces. The dissipation occurs at a time scale that is assumed to be long compared to $T_{1,1}$, such that the ratio $\epsilon_D/E_M = 2\alpha$ can be considered constant over a period of

oscillation. For a fraction of oscillation $\delta t/T_{1,1}$, the increase δE_M of mechanical energy is given by:

$$\frac{\delta E_M}{E_M} = -\frac{\epsilon_D}{E_M}\frac{\delta t}{T_{1,1}}, \tag{3.93}$$

which integrated from 0 to t gives $E_M(t) = E_M(t=0)\exp\left(-2\alpha t/T_{1,1}\right)$. Because the energy is proportional to the square of the standing wave's amplitude, we also have $\beta_{1,1} = \beta_{1,1}(t=0)\exp\left(-\alpha t/T_{1,1}\right)$. Furthermore, the decay of a damped harmonic oscillator as in Eq. (3.85) when there is no excitation is proportional to $\exp(-\xi_1\sigma_{1,1}t)$. By identification, $\xi_1 = \alpha/(2\pi)$.
ϵ_D/E_M is in reality dependent on the wave amplitude $\beta_{1,1}(t)$, which decays with t. However, for low ξ_1, it is reasonable to the assume that ϵ_D/E_M does not vary much over one period of oscillation. In practice, the damping ratio can hence be estimated from the average rate of energy dissipated over one period of oscillation, given by $D = \epsilon_D/T_{1,1}$ where ϵ_D is the work over one period of the dissipative forces, and from the mechanical energy of undamped standing waves E_M (cf. Eq (3.91)-(3.92)):

$$\xi_1 = \frac{D}{2\sigma_{1,1}E_M}. \tag{3.94}$$

3.5.2 Damping caused by solid and perforated annular baffles

The energy dissipated D_B in the dock due to the annular baffle can be estimated as the work produced by dissipative forces on the baffle. We assume strip theory to hold, and integrate the two-dimensional loads on each angular section of the baffle, which are estimated by Morison's formula for a flat plate:

$$F_D(\theta,t) = \frac{1}{2}\rho\, a_B\, C_D(\theta)\, v_r(\theta,t)|v_r(\theta,t)| + \frac{1}{4}\rho\pi a_B^2 C_M\, \dot{v}_r(\theta,t) \tag{3.95}$$

where $v_r(\theta,t)$ is the relative vertical flow velocity on the baffle, calculated at the wall in $r = a$ in a tank-fixed coordinate system:

$$v_r(\theta,t) = R_{1,1}(t)\frac{\partial\varphi_{1,1}}{\partial z}\Big|_{\substack{r=a\\z=-d_B}} + \dot{\eta}_5^{(2)}(t)\left[\frac{\partial\Omega^{(2)}}{\partial z}\Big|_{\substack{r=a\\z=-d_B}} + a\cos(\theta)\right] + \frac{\partial\Omega^{(1)}}{\partial z}\Big|_{\substack{r=a\\z=-d_B}}\dot{\eta}_5^{(1)}(t). \tag{3.96}$$

In case there is no spar, the last term of Eq. (3.96) is null, and $\Omega^{(2)}$ is replaced by Ω for the dock alone as given in Sec. 3.2.1. With Eq. (3.95), we in particular disregard the three-dimensional viscous effects.
Keulegan and Carpenter (1958) conducted large series of experiments of periodic flow on cylinders and plates in infinite fluid, and first emphasized the dependency of the added mass coefficient C_M and drag coefficient C_D in Eq. (3.95) on the parameter:

$$KC = U_m T/(2a_B), \tag{3.97}$$

also known as the Keulegan-Carpenter (KC) number. U_m is the amplitude of the relative ambient flow velocity on the baffle v_r, T its period, and $2a_B$ the characteristic length of the body, here set as the length of the baffle mirrored through the wall of the dock. Their experiments included a large range of KC numbers with $KC > 2$. In our simulations, typical KC numbers on the angular section $\theta = 0°$ at sloshing resonance range between 0.55 to 0.75 (see more details in Sec. 6.2). Low KC numbers (KC<2) were studied by Graham (1980), who analysed the forces caused by the shedding of vortices from sharp edges. For flat plates, he established the following expressions for the added mass and drag coefficients:

$$C_M = \frac{A^{\text{plate}}}{A_0^{\text{plate}}} = \alpha_0 + \alpha_1 \text{KC}^{\frac{2}{3}}, \tag{3.98}$$

$$C_D = \alpha_2 KC^{-\frac{1}{3}}, \tag{3.99}$$

where A^{plate} is here half the added mass of a flat plate of length $2a_B$, which accounts for viscous effects due to flow separation. For a solid plate, $\alpha_0 = 1$. Graham (1980) provided analytical values and experimental values based on curve fitting for the two coefficients α_1 and α_2, with a significant difference between both methods. Hence, his theoretical values of α_1 and α_2 are 0.25 and 11.8, respectively, while its experimental values are 0.2 and 8.0, respectively. In the present work, we use the coefficients $\alpha_1 = 0.21$ and $\alpha_2 = 10.1$ obtained empirically by Mentzoni and Kristiansen (2019) through CFD simulations on two-dimensional plates in infinite fluid (see also Mentzoni et al. (2018); Mentzoni and Kristiansen (2020); Mentzoni (2020)). In their work, Mentzoni and Kristiansen (2019) extended Graham's formulas to perforated baffles, running numerous CFD simulations for KC numbers between 0.24 and 2.2. This approach has the advantage of being easy to implement, and gives good estimations of the loads on the baffle, as long as $\tau < 0.35$ and $KC > 0.24$. For higher perforations ratio, or lower KC-numbers, Mentzoni and Kristiansen (2019) observe a sharp increase of the discrepancy between the results from his CFD simulations and from Graham's formulas, due to that these last were established for a solid plate, and only account for the flow separation at the edge of the baffle and not for the flow separation through the holes of perforated plates. Their coefficients are given in Table 3.2 for solid plates ($\tau = 0$) and the two perforation ratios that we have used $\tau = 0.15$ and $\tau = 0.3$. For these perforation ratios, the viscous loads caused by the flow separation at the sharp edge still dominate compared to the loads caused by the flow separation through the perforation holes (Mentzoni, 2020), such that Graham's functional forms (3.98) and (3.99) remain relevant. One should note that the scaling effects

on the hydrodynamic loads caused by the flow separation on the sharp edge are not expected to matter (Mentzoni, 2020), such that the coefficients from Table 3.2 can be used as given.
The added mass of the baffle A_0^{plate} is replaced by A^{plate} in Eq. (3.84) to estimate the shifted sloshing frequency $\sigma'_{1,1}$, which becomes KC dependent. Analytical expressions of $\sigma'_{1,1}$ are given for the dock with and without spar in Appendix B.5.

Table 3.2: *Empirical coefficients from Graham's formulas provided by Mentzoni and Kristiansen (2019) for flat plates of perforation ratio τ in infinite fluid. $\tau = 0$ corresponds to a solid plate.*

τ	α_0	α_1	α_2
0	1.000	0.216	10.1
0.15	0.281	0.271	8.72
0.30	0.017	0.181	5.48

Only the first term of Eq. (3.95) is dissipative. The average time rate of energy dissipated over the whole baffle during one period, denoted D_B, is given by:

$$D_B = \frac{1}{T}\int_0^T \int_0^{2\pi} \frac{1}{2}\rho\, a_B C_D v_r^2 |v_r| a \mathrm{d}\theta \mathrm{d}t, \tag{3.100}$$

where v_r is the relative velocity along the tank wall in Eq. (3.96), computed by the mode shapes obtained when the baffle is not there. Finally, the damping ratio caused by solid annular baffle is determined by:

$$\xi_1 = \frac{D_B}{2\sigma'_{1,1} E_M}, \tag{3.101}$$

3.6 Other sources of damping

There are several sources of damping associated with sloshing waves. Some are expected to be negligible in our study, as the turbulent flow dissipation which matters for violent sloshing resonances, or the damping caused by the surface tensions, which would only matter for tanks much smaller than the dock. The importance of the dissipation occurring from the viscous boundary layers on the walls in our model tests is less clear, and briefly discussed in this section. Analytical methods have been established to estimate the local energy dissipated from laminar viscous boundary layers (Schlichting, 1979). We give an example below how such model can be used in the case of the dock without spar nor baffle. In reality, the boundary layers are always turbulent, and the associated damping is sometimes estimated by empirical formulas based on experiments, which we also discuss below.

The walls of the dock are assumed to be smooth. For laminar boundary layers, the average time rate of energy dissipation per unit area can be expressed as (Faltinsen and Timokha, 2009):

$$D_{\mathrm{BL}}(z,\theta) = \frac{1}{2}\rho\nu\sqrt{\frac{\sigma_{1,1}}{2\nu}}\tilde{U}^2(z,\theta). \tag{3.102}$$

for a flow oscillating at the frequency $\sigma_{1,1}$ on a vertical wall, where $\nu = 10^{-6}\,\mathrm{m^2 s^{-1}}$ is the kinematic viscosity of water, and $\tilde{U}(\theta,z)$ is the amplitude of the local vertical velocity on the wall. Considering as standing wave of amplitude $|\beta_{1,1}|$ and frequency $\sigma_{1,1}$ in the dock without spar nor baffle, the vertical flow velocity is determined by the first sloshing mode, and the total rate of energy dissipation obtained by integrating D_{BL} over the internal walls of the dock:

$$D_{\mathrm{BL}} = \int_0^{2\pi}\int_{-d}^{0} D_{\mathrm{BL}}(\theta,z)\, a\, \mathrm{d}z\mathrm{d}\theta \tag{3.103}$$

$$\text{or}\quad D_{\mathrm{BL}} = \frac{1}{2}\rho\nu\sqrt{\frac{\sigma_{1,1}}{2\nu}}\frac{|\beta_{1,1}|^2\sigma_{1,1}^2 a\pi}{\sinh^2\left(\frac{\iota_{1,1}d}{a}\right)}\left[\frac{a}{4\iota_{1,1}}\sinh\left(\frac{2\iota_{1,1}d}{a}\right) - \frac{1}{2}d\right]. \tag{3.104}$$

We have here neglected both the contribution of the bottom's surface or the Stokes-Joukovski potential. These viscous effects can be modelled in the modal equations through the damping ratio

$$\xi_{\mathrm{BL}} = \frac{D_{\mathrm{BL}}}{2\sigma_{1,1}E_M}. \tag{3.105}$$

We note that both E_M and D_{BL} are proportional to $|\beta_{1,1}|^2$, such that ξ_{BL} does not depend on the sloshing wave amplitude, which was not the case for the damping ratio caused by the baffle. In reality, full-scale boundary layer flows are always turbulent, for which the energy dissipated can only be estimated through semi-empirical formulas based on experimental works. In Fig. 3.11, ξ_{BL} is presented as a function of the dock draft-to-radius ratio as in Eq. (3.105), and compared to the formulas proposed by Mikishev and Dorozhkin (1961) and Stephens et al. (1962) for turbulent boundary layers (see Appendix B.6). ξ_{BL} remains almost constant for $d/a > 2.5$, which was expected since most of the energy is dissipated near the free surface where the flow velocity is maximum. In overall, these damping ratios are very low, all below 0.12%. The ratios ξ_{BL} estimated by the empirical formulas are almost twice the ones estimated from Eq. (3.105), even though these former results should be considered with caution as such empirical formulas often depend on the set-up of the experiments they are based on.
For forced motions, even low damping generally matter to study the sloshing response. In this work however, the dock is subjected to incident waves, and the

sloshing response is coupled with the motions of the dock, which dissipate energy through radiation. The viscous boundary layers will hence be shown to have very little effects on the sloshing response (see later Sec. 5.1.3).

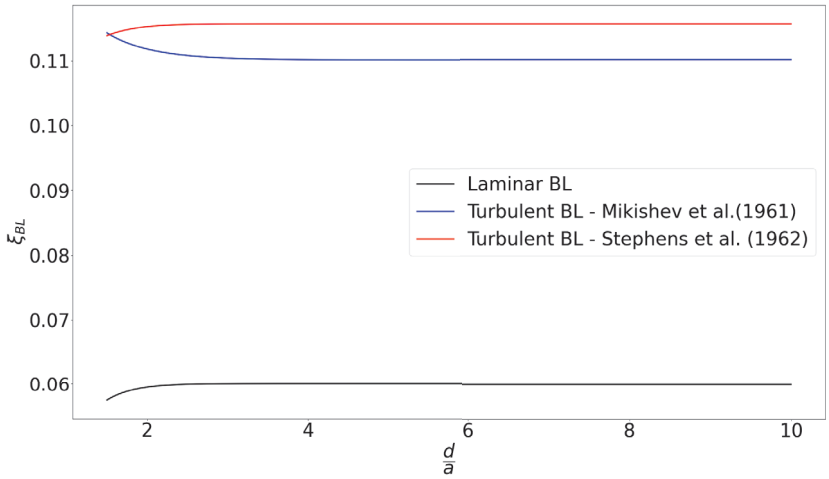

Figure 3.11: *Damping ratio caused by viscous boundary layer (BL) flows on smooth walls, either for laminar or turbulent flows, as a function of the dock draft-to-radius ratio. In this work, we mostly consider* $d/a = 2.7$.

4 | Model tests

Dedicated model tests were performed in the extension of the large towing tank at SINTEF Ocean. The length of the tank is 85m, its width 10.5m and its depth 10m. Two series of tests were made in November 2018 and November 2019 with the same model for different configurations. 2019 tests included the spar of a wind turbine inside the dock. Detailed descriptions of the model's components, incident waves, and of the methodology used to post-proceed the data are presented in this section.

4.1 Experimental set-up

4.1.1 The model

The model included several components that were tested in different configurations at an imagined model scale 1:100. First, we considered the dock alone. The model of the dock was made of 3mm thick aluminium plates, including eight stiffening vertical aluminium plates in the empty space between the internal and external radii. A plexiglass cover was added on the top to prevent water to come inside. Ballasts were inserted inside the model in order to obtain either 0.50m or 0.80m draughts (cf. Fig. 4.1), while keeping the centre of gravity at $x_G = y_G = 0$m, and 0.25m above the bottom of the model for both draughts. At the bottom, the upper-part of the bilge-boxes was made of Divinycell foam, screwed on the aluminium structure (see Fig. 4.2). Two sizes of bilge boxes were tested: the largest dimensions $H_{skm} = 0.05$m and $B_{skm} = 0.09$m were used for most of the tests, but smaller bilge boxes $H_{skm} = 0.04$m and $B_{skm} = 0.05$m were also tested for the dock alone. The model was moored at mid-distance between the wave maker and the parabolic beach by four nearly-horizontal mooring lines and springs (see Sec. 4.1.4 for more details about mooring).

The spar of a FOWT was also modeled at the same scale 1:100, inspired from the Hywind wind turbines, with a radius $a_0 = 0.07$m and draught $d_0 = 0.80$m (cf. Fig. 4.3). The spar was floating in the dock, moored to the dock by eight springs (cf. Sec. 4.1.4)). Tests with the spar were made for the dock's draught $d + s = 0.80$m, and the biggest bilge boxes' size. Both the dock and spar had a 0.25m height above water to prevent any water to come above the structures. The main dimensions of the models are summarised in Table 4.1.
The masses of the different components of the bodies (main structures, ballasts, instrumentation, etc.) were measured by a weight scale, both individually and assembled. However, the moments of inertia in pitch $I^{(1)}_{5,5}$ and $I^{(2)}_{5,5}$ of the spar and the dock, respectively, could not be measured directly from the model, and had to

(a) $d + s = 0.50m$. *(b)* $d + s = 0.80m$.

Figure 4.1: *Photos of the model during tests in regular waves for both draughts. November 2018.*

Table 4.1: *Dimensions of the dock and spar used for most of the model tests. Notations referring to the geometry are defined in Fig. 2.1, while H_{skm} and B_{skm} are defined in Fig. 4.2. Some tests for the dock without spar and without damping devices were made for a lower draught $d + s = 0.50m$, as well as with smaller bilge boxes $H_{skm} = 0.04m$ and $B_{skm} = 0.05m$.*

Parameter	Unit	Value	Description
a	[m]	0.30	Dock's inner radius
b	[m]	0.40	Dock's outer radius
$d + s$	[m]	0.80	Dock's draught
$H_{skm} = s$	[m]	0.05	Bilge box's height
$B_{skm} = c - b$	[m]	0.09	Bilge box's width
a_0	[m]	0.07	Spar's radius
d_0	[m]	0.80	Spar's draught

be estimated afterward using the parallel axis theorem. Since most components of the models were annular circular cylinders with a homogeneous mass M_i, internal radius r_i^{In}, external radius r_i^{Out}, height h_i, and geometric centre at z_{B_i} from the free surface, the following general formula was used to calculate the total moment of inertia of each body at the mean free surface:

$$I_{5,5} = \sum_i \frac{M_i}{12}\left[3({r_i^{In}}^2 + {r_i^{Out}}^2) + h_i^2\right] + M_i z_{B_i}^2. \tag{4.1}$$

The masses, moments of inertia and centres of gravity of both bodies are summarised in Table 4.2.

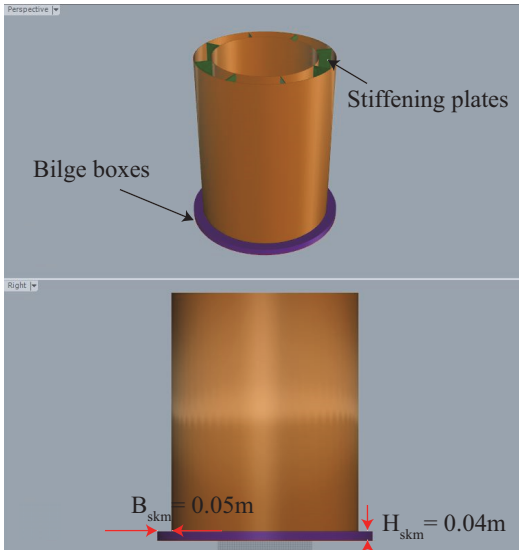

(a) Smallest bilge boxes.

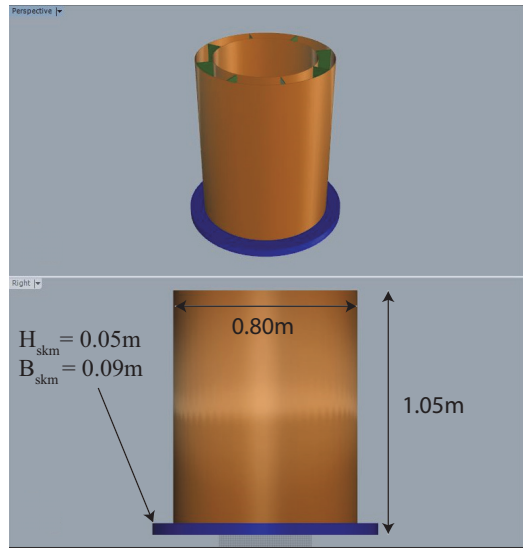

(b) Biggest bilge boxes.

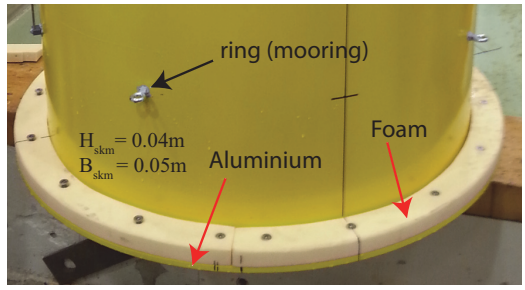

(c) Photo of the model (smallest bilge boxes).

Figure 4.2: *Three-dimensional modelling of the dock with both sizes of bilge boxes, made on the software Rhinoceros 3D by Trond Innset, and a photo of the bottom of the dock's model, showing the Divinycell foam screwed on the lower-aluminium part of the bilge boxes. November 2018.*

Table 4.2: *Mass properties of the spar and the dock for both draughts with $H_{skm} = 0.05m$ and $B_{skm} = 0.09m$. M is the mass of each body, $I_{5,5}$ the moment of inertia with respect to $z = 0$, and z_G the vertical location of the centre of gravity from the mean free surface.*

Body	M [kg]	$I_{5,5}$ [kg.m^2]	z_G [m]
Dock ($d + s = 0.50$m)	122.5	25.2	-0.25
Dock ($d + s = 0.80$m)	188.3	76.2	-0.55
Spar ($d + s = 0.80$m)	12.3	4.3	-0.50

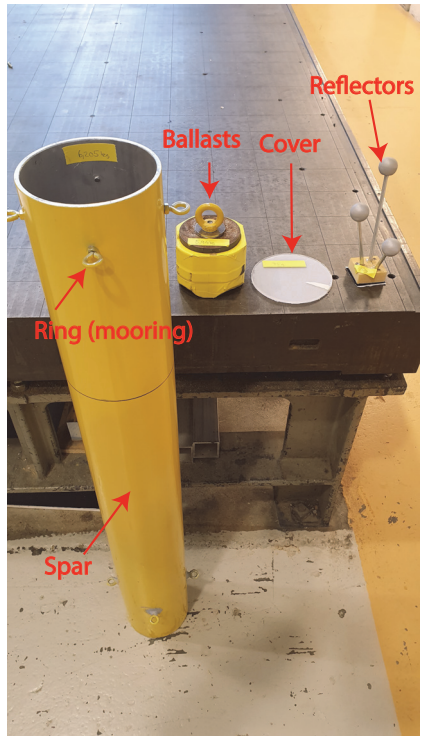

Figure 4.3: *Photo of the spar's model, including the main aluminium structure, the ballasts, which were placed in the bottom of the body, and the spherical reflectors fixed on the plexiglass cover used for the video positioning system. November 2019.*

4.1.2 Damping devices

Two types of damping devices, namely annular baffles and polystyrene foam balls, were introduced in the model during the 2019 experimental campaign to damp sloshing waves and reduce the body motions. These tests were all made with the highest draught $d + s = 0.80$m and the largest bilge boxes. First, three types of annular baffles with perforation ratio $\tau = 0$ (solid baffle), $\tau = 0.15$ and $\tau = 0.30$ were each rigidly fixed against the internal wall of the dock. The baffles were made of 0.005m thick PVC plastic with a width $a_B = 0.05$m. Both perforation ratios $\tau = 0.15$ and $\tau = 0.30$ were obtained by piercing evenly circular holes of 0.015m diameter. In addition, four rectangular holes were made around the four wave probes also fixed on the internal wall (see Fig. 4.4). The baffles were successively installed at $d_B = 0.03$m, $d_B = 0.05$m and $d_B = 0.08$m below the free surface. Then, free floating polystyrene (PS) foam balls with a mean diameter of 0.001m, and then 0.003m were successively inserted inside the dock in various quantities: 1.2 litres (L), 2.4L and 3.6L. Each of these volumes would form a layer of free-floating balls inside the dock, the heights of which are summarised in Table 4.3. Fig. 4.4 shows selected photos of the damping devices installed inside the dock with and

without the spar, either with baffles or PS foam balls.

Table 4.3: *Height of the PS foam balls' layers in full and model scales.*

Volume of balls [L]	Layer's height [m] Model scale -	Layer's height [m] Full scale
1.2	0.004	0.40
2.4	0.008	0.84
3.6	0.012	1.20

4.1.3 Instrumentation

The six degrees of freedom motions of both the dock and the spar were measured with the video positioning system OQUS, using three spherical reflectors fixed on the top of each body and a set of four cameras. In addition, three accelerometers were fixed at the top of the model, two vertically and one horizontally, as shown in Fig. 4.5, to capture the surge, heave and pitch accelerations of the dock (see Sec. 4.4.2 for more details). One vertical and one horizontal accelerometer were also placed on the top of the spar, but eventually not used. The wave elevation was measured at different positions by eight wave probes (denoted WP1-8), calibrated before the tests. Four wave probes (WP1-4) were inside the dock to measure sloshing waves, rigidly fixed at 0.01m from the aluminium, for the metal not to disturb the probes' measures. Two were aligned with incident waves (WP1 and 3), and two placed on the transversal sides (WP2 and 4) as shown in Fig. 4.5. Four wave probes (WP5-8) were fixed to the tank: two in front of the structure measuring the incident waves, and two on each side aligned with the dock, installed at 0.6m from the side walls. Four strain gauges were measuring the forces (F1-4) in the mooring lines connecting the dock to the tank. They were in particular used to control the pretension of the mooring lines, maintained around 70N for all tests. Linear calibrations were made for all the sensors once before the tests. Data acquisition was made with the software CATMAN, and the offset of the signals was automatically removed, ensuring their synchronisation. The motions from the video recording system OQUS were captured at the sampling frequency 50Hz, while the accelerometers, wave probes and strain gauges at 200Hz. The instrumentation used for the 2018 and 2019 experimental campaigns were almost identical. Although, 2018 tests included two additional wave probes: WP9, fixed on the external wall of the dock and facing incident waves, and WP10 and WP11 instead of WP8. If not precised, the notation ζ_{WP8} will be used to present the free-surface elevation either at WP8 for 2019 tests or at WP10 for 2018 tests. Fig. 4.6 show photos of the instrumentation during the tests. Videos of several tests were also made thanks to two cameras: one on the side and one above the model.

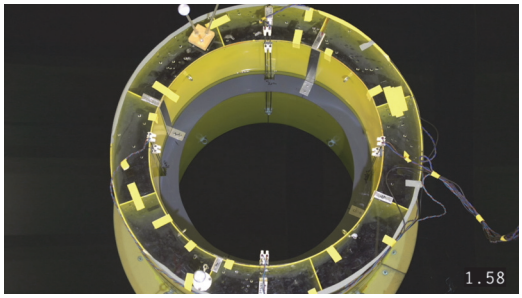

(a) Solid baffle - $\tau = 0$.

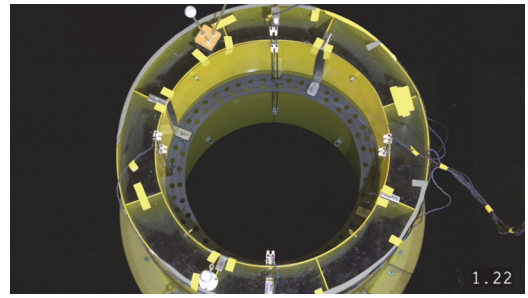

(b) Perforated baffle - $\tau = 0.15$

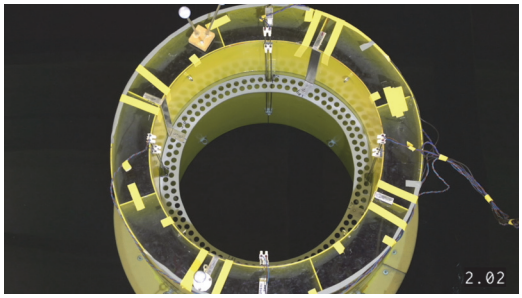

(c) Perforated baffle - $\tau = 0.30$

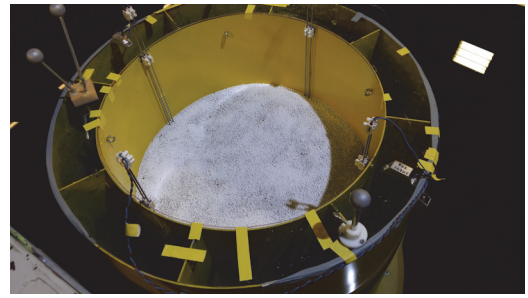

(d) $0.003m$ PS foam balls ($1.2L$).

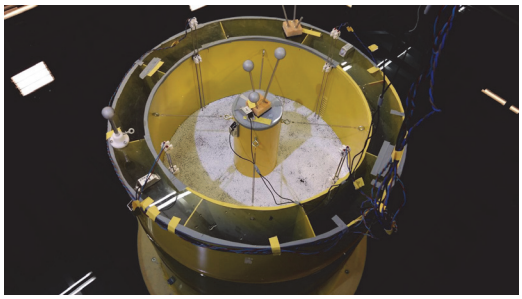

(e) Dock with spar ($0.003m$ balls, $1.2L$).

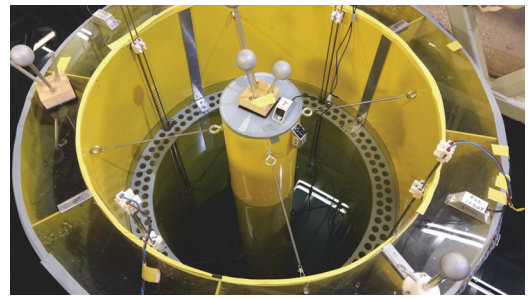

(f) Dock with spar ($\tau = 0.30$).

Figure 4.4: *Photos of the different types of damping devices installed inside the dock, with and without the spar. November 2019.*

4.1.4 Mooring

The four mooring lines maintaining the dock were stretched as symmetrically as possible outside the dock with a pretension force $F_{\text{pre-tension}} \simeq 70\text{N}$. The lines were attached to the dock at 0.25m from the model's bottom, i.e. at $z = z_G$, and the other extremities attached to the tank around 0.40m above water to keep the springs and strain gauges dry. The lines thus had a slight inclination relative to the horizontal plane of $\alpha^{\text{M}} \simeq 11°$ for the draught $d + s = 0.80m$, and $\alpha^{\text{M}} \simeq 5.2°$ for $d + s = 0.50m$. The springs at the end of each line had a stiffness of $k^{M} = 120N/m$, chosen so that the natural period in surge was higher (more than ten times) than

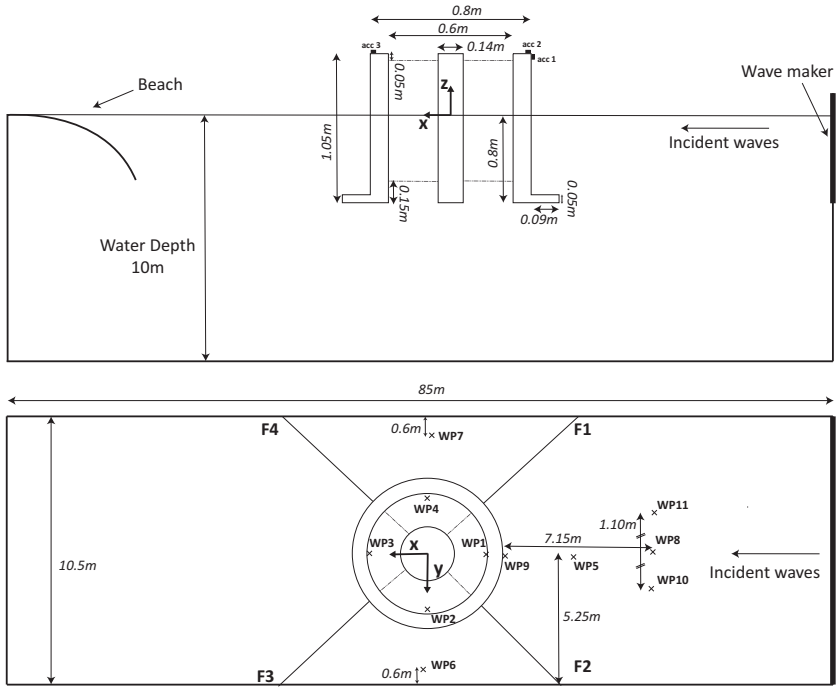

Figure 4.5: *Side and bird's-eye views of the experimental set-up when both the spar and the dock are installed. The four wave probes WP1 to 4 are fixed to the dock, and WP5 to WP8 are fixed to the tank. Three accelerometers are fixed on the dock, giving positive values for accelerations along the normal pointing inward the body. The sketch is not to scale.*

the first natural sloshing period. The restoring coefficients due to the mooring lines in surge and heave, and restoring moment in pitch acting on the dock were estimated as follow:

$$c_{1,1}^{(2),M} = 4k^M \cos^2(\alpha^{\mathrm{M}}) \cos^2(\frac{\pi}{4}), \tag{4.2}$$

$$c_{3,3}^{(2),M} = 4k^M \sin^2(\alpha^{\mathrm{M}}) + \frac{4F_{\text{pre-tension}}}{B_{tank}\sqrt{2} - b}, \tag{4.3}$$

$$c_{5,5}^{(2),M} = c_{1,1}^{(2),M} |z_G^{(2)}|^2 + 2bF_{\text{pre-tension}} \cos^2(\alpha^{\mathrm{M}}) \cos(\frac{\pi}{4}), \tag{4.4}$$

$$c_{1,5}^{(2),M} = c_{5,1}^{(2),M} = c_{1,1}^{(2),M} z_G^{(2)}, \tag{4.5}$$

where $B_{tank} = 10.5$m is the width of the tank. We note that the pretension of the

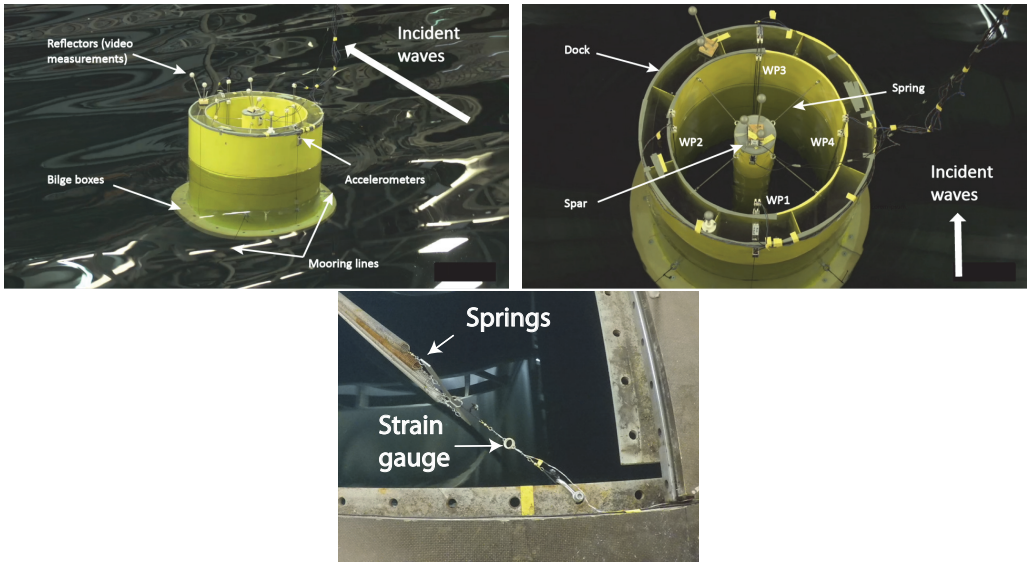

Figure 4.6: *Photos from the 2019 model tests. Top left: side view of the installation, two distinct video positioning systems measure the motions of the dock and the spar. Top right: bird's-eye view, four wave probes WP1-4 measure the free-surface elevation inside the dock. Bottom: Extremity of the mooring line 2 connecting the dock to the tank, and showing the strain gauge measuring F2. November 2019.*

lines also adds a linear restoring force in heave and a linear restoring moment in pitch, which does not come from the change of the lines' elongation. In heave, it is caused by the change of orientation of the force $F_{\text{pre-tension}}$ in each of the four lines. A similar term exists in surge that has been neglected as the lines are nearly horizontal. In pitch, this moment is caused by the vertical arm between the two frontward and the two backward lines. This restoring moment caused by the pretension forces is not negligible, as it represents near 30% of $c_{5,5}^{(2),M}$ for the higher draught $d + s = 0.8$m.

The spar was maintained at the centre inside the dock by eight springs, four at the top of the spar above water at $z_{up} = 0.20$m, and four under water at $z_{down} = -0.65$m (see Fig. 4.5). Each spring had a stiffness of $k_s = 28$N/m and a length $L_s = 0.20$m. It was difficult to find springs of this size with a higher stiffness, as a result the natural periods of the spar's motions were close the first natural sloshing period (cf. Sec. 4.2). These springs induced new coupled restoring forces and moments for the dock and the spar. The corresponding restoring coefficients can be expressed as:

$$\begin{cases} c_{1,1}^{(k),M} = 2\tilde{k}^M, \\ f_{1,1}^{(k),M} = -2\tilde{k}^M, \\ c_{1,5}^{(k),M} = (z_{up} + z_{down})\tilde{k}^M, \\ f_{1,5}^{(k),M} = -(z_{up} + z_{down})\tilde{k}^M, \end{cases} \quad \begin{cases} c_{5,5}^{(k),M} = (z_{up}^2 + z_{down}^2)\tilde{k}^M, \\ f_{5,5}^{(k),M} = -(z_{up}^2 + z_{down}^2)\tilde{k}^M, \\ c_{5,1}^{(k),M} = (z_{up} + z_{down})\tilde{k}^M, \\ f_{5,1}^{(k),M} = -(z_{up} + z_{down})\tilde{k}^M, \end{cases} \tag{4.6}$$

for $k \in \{1, 2\}$, where $\tilde{k}^M = 4k_s \cos^2(\frac{\pi}{4})$. Each restoring coefficient $f_{i,j}^{(k)}$ in Eq. (4.6) corresponds to the restoring force applied to the i-th degree of freedom of the body k due to motions in the j-th degree of freedom of the body k', $(k, k') \in \{1, 2\}^2$, $k \neq k'$. These eight springs were also pretensioned with a force $\tilde{F}_p \simeq 1.2$N, adding the following restoring coefficients:

$$\begin{cases} c_{3,3}^{(k),M} = -f_{3,3}^{(k),M} = \dfrac{8\tilde{F}_p}{L_s} \\ c_{5,5}^{(1),M} = -f_{5,5}^{(1),M} = 8a_0\tilde{F}_p \cos\left(\frac{\pi}{4}\right) \\ c_{5,5}^{(2),M} = -f_{5,5}^{(2),M} = 8a\tilde{F}_p \cos\left(\frac{\pi}{4}\right) \end{cases} \tag{4.7}$$

4.2 Decay tests

Decay tests were carried out, giving indications on the natural periods of the system. These tests were made for each degree of freedom individually, even though coupling between the motions was often observed from the time series. Several configurations for the dock without and with the spar or damping devices were tested, as detailed below. Fig. 4.7 shows examples of time series obtained from decay tests in surge, heave and pitch for the dock with spar and without damping devices. It is was not always possible to extract natural periods from the time series, either because the coupling with other degrees of freedom was too strong, or because the system was near critically damped and the oscillations either too quickly damped out or lacking any clear frequency peak. This was especially true for the spar's surge motion $\eta_1^{(1)}$, for which decay tests could not be exploited. A Fourier transform of these time series were made over a whole number of oscillations to estimate natural periods (cf. Appendix C.1).

4.2.1 Natural periods

First results are presented in Table 4.4 for the dock alone, with the two size of bilge boxes and two draughts. The resonant periods in surge are more than 10 times

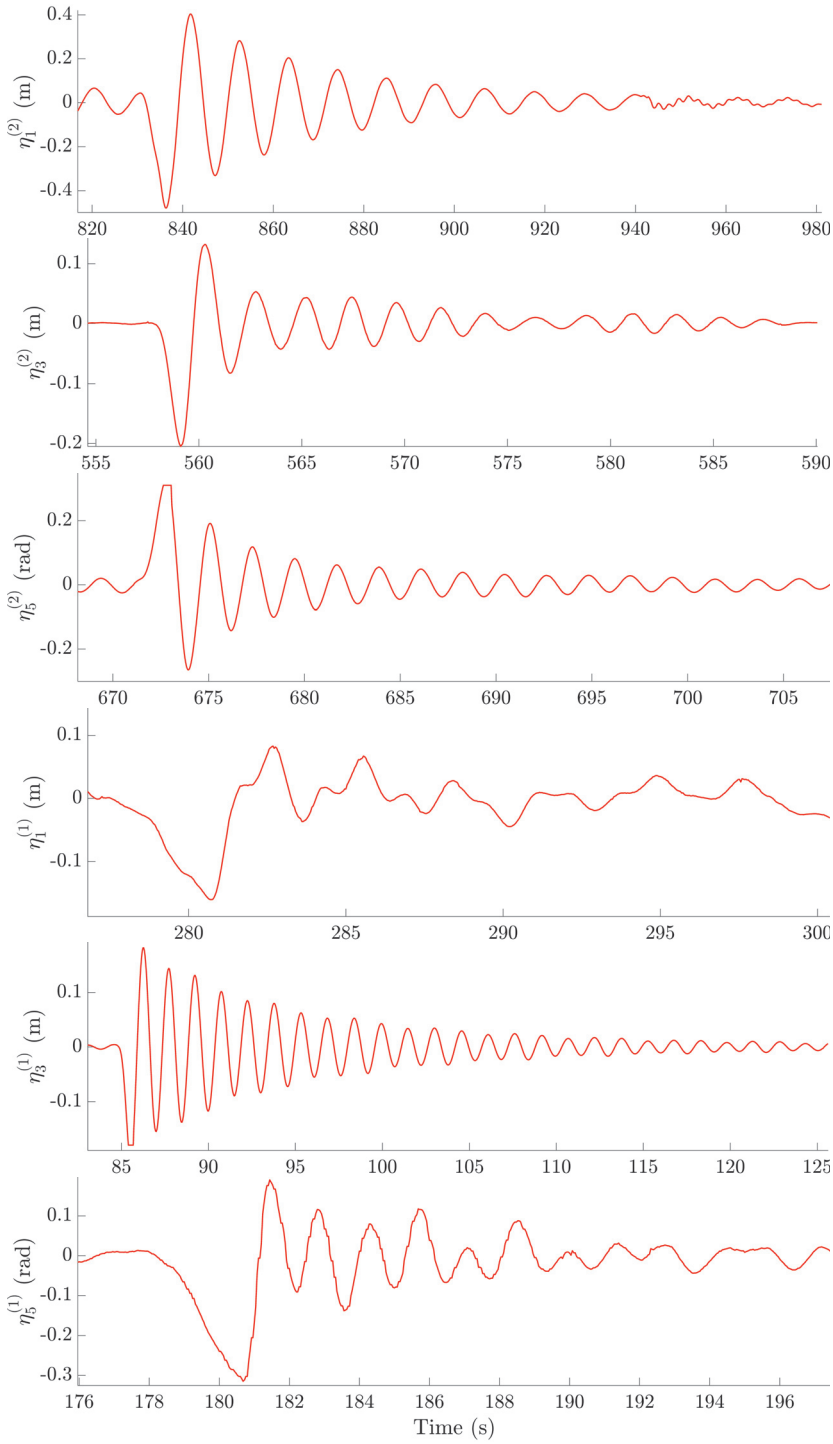

Figure 4.7: *Example of time series from decay tests achieved in surge, heave an pitch for both the dock and the spar when no damping devices are installed.* $d + s = 0.5m$, $H_{skm} = 0.05m$ *and* $B_{skm} = 0.09m$.

higher than the sloshing natural period $T_{1,1}$, which was an objective when choosing the stiffness of the mooring lines. The natural periods in heave and pitch are also higher than $T_{1,1}$, but both are in the same range as the piston mode natural period, estimated from the radiation problem in Sec. 2.4 at $T_{piston} = 2.0$s for $d + s = 0.8$m. As expected, natural periods for the larger bilge boxes are slightly higher due to higher added masses. They are in average increased by 7.8% in heave, and 4.9% in pitch. The draught also have a clear influence on the natural periods, in average 12.5 % higher in heave and 15.9 % lower in pitch for $d + s = 0.8$m compared to $d + s = 0.5$m. This last observation can be explained by a lower center of gravity, such that the restoring moment in pitch which depends on $|z_G^{(2)}|^2$ is higher for the higher draught, resulting in lower natural periods, despite a higher moment of inertia and added mass. One should note that if the definition of a realistic mooring system is out of the scope of the present study, the natural periods of dock's rigid body motions are however expected to remain much higher than the wave periods in operation that are considered in this work. For instance, in their design optimization study, Jiang et al. (2020) consider a slightly more realistic mooring system consisting of 12 mooring lines attached from 4 anchor points on the dock, with a natural period in surge around 400s, and in pitch around 26s-27s, both far above sloshing resonance (around 8s in full scale). Two decay tests were also made without the mooring lines for both draughts. Results in heave are unchanged compared to the moored situation, confirming that the additional restoring term due to mooring in heave is very small. Natural periods in sway, roll and yaw are also provided in Appendix C.1. Because of the symmetry of the installation, results in surge and sway were almost identical, as for roll and pitch.

Table 4.4: *Natural periods in seconds estimated from the decay tests for the dock without spar and without damping devices. BB1 corresponds to the smaller bilge boxes: $H_{skm} = 0.04m$ and $B_{skm} = 0.05m$, and BB2 to the bigger bilge boxes: $H_{skm} = 0.05m$ and $B_{skm} = 0.09m$.*

	$d + s = 0.5$m BB1	$d + s = 0.5$m BB2	$d + s = 0.8$m BB1	$d + s = 0.8$m BB2	$d + s = 0.8$m BB2 unmoored	$d + s = 0.8$m BB2 unmoored
$\eta_1^{(2)}$	7.94	8.26	10.64	10.67	/	/
$\eta_3^{(2)}$	1.88	2.05	2.14	2.28	2.05	2.3
$\eta_5^{(2)}$	2.41	2.54	2.09	2.18	3.01	2.35

Decay tests were also performed for the dock with the highest draught, and largest bilge boxes, when either damping devices or the spar were installed inside. See Table 4.5. There were no significant difference on the natural periods.

Table 4.5: *Natural periods in seconds estimated from the decay tests for the dock with damping devices or with the spar. Bilge boxes have the larger dimensions:* $H_{skm} = 0.05m$ *and* $B_{skm} = 0.09m$ *(BB2). The baffles are mounted at* $d_B = 0.05m$ *from the mean free surface. Both the diameter and volume of the polystyrene foam balls are indicated. Dock's draught:* $d + s = 0.80m$.

	Baffle $\tau = 0$	Baffle $\tau = 0.3$	Foam balls 0.001m, 1.2L	Foam balls 0.003m, 1.2L	Foam balls 0.003m, 2.4L	With spar
$\eta_1^{(2)}$	10.86	10.88	11.24	10.95	10.72	11.39
$\eta_3^{(2)}$	2.26	2.28	2.28	2.32	2.33	2.34
$\eta_5^{(2)}$	2.23	2.22	2.22	2.24	2.21	2.17

Results for the spar moored inside the dock are given in Table 4.6. Oscillations from decay tests in surge were too irregular to extract a single estimate of its natural period (see Fig. 4.7), most likely due to coupling with pitch. Resonant periods in both heave and pitch for the spar were not far way from $T_{1,1}$, due to that we could not find springs of this size between the spar and the dock with a lower stiffness. The presence of foam balls had little effects on the natural periods of $\eta_3^{(1)}$ and $\eta_5^{(1)}$. Decay tests in heave and pitch were also performed for the unmoored spar, both inside the dock and in open water, with no significant difference between the two situations (see the two rightmost columns in Table 4.6). This implies that hydrodynamic interaction between the two bodies in both pitch and heave are secondary at heave and pitch resonance. It also confirms that the eight mooring lines had a non-negligible effects: the heave natural period decreased from about 1.81s to 1.54s, and the pitch from about 2.56s to 1.40s. It can be noted that tests for spar in yaw showed natural periods around 1s (not presented here), even though no twisting motions were observed, neither from the time series nor the videos.

Table 4.6: *Natural periods in seconds estimated from the decay tests for the spar. Unless specified, the spar is moored inside the dock by eight mooring lines, either with or without the presence of damping devices. For the last column, the spar is free floating in open water without any mooring.*

	No damping device	Foam balls 0.003m, 1.2L	Unmoored	Open water
$\eta_3^{(1)}$	1.54	1.55	1.81	1.84
$\eta_5^{(1)}$	1.40	1.39	2.56	2.58

4.2.2 Linear and quadratic damping

We disregard once again the coupling between surge and pitch, and consider the dock's surge motion as a one degree of freedom system. Assuming linear and quadratic damping, the equation in surge during a decay test can be written

$$M^T_{1,1}\ddot{\eta}^{(2)}_1 + B_{1,1}\dot{\eta}^{(2)}_1 + B^Q_{1,1}\dot{\eta}^{(2)}_1|\dot{\eta}^{(2)}_1| + C_{1,1}\eta^{(2)}_1 = 0, \tag{4.8}$$

where $M^T_{1,1}$ is the total mass which includes the added mass in surge, B and B^Q are the linear and quadratic damping coefficients, respectively, and $C_{1,1}$ is the restoring coefficient due to mooring, which is known from the previous section. While linear damping can be related to radiation damping, the quadratic component might be caused by flow separation on the sides of the cylinder. Eq. (4.8) can be reduced to an equivalent linear damped oscillator by requiring that the equivalent linear damping dissipates the same amount of energy over one period of oscillation. We can write

$$M^T_{1,1}\ddot{\eta}^{(2)}_1 + B^E_{1,1}\dot{\eta}^{(2)}_1 + C_{1,1}\eta^{(2)}_1 = 0, \tag{4.9}$$

where $B^E_{1,1} = B_{1,1} + \frac{8}{3\pi}\omega_N \bar{\eta}^{(2)}_{1,i} B^Q_{1,1}$ is the equivalent linear damping, $\bar{\eta}^{(2)}_{1,i}$ the amplitude of the oscillation, and ω_N the natural frequency. For each oscillation, the damping coefficient $\xi = \dfrac{B^E_{1,1}}{2\omega_N M^T_{1,1}}$ can be estimated from the logarithmic decrement as follow:

$$\Delta = \ln\left(\frac{\bar{\eta}^{(2)}_{1,i}}{\bar{\eta}^{(2)}_{1,i+1}}\right) = 2\pi\frac{\xi}{\sqrt{1-\xi^2}} \simeq 2\pi\xi. \tag{4.10}$$

By plotting $B^E_{1,1}$ as a function of $\bar{\eta}^{(2)}_{1,i}$, the linear and quadratic damping can thus be determined through a linear regression, respectively as the intercept and the slope of the curve. An example is given in Fig. 4.8. Results are given in Table 4.7, showing little influence of the draught on damping coefficients. These results were obtained over only few oscillations, such that relatively high uncertainties are expected. Since the data points fall in general quite well onto the regression line, a quadratic damping model seems reasonable. The linear damping is very low, $B_{1,1}/\rho\omega b^4 < 0.6$, which was expected since there is almost no wave-radiation damping at these high periods.

4.3 Description of the tests in waves

A brief description of the incident wave conditions that were tested experimentally both during the 2018 and 2019 campaigns are given in this section. Both regular

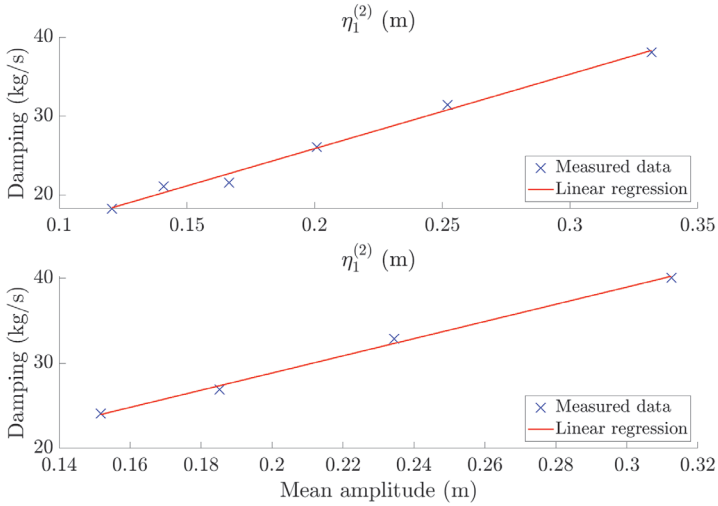

Figure 4.8: *$B^E_{1,1}$ as function of $\bar{\eta}^{(2)}_{1,i}$, plotted from decay tests' time series for the dock without spar and without damping devices. Linear and quadratic damping are estimated thanks to a linear regression. Draught: $d + s = 0.8m$. Top: large bilge boxes: $H_{skm} = 0.05m$ and $B_{skm} = 0.09m$. Bottom: small bilge boxes: $H_{skm} = 0.04m$ and $B_{skm} = 0.05m$.*

Table 4.7: *Linear and quadratic damping coefficients extracted from decay tests in surge for the dock. BB1 and BB2 are defined as in Table 4.4. Similar results for the dock's pitch motions are given in Appendix C.1.*

	$d + s = 0.5$m BB1	$d + s = 0.5$m BB2	$d + s = 0.8$m BB1	$d + s = 0.8$m BB2
$B_{1,1}$ [kg/s]	6.46	7.51	8.64	6.98
$B^Q_{1,1}$ [kg/m]	196.60	202.90	203.98	189.52

and irregular waves were tested with different configurations combining the dock, the spar, the bilge boxes, and the damping devices.

4.3.1 Regular waves

Most incident regular waves were generated in the range $T = 0.5$s to $T = 1.0$s (model scale). Only few tests included higher wave periods, up to $T = 3$s. The wave steepness was $\epsilon = 2\zeta_A/\lambda = 1/60$ for most of the test, even though $\epsilon = 1/45$ and $\epsilon = 1/30$ were also considered. The tests were generated automatically with an interval of three minutes between two consecutive tests. If this interval was sufficient for the water to come back at rest for tests with $T < 1.0$s, it was more questionable for the higher wave periods, for which disturbances visible from the videos would remain during the next test.
Both the measured incident wave periods and amplitudes were deduced from the

wave probes in front of the model. They are shown in Fig. 4.9, compared to the specified values indicated to the wave maker. The wave periods were generally very close to the one specified. It turned out that the few wave periods below $T = 0.55$s were below the bandwidth of the wave maker, which explains why these tests all have the same wave period. Precise wave steepnesses were more difficult to generate because of the small scale and the physical constraints of the wave maker. In general, the obtained wave steepnesses were slightly higher than specified, up to 20% higher. For WP5 and WP8, a time window before reflections from the beach was used.

Experimental results for tests in regular waves are presented in Chapter 6, mostly in term of responses amplitude operators (RAO) as function of the non-dimensional frequency $\omega^2 b/g$. Table 4.8 gives the correspondence between dimensional and non-dimensional wave frequencies for periods of interest.

Table 4.8: *Correspondence between dimensional incident wave periods in model scale and non-dimensional incident wave frequencies.*

	Lowest tested period	Resonant peak	$T_{1,1}$	Piston mode	Highest tested period
T [s]	0.50	0.75	0.81	2.00	3.00
ω [rad/s]	12.57	7.76	8.49	3.14	2.09
$\omega^2 b/g$	6.44	2.45	2.94	0.40	0.18

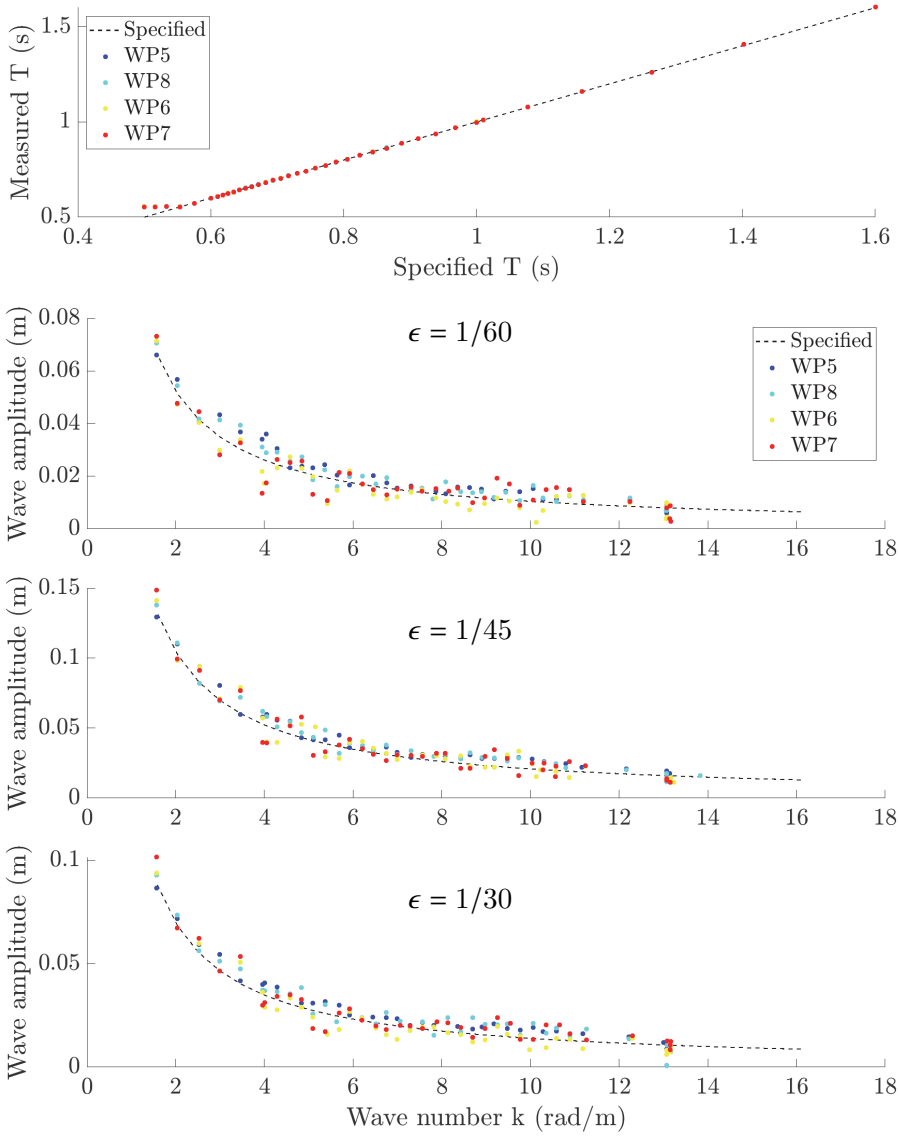

Figure 4.9: *Example of specified and measured incident wave period and amplitudes for* $\epsilon = 1/60$, $1/45$ *and* $1/30$. *The free-surface elevation is measured by the two wave probes WP5 and 8 in front of the model, and WP6 and 7 near the walls on both sides of the model. Measurements from WP6 and 7 include reflections from the model, while WP5 and 8 do not. Tests including higher incident wave periods are given in Appendix C.2.*

4.3.2 Irregular waves

Tests with irregular waves were performed for which the incident waves were defined by the standard JONSWAP spectrum (DNV RP-C205, 2019):

$$S_J(\omega) = A_\gamma S_{PM}(\omega)\gamma^{\exp\left[-0.5\left(\frac{\omega-\omega_p}{\sigma_J\omega_p}\right)^2\right]}, \tag{4.11}$$

where $A_\gamma = 1 - 0.287\ln(\gamma)$, the spectral width parameter σ_J is given by $\sigma_J = \begin{cases} 0.07, \omega \leq \omega_p \\ 0.09, \omega > \omega_p \end{cases}$, the peak enhancement coefficient fixed to $\gamma = 3$, and S_{PM} is the Pierson-Moskowitz spectrum:

$$S_{PM}(\omega) = \frac{5}{16}H_S^2\omega_p^4\omega^{-5}\exp\left[-\frac{5}{4}\left(\frac{\omega}{\omega_p}\right)^{-4}\right]. \tag{4.12}$$

The spectrum was discretised with random phases in $[0, 2\pi]$ to generate time series over 600s, sent as command to the wave maker. Due to mechanical limitations of the wave maker, frequencies above $\omega = 11.3$ rad/s could not be generated. The energy of the waves above this frequency were removed, and re-injected uniformly over the rest of the spectrum in order to conserve the specified wave height $H_s = 4\sqrt{\int_0^\infty S_J(\omega)\,\mathrm{d}\omega}$. This truncation was also reproduced for the semi-analytical model.
Several sea-states commonly measured in the North Sea (Faltinsen, 1990) and characterised by their peak period T_p and significant wave height H_s were tested in model scale for the dock with and without spar or damping devices. The peak period was specifically chosen near sloshing resonance, but higher periods were also considered. The description of all the tests in irregular waves are summarised in Table 4.9.

4.4 Data Analysis

Numerical methods used to post-process the experimental raw signals are described in this section. First, few general procedures common to all tests are presented, then for regular and irregular waves

4.4.1 General procedures

The surge, pitch and heave motions of the dock were calculated from the time series delivered by the three uni-directional accelerometers $Acc1$, $Acc2$ and $Acc3$

Table 4.9: *Peak periods T_p with their corresponding non-dimensional peak frequencies $\omega_p^2 b/g$, and non-dimensional significant wave heights H_s/b ($b = 0.4$) of the JONSWAP spectra tested for different configurations of the model. Damping devices include here either a solid baffle ($a_B/a = d_B/a = 0.17$) or 3mm polystyrene foam balls (1.2L). BB1 corresponds to the smaller bilge boxes, and BB2 to the bigger bilge boxes.*

Model	T_p [s]	$\omega_p^2 b/g$	H_s/b	Experimental campaign
Dock $(d+s)/b = 2$, BB2	0.8	2.52	1.5/40	2018
	1.5	0.72	2.5/40	2018
	0.8	2.52	1/40	2019
	0.8	2.52	3/40	2019
	1.2	1.12	8/40	2019
Dock $(d+s)/b = 2$, BB1	0.8	2.52	1.5/40	2018
	1.5	0.72	2.5/40	2018
Dock $(d+s)/b = 1.25$, BB2	0.8	2.52	1.5/40	2018
	1.5	0.72	2.5/40	2018
Dock, $(d+s)/b = 2$, BB2 + Damping devices	0.8	2.52	3/40	2019
	0.8	2.52	3/40	2019
	1.2	1.12	8/40	2019
Dock, $(d+s)/b = 2$, BB2 + spar	0.8	2.52	3/40	2019
	0.8	2.52	3/40	2019
	1.2	1.12	8/40	2019

(see Fig. 4.5). First the motions' accelerations were calculated as follow:

$$\ddot{\eta}_3^{(2)} = \frac{Acc3 + Acc2}{2}, \tag{4.13}$$

$$\ddot{\eta}_5^{(2)} = \frac{Acc3 - Acc2}{L_z}, \tag{4.14}$$

$$\ddot{\eta}_1^{(2)} = Acc1 + g\eta_5^{(2)} - f_z\ddot{\eta}_5^{(2)}, \tag{4.15}$$

where $L_z = 0.70$m is the horizontal distance between $Acc1$ and $Acc2$, and $f_z = 0.25$m the vertical distance of the accelerometers from the mean free surface. The motions were then deduced by two successive integrations with respect to time. For low

incident wave periods, the motions of the dock were particularly low, reaching the limit of the accuracy range that could be measured by the video positioning system. Hence, accelerometers were preferably used to obtain the dock's motions. Fig. 4.10 shows a comparison between both measurement systems for the RAO of the dock's surge motions in regular incident waves.

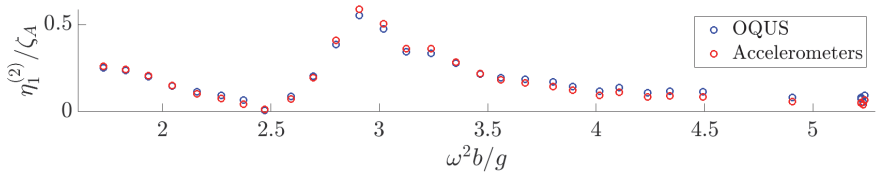

Figure 4.10: *Comparison between measurements from accelerometers and the video positioning system OQUS. RAO of* $\eta_1^{(2)}$ *for the dock without spar and without baffle. Regular incident waves,* $\epsilon = 1/60$ *(2019 test).*

The time series of WP1-4 were measured in a body-fixed coordinate system The wave elevation in an Earth-fixed coordinate system was then obtained as $\zeta^{Earthfixed} = \zeta^{Bodyfixed} + \eta_3^{(2)} - x\eta_5^{(2)}$ for WP1 and WP3 positioned along the x-axis and $\zeta^{Earthfixed} = \zeta^{Bodyfixed} + \eta_3^{(2)} + y\eta_4^{(2)}$ for WP2 and WP4. Signals from WP1 to WP4 were then linearly interpolated to the same sampling frequency as the body motions when the video positioning measurement were used. On the contrary, the spar's motions were measured in an Earth-fixed coordinate system. A change of coordinate system was still necessary to study the relative motions of the spar and the dock, and is detailed in Appendix C.4.
The phases of the signals were defined as for the semi-analytical model, i.e. with respect to incident waves at the origin of the coordinate system (centre of the dock). Incident waves were measured from WP8. It was generally difficult to obtain accurate phases, as any small drift or displacement of a sensor would shift the phase of the measured signal, especially for the highest wave frequencies. A mean drift force on the dock was estimated from WAMIT (cf. Fig. 4.11) which could lead to drifts in surge as high as 0.10m near sloshing resonance, which needed to be taken into account when post-proceeding phases.

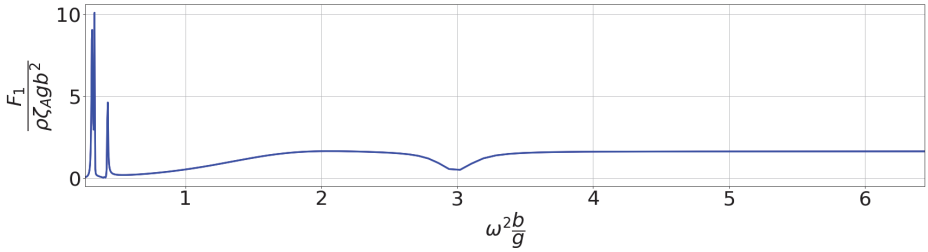

Figure 4.11: *Mean drift force in surge from WAMIT. Dock's draught:* $(d+s)/b = 2$.

4.4.2 Post-processing in regular waves

The signals were band-pass filtered and post-processed before reflections from the beach at end of the tank reached back to the model, assuming deep water to calculate the group velocity of the waves: $C_g = \frac{g}{2\omega}$. The same formula was applied to only use the part of the signal measured by WP8 before the wave reflected from the model reached the wave probe. Signals were analysed once they reached their steady states, even though it was not always possible to know precisely when that state was reached, especially for the tests without damping devices, for which the transient phases were particularly long. Fig. 4.12 presents an example of time series for ζ_{WP1} and for three different incident wave periods around sloshing resonance. As shown on the figure, beating with the natural sloshing period was often observed for $T < T_{slosh} = 0.81s$. For $T = 0.74$s, the transient phase before the sloshing to be fully established is about 60-70% shorter with the presence of the baffle, thanks to the additional viscous damping (same comments can be made for the foam balls, see Appendix C.3).
A special care was brought to calculate the mean amplitude of the motions over a whole number of beating periods $T_{beating} = 1/|1/T - 1/T_{1,1}|$, as well as over a whole number of incident wave periods T.

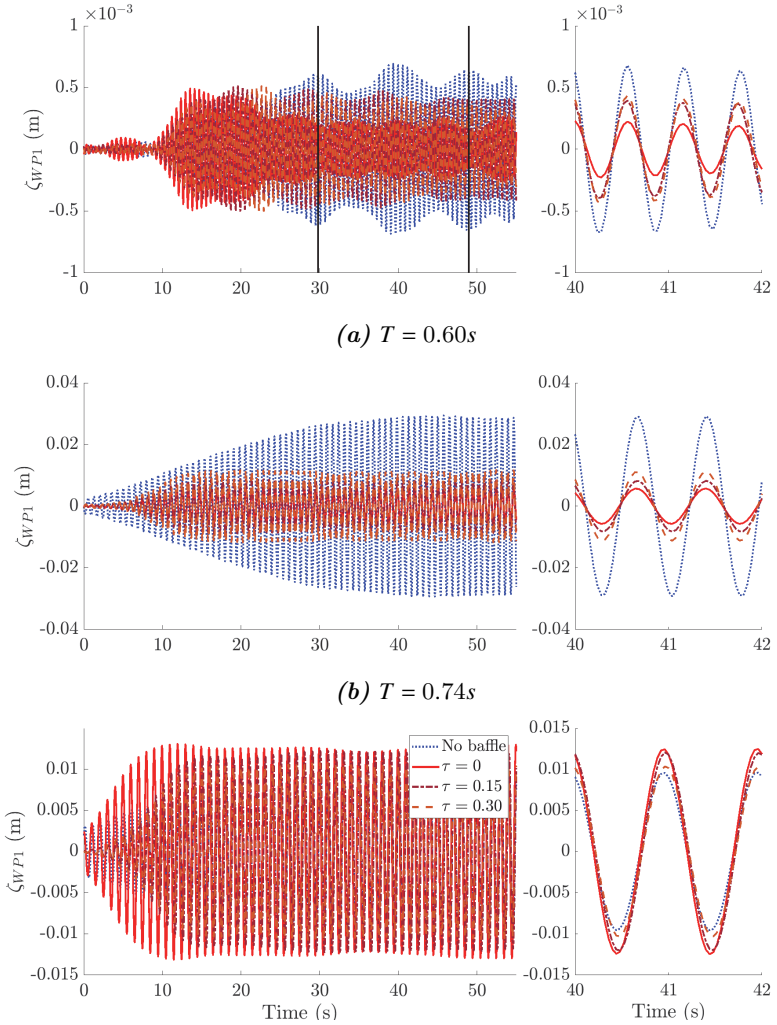

(a) $T = 0.60s$

(b) $T = 0.74s$

(c) $T = 1s$

Figure 4.12: *Examples of experimental time series of the wave elevation inside the dock in an Earth-fixed reference frame for three incident wave periods. The full time series (left side) are shown together with a focus between t=40s and 42s (right). Results for the dock without spar. Baffles' submergence:* $d_B/a = 0.17$. *Wave steepness* $\epsilon = 1/60$. *Top:* $T = 0.60s$ *, the vertical bars delimit two beating periods . Middle:* $T = 0.74s$. *Bottom:* $T = 1s$.

4.4.3 Post-processing in irregular waves

The signals were band-pass filtered for a range of periods containing 98% of the energy from the theoretical wave spectra, over a time window from 2.5min to 8.5min selected from the 10min tests. An example of time series of $\eta_1^{(1)}$, $\eta_1^{(2)}$ and ζ_{WP1} in irregular waves is shown Fig. 4.13. Their power spectral density $S(\omega)$ were then calculated from a fast Fourier transform. A Gaussian filter was applied to smooth the spectra. The RAOs $H(\omega)$ of the motions were then obtained in the usual manner:

$$|H(\omega)|^2 = \frac{S(\omega)}{S_{WP8}(\omega)}. \tag{4.16}$$

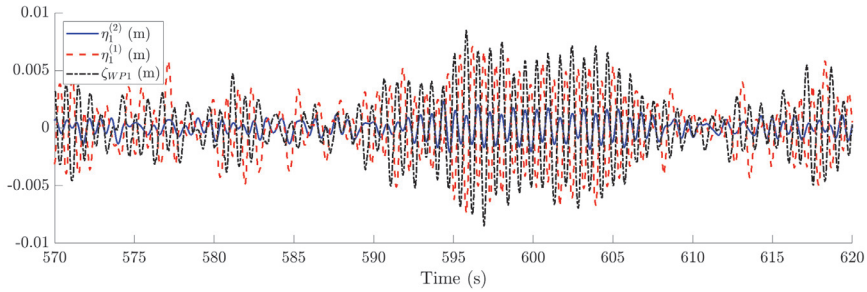

Figure 4.13: *Time series of $\eta_1^{(1)}$, $\eta_1^{(2)}$ and ζ_{WP1} from the same test in irregular waves. $\omega_p^2 b/g = 2.52$ and $H_s/b = 1/40$.*

There are uncertainties related to that the duration of the tests are not infinite, and the choice of the selected time window had an influence on the results. This is illustrated in Fig. 4.14 where the RAOs of the dock's motion in surge are presented for four different time window selections, with a mean standard deviation of 10% over the range of frequency presented on the figure.
The Gaussian filtering, characterised by its standard deviation σ_G, also had a significant impact on the visual representation of the results (see Fig. 4.15), and the values of σ_G are hence indicated for each result in Chapter 7.
The spectra of incident waves measured at WP8 have been compared to the theoretical ones for verification, as shown in Fig. 4.16 for the 2019's model tests with the spar. The spectra for all tests are given in Appendix C.6. Discrepancies with the theoretical values might be partly due to the wave reflection from the beach and the model. For the sea-states defined by $T_p = 1.2$s and $H_s/b = 8/40$, and only for these sea-sates, few cases of wave breaking were sporadically observed from the videos. These wave breaking occurred either on the dock itself, or either before or after it (see left part of Fig. 4.17). For the same sea-sates and for tests with a solid baffle, strongly non-linear flow was observed inside the dock, including splashing, and which was not observed for other tests either with or without the baffle.

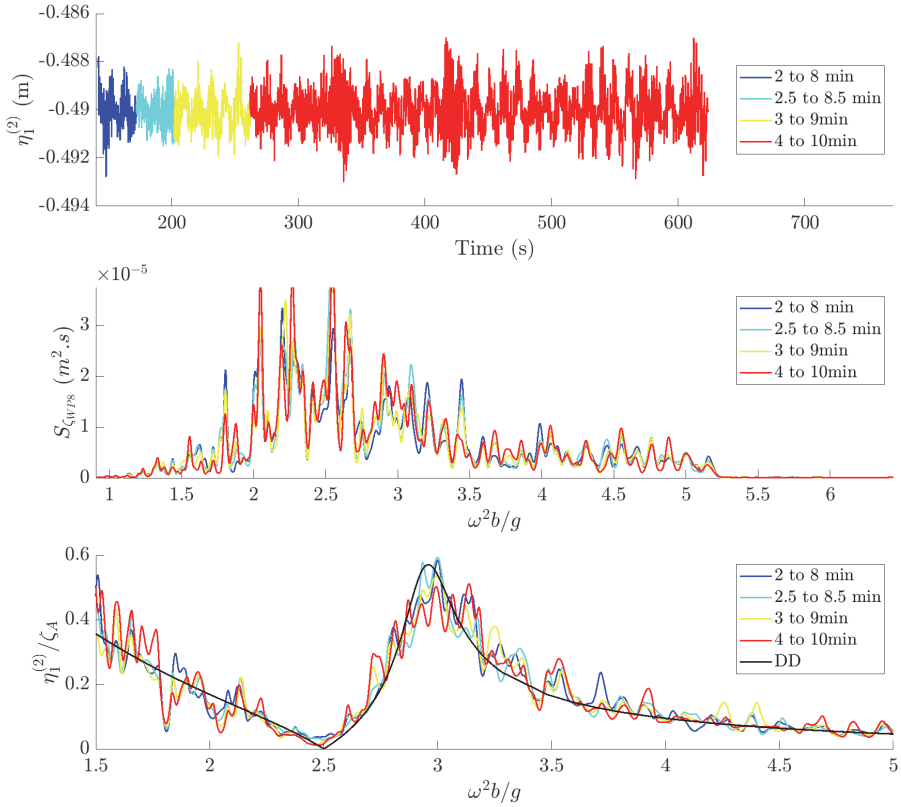

Figure 4.14: *Influence of the selection of a time window from the time series, case for the dock without spar nor damping device, $T_p = 0.8s$, $H_s = 0.01m$ (or $H_s/b = 1/40$). Top: time history of the dock's surge motions. Middle: spectra of incident waves for different time window selections. Bottom: RAOs of the dock's surge motions for the same time window selections.*

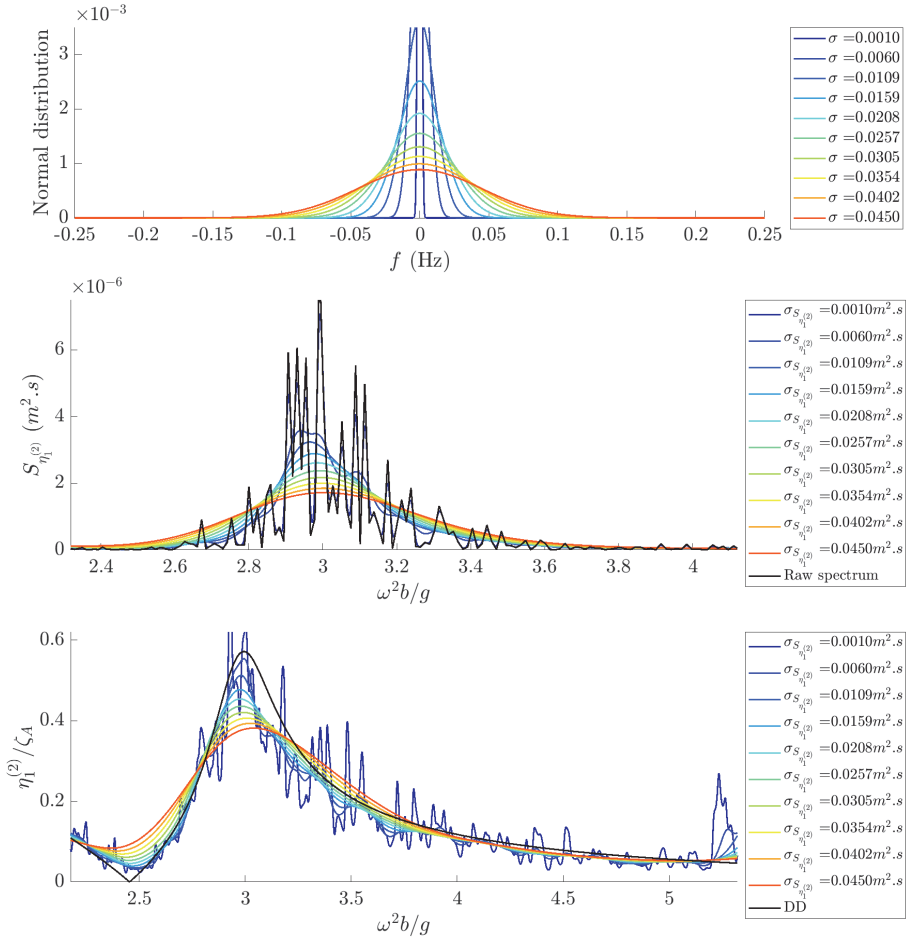

Figure 4.15: *Example of filtering for the surge motion of the dock without spar nor damping devices, $T_p = 0.8s$, $H_S = 0.01m$ (or $H_s/b = 1/40$). Top: Gaussian distributions for several standard deviations used to smooth signals in irregular waves. Middle: Spectra of the dock's surge motions for the different Gaussian filtering. Bottom: RAOs of the dock's surge motions for the same Gaussian filtering.*

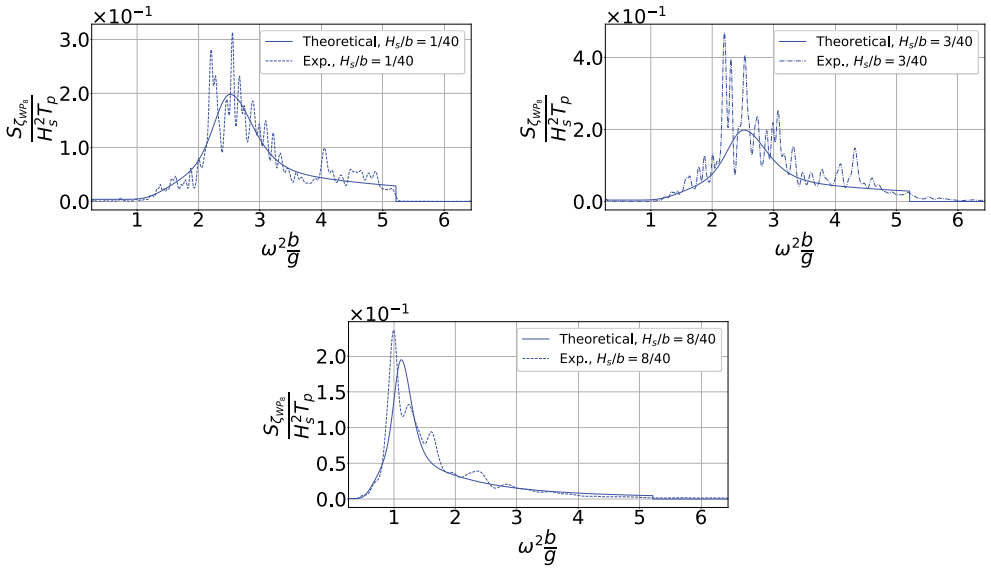

Figure 4.16: *JONSWAP spectra of incident waves, as instructed to the command of the wave maker (theoretical), and measured in front of the dock with spar at the wave probe WP8 with the model in place (experimental).* $\sigma_G = 0.006$ *the upper subfigures,* $\sigma_G = 0.0208$ *for the bottom one. Tests from 2019.*

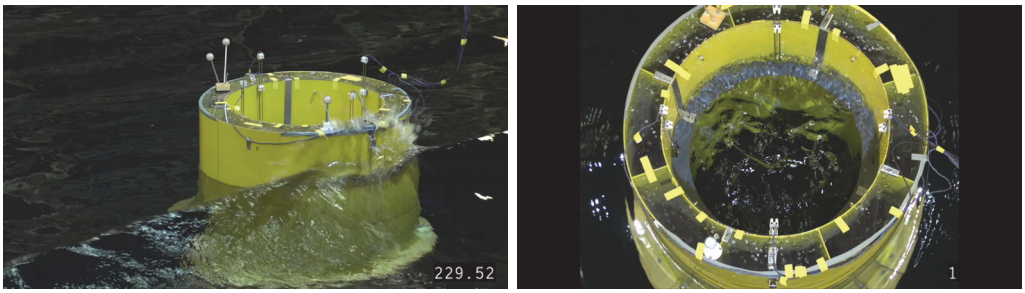

Figure 4.17: *Photos from the 2019 model tests in irregular waves with* $T_p = 1.2s$ *and* $H_s/b = 8/40$*. Left: a wave breaks on the model. Right: strongly non-linear flow is observed inside the dock for the case with baffle.*

4.5 Errors and uncertainties

4.5.1 Repetition tests

Selected regular wave conditions were repeated once to investigate the importance of random error for three configurations: the dock alone, the dock with a solid baffle, and the dock with the spar. Mean values and standard deviations of the RAOs resulting from these repetition tests are presented in Figs. 4.18 and 4.19, all from the 2019 model test campaign. The average standard deviation was in the range of 1.5%–3% for the motions of the dock, and 5%–10% for the motions of the spar, with the largest error near the coupled resonant peak. The standard deviation for the free-surface elevation was higher, in the range of 5%–10% for the cases with the baffle or with the spar, and up to 20% for the dock alone. Variations of the incident wave frequencies generated by the wave maker were generally low (below 1%), which is similar to the variations with the frequencies specified in command that were discussed in Sec 4.3.1. It is worth to note that there is considerable uncertainty related to the standard deviation when only two samples are available. We would expect these to be lower given more repetitions. Still, the presented data gives an impression of which responses, at which frequencies, are most prone to random errors in our tests.

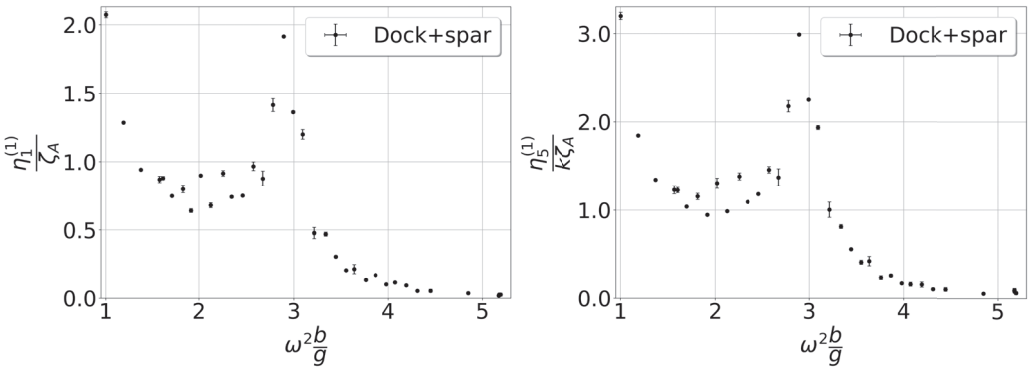

Figure 4.18: *Mean values and standard deviations of the RAOs of the spar's surge and pitch motions for the same tests as in Fig. 4.19. Results for* $\eta_3^{(1)}$ *are given in Appendix C.5.*

In addition, for the dock alone, tests were also made during the 2018 model test campaign in the same range of incident wave frequencies. The set-up in that case was remade identically for the tests of 2019, providing indications about the bias error. The tests are compared in Fig. 4.20 for the free-surface elevation ζ_{WP1} (the dock's motions are also given in Appendix C.5), with slightly higher discrepancies than the ones observed for the 2019 tests only in Fig. 4.19, especially at the resonant peak, and for frequencies lower than $\omega^2 b/g = 2$. This could be explained

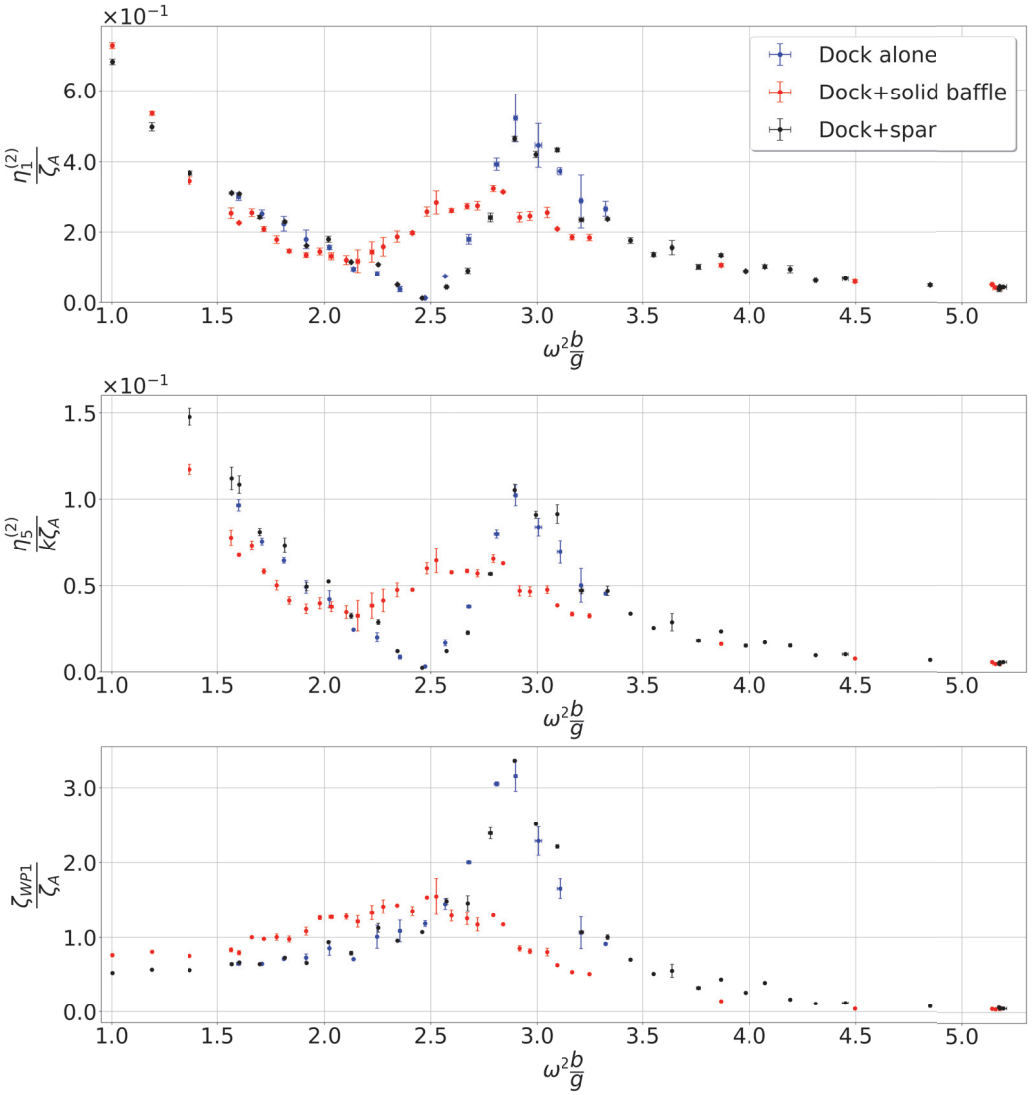

Figure 4.19: *Mean values and standard deviations of the RAOs of the dock's surge and pitch motions and the free surface elevation at WP1 from repetition tests. Each series of tests for the dock alone, dock with a solid baffle ($d_B/a = 0.17$), and dock with the spar were repeated twice during the 2019 model test campaign. $\epsilon = 1/60$, draught of the dock: $d + s = 0.8m$, larger bilge boxes' size (BB2).*

by the inaccuracies made when reproducing the same set-up, from the installation of the ballasts inside the model, and the fixations of the mooring lines. Despite the documented bias error, we believe that the reconstruction of the set-up in 2019 was quite acceptable.
Repeated tests are denoted "Set 1" and "Set 2" in the rest of the thesis.

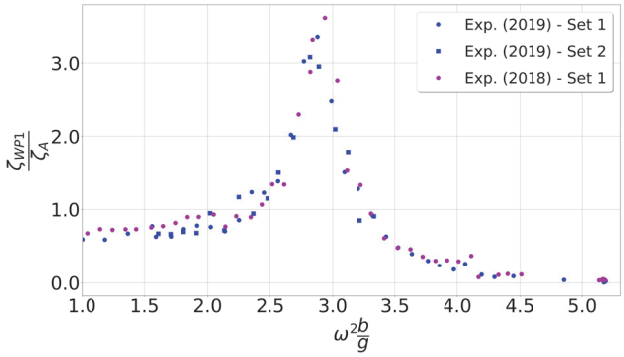

Figure 4.20: *Comparisons of ζ_{WP1}'s RAOs for several tests made with the dock alone from the 2018 and 2019 tests. The set-up was attempted to be remade identical for 2019 tests as for 2018. $\epsilon = 1/60$, draught of the dock: $d + s = 0.8m$, larger bilge boxes' size (BB2).*

4.5.2 Other sources of error

The dock's motions during the experiments were very small, and reaching the limit of the accuracy range that could be measured by the video positioning system. In addition, light reflections in the water were suspected to cause spurious data. Measurements from accelerometers were preferred to obtain the motions of the dock from the 2019's tests, but only OQUS's system was used for 2018's tests. Measurements of the spar's motions however were generally much higher and measurements from OQUS are expected to be reliable. Besides, the wave probes were sensitive to the variations of temperature. Their calibration were done only once a week due to time constraints.

Longitudinal standing waves (seiching) were sometimes observed in the time series for the longest waves. However, their period $T_{seiching} = 2L/\sqrt{gh} = 17.16$s was filtered efficiently. Reflection from the lateral walls was also an issue. The waves' amplitude measured by WP6 and WP7 at the walls could differ up to 30% compared to WP8 in front of the model, especially for short waves. Yet, few simulations were made with WAMIT in a channel, with almost no difference from the case in open water.

Fianlly, the model was not perfectly symmetric, due to several factors: the compartmentalising of the ballasts in eight slots, a variation of few millimetres in the internal and external radii from the fabrication, non-identical pre-tension in each mooring line. This may explain partially the observation of very small roll and sway motions during the tests. The eight springs fixing the spar inside the dock varied in lengths of few millimeters. As a result, the spar was not perfectly at the center of the dock, with a deviation less than 0.01m.

5 | Equations of motion

The equations of motion of the dock with and without baffles and spar are presented in this section. The mathematical models developed in Chapters 2 and 3 are used to describe the hydrodynamic loads on the bodies. A special care is brought to describe how the local viscous loads caused by the baffles can be combined with the external linear potential flow solution for an open-bottom dock. The geometry, mass matrix and restoring coefficients of the numerical model are taken as closely as possible from the physical model presented in Chapter 4.

First the hydrodynamic loads in the closed-bottom dock with baffle are derived in Sec. 5.1.1 for the dock without spar to present the method. When considering the open-bottom dock, a hybrid semi-analytical model is proposed in Sec. 5.1.2 that combines the modal equations, used to describe the local effects of the baffle, and a domain decomposition method to describe the flow through the open bottom. The equations of motions are then established in Sec. 5.1 for the dock without the spar. Similar hybrid model and equations of motions are then derived in Sec. 5.2 for the open-bottom dock with spar, and an eigenvalue analysis is carried out in Sec. 5.4.

5.1 Equations for the dock without spar

5.1.1 Closed-bottom dock with annular baffle

The linear potential flow solution inside the closed-bottom dock with either solid or perforated baffles was determined in Sec. 3.5, modelling the effects of the baffle through the modal equations obtained from the free-surface boundary conditions. The hydrodynamic loads inside the dock can then be calculated by linear pressure integration on the internal walls of the dock. We first disregard the loads on the baffle itself, which will be considered afterwards. From the expression of the potential flow in Eq. (3.33) for the dock without spar, the force in surge and moment in pitch due to the internal flow can be expressed:

$$F_1 = \overbrace{-\rho a^2 \pi (d+s)}^{-A_{1,1}^{\text{filled}}} \ddot{\eta}_1 + \overbrace{\rho \frac{a^2 (d+s)^2 \pi}{2}}^{-A_{1,5}^{\text{filled}}} \ddot{\eta}_5 + \sum_{q=1}^{\infty} \overbrace{-\rho \Big[\frac{\pi a^2}{\iota_{1,q}} \tanh(\iota_{1,q} \frac{d+s}{a}) \Big]}^{g_{q,1}} \dot{R}_{1,q}(t), \tag{5.1}$$

$$F_5 = \overbrace{\rho a^2 \pi \frac{(d+s)^2}{2}}^{-A_{5,1}^{\text{filled}}} \ddot{\eta}_1 + \overbrace{\rho\Big[-\frac{a^2(d+s)^3\pi}{3} + \sum_{j=1}^{\infty} \frac{4a^3\pi}{\iota_{1,j}(\iota_{1,j}^2-1)k_{1,j}^2} \frac{k_{1,j}(d+s)\cosh(k_{1,j}\frac{d+s}{2}) - 2\sinh(k_{1,j}\frac{d+s}{2})}{\cosh(k_{1,j}\frac{d+s}{2})} \Big]}^{-A_{5,5}^{\text{filled}}} \ddot{\eta}_5 + \sum_{q=1}^{\infty} \underbrace{\rho\Big[\frac{a^3\pi(\cosh(\iota_{1,q}\frac{d+s}{a})-1)}{\cosh(\iota_{1,q}\frac{d+s}{a})\iota_{1,q}^2}\Big]}_{g_{q,5}} \dot{R}_{1,q}.(t) \tag{5.2}$$

The first two terms in Eqs. (5.1) and (5.2) are due to the motion of the water volume (or "filled volume") if we assume a rigid free surface that moves with the dock. These are written as pure added masses for harmonic motions, and are identical to the ones presented in Sec. 3.3.2 for the case without baffle. We note that we have in particular neglected the effects of the baffles on the Stokes-Joukowski potential. We should also remark that we now consider the full draught of the dock $d+s$ that includes the bilge boxes' height, instead of simply d as in Chapter 3. Unlike in Sec. 3.3.2 however, the forces induced by the sloshing waves, i.e. the last terms of Eqs. (5.1) and (5.2), can not be interpreted as pure additional added masses because of the phase shift introduced by the damping ratio. The loads due to sloshing waves when a baffle is installed are now expressed as both added mass and damping coefficients inside the closed-bottom dock, given by:

$$A_{1,1}^{\text{slosh}} + \frac{i}{\omega} B_{1,1}^{\text{slosh}} = i\omega \sum_{q=1}^{\infty} g_{q,1} f_q(\omega) \tilde{P}_{q,1}(\omega), \tag{5.3}$$

$$A_{1,5}^{\text{slosh}} + \frac{i}{\omega} B_{1,5}^{\text{slosh}} = i\omega \sum_{q=1}^{\infty} g_{q,1} f_q(\omega) \tilde{P}_{q,5}(\omega), \tag{5.4}$$

$$A_{5,5}^{\text{slosh}} + \frac{i}{\omega} B_{5,5}^{\text{slosh}} = i\omega \sum_{q=1}^{\infty} g_{q,5} f_q(\omega) \tilde{P}_{q,1}(\omega), \tag{5.5}$$

$$A_{5,1}^{\text{slosh}} + \frac{i}{\omega} B_{5,1}^{\text{slosh}} = i\omega \sum_{q=1}^{\infty} g_{q,5} f_q(\omega) \tilde{P}_{q,5}(\omega), \tag{5.6}$$

where the coefficients $f_q(\omega)$ and $\tilde{P}_{q,i}$ were given in Eqs. (3.48) and (3.87), and the $g_{q,i}$ coefficients are defined in Eqs. (5.1) and (5.2).

In addition, the moment in pitch caused by the loads acting on the baffle itself is expressed from Morison's 2D equation as follows:

$$F_5^M = -\int_0^{2\pi} a \left[\frac{1}{2}\rho\, a_B\, C_D(KC,\theta)\, v_r(\theta,t)|v_r(\theta,t)| + \frac{1}{4}\rho\pi a_B^2 C_M\, \frac{\partial v_r(\theta,t)}{\partial t} \right] \cos(\theta) d\theta. \tag{5.7}$$

All the loads inside the dock with baffle have now been determined. The radiation and diffraction problems were also solved in Chapter 2 for the external flow around the closed-bottom dock, such that it would be possible to combine both approaches to estimate the motions of the closed-bottom dock with baffles in waves. In our work, the dock has an open bottom, and few modifications need to be made to account for this change of geometry.

5.1.2 Open-bottom dock with annular baffle

The added mass coefficients $A_{i,j}^{\text{filled}}$ do not account for the flow through the open bottom. We propose in this section to solve the radiation problems for the dock with a baffle through a domain decomposition approach, similar to the ones solved in Sec. 2.3.1. The domain Ω is decomposed in the same four subdomains I-IV. Only the potential expansions in the subdomain IV are modified compared to the case without baffle. The total radiation potential in IV is now written:

$$\Phi^{IV}(r,\theta,z,t) = \sum_{j\in\{1,5\}} \Phi_j^{(2),\text{RFS}}(r,\theta,z,t) + \sum_{q=1}^{\infty} R_{1,q}(t)\varphi_{1,q}(r,\theta,z), \tag{5.8}$$

where the radiation potentials in surge and pitch $\Phi_j^{(2),\text{RFS}} = \phi_j^{IV,\text{RFS}}(r,z)\cos(\theta)\dot{\eta}_j^{(2)}$ satisfy the rigid free-surface condition $\partial\Phi_j^{(2),\text{RFS}}/\partial z = \eta_j^{(2)} n_5^{(2)}$ on $z = 0$ inside the dock. Matching conditions with the external subdomains below the dock are imposed on $\Phi_j^{(2),\text{RFS}}$ only, while the eigenmodes $\varphi_{1,q}$ satisfy the free-surface boundary conditions in a dock-fixed coordinate system. We can reasonably assume that both the shape of the sloshing eigenmodes and the local effects of the baffles near the free surface are not affected by the flow through the bottom of the dock, due to its high draught, and due to that the heave motions are negligible in this range of frequencies. We also assume as previously that the perturbation caused at the bottom of the dock by sloshing waves in a dock-fixed coordinate are negligible. Then, the potentials $\Phi_j^{(k),\text{RFS}}$ are solved through the same domain decomposition method as in Sec. 2.3.1. The derivations of the matching conditions are very similar to the ones in Sec. 2.3.1, and are therefore not detailed here. The only difference comes from the potential flow expansion in the subdomain IV that must now satisfy the rigid free-surface boundary condition. Expressing $\phi_j^{IV,\text{RFS}} = \phi_{j,h}^{IV,\text{RFS}} + \phi_{j,m}^{IV,\text{RFS}}$ as the combination of a homogeneous and particular solution, respectively, it is given by:

$$\phi_{j,h}^{IV,\mathrm{RFS}}(r,z) = \psi\epsilon_0 A_0^{IV}\frac{r}{a} + \psi\sum_{p=1}^{\infty}\epsilon_p A_p^{IV}\frac{I_1\left(\frac{p\pi}{h}r\right)}{I_1\left(\left(\frac{p\pi}{h}a\right)\right)}\cos\left(\frac{p\pi}{h}\pi(z+h)\right), \tag{5.9}$$

$$\phi_{1,m}^{IV,\mathrm{RFS}}(r,z) = 0, \tag{5.10}$$

$$\phi_{5,m}^{IV,\mathrm{RFS}}(r,z) = -\frac{r(z+h)^2 - \frac{r^3}{4}}{2h}. \tag{5.11}$$

Inside the dock, the free-surface elevation is entirely described by the eigenmodes (cf. Eq. (3.35)). Inserting the expression of the total potential Φ^{IV} from Eq. (5.8) and ζ in the kinematic and dynamic free surface boundary conditions results in similar modal equations as obtained for the closed-bottom dock with baffle (cf. Eq. (3.85)). Only the exciting coefficients $K_{1,q}(t)$ in the right hand side of Eq. (3.85) are changed:

$$K_{1,q}(t) = -\frac{1}{\mu_{1q}}\left[\lambda_{1,q,1}\ddot{\eta_1}^{(2)} + \left(\lambda_{1,q,5} + \lambda_{1,q,2}\right)\ddot{\eta_5}^{(2)} - \lambda_{1,q,3}g\eta_5^{(2)}\right], \tag{5.12}$$

where $\mu_{1,q}$ were given by Eq. (3.39) and the λ coefficients now depend on the radiation potential $\phi_j^{IV,\mathrm{RFS}}$:

$$\lambda_{1,q,j} = \rho\int_{\Sigma_0}\phi_{j,h}^{IV,\mathrm{RFS}}(r,0)\cos(\theta)\varphi_{1,q}(r,\theta,0)rd\theta dr, \tag{5.13}$$

$$\lambda_{1,q,2} = \rho\int_{\Sigma_0}\phi_{5,m}^{IV,\mathrm{RFS}}(r,0)\cos(\theta)\varphi_{1,q}(r,\theta,0)rd\theta dr, \tag{5.14}$$

$$\lambda_{1,q,3} = \rho\int_{\Sigma_0} r\cos(\theta)\varphi_{1,q}(r,\theta,0)rd\theta dr. \tag{5.15}$$

One of the major difference with fully closed domains as in Faltinsen and Timokha (2009), is that the λ coefficients depend now on the forcing frequency ω of the incident waves, and not only on the geometry of the domain. It would for example become more complicated to solve the modal equations in time domain. We can write $K_{1,q} = -\omega^2\tilde{P}_{q,j}\overline{\eta}_j^{(2)}e^{-i\omega t}$, where $\tilde{P}_{q,1}$ and $\tilde{P}_{q,5}$ are the real coefficients:

$$\begin{cases} \tilde{P}_{q,1} = -\lambda_{1,q,1}/\mu_{1,q}, \\ \\ \tilde{P}_{q,5} = -\left(g\lambda_{1,q,3}\omega^{-2} + \lambda_{1,q,5} + \lambda_{1,q,2}\right)/\mu_{1,q}. \end{cases} \tag{5.16}$$

The hydrodynamic loads caused by the total radiation potentials are calculated by pressure integration over the dock's immersed surface $S_0^{(2)}$ with the open bottom

(cf. Fig. 2.1), and expressed in terms of added mass and damping coefficients in surge and pitch. The contribution of the loads caused by the second term of (5.8), i.e. by sloshing waves in a dock-fixed coordinate system on the internal surface of the dock, are expressed as $A_{p,j}^{\text{slosh}}$ and $B_{p,j}^{\text{slosh}}$. They are given by Eqs. (5.3) to (5.6) with the expressions of $\tilde{P}_{q,j}$ and $\tilde{P}_{q,5}$ in Eq. (5.16) for the open-bottom dock. The loads caused on the entire dock's surface for the problem with an internal rigid free surface, which only account for the first term of (5.8) in the internal subdomain IV are written $a_{p,j}^{\text{RFS}}$ and $b_{p,j}^{\text{RFS}}$, and calculated as in Eq. (2.83). The total added mass and damping coefficients from the radiations problems in surge and pitch are them given by $a_{p,j} = a_{p,j}^{\text{RFS}} + A_{p,j}^{\text{slosh}}$ and $b_{p,j} = b_{p,j}^{\text{RFS}} + B_{p,j}^{\text{slosh}}$.
The damping ratio and the shifted natural frequency in the modal equations are estimated as in Sec. 3.5.2 for the closed-bottom dock. In practice, we only use the first mode near sloshing resonance. The relative flow velocity on the baffle v_r used to estimated the energy dissipation is now expressed as:

$$v_r(\theta,t) = R_{1,1}(t)\frac{\partial \varphi_{1,1}}{\partial z}\bigg|_{\substack{r=a\\z=-d_B}} + \dot{\eta}_5^{(2)}(t)\left[\frac{\partial \phi_5^{IV,\text{RFS}}}{\partial z}\bigg|_{\substack{r=a\\z=-d_B}} + a\cos(\theta)\right]$$

$$+ \dot{\eta}_1^{(2)}(t)\frac{\partial \phi_1^{IV,\text{RFS}}}{\partial z}\bigg|_{\substack{r=a\\z=-d_B}}\cos(\theta) \tag{5.17}$$

Added mass coefficients resulting from the integration of the pressure on $S_0^{(2)}$ in the internal subdomain IV only are presented in Fig. 5.1. The coefficients calculated in Chapter 2 for the dock without baffle (blue curve) are compared to the one obtained with the one calculated in this section, and which follow the decomposition of the potential as in Eq. (5.8). When $\sigma' \to \sigma$ and $\xi_1 \to 0$ in the modal equations, i.e. when the effects of the baffle becomes negligible, it is shown on the figure that the added mass coefficients (magenta curve) converge to the one obtained in Chapter 2. $A_{p,j}^{\text{slosh}}$ is calculated solely from the first sloshing mode. This approximation seems reliable as the total added mass $a_{p,j}^{\text{RFS}} + A_{p,j}^{\text{slosh}}$ converges to the exact solution calculated in Chapter 2 over the wide range of frequencies around resonance.
The difference of loads on the internal surfaces of the closed- and open-bottom docks is mostly characterized by the difference observed between the A^{filled} (dash red curves) and $a^{IV,\text{RFS}}$ (solid red curves), respectively. These last are almost twice the former for the radiation problem in pitch.

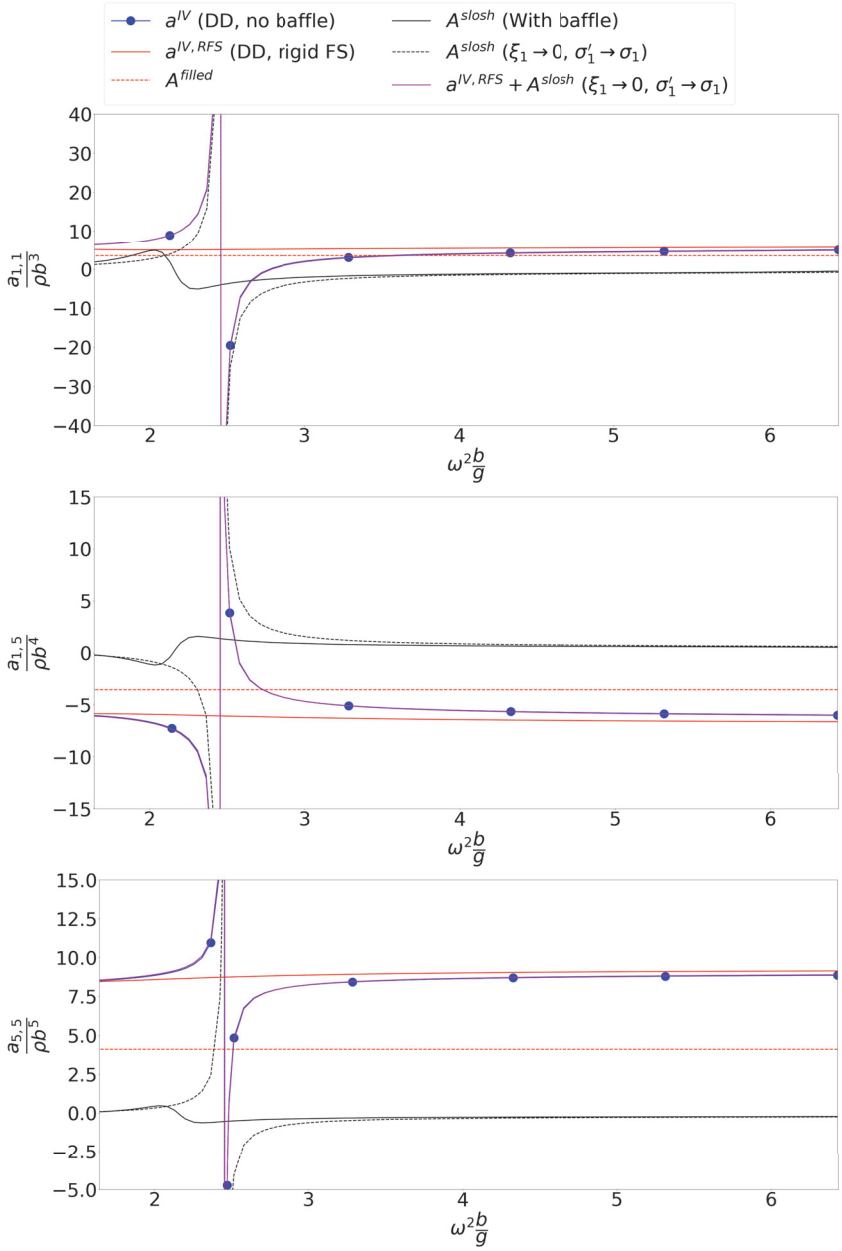

Figure 5.1: *Added mass coefficients $a_{1,1}$ (top), $a_{1,5}$ (middle) and $a_{5,5}$ (bottom) for the dock without spar, calculated by integrating the pressure on the part of the dock's surface in the subdomain IV. a^{IV} is calculated with a DD method for the case without baffle (cf. Sec. 2.3.1), $a^{IV,RFS}$ and A^{slosh} are the added mass coefficients calculated for the open-bottom dock with baffle. In that case, the equations of motion presented in the next section have been solved to estimate ξ_1 and $\sigma'_{1,1}$, with incident waves' steepness $\epsilon = 1/60$ (black curves). When the effects of the baffles are set to 0 ($\sigma' \to \sigma$ and $\xi_1 \to 0$), we verify that this model converges to a^{IV}. Similar to $a_{1,5}$, $a_{5,1}$ is given in Appendix B.7.*

5.1.3 Equations of motion of the dock

The coupled equations of motion in surge and pitch in the frequency domain for the dock without spar are given by:

$$\sum_{j\in\{1,5\}} \left[-\omega^2\left(M_{p,j}+a_{p,j}\right)-i\omega b_{p,j}+c_{p,j}\right]\overline{\eta}_j^{(2)} = F_p, \quad p\in\{1,5\}, \tag{5.18}$$

where $M_{1,1}=M$ is the mass of the dock, $M_{1,5}=M_{5,1}=Mz_G$ and $M_{5,5}=I_{5,5}$. The coefficients $c_{p,j}$ include both the restoring coefficients due to the mooring line, given in Sec. 4.1.4, and the hydrostatic coefficient in pitch (Faltinsen, 1990):

$$c^H_{5,5}=\rho gV(z_B-z_G)+\rho g\iint_{A_{WP}} x^2\mathrm{d}s, \tag{5.19}$$

where A_{WP} is the water plane area, V the immersed volume, and z_B the centre of buoyancy.
F_p in Eq. (5.18) are the wave exciting loads F_p^S from the diffraction problem (cf. Sec. (2.2)), plus the moment in pitch F_5^M on the baffle when there is a baffle. We note that F_p^S are unchanged when there is a baffle since incident waves do not perturb the free surface inside the dock in our model, which would not be the case if the dock had a shallow draught.

The use of potential flow theory in Chapter 2 was justified by that there is no flow separation around the dock due to its dimensions compared to incident wave's heights. Even for the steepest waves considered during model test, $KC=2\pi\zeta_A/(2b)\leq 0.2$, while flow separation around circular cylinders occurs at much higher KC (Sarpkaya, 1986), typically at $KC\geq 1.5-2$. However, flow separation is most likely to occur on the sharp edges of the bilge boxes, which where initially conceived to introduce damping in the equations of motions. Extensions of potential flow methods that incorporate the viscous effects of flow separation can be found in the literature for ship roll motions (Belibassakis, 2010), or even rectangular moonpools (Kristiansen and Faltinsen, 2008). It is however not explored thoroughly in the present thesis. To account for viscous dissipation, a simple quadratic drag force is introduced in the right hand side of the equation of motion in surge (Molin and Legras, 1990):

$$F_1^D=-\frac{1}{2}\rho C_D 2b(d+s)\dot{\eta}_1^{(2)}|\dot{\eta}_1^{(2)}|. \tag{5.20}$$

The force is linearised, such that the energy dissipated over one period of oscillation is identical:

$$F_1^D\simeq i\omega^2\frac{8}{3\pi}C_D b(d+s)\bar{\eta}_1^{(2)}|\bar{\eta}_1^{(2)}|e^{-i\omega t}. \tag{5.21}$$

Because of the complexity of the flow around the bilge boxes (cf. Appendix D.1), the estimation of such damping coefficients by existing formulas for more simple

geometries does not appear relevant. A heuristic damping coefficient of $C_D = 3$ provides calculated results closed to the experimental ones, and is discussed further in the later section 6.1.2. This value is higher that the ones obtained from the decay tests in Sec. 4.2.2. For instance for $(d+s)/b = 2$ (BB2), the quadratic damping coefficient was $B^Q_{1,1} = 189.52$kg/m, corresponding to $C_D = 0.6$.

The equations of motion of the semi-analytical model are now complete for the dock without spar, both with and without baffle. They include in particular several non-linear loads with respect to the motions' amplitude, either it is through the damping ratio ξ_1 due to baffles, the drag force F_1^D (bilge boxes), or the moment F_5^M. An iterative scheme is thus implemented. An initial iteration is run without any non-linear loads. The complete equations are then solved until convergence of the RAOs $|\eta_1^{(2)}/\zeta_A|$, $|\eta_5^{(2)}/(k\zeta_A)|$, and $|\zeta_{WP1}/\zeta_A|$, with a convergence criterion of 10^{-3}.
The influence of the damping caused by the boundary layers inside the dock without baffle and estimated as in Sec. 3.6 was briefly investigated. Simulations with ξ_{BL} and then $\xi_{BL} = 0$ were run for incident waves' steepness of $\epsilon = 1/60$, resulting in an average standard deviation between the motions' RAOs below 1% for incident wave frequencies near resonance.

In heave, the equation of motion is given by:

$$\left[-\omega^2\left(M + a_{3,3}\right) - i\omega b_{3,3} + c_{3,3}\right]\overline{\eta}_3^{(2)} = F_3^S, \tag{5.22}$$

where, $c_{3,3}$ include both the restoring coefficients from the mooring lines, and the hydrostatic coefficient:

$$c^H_{3,3} = \rho g A_{WP}. \tag{5.23}$$

5.2 Equations for the dock with spar

5.2.1 Dock with both a spar and an annular baffle

As in Sec. 5.1.2, the effects of annular baffles for the dock with a spar are included through the radiation problems, tackled by a domain decomposition approach. The radiation potential from Sec.2.3.2 is modified to include the effects of the baffle in the subdomain IV between the dock and the spar. In this subdomain, the potential is written:

$$\Phi^{IV}(r,\theta,z,t) = \sum_{\substack{j\in\{1,5\}\\ k\in\{1,2\}}} \Phi_j^{(k),\mathrm{RFS}}(r,\theta,z,t) + \sum_{q=1}^{\infty} R_{1,q}(t)\varphi_{1,q}(r,\theta,z), \tag{5.24}$$

where the radiation potentials in surge and pitch $\Phi_j^{(k),\mathrm{RFS}} = \phi_j^{(k),IV,\mathrm{RFS}} \cos(\theta)\dot{\eta}_j^{(k)}$ for both bodies satisfy the rigid free-surface bondary condition $\partial\Phi_j^{(k),\mathrm{RFS}}/\partial z = \eta_j^{(k)} n_5^{(2)}$ on $z = 0$. The same radiation problems as in Sec.2.3.2 are solved, but with now the potential $\phi_j^{(k),IV,\mathrm{RFS}}$ in the subdomain IV which satisfies the rigid free-surface condition. The expansions used for $\phi_j^{(k),IV,\mathrm{RFS}}$ are presented in Appendix B.3, and are similar to the ones in the subdomain II below the bilge boxes. As for the dock without spar in Sec. 5.1.2, we assume that the sloshing waves described in a tank-fixed coordinate system by the second term of Φ^{IV} in Eq. (5.24) do not communicate with other subdomains below the dock.
The damped modal equations (3.85) are established by imposing the free-surface kinematic and dynamic boundary conditions for the total potential Φ^{IV} in the subdomain IV. The excitations $K_{1,q}$ in the modal equations differ from the case with a closed-bottom:

$$K_{1,q}(t) = -\frac{1}{\mu_{1,q}}\left[\lambda_{1,1,q}^{(1)}\ddot{\eta}_1^{(1)} + \lambda_{1,1,q}^{(2)}\ddot{\eta}_1^{(2)} + \lambda_{5,1,q}^{(1)}\ddot{\eta}_5^{(1)} + \left(\lambda_{5,1,q}^{(2)} + \lambda_{2,1,q}\right)\ddot{\eta}_5^{(2)} - \lambda_{3,1,q} g \eta_5^{(2)}\right], \tag{5.25}$$

which can also be written as $K_{1,q}(t) = -\omega^2 \tilde{P}_{q,j}^{(k)} \overline{\eta}_j^{(k)} e^{-i\omega t}$. The coefficients μ, λ and $\tilde{P}_{q,j}^{(k)}$ are given in Appendix B.3.
Added mass and damping coefficients of the two-body system are calculated by pressure integration over the bodies' surface. The contribution to the loads of sloshing waves in the subdomain IV, i.e. by the second term of Eq. (5.24), are written under first mode approximation:

$$A_{s,j}^{(k),\mathrm{slosh}} + \frac{i}{\omega} B_{s,j}^{(k),\mathrm{slosh}} = i\omega g_s^{(k)} f_1(\omega) \tilde{P}_j^{(k)}(\omega), \tag{5.26}$$

$$D_{s,j}^{(k),\mathrm{slosh}} + \frac{i}{\omega} E_{s,j}^{(k),\mathrm{slosh}} = i\omega g_s^{(k)} f_1(\omega) \tilde{P}_j^{(k')}(\omega), \tag{5.27}$$

where $(s,k) \in \{1,5\}^2, (k,k') \in \{1,2\}^2,\ k \neq k',\ g_s^{(k)} = \rho \int\int_{S_0^{(k),IV}} \varphi_{1,1} n_s^{(k)} \mathrm{d}S$ and $S_0^{(k),IV}$ is the part of the bodies' surface restricted to the subdomain IV. The radiation potentials in the entire domain Ω for the problems with a rigid free surface inside the dock provide the remaining added mass and damping coefficients on both bodies. They are denoted with the superscript $^{\mathrm{RFS}}$. The total added mass and damping coefficients are then:

$$a_{s,j}^{(k)} = a_{s,j}^{(k),\mathrm{RFS}} + A_{s,j}^{\mathrm{slosh}}, \text{ and } b_{s,j}^{(k)} = b_{s,j}^{(k),\mathrm{RFS}} + B_{s,j}^{\mathrm{slosh}}, \tag{5.28}$$

$$d_{s,j}^{(k)} = d_{s,j}^{(k),\mathrm{RFS}} + D_{s,j}^{\mathrm{slosh}}, \text{ and } e_{s,j}^{(k)} = e_{s,j}^{(k),\mathrm{RFS}} + E_{s,j}^{\mathrm{slosh}}. \tag{5.29}$$

Each of the radiation potential $\Phi_j^{(k)}$ produces a vertical velocity component on the baffle, even in surge, which differ from the closed-bottom case studied in Chapter 3. The relative velocity on the baffle v_r which include all the radiation velocities for the open-bottom dock with baffle is given in Appendix B.3.
The added mass coefficients in pitch obtained by integration of the pressure on the bodies' surface in the internal subdomain IV only are presented in Fig. 5.2. The remaining added mass coefficients are also given in Appendix B.7. The added mass coefficients calculated in this section for the case with baffle and under first mode approximation are compared to the one obtained in Chapter 2 for the dock with a spar without baffle. We here verify that the results calculated in this section converge to the ones obtained in Chapter 2 when the effects of the baffle goes to 0.

It should be emphasised that the potential of the dock without spar solved in Sec. 5.1.2 should not directly be used to calculate hydrodynamic loads on the spar, e.g. by using Morison-type loads, or even by direct pressure integration. Since $\lambda_{1,1}/(2a_0) = 7.3$ is high, Morison's formula could indeed appear as an appealing way to estimate the loads on the spar without having to derive the tedious calculations of a domain decomposition method such as the one derived in this section. However, the first sloshing eigenmode is changed with the presence of the spar (see Fig. 5.3), and more important, the first sloshing eigenfrequency is significantly reduced compared to the one for the dock alone. To illustrate the issue, we consider the loads on the spar caused by the radiation potential $\Phi_1^{(2)}$, itself caused by the surge motion of the dock. The spar is assumed fixed, and the radiation potential calculated as in Sec. 5.1.2 for the case without spar. The linear Morison's force on a section of the spar in $x = y = 0$ is expressed as:

$$dF^{\text{Morison}} = \pi a_0^2 \rho C_M \frac{\partial^2 \Phi_1^{(2)}}{\partial x \partial t} dz, \tag{5.30}$$

with $C_M = 2$. In $x = y = 0$ and near resonance, $KC = 2\pi|\zeta_{max}|/(2a_0) \leq 1$, such that viscous loads were neglected in Eq. (5.30) (Sarpkaya, 1986). The radiation potential in surge $\Phi_1^{(2)}$ is proportional to the surge velocity of the dock. Thus, the total load integrated over the height of the spar can be written under the form:

$$F_1^{\text{Morison}} = -e_{1,1}^{\text{Morison}} \ddot{\eta}_1^{(2)}, \tag{5.31}$$

where $e_{1,1}^{\text{Morison}}$ is the added mass coefficient of the spar in surge caused by the surge motions of the dock. These coefficients are compared in Fig. 5.4 to the one derived in Eq. (5.27) by the domain decomposition approach, with significant differences near resonance as the simplified Morison approach does not model the change of the first sloshing eigenmode and eigenfrequency.

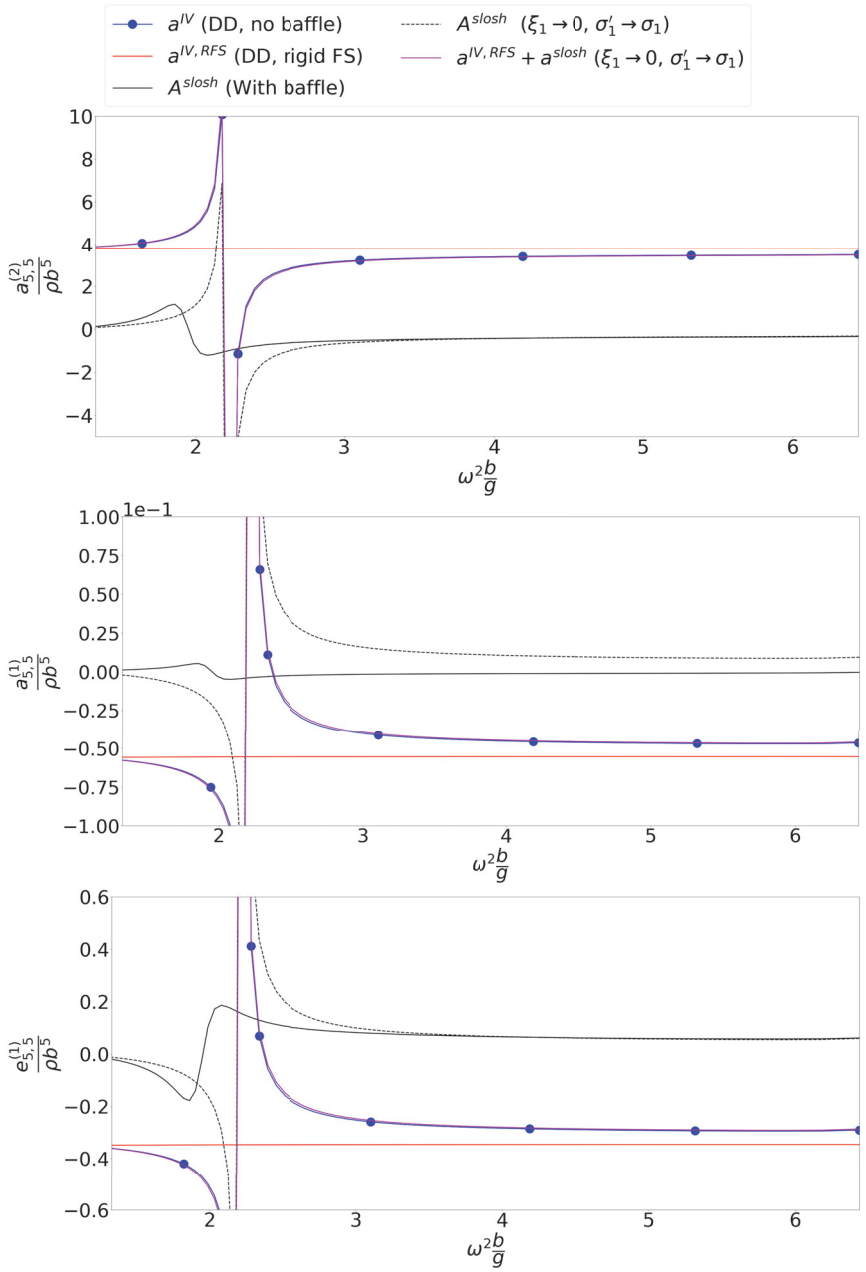

Figure 5.2: *Added mass coefficients $a^{(2)}_{5,5}$ (top), $a^{(1)}_{5,5}$ (middle) and $e^{(1)}_{5,5}$ (bottom) for the dock with spar, calculated by integrating the pressure on the bodies' surface in the subdomain IV. a^{IV} is calculated with a DD method for the case without baffle (cf. Sec. 2.3.2), $a^{(k),IV,RFS}$ (or $e^{(k),IV,RFS}$) and A^{slosh} are the added mass coefficients calculated for the open-bottom dock with baffle. In that case, the equations of motion presented in the next section have been solved to estimate ξ_1 and $\sigma'_{1,1}$, with incident waves' steepness $\epsilon = 1/60$ (black curves).*

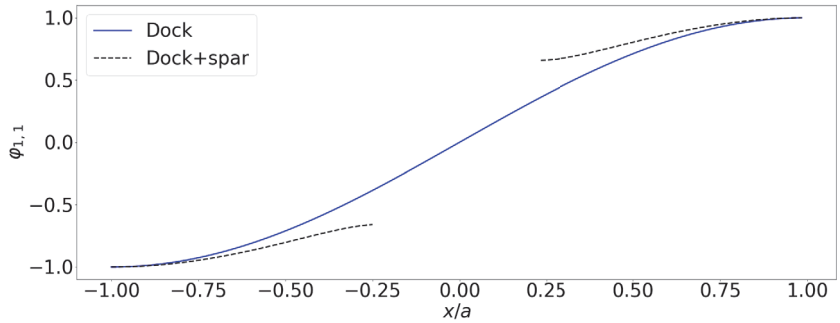

Figure 5.3: *Profile for the normalised eigenmode $\varphi_{1,1}$ in $(y,z) = (0,0)$ for the dock without and with the spar.*

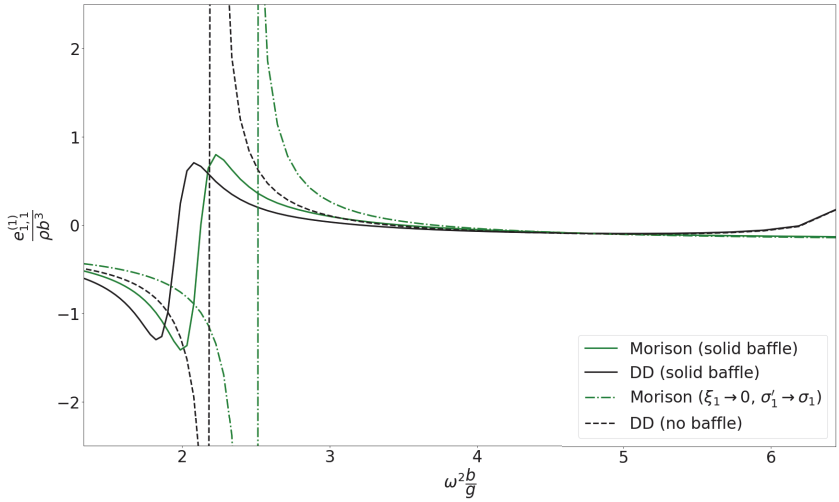

Figure 5.4: *Added mass coefficients $e_{1,1}^{(1)}$ estimated both by a DD method or a simplified approach based on a Morison-type force on the spar. For the case with baffle, the equations of motion presented in Sec. 5.2.2 have been solved to estimate ξ_1 and $\sigma'_{1,1}$, with incident waves' steepness $\epsilon = 1/60$.*

5.2.2 Equations of motion of the dock with spar

The coupled equations in surge of the pitch for the dock and the spar are written:

$$\sum_{j=1,5} \left[-\omega^2 \left(M_{p,j}^{(k)} + a_{p,j}^{(k)}\right) - i\omega b_{p,j}^{(k)} + c_{p,j}^{(k)}\right] \overline{\eta}_j^{(k)} + \left[-\omega^2 d_{p,j}^{(k)} - i\omega e_{p,j}^{(k)} + f_{p,j}^{(k),M}\right] \overline{\eta}_j^{(k')} = F_p^{(k)}, \tag{5.32}$$

$p \in \{1,5\}^2$ $(k,k') \in \{1,2\}^2$, $k \neq k'$. For each body k, $M_{1,1}^{(k)}$ is the mass of the body, $M_{5,5}^{(k)} = I_{5,5}^{(k)}$ the moment of inertia in pitch, $M_{1,5}^{(k)} = M_{5,1}^{(k)} = M_{1,1}^{(k)} \times z_G^{(k)}$ where $z_G^{(k)}$ is the centre of gravity. The restoring coefficients $c_{p,j}^{(k)}$ include both the static terms caused by the mooring lines given in Sec. 4.1.4 and the hydrostatic coefficient in

pitch (5.19) for each body. The forces F_p are the exciting forces and moments calculated in Chapter 2 from the diffraction problem, plus a heuristic quadratic damping load in surge (cf. Eq. (5.21)) for both bodies, with a drag coefficient $C_D = 3$ for the dock and $C_D = 1$ for the spar.
When a baffle is installed inside the dock, the added mass and damping coefficients are calculated as in Sec. 5.2.1, otherwise as in Chapter 2. The moment in pitch on the baffle F_5^M is included in the right hand side of the equation in pitch of the dock in Eq. (5.32).

The equations in heave for the two bodies are also coupled, written:

$$\left[-\omega^2\left(M^{(k)} + a_{3,3}^{(k)}\right) - i\omega b_{3,3}^{(k)} + c_{3,3}^{(k)}\right]\overline{\eta}_3^{(k)} + \left[-\omega^2 e_{3,3}^{(k)} - i\omega d_{3,3}^{(k)} + f_{3,3}^{(k),M}\right]\overline{\eta}_3^{(k')} = F_3^{(k),S}, \tag{5.33}$$

where the restoring coefficients $c_{3,3}^{(k)}$ are caused both by mooring lines and hydrostatic forces (cf. Eq. (5.23)). As indicated by the decay tests in Sec. 4.2.1, the hydrodynamic coupling in heave is quite small.

5.3 Sensitivity analysis

The responses of the semi-analytical model are sensitive to the parameters related to the geometry, mass distribution of the bodies and to the mooring installation. Comparisons with experimental results hence suffer from uncertainties caused by an inaccurate modelling of the experimental set-up. In an attempt to identify the most sensitive parameters and quantify these uncertainties, a sensitivity analysis is carried out for the dock with the spar without any damping device. First, a brief description is given of the systematic method applied to quantify the variations of the semi-analytical responses' amplitude and frequency at resonance, then the results are presented for various input parameters.

The semi-analytical RAO's amplitude at resonance, denoted A_r^*, and the corresponding non-dimensional frequency ω_r^* are calculated successively for parametric variations of each of the geometrical, inertial and stiffness constants characterizing the two-bodies system, all the other parameters being constant beside, and equal to their values given in Sec. 4.1 for the experimental model, that we call nominal values in this section. The star symbol $*$ indicates non-dimensional variables, for which physical values are divided by their nominal values. Fig. 5.5 shows an example of such parametric simulations, presenting $|\eta_1^{(1)}/\zeta_A|$ for several values of the moment of inertia in pitch $I_{5,5}^{(2)*}$ around its nominal value $I_{5,5}^{(2)*} = 1$. The variations of ω_r^* and A_r* as functions of $I_{5,5}^{(2)*}$ are then given in Fig. 5.6 for all

the bodies' motions. Polynomial regressions are made for each curve in order to estimate the variation rates $\delta A_r^* = \partial A_r^* / \partial I_{5,5}^{(2)*}$ in $I_{5,5}^{(2)*} = 1$, and $\delta \omega_r^* = \partial \omega_r^* / \partial I_{5,5}^{(2)*}$ in $I_{5,5}^{(2)*} = 1$. This method is then repeated for other parameters.

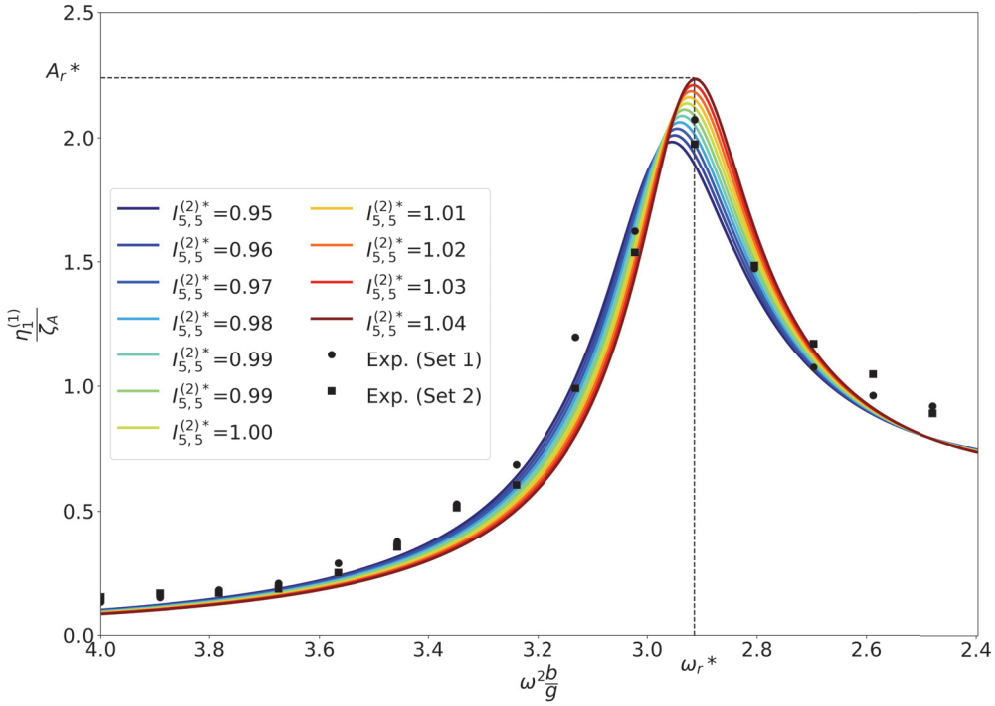

Figure 5.5: *Example of RAOs of the spar's surge motion for different values of the non-dimentional moment of inertia in pitch of the dock $I_{5,5}^{(2)*}$ around a nominal value $I_{5,5}^{(2)*} = 1$. Solid lines are semi-analytical results. The non-dimensional frequency ω_r^* and amplitude A_r* measured at the peak resonance are here indicated for the highest value of $I_{5,5}^{(2)*}$. 88 simulations were run for each of the parametric studies, only 11 simulations are presented on this plot for the sake of clarity. Experimental results from 2019 tests.*

Fig. 5.7 presents the results of the sensitivity analysis. It can be noted that the variations of ω_r^* are similar for all motions, and in general relatively low. The coupled resonance occurs indeed at about the same frequency for all motions, and the differences between ω_r^* for two different motions, all parameters identical otherwise, are always below 0.25%. It is also without surprise that the internal radius of the dock, a, affects ω_r^* the most, since it also drives the value of the sloshing natural frequency $\sigma_{1,1}$.
The variations of the peak amplitude A_r^* are on the other hand more significant, with large disparities between the motions. The spar's surge motion is generally much more sensitive than pitch, and very dependent on the spar's mass distributions, but also on the dock's mass distribution which has a strong influence on the sloshing

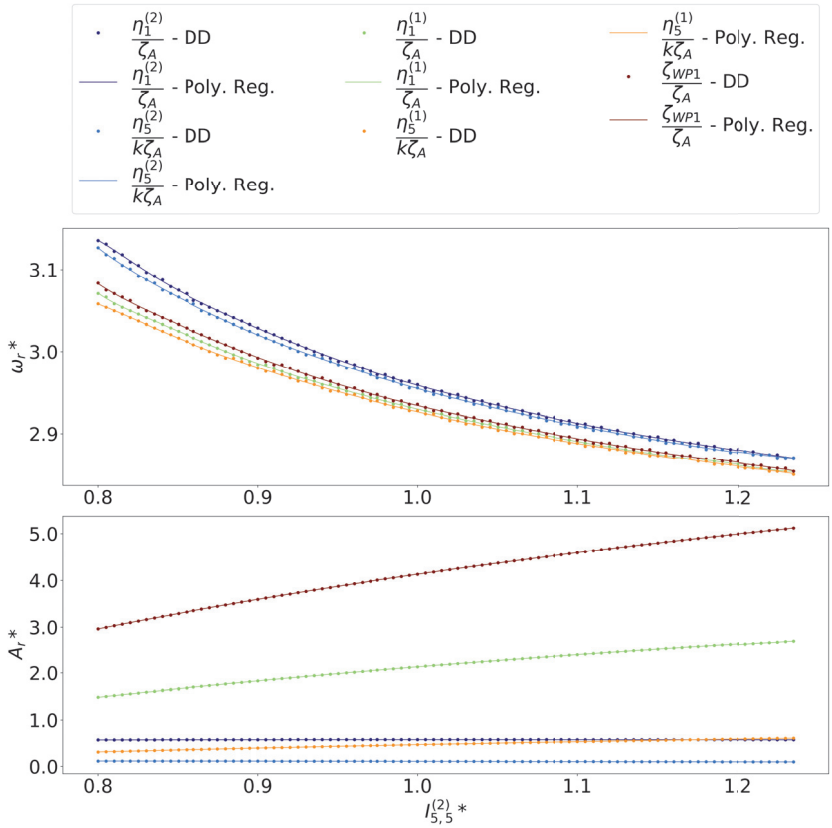

Figure 5.6: *Example of parametric study made for $I_{5,5}^{(2)*}$. The variations of ω_r^* and A_r^* are presented near the nominal value $I_{5,5}^{(2)*} = 1$ for all the RAOs of the bodies' motions in surge and pitch, as well as $|\zeta_{WP1}/\zeta_A|$. The discrete results are simulated with the semi-analytical model, which are then approximated by a polynomial regression (Pol. Reg.) of order 11.*

wave amplitude.

Let us for instance focus on a 1% increase of $z_G^{(2)}*$. The frequency ω_r* of $|\eta_1^{(2)}/\zeta_A|$, which is a main excitation for the sloshing wave, is increased by about 1.1%, and thus moved away from the sloshing natural period $\sigma_{1,1}$. In the same time, the peak amplitude of $|\eta_1^{(2)}/\zeta_A|$ is identical. As a result, the peak of $|\zeta_{WP1}/\zeta_A|$ is decreased by 9.8%. Inversely, a 1% increase of $I_{5,5}^{(2)}*$ reduces ω_r* for $|\eta_1^{(2)}/\zeta_A|$ by 0.6%, moving it closer to the natural sloshing frequency, still without influencing the amplitude of the excitation. As a consequence, the peak amplitude of $|\zeta_{WP1}/\zeta_A|$ is increased by 5.0%.
We can also note that increasing the external radius of the dock could help to reduce critical motions of the spar. Similar simulations were made relatively to the connection points' location and stiffness of the mooring lines, showing a smaller influence on the results.

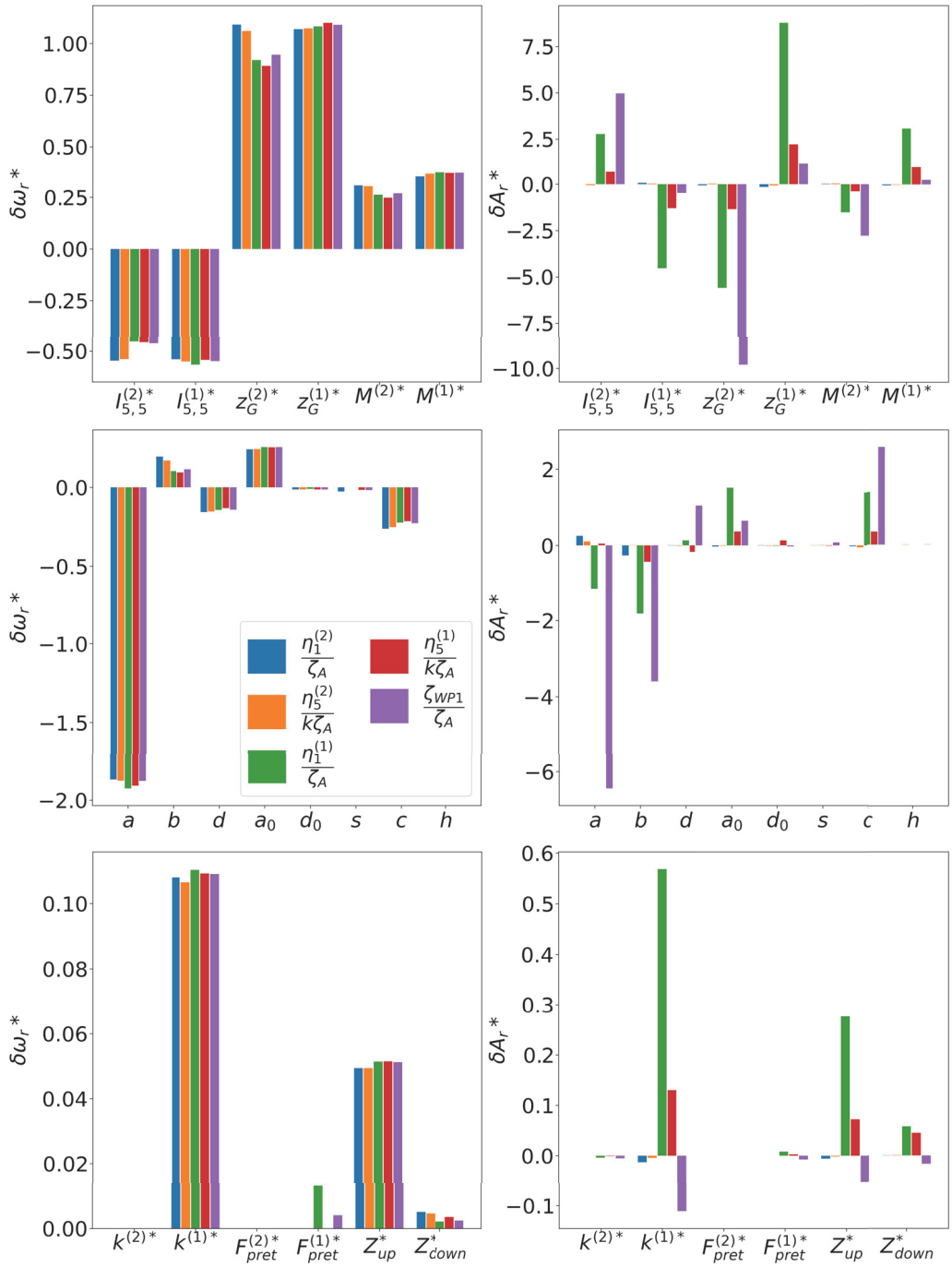

Figure 5.7: *Sensitivity of the RAOs' peak amplitudes and frequencies at resonance.* δA_r* *and* $\delta\omega_r^*$ *are given for all the motions' RAOs, as well as for* $|\zeta_{WP1}/\zeta_A|$*. For example* $\delta\omega_r^* = -0.5$ *for* $I_{5,5}^{(2)*}$ *means that* ω_r^* *decreases by* 0.5% *when* $I_{5,5}^{(2)*}$ *increases by* 1%*.*

5.4 Eigenvalue analysis

An eigenvalue analysis of the system is performed from the equations of motion of the semi-analytical models without exciting forces to estimate the natural periods of the dock and spar's motion. The eigenvalue problem can be written as:

$$\left[-\omega^2 \left(\boldsymbol{A} + \boldsymbol{M}\right) + \boldsymbol{C}\right] \cdot \boldsymbol{X} = \boldsymbol{0}, \tag{5.34}$$

where $\boldsymbol{M}$ is the mass matrix, $\boldsymbol{A}$ the added mass matrix and $\boldsymbol{C}$ the stiffness matrix. These matrices are filled with the coefficients defined in the equations of motions in the previous sections, either for the dock with or without the spar. $\boldsymbol{X}$ is an eigenvector of the rigid body motions, either surge and pitch or heave. Eq. (5.34) is solved for ω by setting the determinant of the matrix inside the brackets equal to 0. Because the system is non-linear due the frequency dependency of the added mass matrix, an iterative scheme is implemented until convergence of the eigenvalue and with a convergence criterion of 10^{-4}. The results are presented in Table 5.1 and 5.2 for the dock alone, and Table 5.3 for the dock with spar. These values can for instance be compared to the ones obtained from the decay tests in Sec. 4.2.1, i.e. with the values from Table 4.5 for the dock without spar and Table 4.6 for the dock with spar and without damping devices. The normalised eigenvector gives the correct shape of the resonant modes, for which several rigid body motions can be coupled. For example in Table 5.1, we see for the eigenmode corresponding to the period 2.313s, a 0.927rad pitch motion of the dock is associated to a 0.375m surge motion. These information were missing in the decay tests, were the motions were incorrectly considered as if they were decoupled. For the case with the spar in Table 5.3, we observe a eigenperiod of 3.251s mostly associated with the surge and pitch motions of the spar. This period could not be measured during decay tests, even though it does seem to be observed from the time series of $\eta_1^{(1)}$ in Fig. 4.7, looking at the successive maximum amplitudes.

Table 5.1: *Normalised eigenvectors and eigenperiods, solutions of the eigenvalue problem* (5.34) *for the dock without spar. Both the case with and without mooring lines are presented. The stiffness matrix of the moored dock include the restoring coefficients from Sec.4.1.4 due to mooring, while it does not for the unmoored dock. Draught of the dock:* $d+s=0.8m$*, BB2.*

	Moored			Unmoored	
$\eta_1^{(2)}$ [m]	0.375	0.998	×	0.381	×
$\eta_3^{(2)}$ [m]	×	×	1.000	×	1.000
$\eta_5^{(2)}$ [rad]	0.927	0.069	×	0.925	×
Eigenperiod T [s]	2.313	10.755	2.273	2.419	2.281
Eigenfrequency $\omega^2 b/g$ [-]	0.301	0.014	0.312	0.275	0.309

Table 5.2: *Normalised eigenvectors and eigenperiods for the moored dock without spar. Results are given for both draughts* $(d+s)/b=1.25$ *and both bilge boxes' sizes BB1 and BB2. The case for* $(d+s)/b=2$ *with BB2 is given in Table 5.3.*

	(d+s)/b=1.25, BB1			(d+s)/b=1.25, BB2			(d+s)/b=2, BB1		
$\eta_1^{(2)}$ [m]	0.999	0.229	×	0.999	0.248	×	0.997	0.364	×
$\eta_3^{(2)}$ [m]	×	×	1.000	×	×	1.000	×	×	1.000
$\eta_5^{(2)}$ [rad]	0.015	0.973	×	-0.016	0.969	×	0.072	0.932	×
T [s]	8.091	2.428	1.818	8.253	2.81	1.988	10.625	2.144	2.127
$\omega^2 b/g$ [-]	0.025	0.273	0.487	0.024	0.204	0.407	0.014	0.350	0.356

Table 5.3: *Normalised eigenvectors and eigenperiods, solutions of the eigenvalue problem* (5.34) *for the dock with spar. Draught of the dock:* $d+s=0.8m$*, BB2.*

$\eta_1^{(2)}$ [m]	0.000	0.706	-0.011	-0.299	×	×
$\eta_3^{(2)}$ [m]	×	×	×	×	-0.805	0.034
$\eta_5^{(2)}$ [rad]	-0.008	0.040	-0.007	-0.730	×	×
$\eta_1^{(1)}$ [m]	0.441	0.707	0.650	-0.291	×	×
$\eta_3^{(1)}$ [m]	×	×	×	×	-0.593	-0.999
$\eta_5^{(1)}$ [m]	0.897	0.005	-0.760	-0.541	×	×
Eigenperiod T [s]	1.399	10.872	3.251	2.328	2.255	1.565
Eigenfrequency $\omega^2 b/g$ [-]	0.822	0.014	0.152	0.297	0.317	0.657

6 | Results in regular waves

Numerical and experimental results for regular incident waves are presented in this chapter, focusing on the first-harmonic RAOs of the bodies' and free-surface elevation's motions near sloshing resonance in an Earth-fixed coordinate system. All results are discussed in model scale, based on the experimental set-up described in Sec. 4.
The semi-analytical models presented in Sec. 5 for the dock with and without spar and damping devices, partially based on a domain decomposition approach, are denoted as "DD models" in this section. First, results are discussed for the dock without spar nor damping devices in Sec. 6.1, in particular for different draughts and bilge boxes' sizes. Then, results for the dock with damping devices - both the foam balls and the baffles - and without the spar are discussed in Sec. 6.2 . Finally, RAOs for the dock with the spar are presented in Sec. 6.3.

6.1 Dock without spar nor damping devices

6.1.1 Motions of the dock

Semi-analytical and experimental results are presented in Fig. 6.1 for the dock's surge and pitch motions and for the free-surface elevation inside the dock at WP1. The fully-linear semi-analytical results are in fair agreement with results from the model tests. The experimental RAOs seem slightly skewer at resonance. The motions of the dock are almost null at the sloshing natural frequency $\sigma_{1,1}^2 b/g = 2.45$, caused by the almost-infinite added mass in surge and pitch at that frequency. A sharp shift of π in the motions' phases is also observed at the same frequency: below $\sigma_{1,1}^2 b/g$ both surge and pitch are in opposition of phases with ζ_{WP1}, while the three motions are in phase above $\sigma_{1,1}^2 b/g$. This could be predicted by Eq. (3.87) when $\xi_1 = 0$: the free-surface elevation inside the dock becomes in opposition of phase with the excitation term C_q, i.e. with surge and pitch accelerations, due to the change of sign at $\sigma_{1,1}^2 b/g$, and so it becomes in phase with surge and pitch motions.
The maximum amplitudes of the dock's motions at the resonant peak, near $\omega^2 b/g = 3$, are relatively low, with $(\eta_1^{(2)}/\zeta_A)_{max} = 0.57$ and $(\eta_5^{(2)}/(k\zeta_A))_{max} = 0.11$ as predicted by the semi-analytical model, but still causing relatively high sloshing waves, with $(\zeta_{WP1}/\zeta_A)_{max} = 3.62$. The velocity profile of a cross-section of the dock near the resonant peak and over a period of oscillation is presented in Fig. 6.2. Vertical velocities of sloshing waves reach up to 0.14m/s along the wall of the dock (i.e. 1.4m/s in full scale), and exponentially decay along the negative z axis. These flow velocities are not negligible, and not beneficial for operating inside the dock at typical weather conditions.

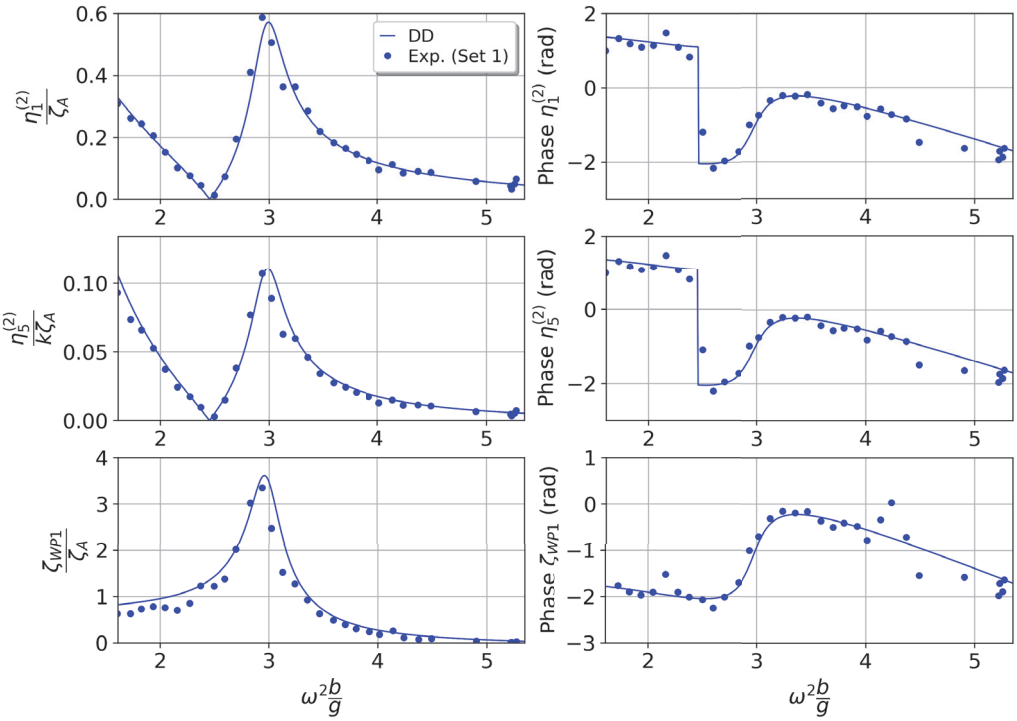

Figure 6.1: *RAOs of the dock's surge and pitch motions when there is no spar, and of the free-surface elevation inside the dock at WP1. Amplitudes and phases, comparison between the semi-analytical model (denoted DD) and experimental results (2019, Set 1). The wave maker could not generate wave periods lower than* $T = 0.55s$ *(cf. Sec. 4.4.2) and, in consequence, few results are packed around* $\omega^2 b/g = 5.25$. $(d+s)/b = 2$, *large bilge-boxes. Wave steepness:* $\epsilon = 1/60$.

The linear heave motions were totally negligible in this range of incident wave periods compared to the other motions, as shown in Fig. 6.3. The experimental results presented on this figure were measured with accelerometers, all exceeding the lower limit of accuracy of the instrumentation.
Because of the high draught of the structure, the diffraction potential calculated by the DD method was negligible inside the dock. Sloshing modes were therefore not excited by the diffraction potential. In particular, it means that there was no axisymmetric sloshing modes. Fig. 6.3 shows the RAOs of the free-surface elevation at the two wave probes WP1 and WP3, which were aligned with respect to the wave propagation, but at opposite sides inside the dock. They both have the same amplitudes while being in opposition of phases, which would not be the case if axisymmetric modes were playing a role. These observations are coherent with the assumptions made in the previous Chapters 3 and 5, for which sloshing waves were described as in a closed-bottom cylinder.

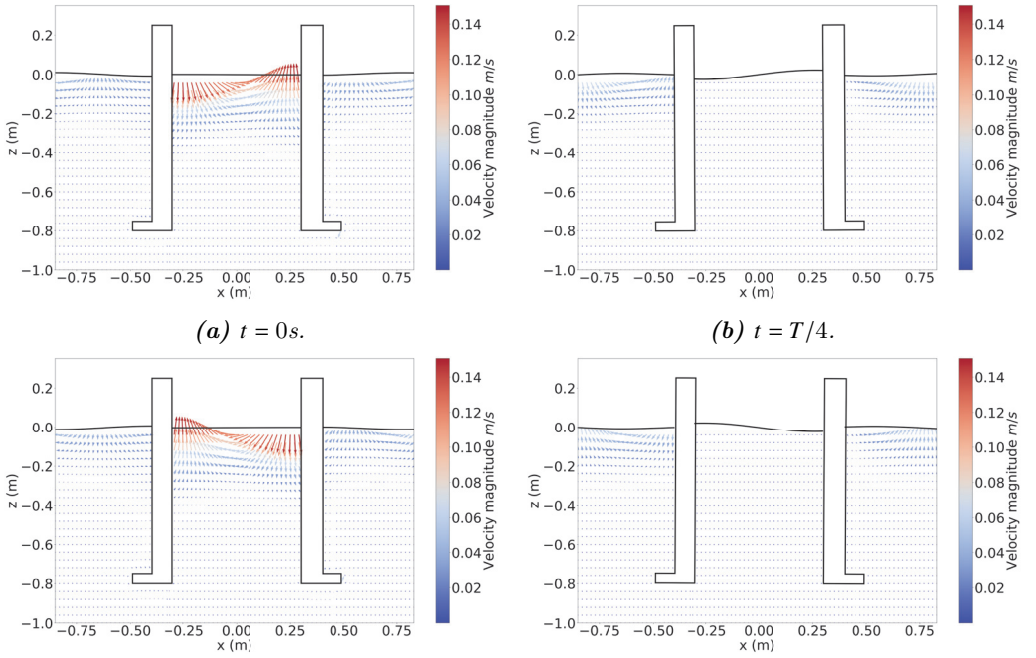

(a) $t = 0s$. *(b)* $t = T/4$.

(c) $t = 2T/4$. *(d)* $t = 3T/4$.

Figure 6.2: *Velocity profile in* $y = 0m$ *in the Earth-fixed coordinate system at the incident wave frequency:* $\omega^2 b/g = 2.94$ *(i.e.* $T = 0.74s$*), calculated from the DD model. The motions of the dock in surge, pitch and heave, as well as the free-surface elevation are reproduced to scale. At* $t = 0s$*, undisturbed incident waves are maximal in* $x = 0m$*, as defined in previous sections. Wave steepness:* $\epsilon = 1/60$.

6.1.2 Influence of the wave steepness

Experimental results of the dock alone and for three wave steepnesses, $\epsilon = 1/60$, $1/45$ and $1/30$ are presented in Fig 6.4 and compared to semi-analytical results (solid curves). The variations due to the different wave steepnesses are in overall quite small. Despite some scattering near resonance, all the experimental results remain within the range of random errors discussed in Sec. 4.5.1.
An heuristic damping was included to the equation of motions in surge (cf. Sec. 5.1.3) for the whole dock, considering the drag coefficient $C_D = 3$ (cf. Eq. (5.21)), resulting in a reduction of the resonant peak's amplitude between 8.8% for $\epsilon = 1/60$ and 15.8% for $\epsilon = 1/30$. Similar rates are observed for ζ_{WP1}, suggesting that viscous forces on the dock could also be used as a mean to damp sloshing waves. Flow separation at the sharp corners of the bilge boxes are also expected to introduce a quadratic damping in pitch and heave, which are expected to play a significant role for lower incident wave frequencies due to higher pitch and heave motions than near sloshing resonance. Such viscous damping coefficients are not included in our model, and would require further investigations as the complexity of the

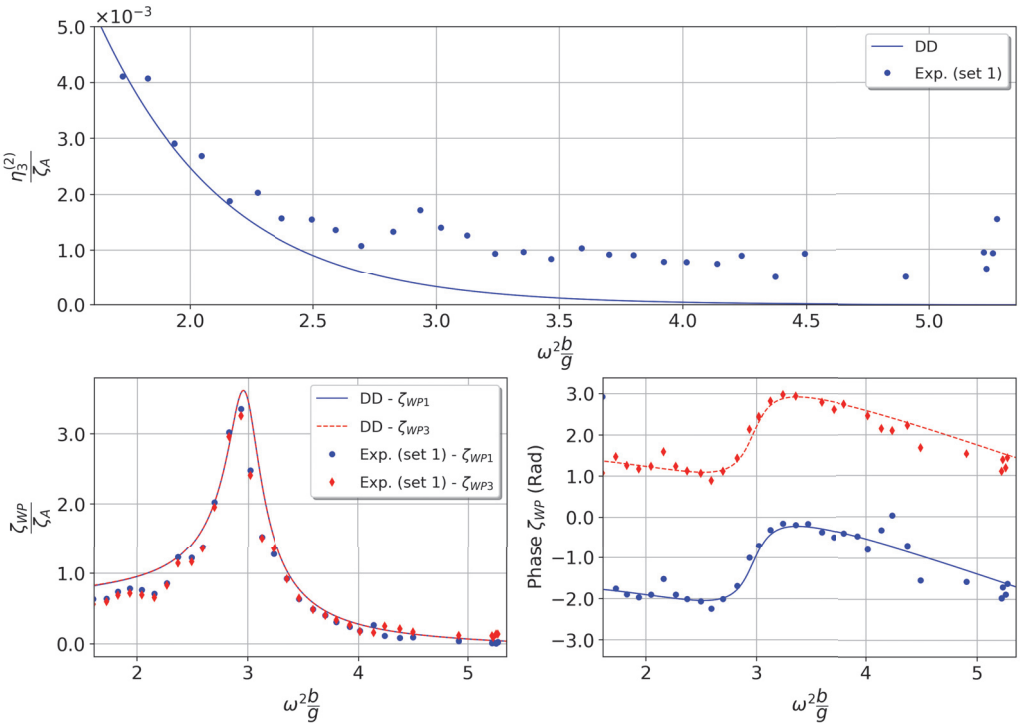

Figure 6.3: *Top: RAOs of the dock's heave motion, negligible for this range of incident wave periods. The experimental values (2019, Set 1) were measured with accelerometers all exceeding the lower limit of accuracy of the instrumentation. Bottom left: RAOs of the free-surface elevation inside the dock at WP1 and WP3, aligned with the direction of the wave propagation and at opposite side inside the dock. Bottom right: phases of the free-surface elevation at WP1 and WP3.* $(d+s)/b = 2$*, large bilge-boxes, wave steepness:* $\epsilon = 1/60$.

flow's velocity profile around the bilge boxes makes it difficult to obtain simple estimations of these damping coefficients (see more details in Appendix D.1).

6.1.3 Several draughts

The conception of the floating dock includes towing phases of the whole dock from one site to the other, without any spar inside the dock (Jiang et al., 2020). During these phases, ballasts are removed from the dock, and the structure towed by tug boats. In his study, Jiang et al. (2020) consider two draughts for the dock in operation and transit conditions, respectively 65m and 20m in full scale. Their design optimisation study includes a constraint on the piston mode natural period in order to keep it above 17s in operation. For the 65m draught, this natural period is indeed around 18s. However, they do not impose such constraint for the transit condition.
In this section, we briefly discuss the influence of the dock's draught on the natural

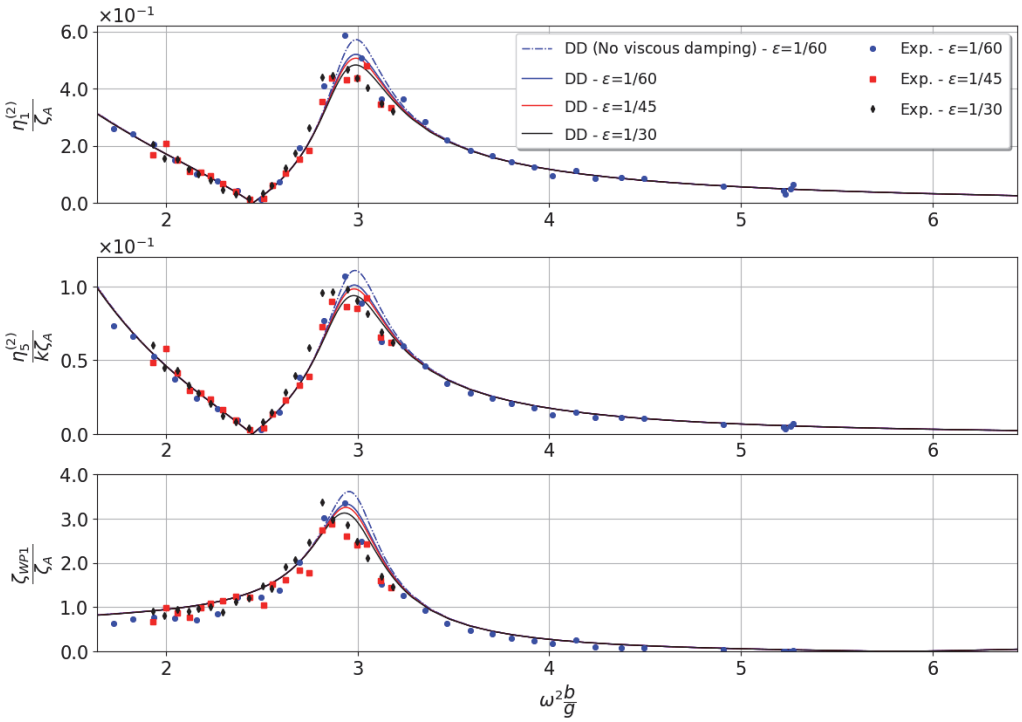

Figure 6.4: *RAO of the dock's surge (top) and pitch (middle), and RAO of the wave elevation inside the dock at WP1 (bottom), calculated from the DD approach and compared to experimental results (2019, Set 1) for three different wave steepnesses, for the case without baffles. The dash curves show the motions calculated analytically without any viscous damping, while a drag force (cf. Eq.* (5.20)*) is added in the equation of surge for the solid curves.*

periods and the body's motions when it is free-floating in waves. In addition to both draughts tested experimentally for the dock in operation conditions, numerical simulations with the semi-analytical model were carried out for two additional lower draughts, for which the dock's characteristics are presented in Table 6.1. For these two additional draughts, masses are calculated from the displacements, and both the center of gravity and moment of inertia in pitch are calculated from the model's mass properties and as the result of removing the required weight of ballasts to reach the desired draughts.

Comparison between experimental and numerical results for $(d+s)/b = 1.25$ and $(d+s)/b = 2$ are presented in Fig. 6.5, as well as the two lower draughts simulated from the DD model. The maximum value of ζ_{WP1}/ζ_A at the resonant peak increases by 17.5% when $(d+s)/b$ decreases from 2 to 1.25, but then quickly decreases for lower draughts. As expected, the responses for the shallowest draught are significantly lower, due to lower hydrodynamic forces caused by internal sloshing waves. It should be emphasised that for shallow draughts $(d+s)/b <$

Table 6.1: *Additional draughts investigated with the semi-analytical method using the mass properties of the dock's model given in Table 4.2.* $H_{skm} = 0.05m$ *and* $B_{skm} = 0.09m$ *(BB2).* $I_{5,5}$ *and* z_G *are given relatively to the mean free surface. Virtually removing all the ballasts was not enough to reach the lowest draught, such that the dry height of the dock also needed to be virtually shorten by* $0.28m$.

Non-dimensional draught $(d+s)/b$ [-]	Dimensional draught $(d+s)$ [m]	M [kg]	$I_{5,5}$ [kg.m^2]	z_G [m]
0.38	0.15	45.57	9.70	0.20
0.75	0.30	78.56	15.92	0.10

1.25, the sloshing eigenfrequencies of the first lateral mode determined for a closed-bottom dock in Chapter 3 do not accurately predict the eigenfrequencies for the open-bottom dock (see Fig. 6.6).
For lower draughts piston modes are shifted to higher frequencies, the piston mode resonance for $(d+s)/b = 0.38$ is for example observed at $\omega^2 b/g = 1.34$, with a 60% lower amplitude than for $(d+s)/b = 0.75$. Similar to sloshing resonance, the motions' RAOs' maxima caused by piston mode resonance do not necessarily occur at the piston natural frequency because of the radiation dissipation. The piston natural frequency is estimated from the added mass in heave (cf. Sec. 2.4) in the DD model. These natural frequencies are given in Fig. 6.7 for several draughts (red curve), which are generally lower than the resonant piston frequencies (black squares) corresponding to maximal motions' RAOs. In this figure, the piston natural frequencies are compared to simple formulas derived by Molin (2001) and Molin et al. (2018) for rectangular and circular moonpools, respectively. These formulas are derived under single mode approximation with the assumption that the external radius b is large with respect to the internal radius a. Even though in our case, the ratio $b/a = 1.33$ is low, these models provides good estimations of the piston natural frequencies for $(d+s)/b \geq 1.25$, except for the two-dimensional rectangular moonpool (solid blue curve) which is paradoxically the one used by Jiang et al. (2020). Surprisingly, the formula used for the three-dimensional square moonpool of side's length $\sqrt{2}a$ (RT2) provides even better estimations than the one for a circular moonpool, and could be used if further parametric studies were to be done.

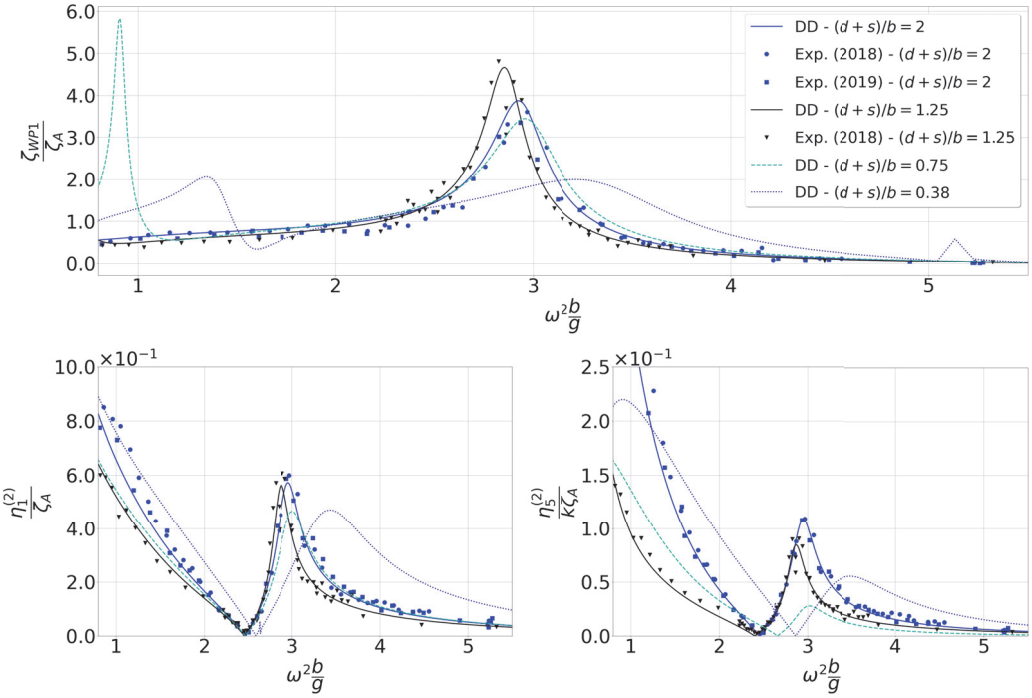

Figure 6.5: *RAOs of the dock's motions and ζ_{WP1} for several draughts. Experimental results from 2018 and 2019 are compared to the semi-analytical (DD) results in regular waves. The two lower draughts are obtained with the same semi-analytical model derived in Sec. 5.1. Experimental results for $(d+s)/b = 2$ include repetitive tests between 2018 (Set 1) and 2019 (Set 1).*

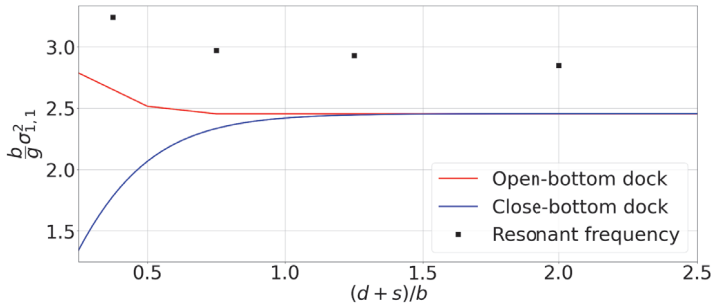

Figure 6.6: *Natural frequency of the first lateral sloshing mode. Estimations from the closed-bottom model are compared to the values obtained for the open-bottom model (cf. Chapter 3 and Appendix D.2). Natural frequencies for the open-bottom model are determined from the added mass in surge (cf. Chapter 2). Resonant frequencies for which the motions' RAOs are maximal are indicated by square points for the four draughts considered in this section.*

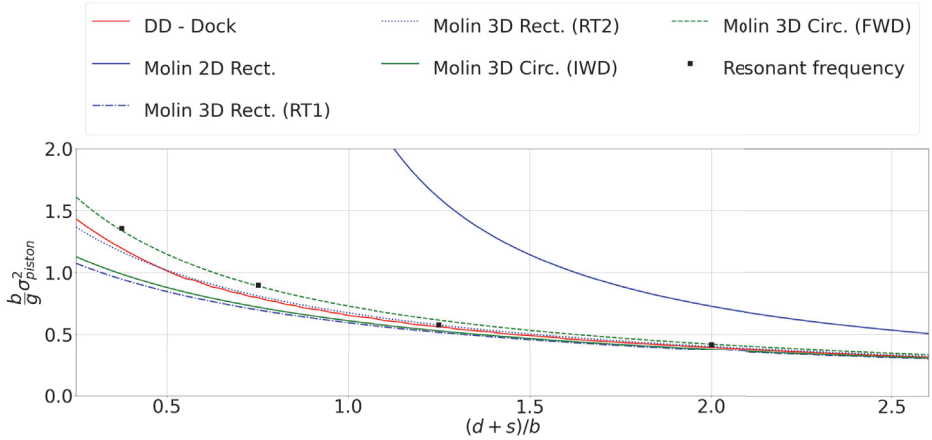

Figure 6.7: *Piston natural frequency as a function of the dock's draught and estimated through different methods. From the DD model, it is estimated from the added mass in heave (cf. Chapter 2). These values are compared to simple estimations derived by Molin (2001) and Molin et al. (2018) for a two-dimensional rectangular moonpool, a three dimensional rectangular moonpool, and three-dimensional circular moonpools with finite water depth (FWT). In this last case, asymptotic values for infinite water depth (IWD) and infinite wall's thickness b/a Molin et al. (2018) are also given. Resonant frequencies for which the motions' RAOs are maximum are indicated by square points for the four draughts studied in Fig. 6.5.*

6.1.4 Influence of the bilge-boxes' size

Semi-analytical simulations were run for the to sizes of bilge boxes BB1 and BB2 tested experimentally (Cf. Sec. 4.1) for the two draughts $(d+s)/b = 2$ and $(d+s)/b = 1.25$. Both numerical and experimental RAOs of the dock's motions in surge and pitch are presented in Fig. 6.8 for $(d+s)/b = 2$, and Fig. 6.9 for $(d+s)/b = 1.25$. Even though it is not the main focus of this work, model tests were made for wave frequencies much lower than the sloshing natural frequency and near natural resonances in pitch, heave and of the piston mode, where the influence of the bilge-boxes' size is expected to matter the most. Numerical simulation were also run for these lower frequencies without any damping, as the heuristic damping in surge introduced in Sec 5.1 is not adapted to model the viscous damping caused by high pitch motions, nor does it account for any damping in heave. Piston mode natural frequencies were estimated at $\sigma^2_{piston} b/g = 0.4$ for $(d+s)/b = 2$ and $\sigma^2_{piston} b/g = 0.58$ for $(d+s)/b = 1.25$ from the DD model (see Sec. 2.4).
For frequencies higher than $\sigma^2_{1,1} b/g = 2.45$, near the sloshing resonant peak, the effects of the bilge boxes' sizes on the motions are not visible for either draught, as the RAOs for BB1 and BB2 are very close and in the range of uncertainties determined from repetition tests. For lower frequencies, natural periods in pitch and heave are shifted to lower frequencies for BB2 compared to BB1 due to the increase of added mass (see Sec. 5.4), which also explains entirely the shift of

RAOs for the semi-analytical results as there is no viscous damping in the model. Experimental RAOs' amplitudes are much lower than the semi-analytical ones for these frequencies, most likely due to non-linear damping caused by flow separations at the inlet of the dock and at the edges of the bilge boxes. The RAOs' resonant peaks' amplitude are generally lower for BB2 from the experimental results, which confirms that the bilge boxes play a role in damping the motions. We can also note that for both draughts, ζ_{WP1}'s RAO's amplitude is lower near piston mode than near the sloshing first lateral mode resonance, despite much higher dock's motions in surge and pitch.

For $(d+s)/b = 2$ two peaks are observed in surge and pitch from the experimental results at low frequencies. Resonance was expected in pitch and surge near the natural frequencies in pitch $\omega^2 b/g = 0.35$ (BB1) and $\omega^2 b/g = 0.3$ (BB2) (again cf. Sec. 5.4). A non-linear coupling with the piston mode is suspected to cause the second resonant peak around $\omega^2 b/g = 0.45$, which is close to the piston natural frequency determined in the previous section. The piston mode is also linearly coupled with the heave motions, the RAOs of which are presented in Fig. 6.10. Natural periods in heave were determined close to the ones in pitch, between $\omega^2 b/g = 0.3$ and 0.5 depending the draught and the BB's size. As for pitch and surge, experimental results in heave are significantly damped compared to the semi-analytical ones, which is typical for moonpools (Fredriksen et al., 2015; Ravinthrakumar et al., 2019; Reiersen et al., 2021). Even though, heaving from model tests was considerable for these low wave frequencies ($T > 18$s in full scale), with maximal vertical motions above the mean sea level measured higher than 15m in full scale for both draughts. These extreme motions were not observed at operational weather condition near sloshing resonance, and it is unlikely that FOWTs' assembly will be operated at these extreme weather conditions. Yet, they might cause structural damages and be a threat for any storage or construction installations present on the top of the dock.

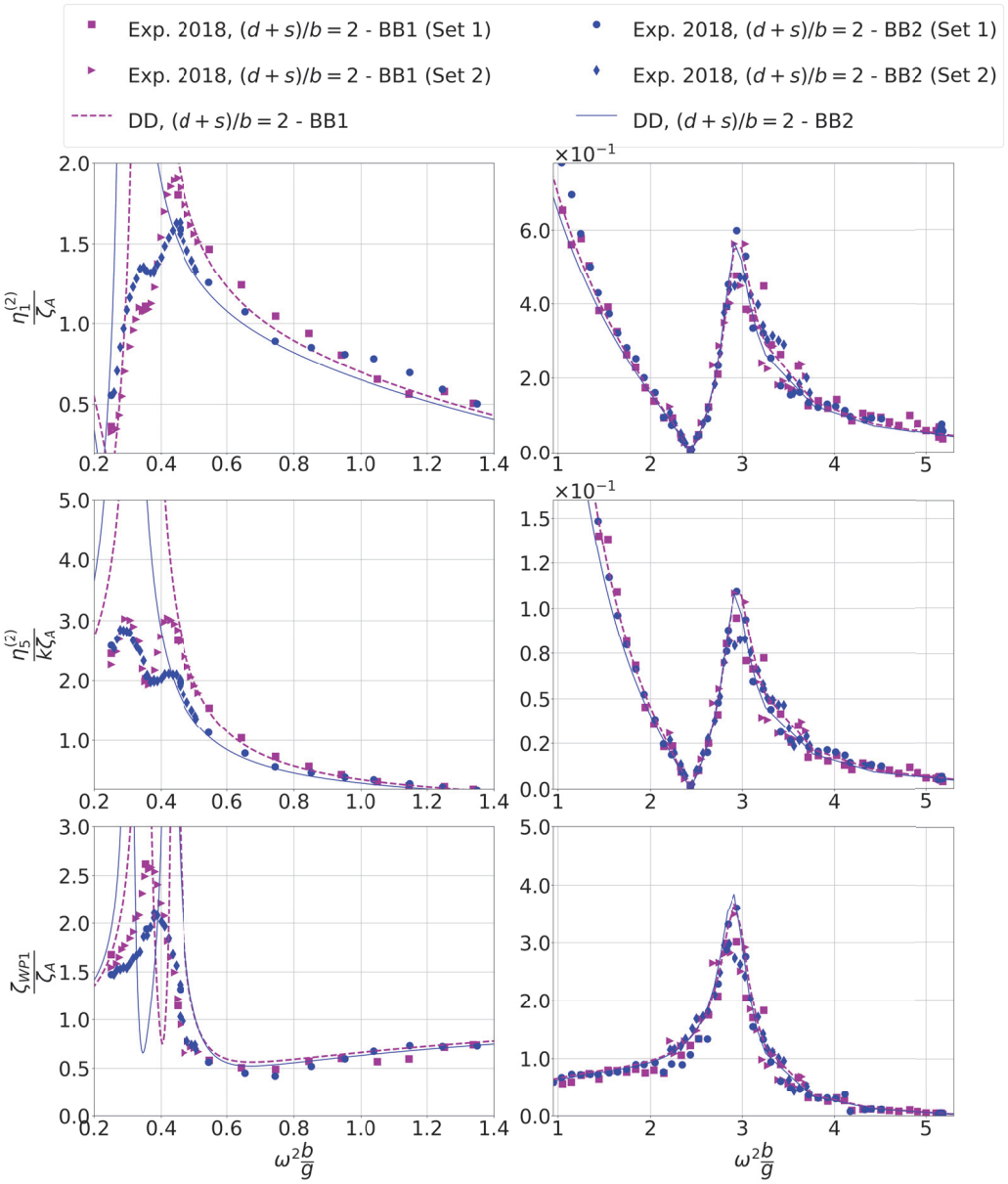

Figure 6.8: *Experimental and semi-analytical RAOs of $\eta_1^{(2)}$, $\eta_5^{(2)}$ and ζ_{WP1} for the dock without spar not baffles. Two BB' sizes BB1 (smaller) and BB2 (bigger) are considered, as defined in Sec. 4.1. Left: lower wave frequencies. Right: zoom on the responses for higher wave frequencies. Draught: $(d+s)/b = 2$, wave steepness: $\epsilon = 1/60$.*

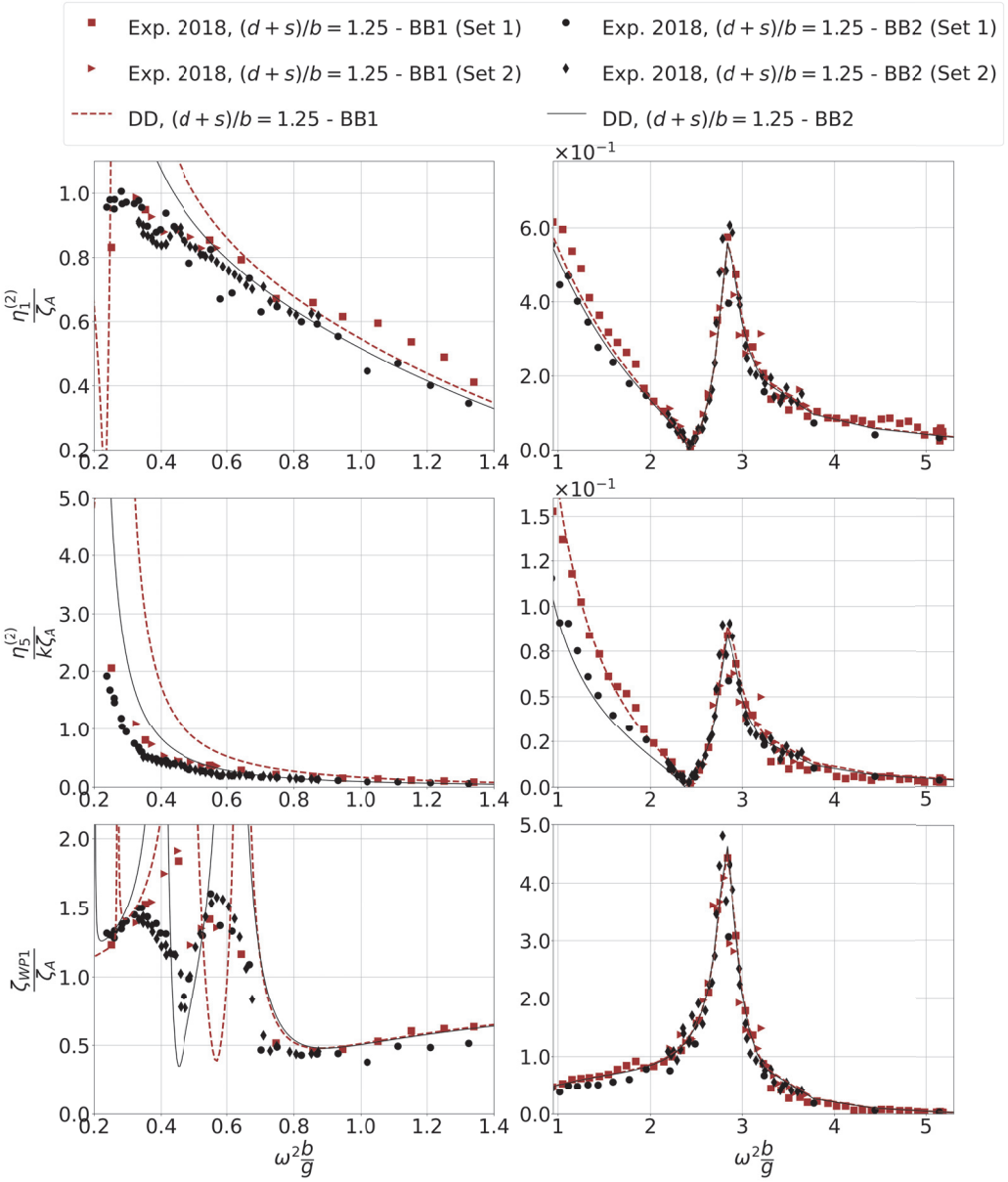

Figure 6.9: *Experimental and semi-analytical RAOs of* $\eta_1^{(2)}$, $\eta_5^{(2)}$ *and* ζ_{WP1} *for* $(d+s)/b = 1.25$ *with two BB' sizes. Wave steepness:* $\epsilon = 1/60$.

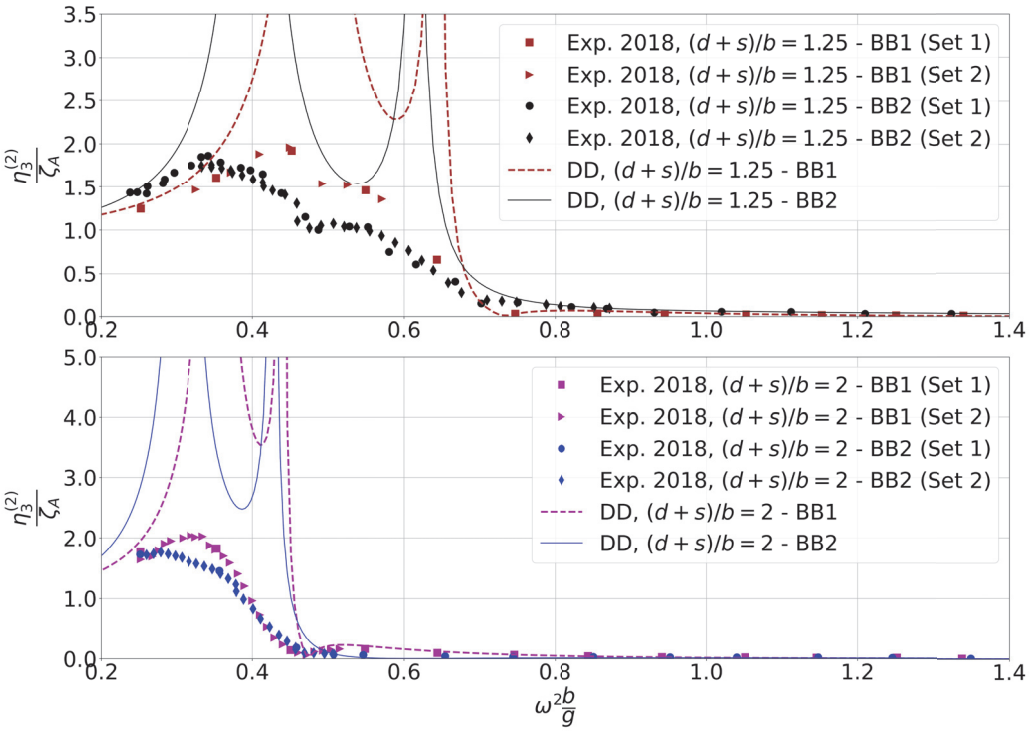

Figure 6.10: *. Experimental and semi-analytical RAOs of* $\eta_3^{(2)}$ *for* $(d+s)/b = 1.25$ *(top) and* $(d+s)/b = 1.25$ *(bottom) and for low incident wave frequencies. Wave steepness:* $\epsilon = 1/60$.

6.2 Dock with damping devices

6.2.1 Solid and perforated baffles

The RAOs of the internal free-surface elevation at WP1 when solid or perforated baffles are installed inside the dock at three different submergences d_B/a are presented in Fig. 6.11. RAOs of the dock's surge and pitch motions are shown in Fig. 6.12 for the same cases. It can first be observed that the three baffles cause a significant reduction of the motions' amplitudes for the three submergences d_B/a. Better efficiencies are generally obtained when the baffle is the nearest to the free surface for the three cases. This was expected, since the damping is function of the relative vertical flow velocity on the baffle caused by sloshing waves, which decay exponentially with the depth.
The amplitude of the relative flow velocity v_r on the solid baffle at $r = a$ and $z = -d_B$ is given in Fig. 6.13. The linear decomposition of the potential flow as described in Sec. 5.1.2 allows us to compare analytically the velocity's amplitudes due to the sloshing waves in a dock-fixed coordinate system, and due to the dock's pitching with a rigid internal free surface. Pitch's contribution increases for lower d_B/a, mostly due to that higher submergences imply less damping, resulting in higher pitch motions (cf. Fig 6.12). The ratio of v_r's amplitude due to pitching by the one due to sloshing increases for lower d_B/a, from around 15% for $d_B/a = 10$ to 40% for $d_B/a = 27$. These observations were also made for the perforated baffles (see Appendix D.3).

The solid baffle at the lowest submergence reduces the sloshing wave's amplitude the most efficiently, with a maximum sloshing amplitude as low as $(\zeta^{WP1}/\zeta_A)_{max} = 1.58$, as predicted by our numerical method for the lowest baffle submergence $d_B/a = 0.10$. This represents a 60% reduction compared to the case without any baffle. Similar amplitude reductions at resonance of 30% and 40% are respectively observed for the surge and pitch motions in Fig. 6.12.
Generally, for forced motions, the viscous damping ξ_1 decreases with higher perforation ratio. Here however, the dock is free-floating, and the amplitude of the flow's velocity on the baffle depends on the coupling between sloshing and the body's motions. At the same incident wave frequencies, the dock's motions vary significantly for different perforation ratios due different shift of the natural sloshing frequency $\sigma'_{1,1}$. Thus, the semi-analytical method predicts almost the same reduction of the RAOs' peak amplitudes in Fig. 6.11 for $\tau = 0.15$ as for the solid baffle. For the same submergence d_B/a, the damping ratio at the resonant peak is indeed only decreased by around 5% from $\tau = 0$ to $\tau = 0.15$, but by around 30-40% from $\tau = 0$ to $\tau = 0.30$, as shown in Fig. 6.14. Perforated baffles with low perforations could hence be a good alternative to solid baffle.

Damping is mainly caused by the flow separation occurring near $\theta = 0°$ (or $\theta = \pi$),

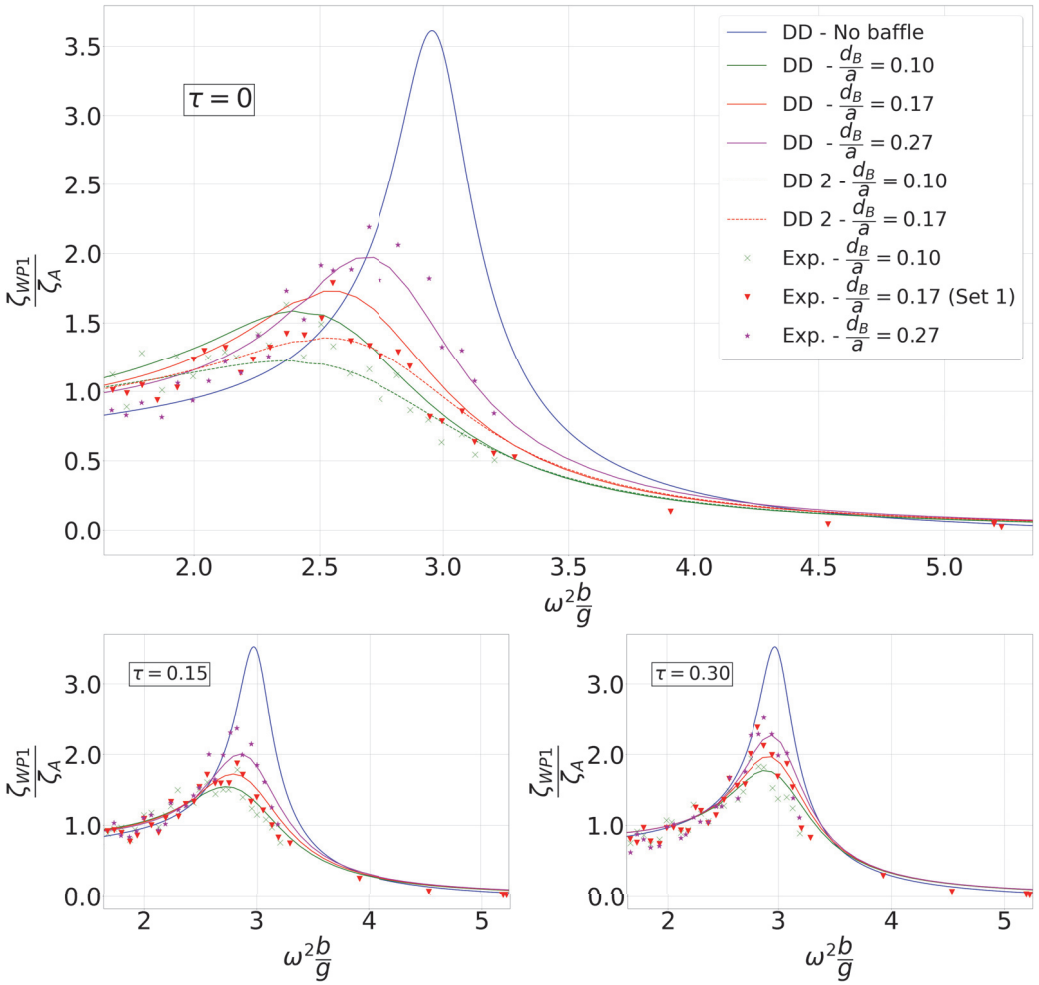

Figure 6.11: *RAOs of ζ_{WP1} for three different submergences d_B/a of the baffle. Top: solid baffle. The dashed lines (DD 2) are obtained for lower, respectively higher, added mass and damping coefficients of the baffle, in order to account for free-surface interaction. Bottom left: $\tau = 0.15$. Bottom right: $\tau = 0.30$. Wave steepness: $\epsilon = 1/60$.*

where the sloshing wave's amplitude is maximum. In Fig. 6.15, we verify that KC numbers estimated from the semi-analytical model at resonance in $\theta = 0°$ range between 0.57 and 0.75 for the three baffles, which is coherent with the assumptions made in Sec. 3.5.2 when using Graham's formulas with the coefficients provided by Mentzoni and Kristiansen (2019) for solid and perforated baffles. For $KC > 0.25$, the flow separation at the sharp edges dominates (Downie et al., 2000) which legitimates the use of these formulas for perforated baffles.
We note that for higher incident wave frequencies, KC numbers sharply decrease in Fig. 6.15. For KC numbers below 0.25, the energy dissipation due to the flow separation through the holes of perforated plates is expected to be non-negligible

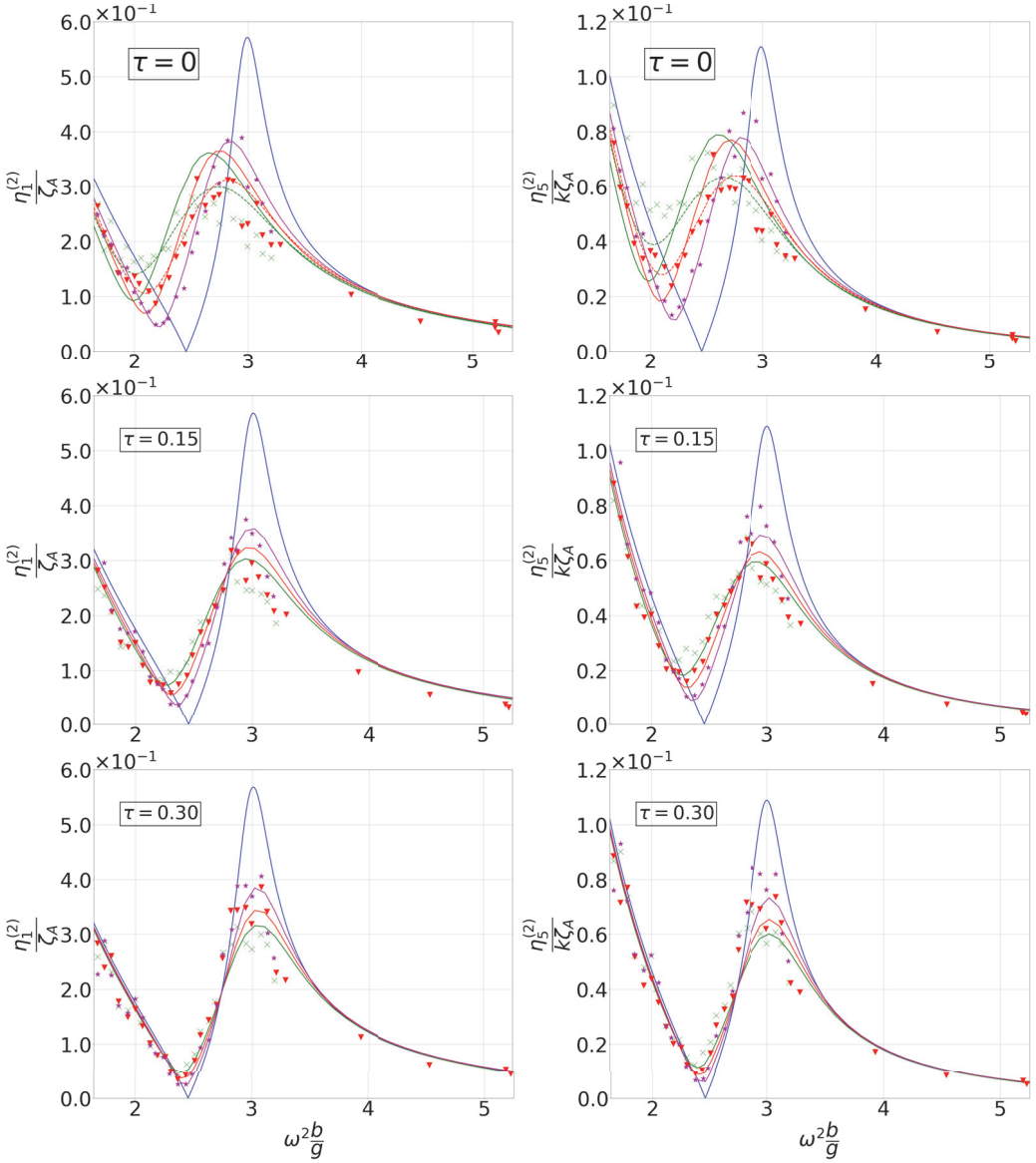

Figure 6.12: *Earth-fixed RAOs of the dock's surge (left) and pitch (right) motions for three different submergences d_B/a of the baffles. Top: solid baffle. Middle: $\tau = 0.15$. Bottom: $\tau = 0.30$. Same legend as Fig 6.11 . Wave steepness: $\epsilon = 1/60$.*

(Song and Faltinsen, 2013). Then, the shape and sharpness of the perforated holes would most likely influence both the damping ratio and the resonant frequency (Abramson, 1966). For instance, Mentzoni and Kristiansen (2020) ran numerical simulations on two-dimensional perforated plates with $\tau = 0.186$ and various holes' sizes. He showed that if the damping coefficients were not significantly affected by the size of the holes, added mass coefficients were much increased for the highest

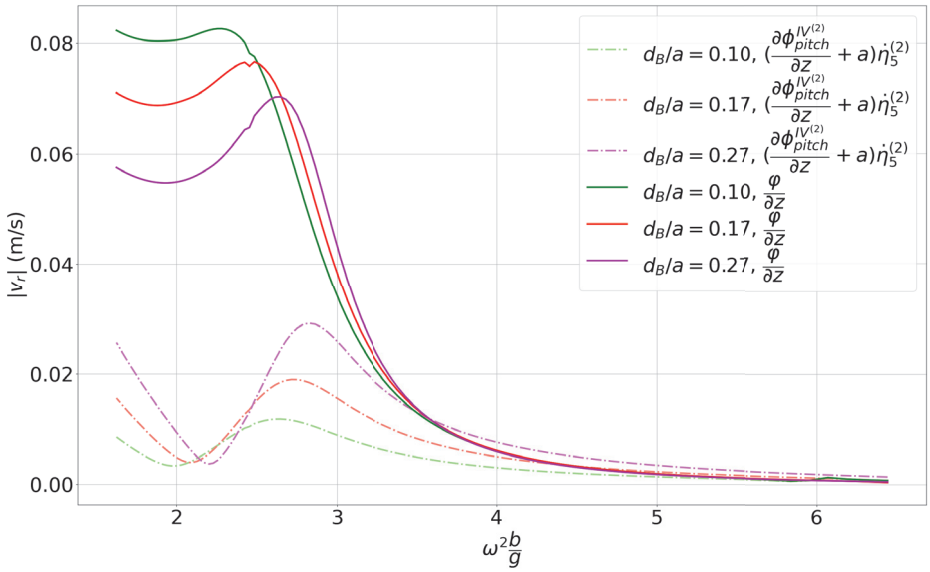

Figure 6.13: *Amplitude of the vertical flow velocity on the baffle in $\theta = 0°$ in a dock-fixed coordinate system. The contributions from the dock's pitching (dash lines) and the sloshing waves (solid lines) to v_r estimated from the DD model for the dock with a solid baffle are here presented separately. $\frac{d_B}{a} = 0.17$. Wave steepness: $\epsilon = 1/60$. Results for perforated baffles are given in Appendix D.3.*

holes' size, and varied more in general for all the holes' sizes for $KC < 0.25$. The dependency of the shifted natural sloshing frequency on both τ or the perforated holes's size at low KC numbers was also reported by Abramson (1966) from experiments with perforated baffles at various submergences d_B in a cylindrical tank. The semi-analytical model developed in Chapter 3 for perforated baffles should therefore be used with caution for $\omega^2 b/g > 3.2$, as we reach the limits of the model's assumptions.

Abramson (1966) pointed out a minimum value of $\sigma'_{1,1}$ for $d_B/a = 0.10$, both for perforated and solid baffles. In addition in his results, when $d_B/a > 0.10$, $\sigma'_{1,1}$ is higher for higher perforation ratios. On the other hand when $d_B/a < 0.10$, $\sigma'_{1,1}$ is lower for higher perforation ratios due to free-surface interactions. From our semi-analytical simulations, the shifted natural frequencies shown in Fig. 6.17 were generally higher for higher perforation ratios, which is coherent with Abramson's results for $d_B/a \geq 0.10$. It could also be predicted by Eq. (3.84) in Sec. 3.4 as $\sigma'_{1,1}$ should convergence to $\sigma_{1,1}$ from below when τ goes to 1, as the added mass of the perforated baffle then converges to 0. From Fig. 6.17, we observe that $\sigma'_{1,1}$ varies up to 10% from $\sigma_{1,1}$ for the solid baffle.
For lower $\sigma'_{1,1}$, the resonant peak for which the motions are maximal also occurred at lower frequencies. We verify in Fig. 6.17 that $\sigma'_{1,1}$ is closer to $\sigma_{1,1}$ for higher

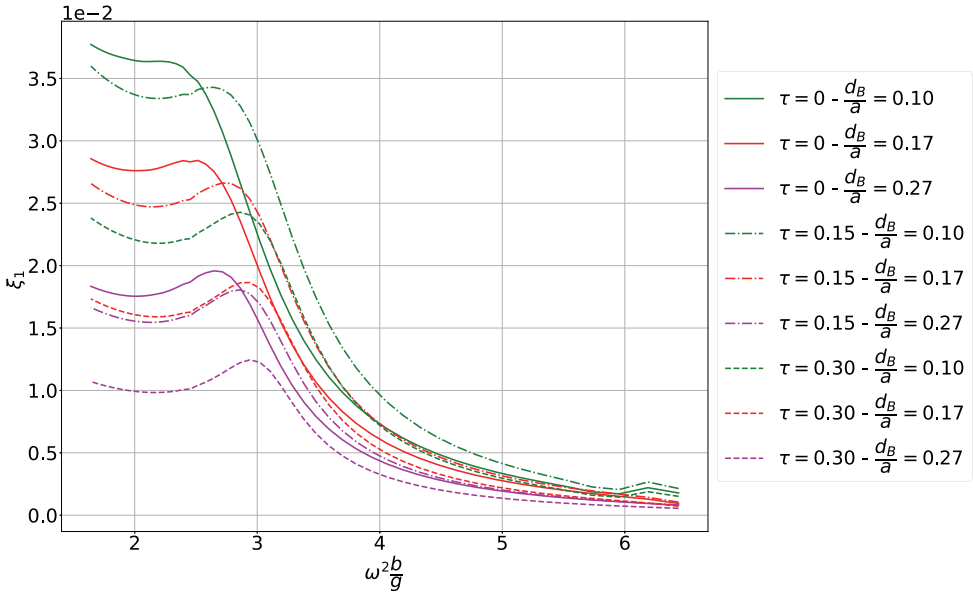

Figure 6.14: *Linear equivalent damping ratio due to the solid and perforated baffles as a function of the frequency of the incident wave as computed by the DD method involving Morison drag model with KC-dependent drag coefficient and strip theory and integration along the azimuthal direction (cf. Eq.* (3.101)*). Wave steepness:* $\epsilon = 1/60$.

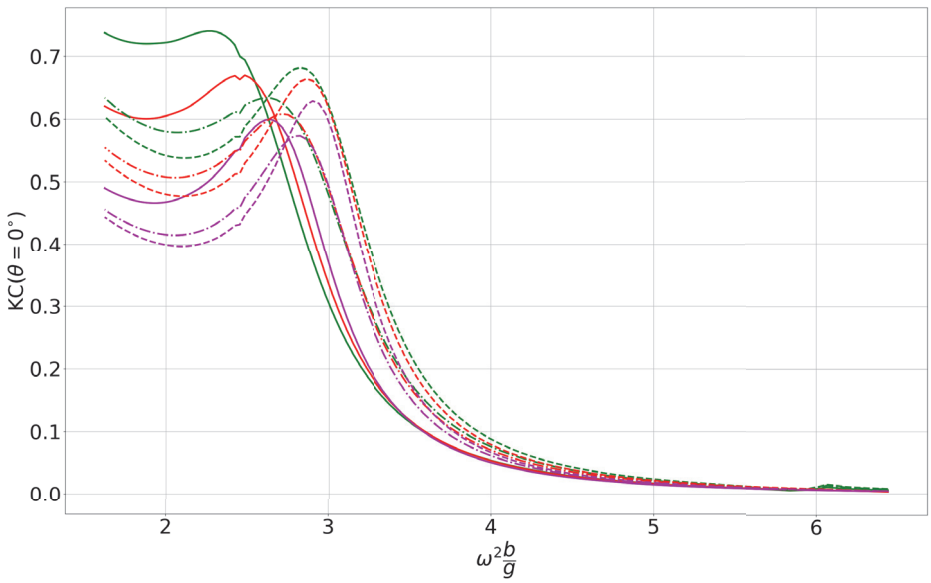

Figure 6.15: *KC numbers on the baffle at* $\theta = 0°$ *for solid and perforated baffles at different incident wave frequencies. Wave steepness:* $\epsilon = 1/60$. *Same legend as in Fig. 6.14.*

d_B/a, as the influence of the baffle on the first sloshing eigenmode decreases. While the dock's motions are nearly zeros at $\sigma_{1,1}$ for the case without baffle, the motions observed at $\sigma'_{1,1}$ in Fig. 6.12 for the cases with a baffle reach a local minimum, which is not zero anymore. Indeed, because of viscous damping, the added mass is significantly reduced at $\sigma'_{1,1}$ when there is a baffle (cf. Fig 5.1 in Sec. 5.1.2).
This damping also has consequences on the phases of the dock's motions presented in 6.16, which become gradually in phases with ζ_{WP1} around $\sigma'_{1,1}$ while a sudden shift is observed for the case without baffle. Some of the measured signals in Fig. 6.16 show unexpected phases, which could not be explained by physical phenomena that would have been visible from the videos. However, in general the main trends remain clearly distinguishable, and tend to be consistent with the semi-analytical approach.
The viscous effects used in the semi-analytical model (cf. Sec. 3.5.2) have significant effects on the motions' amplitude, but generally small effects on the natural sloshing frequencies. It is for instance observed in Fig. 6.18, where experimental and semi-analytical RAOs of ζ_{WP1} and $\eta_1^{(2)}$ for the case with solid baffle are compared with results from WAMIT simulations, for which the baffle had been meshed. Simulations in WAMIT do no account for any viscous effects. The shifted natural sloshing frequency $\sigma'_{1,1}$ in WAMIT ranges from 0 to 5% lower than the one estimated with the DD model. This results show in particular that $\sigma'_{1,1}$ has a low dependency on the KC number in our model (see more details in Appendix D.4).

The semi-analytical results in Figs. 6.11 and 6.12 are in overall in good agreement with the experimental results for the highest submergence $d_B/a = 0.27$. However, the damping at lower submergence is under-predicated for the solid baffle, resulting in higher predicted responses than found in the model tests. This means in particular that our model is conservative. Local non-linear behaviour of the free-surface flow was observed from videos of the experiments for $d_B/a = 0.10$, which could also explain somewhat more scatter in the experimental RAOs for the two lower submergences, and especially the wide span of results obtained for the two repetition tests with a solid baffle (cf. Fig 6.19). The increase of the damping coefficient for flat plates at low submergence is a known phenomenon that has been pointed out in several studies. For instance, Song and Faltinsen (2013) performed experiments on solid and perforated rectangular plates under forced heave motions, and built an analytical model similar to Molin et al. (2007) that includes a pressure drop coefficient through the plate, as a function of both the square velocity and a discharged damping coefficient which depends on the perforation ratio. In their work, they consider $\tau = 0.079$ and $\tau = 0.159$ for plates at the mean submergences 0.10m and 0.70m below the free surface. They emphasise the importance of non-linear free-surface effects when the ratio of the heaving amplitude to the mean submergence becomes close to one. As Molin et al. (2007), they point out that the coefficient α_2 from Graham's formula depends on the heaving amplitude and frequency as the plate is near to the free-surface, which we

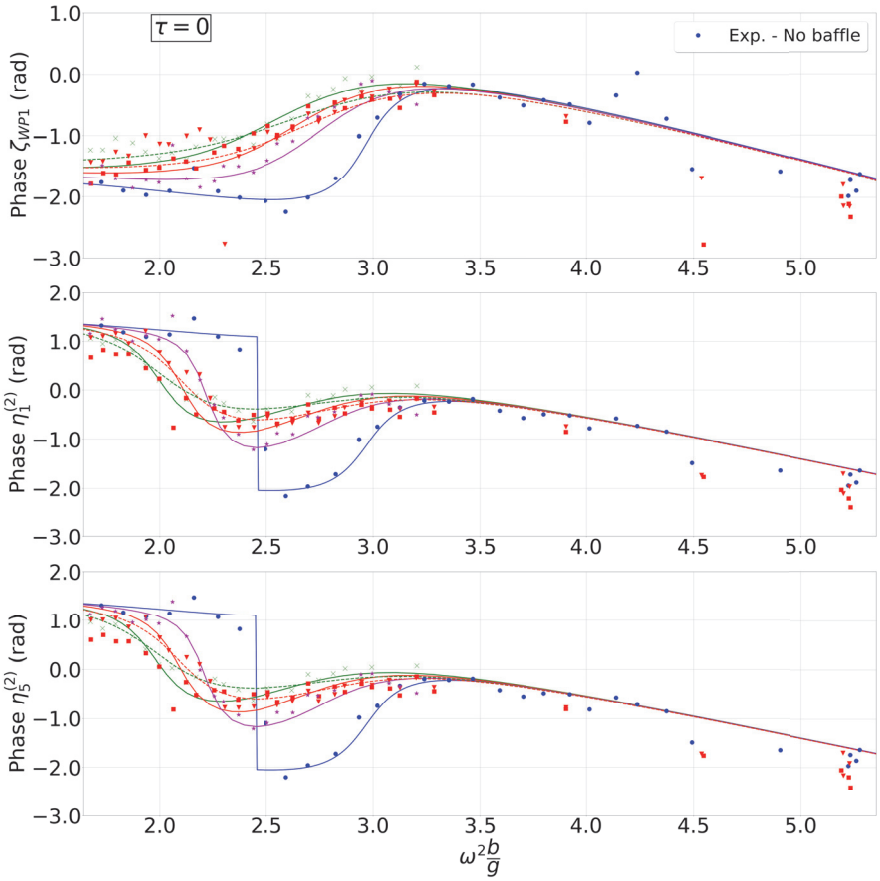

Figure 6.16: *Phases of WP1 (top), surge (middle) and pitch (bottom) relative to the incident wave at the origin of the Earth-fixed coordinate system for the dock with a solid baffle and for three different submergences d_B/a of the baffles. Same legend as Fig 6.11, with the addition of experimental results for the dock alone (2019, Set 1). Wave steepness:* $\epsilon = 1/60$.

do not include in our model.
Nevertheless, in order to account for the free-surface interaction near sloshing resonance in our semi-analytical model, the α_i coefficients in Eqs. (3.98) and (3.99) in Sec. 3.5.2 are tuned to match the experimental results. Examples are provided in Figs. 6.11 and 6.12 for the solid baffle, represented by the dashed curves denoted DD2 in the legend. The coefficients from Table 3.2 are here replaced (dash lines) by $\alpha_1 = 0.21$ and $\alpha_2 = 18.18$ for $d_B/a = 0.10$, and $\alpha_1 = 0.19$ and $\alpha_2 = 19.70$ for $d_B/a = 0.17$. This means that the drag coefficient is almost doubled. The results indicate that improvements can be made to our model.

The shifted natural frequency $\sigma'_{1,1}$ corresponds in Fig. 6.12 to the minima of the motions near $\omega^2 b/g = 2$, similar to that $\sigma_{1,1}$ corresponds to the cancellation period

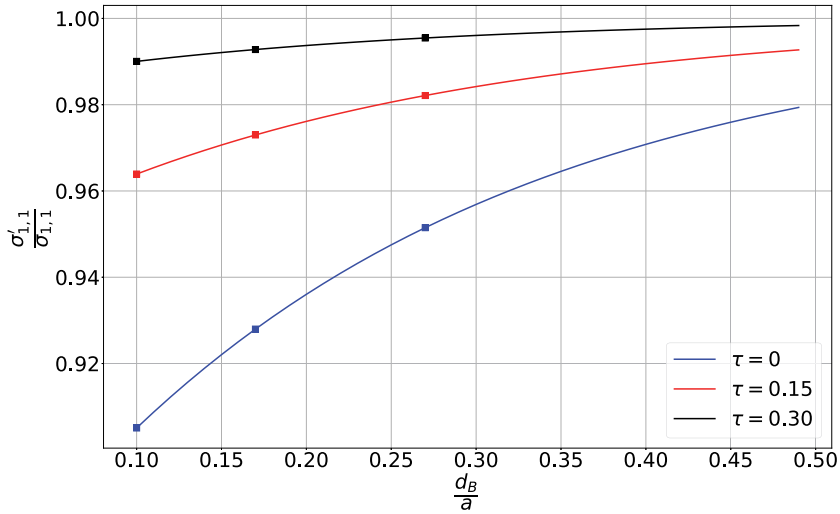

Figure 6.17: *Effect of baffles on the lowest natural sloshing frequency $\sigma'_{1,1}$, for solid ($\tau = 0$) and perforated baffles ($\tau = 0.15$ and $\tau = 0.30$) at different submergences d_B/a. The equations of motions are solved for incident waves of period $\omega = \sigma_{1,1}$ and wave steepness $\epsilon = 1/60$. The three submergences tested experimentally are indicated by square points. Baffles' width: $a_B/a = 0.17$.*

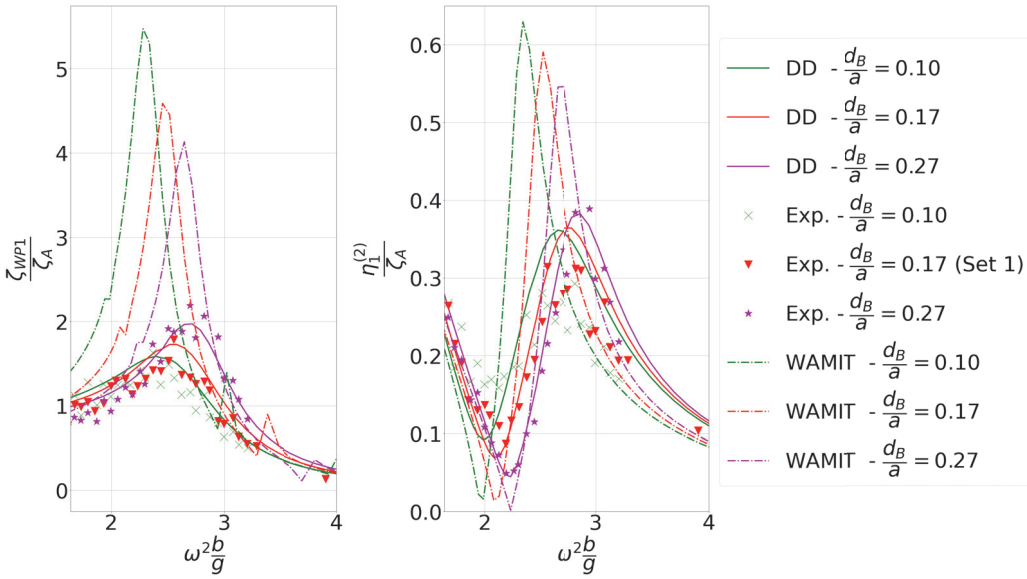

Figure 6.18: *Comparison between results from WAMIT, the semi-analytical model, and experiments for the dock with a solid baffle. Left: ζ_{WP1}, right: $\eta_1^{(2)}$. Wave steepness: $\epsilon = 1/60$.*

$\omega^2 b/g = 2.45$ when there is no baffle. In this figure, we see that the discrepancy

between the experimental and semi-analytical natural frequency $\sigma'_{1,1}$ increases for lower d_B/a, especially for the solid baffle. This was expected from the potential flow analysis made in Sec. 3.4, only valid for $d_B/a_B \geq 1$. The case $d_B/a = 0.17$ corresponds to the limiting case $d_B/a_B = 1$ for which the formula (3.84) presented in that section should be used. This point is also discussed by Faltinsen and Timokha (2009) who compare the frequencies obtained from the same formula (3.84) to experimental natural frequencies obtained by Mikishev and Churilov (1977) for a solid annular baffle in a closed-bottom cylindrical tank for various values of d_B/a. In one of their comparison, the cylinder height-to-radius ratio is $d/a = 1.7$ and the baffle width-to radius ratio either $a_B/a = 0.2$, close to our values ($a_B/a = 0.17$), and with a good agreement between analytical and experimental frequencies as long as $d_B/a < 0.2$, which is coherent with our results.
It must be emphasised that the baffles always remained submerged in this range of incident wave frequencies during the experiments, even for $d_B/a = 0.10$. According to the amplitude of the dock's heaving and piston mode resonance discussed in Sec. 6.1.4 near $\omega^2 b/g = 0.4$, in-and-out water motions on the baffles are likely to occur for lower incident wave frequencies and for the three submergences d_B/a that were tested, which might cause extreme loads on the baffles.

Because of the non-linear viscous effects, our semi-analytical model with a baffle is strongly dependent on the wave steepness. A comparison between experimental and semi-analytical RAOs are presented in Fig. 6.19 for the solid baffle and two wave steepnesses $\epsilon = 1/60$ and $\epsilon = 1/45$. These results include a repetition test for $\epsilon = 1/60$, and numerical RAOs for two additional steepnesses $\epsilon = 1/30$ and $\epsilon = 1/100$. As expected, ζ_{WP1}'s RAOs estimated from the DD model are lower for higher wave steepnesses, as the damping generally increases for higher flow velocities. Experimental results for the two wave steepnesses are difficult to distinguish, which might be due to that the random error is high for the solid baffle at $d_B/a = 0.17$ (cf. Sec. 4.5.1).

The iterative scheme set up in Sec. 5.1 to deal with the non-linear effects of the baffles converged relatively quickly, with a number of iterations always inferior to 20 (cf. Appendix D.4). The loads on the annular baffle estimated by Morison's formula (5.7) were not negligible. Near resonance, the total moment in pitch F_5^M on the baffle was for instance about 10% of the scattered moment F_5^S on the entire dock (cf. Sec. 2.4). More details are given in Appendix D.4. For the solid baffles, these loads were generally viscous dominated for $\omega^2 b/g < 2$, and inertia dominated for $\omega^2 b/g > 3$ in our simulations. As expected, F_5^M was lower for the perforated baffles, and the relative contribution of the inertial forces compared to damping forces generally decreased with higher perforation ratios.
The baffles that we consider in this work are thin, cantilevered from the dock with a 5m width in full scale. Further structural analysis might therefore be needed to predict the effects of these high hydrodynamic loads on the baffles.

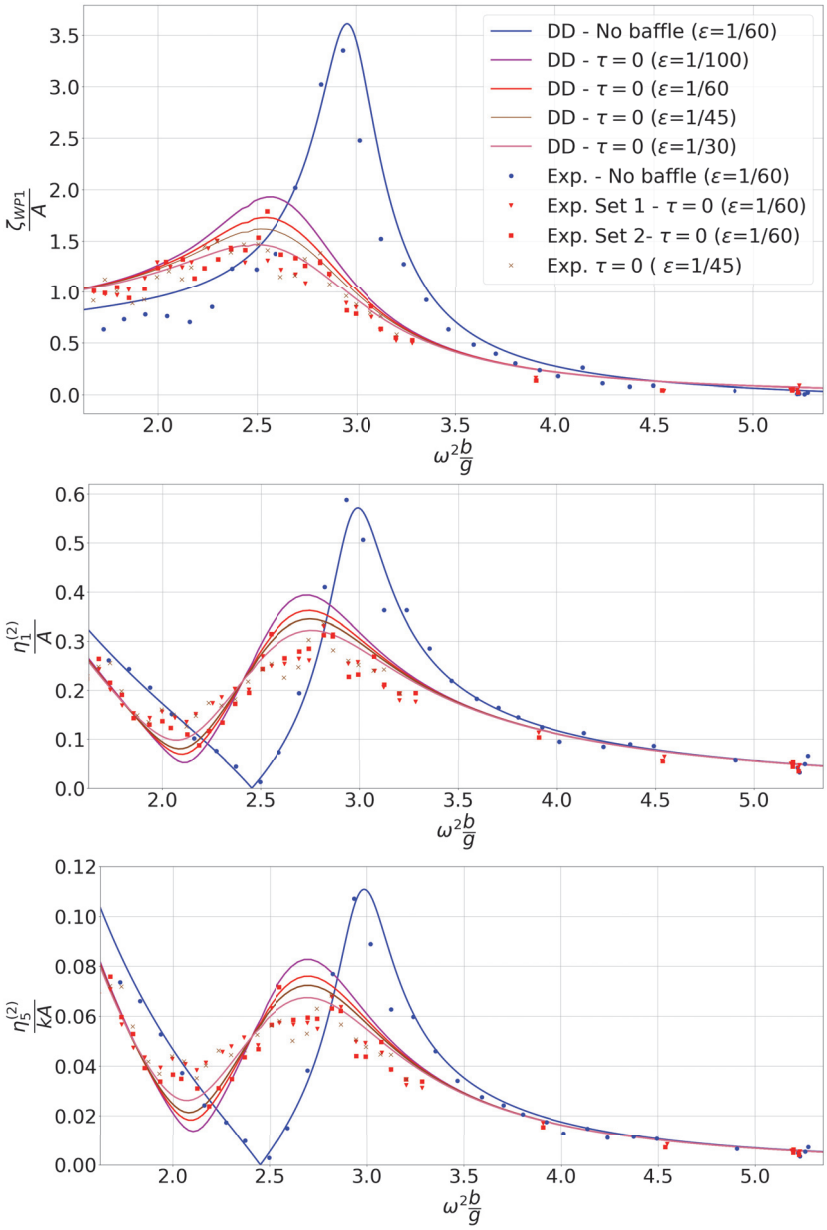

Figure 6.19: *Experimental and semi-analytical RAOs for the dock alone (2019, Set 1) or with a solid baffle fixed at* $d_B/a = 0.17$*, for three different incident wave steepnesses.*

6.2.2 Polystyrene foam balls

Experimental results with foam balls were in general found to be very close to the case without damping devices (cf. Fig. 6.20). Only the highest volume of foam balls (3.6L) shows a clear damping of the resonant peak, comparable to the

performance of perforated baffles. This would represent a 1.20m high layer of balls with a diameter of 0.10m each, which is most likely unrealistic to set up in practice. During the tests, the foam balls were very sticky. Scale effects caused by the friction between balls and with the free surface are expected to matter, which is not investigated here.

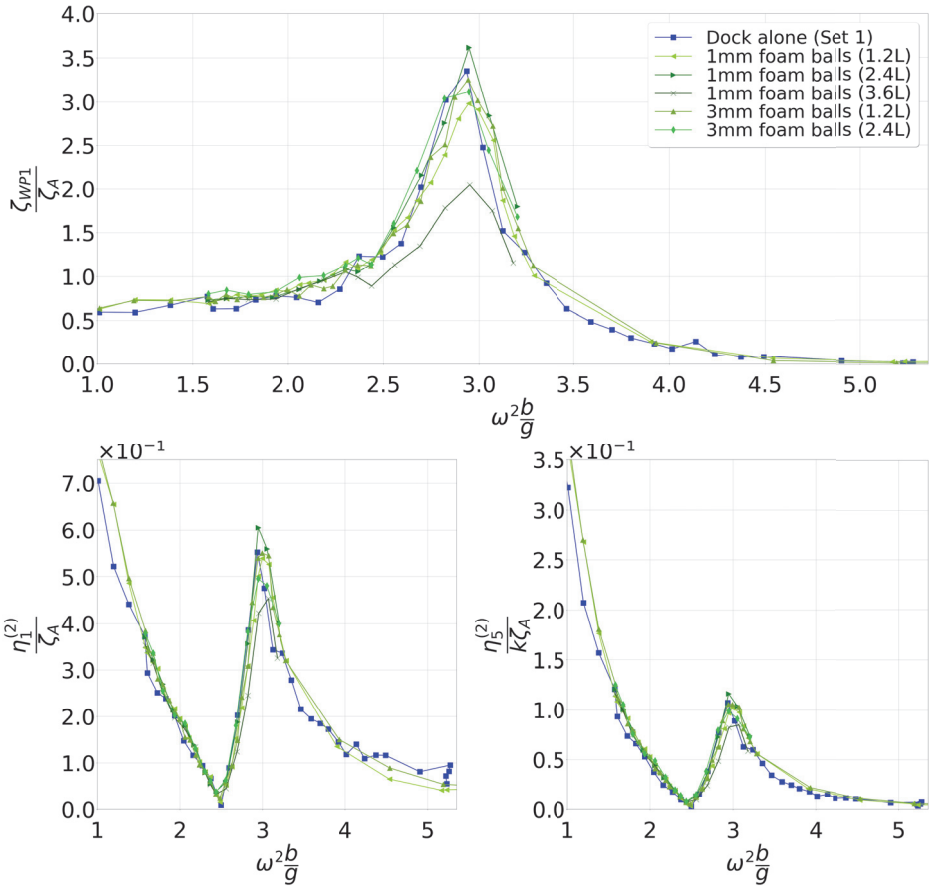

Figure 6.20: *Experimental RAOs of $\eta_1^{(2)}$, $\eta_5^{(2)}$ and ζ_{WP1} for various sizes and quantities of polystyrene foam balls. Tests from 2019. Wave steepness: $\epsilon = 1/60$.*

6.3 Dock with spar

RAOs in regular waves for the dock with a FOWT's spar are presented in Fig. 6.21 for the dock's motions and ζ_{WP1} and in Fig. 6.22 for the spar's motions. For the case without baffle (blue curves and markers), semi-analytical results are fairly consistent with the experimental ones. As expected, the motions of the dock have similar amplitudes as for the case without spar. The cancellation frequency, for which $\zeta_1^{(2)}$ and $\zeta_5^{(2)}$ are almost null and their phases shift to 180° (cf. Fig.

6.23), occurs near to the sloshing natural frequency of the dock without spar $\sigma_{1,1}^2 b/g = 2.45$, and not the sloshing natural frequency of the dock+spar system $\sigma_{1,1}^2 b/g = 2.2$. This is an indication that the spar "follows" the sloshing wave. The highest discrepancies are observed for the surge and pitch motions of the dock, and might be caused by inaccuracies when modeling the inertial and stiffness matrices of the dock for the semi-analytical model.
Furthermore, a resonant peak is observed for $\eta_3^{(1)}$ in Fig. 6.22, even though $\eta_3^{(1)}$ is not linearly coupled with the first sloshing mode. That is if the spar is exactly in the center of the dock, but few asymmetries in the experimental placement, and in the mooring system between the spar and the dock might explains this resonance in heave. Still, $\eta_3^{(1)}/\zeta_A$ remains very low, around 15 times lower than $\eta_1^{(1)}/\zeta_A$ for the same frequencies. In particular, the heave motion's amplitude $|\bar{\eta}_3^{(1)}|$ always remains below 0.1m in full scale, which is a typical strict requirement imposed for the installation of the FOWT's blades on the rotor.

Figs. 6.21 and 6.22 include results with damping devices for the dock+spar system. Both numerical and experimental results are presented for either a solid ($\tau = 0$) or a perforated ($\tau = 0.3$) baffles. Numerical results for a perforated baffle with $\tau = 0.15$, and experimental results for the lowest quantity of 3mm foam balls are also given. The baffles, both solid and perforated, have a major influence on the responses. The reduction of the peak amplitude when comparing with the case without baffle is particularly important for the spar motions and free-surface elevation. With a solid baffle this reduction is around 54% for $\eta_1^{(1)}/\zeta_A$, 45% for $\eta_1^{(5)}/\zeta_A$ and 68% for ζ_{WP1}/ζ_A (from experimental RAOs). The frequency for which the maximum peak amplitudes are reached is different for the dock, and spar's motions, around 10% lower for the latter. The analytical results succeed to catch the shift of the natural sloshing frequency due to the baffles, and compare relatively well with the spar's experimental motions. However, the motions of the dock are under-predicted and the resonant peak frequency is about 6% higher than the experimental one. These discrepancies were not as high for the dock without spar in Sec. 6.2.1. As discussed in Sec. 3.4, the shape of the first sloshing mode $\varphi_{1,1}$ in the internal domain does not account for the baffle in our model. This internal domain is narrower for the case with spar than without the spar, even thought the width of the baffle remain the same. Thus, the error brought by this assumptions when calculating the loads on the dock (cf. Chapter 5) is expected to be higher for the case with the spar than without the spar. In addition, non-linear free-surface interaction associated with the baffle are also expected.
Baffle with a perforation ratio $\tau = 0.3$ are not as efficient in damping the sloshing waves, with 51% reduction of ζ_{WP1}/ζ_A's peak amplitude. However, they show similar performances to the solid baffle when it comes to reduce the spar's motions' peak amplitude: 50% for $\eta_1^{(1)}/\zeta_A$, 46% for $\eta_5^{(1)}/\zeta_A$. RAOs with foam balls are similar to the case without spar: the resonant and cancellation frequencies are

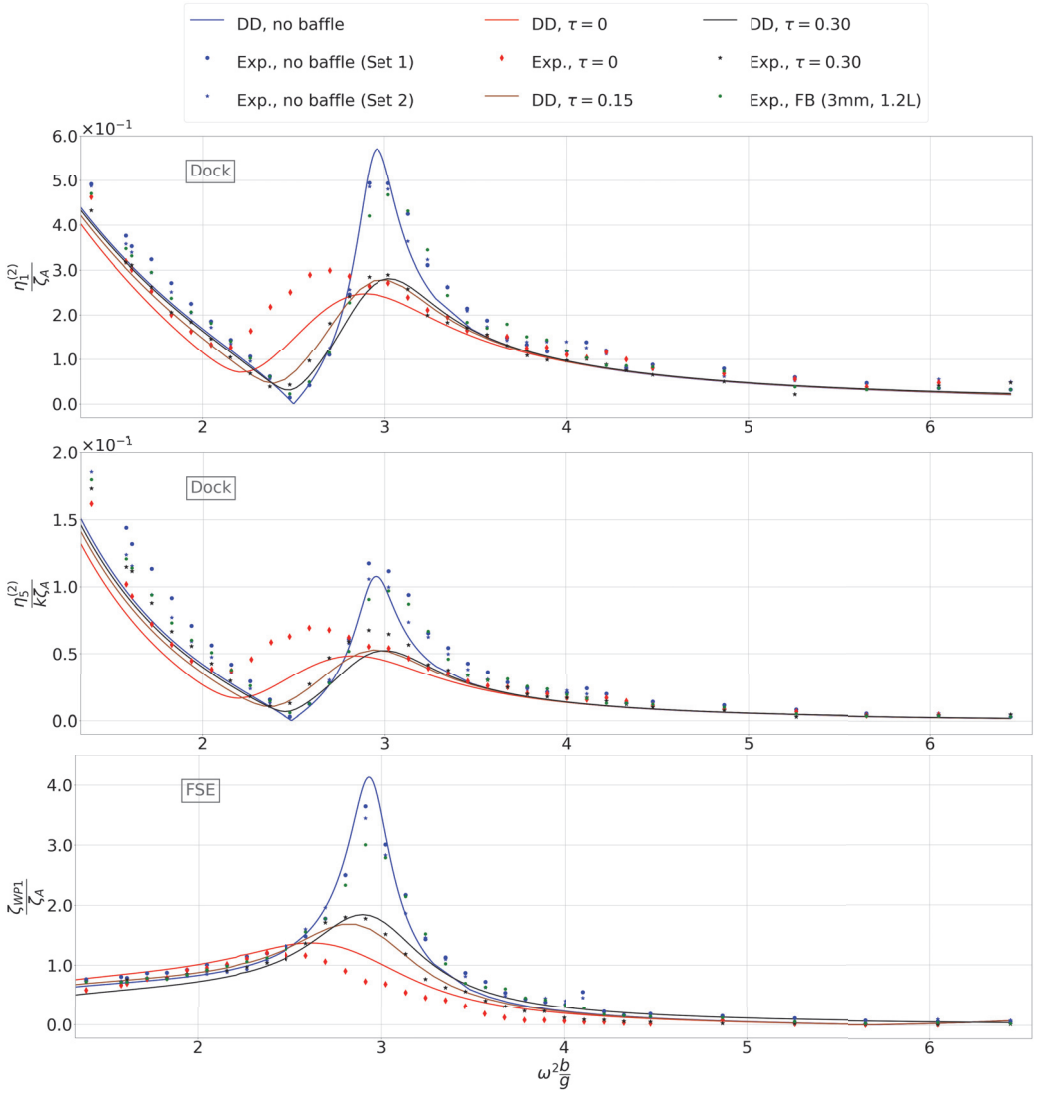

Figure 6.21: *RAOs of $\eta_1^{(2)}$, $\eta_5^{(2)}$ and ζ_{WP1} for the dock+spar system. Experimental and analytical results are compared for cases without baffle (sets 1 and 2 from 2019), with a solid annular baffle ($\tau = 0$) and perforated baffle ($\tau = 0.30$). The baffle width $a_b/a = 0.17$ and their submergence $d_B/a = 0.17$. Numerical results for the perforated baffle with $\tau = 0.15$ and experimental results with polystyrene foam balls (3mm, 1.2L) are also indicated. More details about the numerical simulations with solid baffle are presented in Appendix D.4. Wave steepness: $\epsilon = 1/60$.*

identical to the case without damping devices, and low amplitude reductions are observed in comparison to the baffles.

Because the tower, nacelle and blades will be installed from the top of the dock,

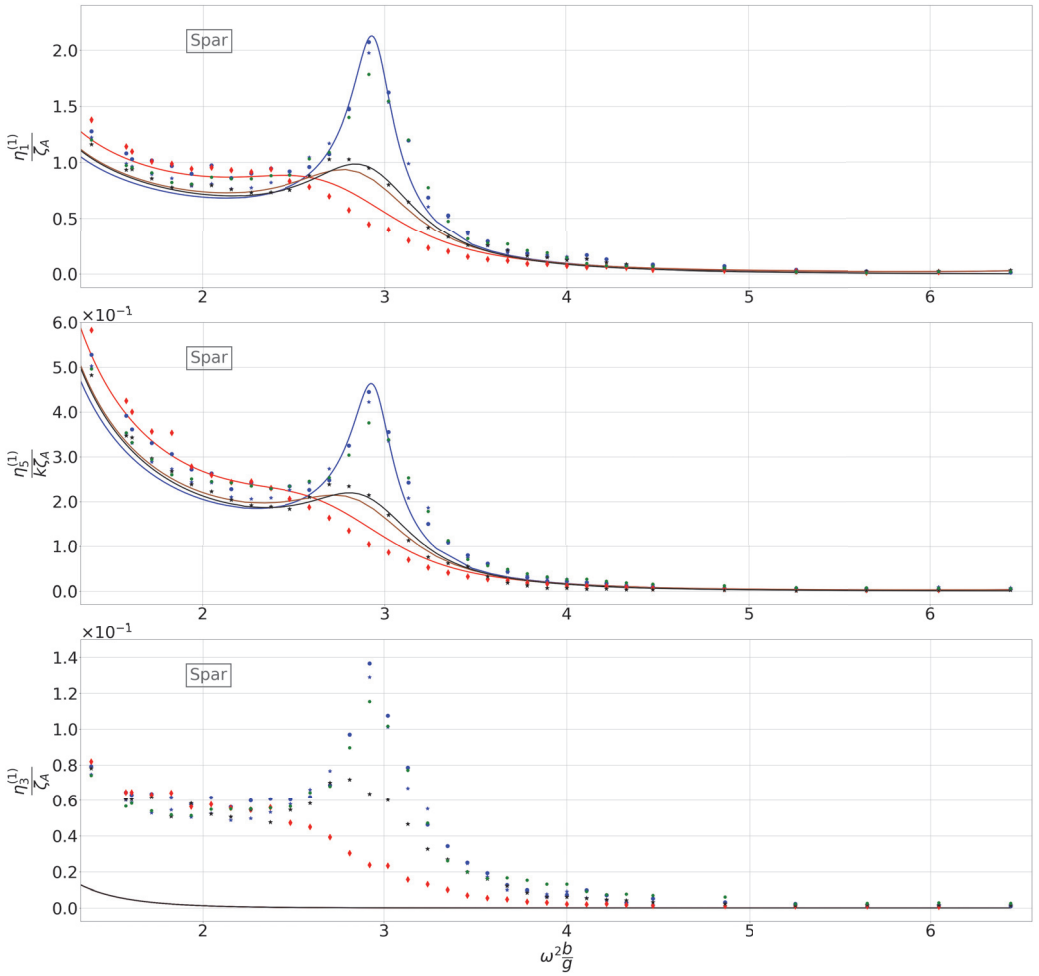

Figure 6.22: *RAOs of the spar's motions $\eta_1^{(1)}$, $\eta_5^{(1)}$ and $\eta_3^{(1)}$ for the same cases as in Fig. 6.21. The spar's motions are given in an Earth-fixed coordinate system.*

the relative motions between the dock and the spar matter. If the dock's heave motions are negligible, it is not true for its surge and pitch motions. Both $\eta_1^{(2)}$ and $\eta_5^{(2)}$ are in phase with the spar's motions for $\omega^2 b/g \leq 2.5$, and in opposition of phases with the spar's motions for $\omega^2 b/g > 2.5$ (cf. Fig. 6.23). In particular, this means that the spar's pitching in a dock-fixed coordinate system (DCS) is higher than in the Earth-fixed coordinate system (ECS) at the sloshing resonant peak (see more details in Appendix D.4), and up to 1.7° as estimated from the DD model for the case without damping devices. With the solid baffle, the spar's maximum pitching in the DCS is reduced to 0.75°. This high reduction is promising, even though these results only stand for the FOWT's spar without the tower. The study of the different stages of the FOWT's assembly are let for further works.

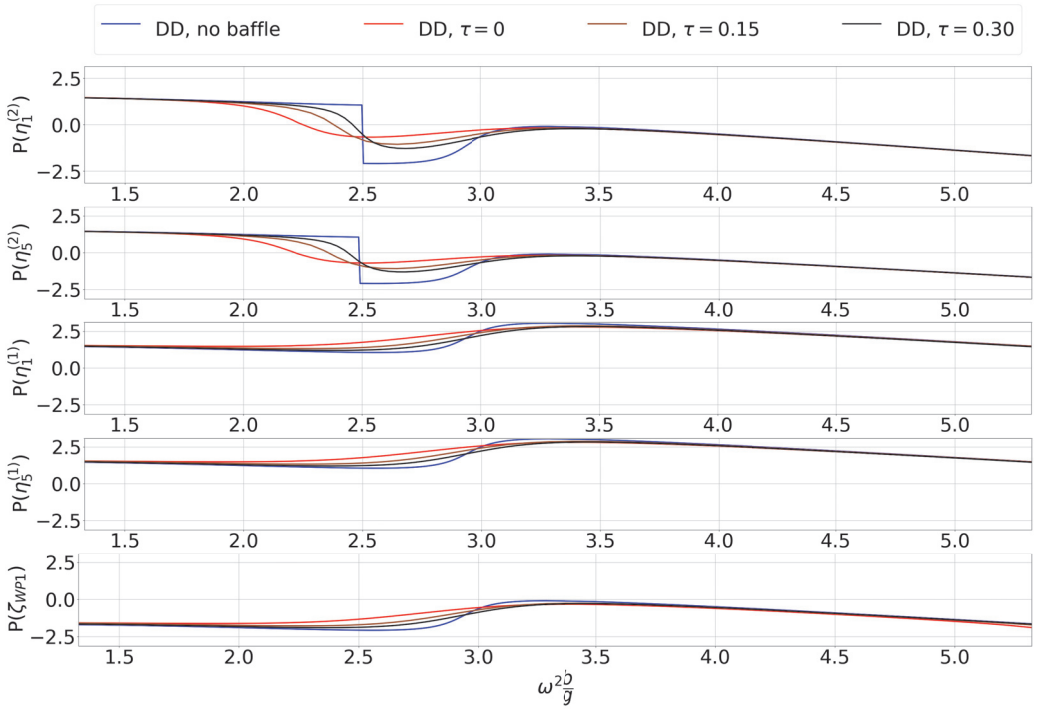

Figure 6.23: *Phases of the dock's and spar's motions in surge an pitch, as well as of* ζ_{WP1} *estimated from the semi-analytical model for the cases with solid and perforated baffles. Wave steepness:* $\epsilon = 1/60$.

7 | Results in irregular waves

Experimental motions of the bodies in an Earth-fixed coordinate system are presented in this chapter for incident irregular waves described by the JONSWAP spectra defined in Sec. 4.3.2. First, for the case without spar in Sec. 7.1, and then with spar in Sec. 7.2. The power spectral density and RAOs of the motions are discussed and compared with semi-analytical results, which are identical to the ones in regular waves for the cases without baffle.

7.1 Dock without spar

Non-dimensional experimental power spectra of the dock's motions and of ζ_{WP1} are presented in Fig. 7.1 for incident wave spectra with a peak frequency $\omega_p^2 b/g = 2.52$, i.e. near the first sloshing natural frequency. Most of the energy of the dock's motions is gathered near the frequency $\omega^2 b/g = 3$, corresponding to the resonant peak observed in regular waves. As expected, the spectra of the motions when there is a solid baffle installed inside the dock (red curves) are shifted to lower frequencies. For the lowest significant wave height $H_s/b = 1/40$, the spectra for the case with baffle contain more energy than for the cases without damping devices (blue curves). This is due to that the resonant frequency of the motions with the baffle becomes closer to the peak frequency $\omega_p^2 b/g$, where there is more energy from incident waves. The free-surface elevation inside the dock from time series were indeed generally higher for the case with baffle for this specific sea-state (cf. Fig. 7.2). It is not the case for the tests with foam balls, for which the resonant frequency is much closer to the one of the tests without damping devices. For the higher significant wave height $H_s/b = 3/40$, the energies for the case with baffle is significantly reduced due to viscous dissipation. We note that the peak observed around $\omega^2 b/g = 0.3$ is close to the natural frequency in pitch estimated in Sec. 5.4. Similar power spectra are presented in Fig. 7.3 for the lower peak frequency $\omega_p^2 b/g = 1.12$, further from sloshing resonance. We then do not observe shift of the power spectras betwen the case with and without baffle at the peak frequency. The energy of sloshing waves is mostly dissipated near $\sigma_{1,1}$. We note that for the cases without baffle, the highest peak of ζ_{WP1}'s energy is still observed at the resonant sloshing frequency $\omega^2 b/g = 3$, even though the energy from the dock's motions is more than ten times lower than at the peak frequency $\omega_p^2 b/g$.

When considering annular baffles in the semi-analytical model, the viscous effects introduce non-linearities in the equations of motion. For regular waves, the equations of motion have been solved in the frequency domain for each incident wave frequency, associated to a given wave amplitude. The equations were linearised with respect to time by equalising the energy dissipated over one period of oscillation.

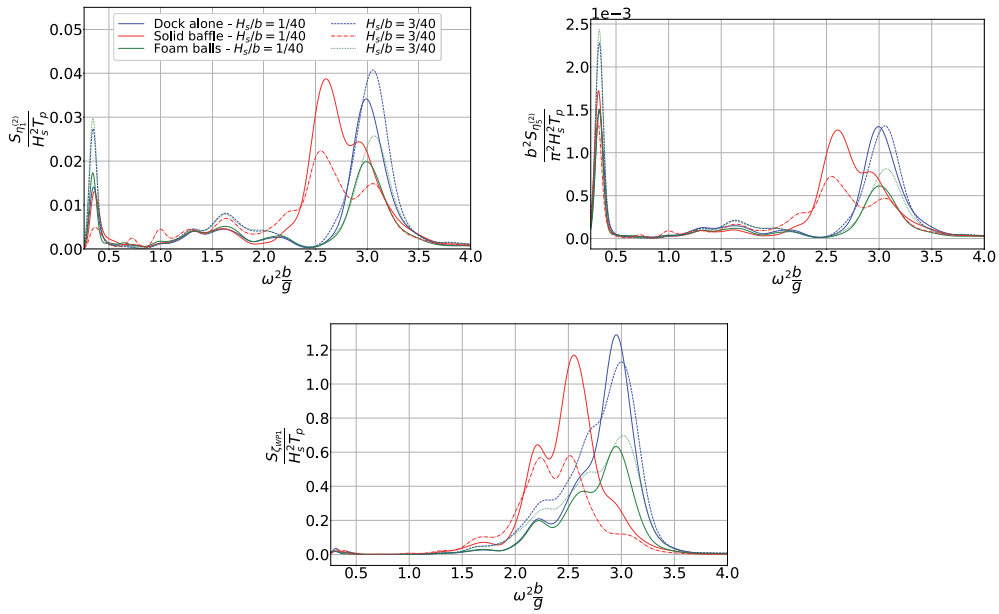

Figure 7.1: *Normalised spectra of the dock's responses in surge (upper left), pitch (upper right), as well as of ζ_{WP1} (bottom) from the 2019 model tests without the spar with a peak frequency of incident waves: $\omega_p^2 b/g = 2.52$. $\sigma_G = 0.0208$. The foam balls are here 3mm large (1.2L). More spectra for the case without spar are given in Appendix C.6.*

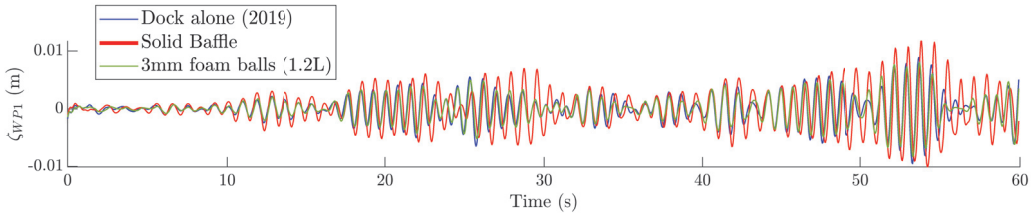

Figure 7.2: *Time history of the free-surface elevation ζ_{WP1} inside the dock without spar in irregular waves for three cases, without damping devices, with foam balls (3mm, 1.2L), and with solid baffle. H_s/b=1/40, $\omega_p^2 b/g = 2.52$.*

However, the equations remain non-linear with respect to the wave amplitude ζ_A of incident waves. A special care should be taken when solving these non-linear equations in frequency domain for irregular waves, as it is unknown which incident wave amplitude should be considered in that case.
First, the viscous part of the moment F_5^M on the baffle is statistically linearised (Borgman, 1967; Roberts and Spanos, 1990; Da Silva et al., 2020) applying the method of least square to statistical expected values. Through this approach, the instantaneous free-surface elevation are represented by a Gaussian distribution with zero mean. Assuming that the system is linear, both the relative velocity

v_r on the baffle and the dock's motions also have a Gaussian probability density function with zero mean, entirely defined by their standard deviations. An iterative scheme is then implemented over the whole range of frequencies of the waves' spectrum to determine these standard deviations.
On the other hand, the damping ratio ξ_1 and the shifted natural sloshing frequency $\sigma'_{1,1}$, both estimated only for wave frequencies close to the sloshing resonance, have been evaluated from the highest individual wave amplitude measured from the experimental time series of the free-surface elevation and are considered constant over the whole range of frequencies that have been simulated. This assumption is quite approximate for ξ_1, which is strongly dependent on the incident wave amplitude, but is expected to provide a relatively safe estimation of $\sigma'_{1,1}$, which was shown to vary less than 1% over the spectra in regular waves. The highest amplitude (crest to crest) of measured individual waves were typically about twice the significant wave height.
An alternative way to deal with irregular wave is to solve the equations of motion in time domain. This approach is much more time consuming, but has the advantage of including the transient part of the signals, and not only the permanent part as in frequency domain. A time domain solver was developed for a simplified representation of the dock and focusing on surge motions. RAOs from the time domain solver were found to be lower than the ones from the frequency domain solver, most likely because of the long transient state that characterizes responses with no or very low damping. The lower the damping, the higher is the difference between the time domain and frequency domain responses. A complete description of the time domain model and results are given in Appendix D.5.

Experimental and numerical RAOs of $\eta_1^{(2)}$, $\eta_5^{(2)}$ and ζ_{WP1} in irregular waves are presented in Fig. 7.4 for $\omega_p^2 b/g = 2.52$ and two values of H_s/b. Without damping devices, the semi-analytical curves are identical as in regular waves. The experimental RAOs are lower than the semi-analytical ones at the resonant peak, most likely because of the transient state of the responses, not caught by the frequency domain solver. Slightly lower RAOs in surge and for $H_s/b = 1/40$ compared to $H_s/b = 3/40$ for the case without baffle might thus be explained by that lower waves introduce less viscous quadratic damping in surge, resulting in a longer transient state.
Semi-analytical results with baffles in Fig. 7.4 catch the shift of the resonant period but tend to under-damp the responses. These observations are coherent with results in regular waves, where similar conclusions were drawn when the baffle was close to the free surface, suggesting possible non-linear interactions with the free surface. It should be emphasised that the reduction in responses with baffles depends both on the damping, which is higher for higher H_s/b, but also on the different amount of energy available at the sloshing resonance from the waves due to the shift of the natural frequency. In the present case, the baffle shifts the sloshing resonance closer to the peak frequency of the incident waves' spectrum at

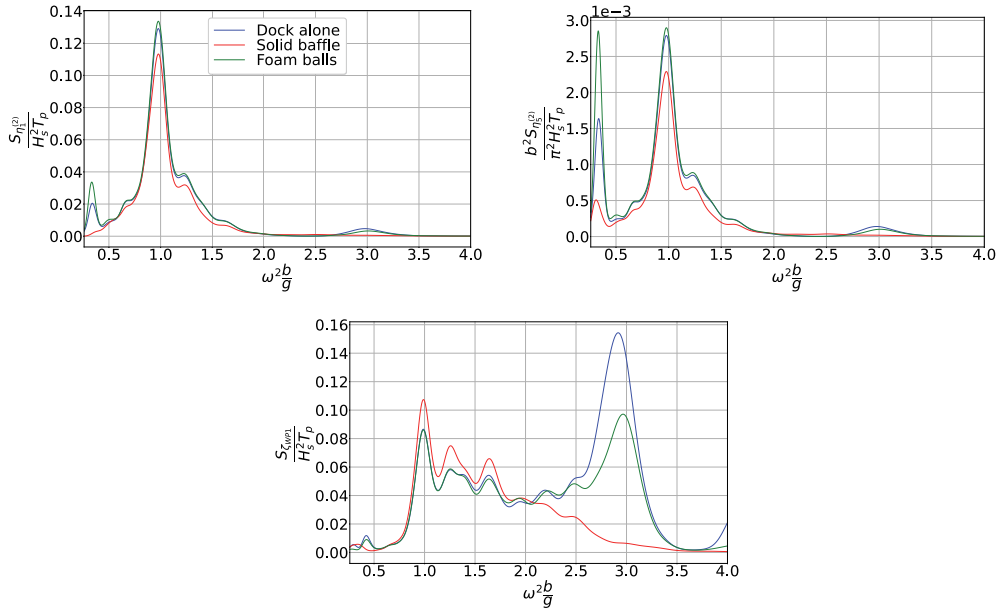

Figure 7.3: *Normalised spectra of the dock's responses in surge (upper left), pitch (upper right), as well as of ζ_{WP1} (bottom) from the 2019 model tests without the spar with a peak frequency and significant wave height of incident waves: $\omega_p^2 b/g = 1.12$ and $H_s/b = 8/40$. $\sigma_G = 0.0208$. The foam balls are here 3mm large (1.2L).*

$\omega^2 b/g = 2.52$, as also noted earlier.

RAOs corresponding to incident wave spectra with a higher peak frequency $\omega_p^2 b/g = 1.12$ and significant wave height $H_s/b = 8/40$ are shown in Fig. 7.5. For the case with a solid baffle, the free surface was observed to be strongly non-linear from the videos of the test. Yet, the semi-analytical results agree surprisingly well with the experimental ones. This is promising that the RAO for the free surface is as low as below unity in this irregular sea-state when a solid baffle is installed, meaning that the dock does not serve as a wave magnifier with given such a relatively simple damping device. Numerical results with baffle are not shown for lower wave frequencies as the semi-analytical model is only valid near sloshing resonance. From the RAO of ζ_{WP1}, a second resonant peak is observed around $\omega^2 b/g = 4$ (or $\omega^2 b/g = 4.9$ with the baffle), corresponding most likely to the excitation of the second sloshing mode. This has not been investigated in details, although of practical interest, and is left for future work.

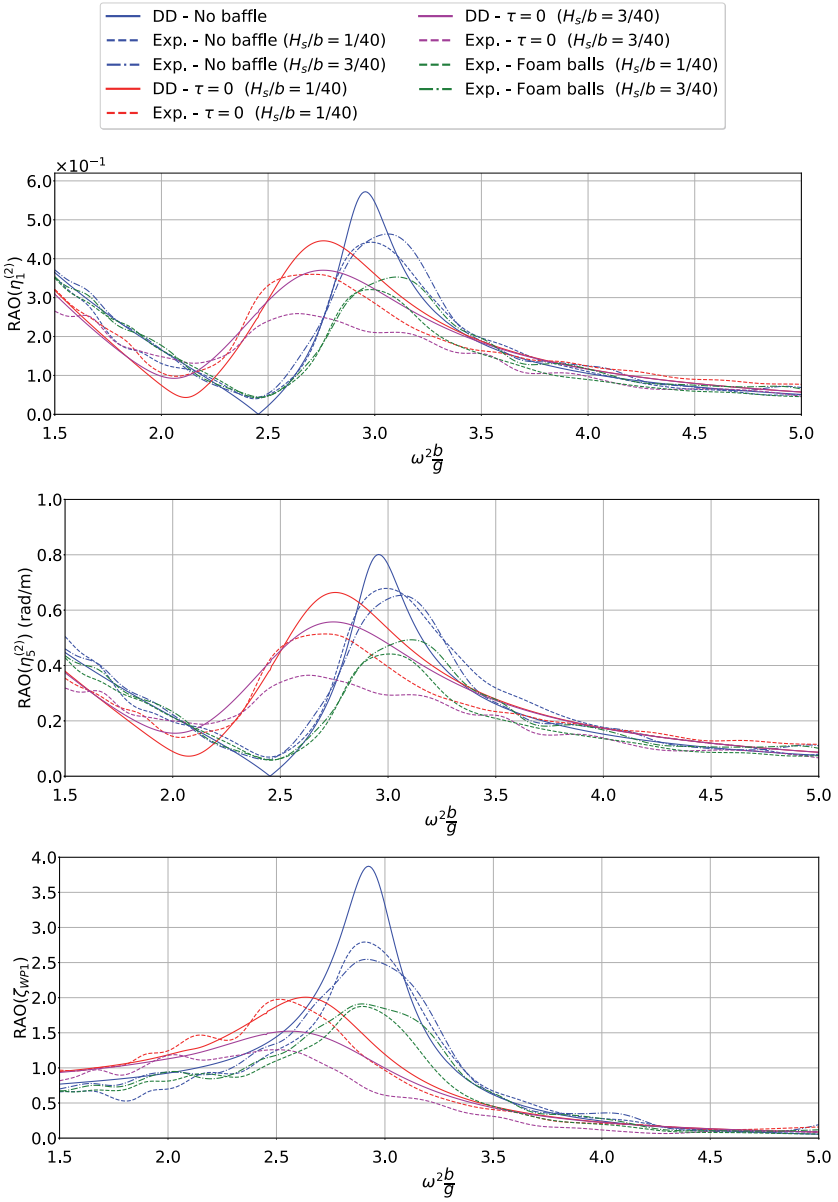

Figure 7.4: *RAOs of the dock's surge (top) and pitch (middle) motions, as well as ζ_{WP1} (bottom) in irregular waves, both from experiments and from the semi-analytical model. Results are presented for the dock alone, with solid baffle ($a_B/a = d_B/a = 0.17$), and with polystyrene foam balls (3mm, 1.2L) for $\omega_p^2 b/g = 2.52$ and both $H_s/b = 1/40$ and $H_s/b = 3/40$. $\sigma_G = 0.0208$. More results that include the lower draught $(d+s)/b = 1.25$ and variations of the BB's sizes are given in Appendix C.6.*

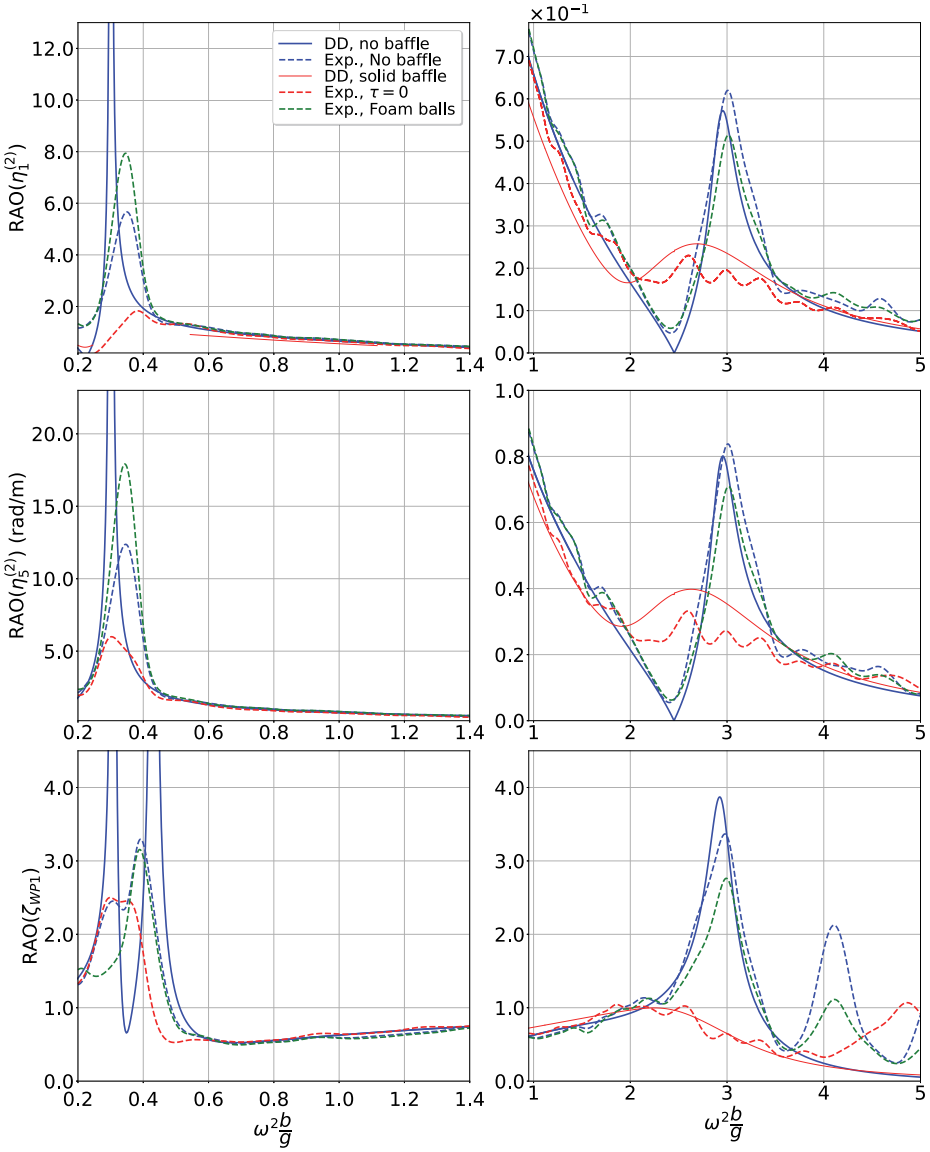

Figure 7.5: *RAOs of the dock's surge (top) and pitch (middle) motions, and of ζ_{WP1} (bottom) in irregular waves, for the same cases as in Fig. 7.4, but for the higher sea-state $\omega_p^2 b/g = 1.12$ and $H_s/b = 8/40$. $\sigma_G = 0.0208$.*

7.2 Dock with spar

Power spectra of the motions of both bodies are presented in Fig. 7.6 for the dock and spar without baffle for irregular waves with $\omega_p^2 b/g = 2.52$. As in Sec. 7.1, energy of the bodies' motions is concentrated around the peak resonance observed in regular waves around $\omega_1^2 b/g = 3$. The spectra of the spar's motions generally contain more energy than the ones of the dock's motions, and are more spread towards the peak frequency of incident waves $\omega_p^2 b/g = 2.52$. The energy of the heave motions for frequencies higher than $\omega^2 b/g = 1$ is less than 0.5% of that in surge for both bodies, confirming that non-linear excitation of these motions were negligible in that range. Resonance of the spar's heaving is observed near $\omega^2 b/g = 0.75$, which was also measured from decay tests and is consistent with our computed heave natural period. The same observation is made for the higher sea state with $\omega_p^2 b/g = 1.12$ (cf. Fig. 7.7), for which mostly the spar's natural period in heave is excited. It can be noted that the eigenfrequency of the spar's pitch motions was estimated to be $\omega^2 b/g = 0.82$ (cf. Sec. 5.4), which is also close to the peak frequency of incident waves. For this lower peak frequency, ζ_{WP1} still displays most energy at sloshing resonance.

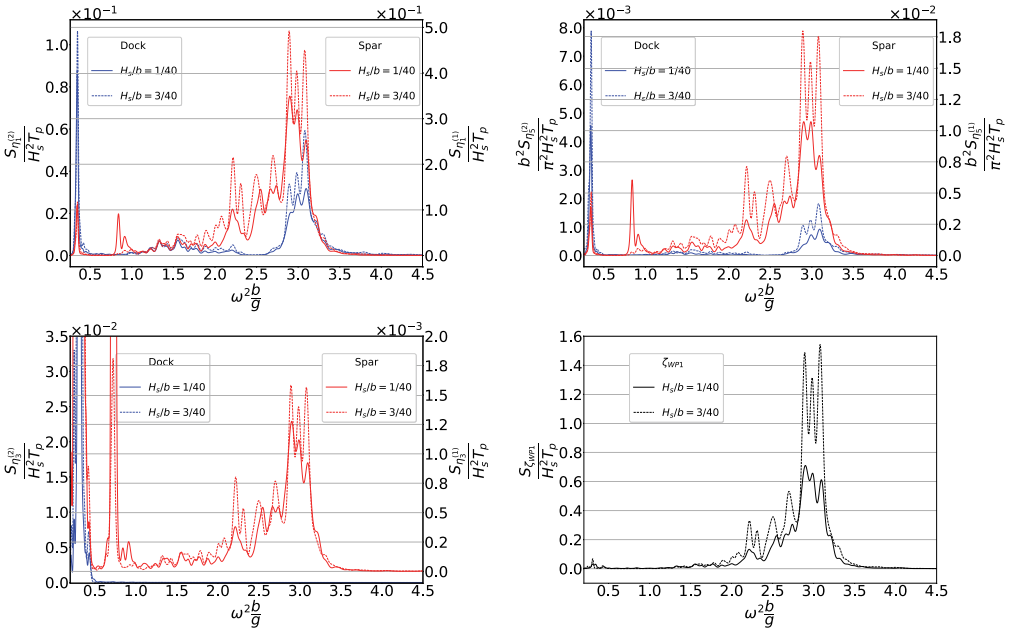

Figure 7.6: *Normalised spectra of the dock's and spar's responses in surge (upper left), pitch (upper right), and heave (lower left) motions as well as of ζ_{WP1} (lower right) from model tests, for two different sea-states in an Earth-fixed coordinate system. Peak frequency of the JONSWAP spectrum: $\omega_p^2 b/g = 2.52$. $\sigma_G = 0.003$.*

Fig. 7.8 shows experimental and numerical RAOs in irregular waves with a

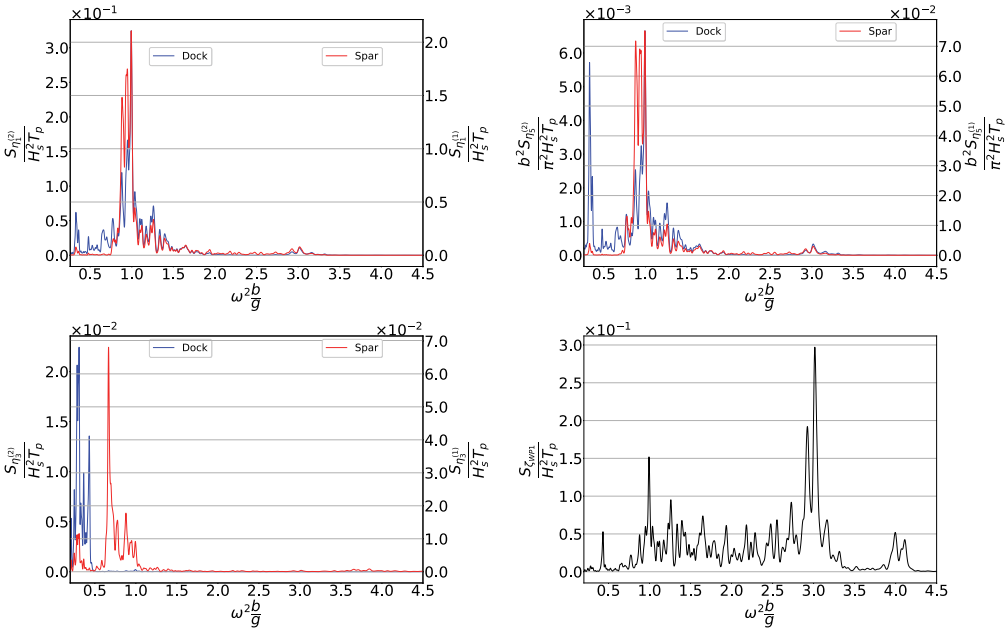

Figure 7.7: *Normalised spectra of the dock's and spar's responses in surge (upper left), pitch (upper right), and heave (lower left) motions as well as of ζ_{WP1} (lower right) from model tests, for $\omega_p^2 b/g = 1.12$ and $H_s/b = 8/40$ in an Earth-fixed coordinate system. $\sigma_G = 0.003$.*

peak frequency $\omega_p^2 b/g = 2.52$ for the dock with a spar. As for the case without spar, experimental results are lower than semi-analytical ones for all the motions, most likely due to the importance of transient responses in time domain. The experimental RAOs for $H_s/b = 1/40$ and $H_s/b = 3/40$ are very similar, and within the range of random uncertainty. These are consistent with the regular wave RAOs, shown on the same figure for several wave steepnesses, including repetition tests for $\epsilon = 1/60$. The maximum responses of the spar are between three and four times higher than the maximum responses of the dock, and dominate the relative motions between both bodies.

Experimental RAOs obtained from the second sea-state with the peak frequency $\omega_p^2 b/g = 1.12$ are shown in Fig. 7.9. Results are similar to the first sea-sate near $\sigma_{1,1}$. For lower wave frequencies (left subfigures), both the natural modes of the spar's and the dock's rigid body motions are excited. Resonant peaks are thus observed around the spar's natural period in pitch ($\omega^2 b/g = 0.82$) and in heave ($\omega^2 b/g = 0.66$) estimated from the eigenvalue analysis (cf. Sec. 5.4). These resonances are caused by the mooring lines used during model tests to maintain the spar in the center of the dock, which are not a realistic representation of the spar's mooring. Resonance of the dock's rigid body natural modes ($\omega^2 b/g = 0.32$ in heave and $\omega^2 b/g = 0.30$ in pitch cf. Sec. 5.4) are observed for lower frequencies,

with similar amplitudes as the ones discussed in the previous section for the case without spar. Due to the strong coupling between the surge and pitch motions of both bodies, the spar's motions are very high at the dock's rigid body natural frequencies, more than twice as high as at the spar's natural frequencies. This coupling should easily be reduced in practice by carefully constructing the lines between the dock and the spar.

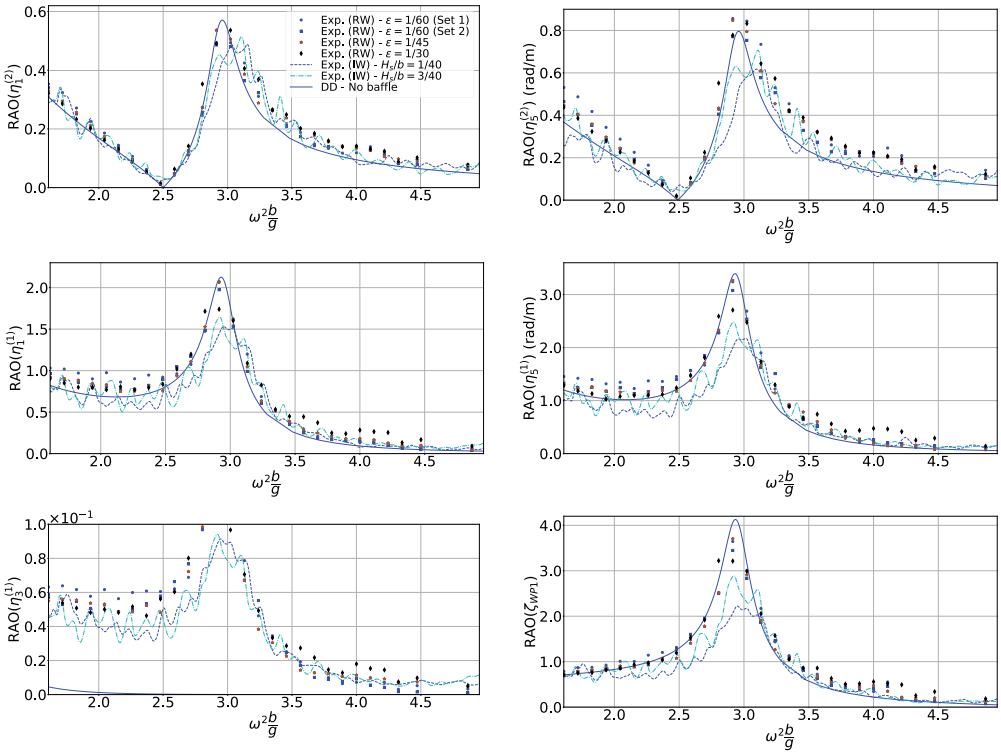

Figure 7.8: *Analytical and experimental RAOs of the motions in irregular waves for the dock+spar system. Experimental results from 2019 for several incident wave steepnesses are also shown. JONSWAP spectrum:* $\omega_p^2 b/g = 2.52$. $\sigma_G = 0.003$.

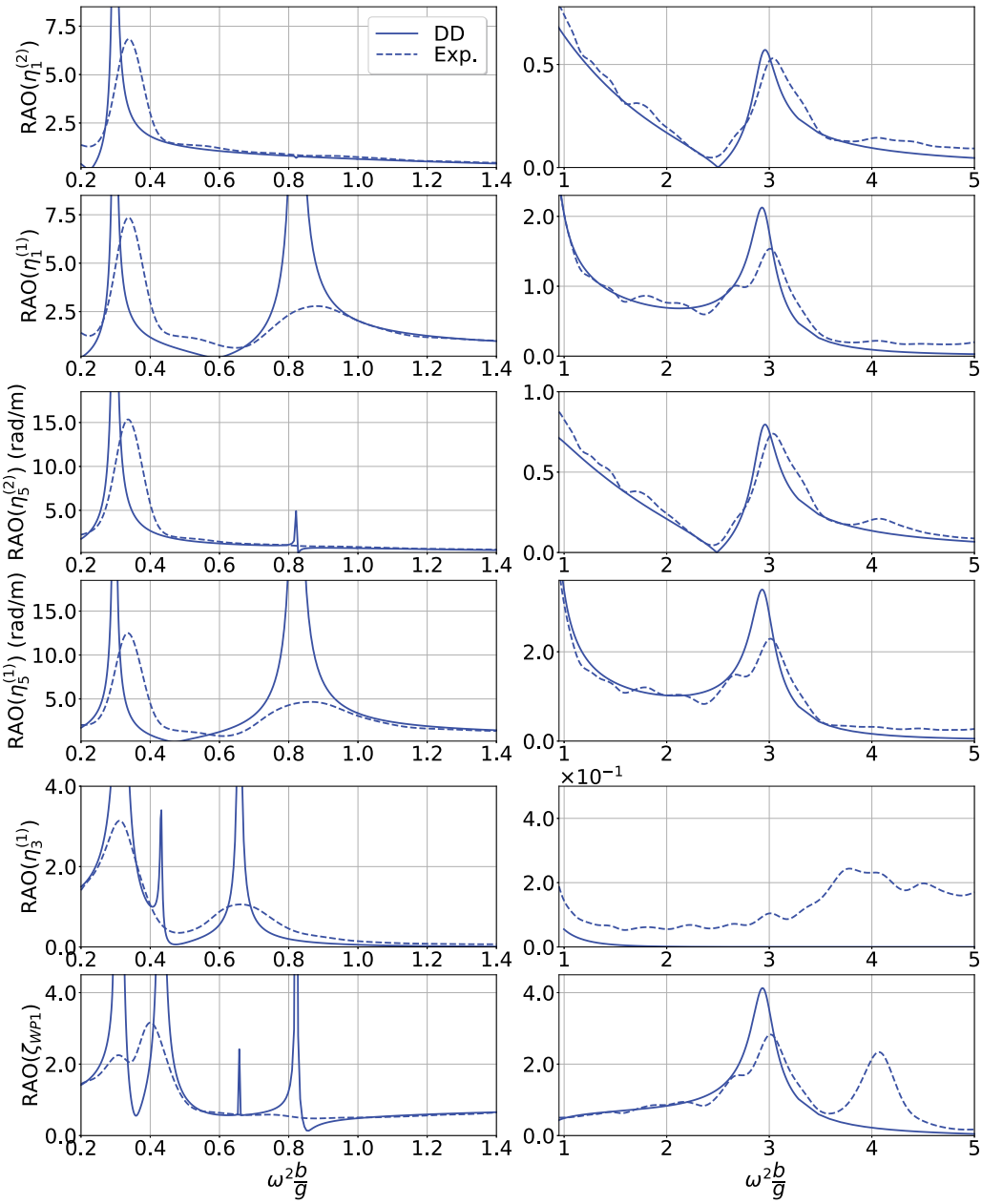

Figure 7.9: *Analytical and experimental RAOs of the dock's and spar's motions in irregular waves. Peak frequency and significant wave height of the JONSWAP spectrum:* $\omega_p^2 b/g = 1.12$ *and* $H_s/b = 8/40$. *Left: lower frequencies which include the natural modes of the bodies' motions. Right: zoom on the motions around the sloshing natural frequency.* $\sigma_G = 0.0208$

8 | Conclusion and further work

8.1 Overall conclusions

The seakeeping capabilities of a floating dock were investigated. The dock forms a large, circular moonpool. The focus was on the response of the first lateral sloshing mode and the rigid body motions with and without a FOWT's spar. A semi-analytical model based on linear potential flow theory combined with the Morison equation drag term with KC-dependency drag coefficient, applied with strip theory assumption was developed which allows both extensive parameter studies of the geometry without the burden of producing new meshes, and the addition of the inertia and viscous effects of damping ring baffles. The method takes advantage of the symmetry of revolution of the dock, which also restricts its possible applications to structures with similar symmetries. Further, the damping model is restricted to draught-to-diameter ratios that are in the order of unity or more. The method was coded in Python, with room left for optimisation. The CPU time was of few seconds per wave frequency on an Intel i7 desktop, and few minutes for one run with 80 frequencies. Parametric simulations run with the semi-analytical model showed in particular a high sensitivity of the sloshing waves and spar's motions on the dock's inertia matrix.
The numerical results in regular and irregular waves were compared to model tests performed at scale 1:100. The experiments included regular and irregular waves, tests with and without baffles, where baffles were both solid and perforated, and tests with and without the spar. Without baffles, linear potential flow theory predicts well the rigid body motions and sloshing in regular waves, but tends to over predict the motions in irregular waves as the time-dependent transient phases of the motions are not negligible. A good agreement was observed for the tests with baffle as long their submergence-to-width ratio remains above unity, while the viscous damping at lower submergence was under-predicted by the semi-analytical model, most likely due to free-surface interaction. The sloshing- induced motions of the FOWT's spar were significantly reduced (>50%) at low wave steepnesses by the presence of both the solid and perforated ($\tau = 0.15$) baffles. In regular waves, the relative pitching of the dock and the spar was exemplified in a relevant sea-state, reduced from 1.7° without the baffle to 0.75° with the baffle in our numerical simulations, which is promising as the installation of the blades on the nacelle imposes very strict limitations on the maximum relative pitching, typically around 1°. The spar heave motion was very low near sloshing resonance in all our tests in regular waves (below 0.1m in full scale), as heave and piston mode resonances occur for higher wave periods (> 15s in full scale). Similar RAOs were found in irregular waves for peak periods $T_p = 8s$ (full scale) as in regular waves. Sea-states measured in the North Sea with peak periods lower or equal to

8s represent at themselves 30% of all the sea-states (Faltinsen, 1990), suggesting relatively high time windows of operation for the installation of FOWTs in the floating dock.

8.2 Further work

The concept of the floating dock is still at its early stage. Many questions that were raised during our investigations or that previously existed remain open. In addition to operational phases where FOWTs are assembled inside the dock, towing of the dock between two installation sites, or sea-keeping in extreme weather conditions are also left for more in-depth further studies. The following points may for instance be of particular interest:

- The relative motions of the dock and the FOWT at different stages of the FOWT's assembly, including the tower, nacelle and blades.
- The dock's motions in extreme sea-states, as piston modes and natural periods in heave and pitch are non-negligible at low incident wave frequencies. These investigations could in particular include a more realistic mooring system.
- The opening gates, as the dock needs to be towed to another emplacement once the FOWT is installed. This opening is still to be defined. Constant angular opening or mechanical gates are for instance two possible options. The constant angular opening might lead to high structural stresses.
- The towing phases of the dock. During these phases, forward speed needs to be considered. The ballasts are most likely to be removed to lower the draught and reduce water resistance.
- The effects of several baffles could be modelled by extending the semi-analytical method used in this thesis.
- The development of higher-order models for the study of second-order effects, extending the applicability of the method to steeper waves.
- Include the effects of currents which occasionally co-exist with waves both in open sea and near the coast.

Bibliography

H. N. Abramson. *The dynamic behavior of liquids in moving containers, with applications to space vehicle technology.* Scientific and Technical Information Division, National Aeronautics and Space Administration; for sale by Supt. of Docs., U. S. Govt. Print. Off., 1966.

R. Barreira, S. Sphaier, I. Masetti, and A. Costa. Behavior of a mono-column structure (monobr) in waves. *OMAE 2005, Halkidiki, Greece*, 2005.

K. A. Belibassakis. Roll response of ship-hull sections in variable bathymetry regions by a hybrid bem-vortex particle method. *Journal of Hydrodynamics*, 22, 2010.

L. Borgman. Random hydrodynamic forces on objects. *The Annals of Mathematical Statistics*, 38(1):37 – 51, 1967.

P. Breeze. *Wind Power Generation.* Academic Press, 2016.

I. Chatjigeorgiou. *Analytical Methods in Marine Hydrodynamics.* Cambridge University Press, 2018.

N. Choudhary and S. Bora. Linear sloshing frequencies in the annular region of a circular cylindrical container in the presence of a rigid baffle. *Sadhana*, 42: 805–815, 2017.

L. Cozzi, B. Wanner, C. Donovan, A. Toril, and W. Yu. *Offshore Wind Outlook 2019.* iea.org [Accessed 15 August 2022], international energy agency edition, 2019.

L. Da Silva, N. Sergiienko, C. Pesce, B. Ding, B. Cazzolato, and H. Morishita. Stochastic analysis of nonlinear wave energy converters via statistical linearization. *Applied Ocean Research*, 95, 01 2020.

DNV RP-C205. *Environmental conditions and environmental loads.* [online]. Available from: https://www.dnv.com/oilgas/download/dnv-rp-c205-environmental-conditions-and-environmental-loads.html [Accessed 15 December 2020], 2019.

F. Dodge. he new dynamic behavior of liquids in moving containers. *Southwest Research Inst. San Antonio, TX, USA, Tech. Rept. SP-106*, 2000.

M. Downie, J. Wang, and J. Graham. The effectiveness of porous damping devices. *Proceedings of the tenth International Offshore and Polar Engineering Conference, Seattle, USA*, 2000.

M. Ezoji, N. Shabakhty, and L. Tao. Hydrodynamic damping of solid and perforated heave plates oscillating at low kc number based on experimental data: A review. *Ocean Engineering*, 253, 2022.

O. Faltinsen, O. Rognebakke, and A. Timokha. Two-dimensional resonant piston-like sloshing in a moonpool. *Journal of Fluid Mechanics*, 575:359–397, 2007.

O. Faltinsen, I. Lukovsky, and A. Timokha. Resonant sloshing in an upright annular tank. *Journal of Fluid Mechanics*, 804:608–645, 2016.

O. M. Faltinsen. *Sea loads on ships and offshore structures (Cambridge Ocean Technology Series)*. Cambridge University Press, reprint edition edition, 1990.

O. M. Faltinsen and A. Timokha. *Sloshing*. Cambridge University Press, first edition edition, 2009.

A. Fredriksen, T. Kristiansen, and O. Faltinsen. Wave-induced response of a floating two-dimensional body with a moonpool. *Philosophical transactions. Series A, Mathematical, physical, and engineering sciences*, 373, 2015.

A. G. Fredriksen, T. Kristiansen, and O. M. Faltinsen. Experimental and numerical investigation of wave resonance in moonpools at low forward speed. *Applied Ocean Research*, 47:28–46, 2014.

C. Garrett. Bottomless harbours. *Journal of Fluid Mechanics*, 43:433–449, 1970.

C. Garrett. Wave forces on a circular dock. *Journal of Fluid Mechanics*, 46: 129–139, 1971.

I. Gavrilyuk, I. Lukovsky, Y. Trotsenko, and A. Timokha. Sloshing in a vertical circular cylindrical tank with an annular baffle. part 1. linear fundamental solutions. *Journal of Engineering Mathematics*, 54, 2006.

V. Gnitko, V. Naumenko, L. Rozova, and E. Strelnikova. Multi-domain boundary element method for liquid sloshing analysis of tanks with baffles. *Journal of Basic and Applied Research International*, 17, 2016.

J. Graham. The forces on sharp-edged cylinders in oscillatory flow at low keulegan-carpenter numbers. *Journal of Fluid Mechanics*, 97:331–346, 1980.

J. Han, X. Zhang, and R. W. Yeung. Hydrodynamic behavior of a circular floating solar pond with an entrapped two-layer fluid. *Physics of Fluids*, 34, 2022.

M. D. Haskind. On wave motion of a heavy fluid. *Prikl. Mat. Mekh.*, 18:15–26, 1954.

M. Ilkişik and M. K. Kafali. The surge motion of a circular cylinder containing a concentric cylindrical hole in finite depth. *Ocean Engineering*, 13:409–406, 1986.

M. Isaacson and S. Premasiri. Hydrodynamic damping due to baffles in a rectangular tank. *Canadian Journal of Civil Engineering*, 28:608–616, 2001.

I. Q. Isaias Quaresma Masetti, A. P. S. Costa, S. H. Sphaier, K. Nishimoto, and G. Machado. Development of a concept of mono-column platform: Monobr. *Int. J. Computer Applications in Technology*, 43:225–233, 2012.

Z. Jiang, R. Yttervik, Z. Gao, and P. Sandvik. Design, modelling, and analysis of a large floating dock for spar floating wind turbine installation. *Marine Structures*, 72, 07 2020.

X. Jin, M. Liu, F. Zhang, and D. Li. Mitigation of liquid sloshing by multiple layers of dual horizontal baffles with equal/unequal baffle widths. *Ocean Engineering*, 263:112–184, 2022.

N. Joukowski. On motions of a rigid body with cavity filled by homogeneous liquid. *Journal of Russian Physical-Mathematical Society (in Russian)*, XVI: 30–85, 1885.

G. Keulegan. Energy dissipation in standing waves in rectangular basins. *Journal of Fluid Mechanics*, 6:30–50, 1959.

G. H. Keulegan and L. H. Carpenter. Forces on cylinders and plates in an oscillating fluid. *Journal of Research of the National Bureau of Standards Research Paper*, 60:423–440, 1958.

K. Kokkinowracho, S. Mavrakos, and S. Asorakos. Behaviour of vertical bodies of revolution in waves. *Ocean Engineering*, 13:505–538, 1986.

D. N. Konispoliatis, I. K. Chatjigeorgiou, and S. A. Mavrakos. Theoretical hydrodynamic analysis of a surface-piercing porous cylindrical body. *Fluids*, 6, 2021.

T. Kristiansen and O. Faltinsen. Application of a vortex tracking method to the piston-like behaviour in a semi-entrained vertical gap. *Applied Ocean Research*, 30:1–16, 2008.

C. Lee and J. Newman. Wamit user manual, versions 6.4, 6.4pc, 6.3s, 6.3s-pc. *WAMIT, Inc., Cambridge, MA*, 2006.

J. Lee and F. Zhao. *Global Wind Report 2020.* gwec.net [Accessed 25 September 2023], global wind energy council (gwec) edition, 2020.

I. Lukovsky, M. Y. Barnyak, and A. N. Komarenko. Approximate methods of solving the problems of the dynamics of a limited liquid volume. *Kiev: Naukova Dumka*, 1984. (in Russian).

I. A. Lukovsky. *Nonlinear dynamics : mathematical models for rigid bodies with a liquid*. De Gruyter studies in mathematical physics ; 27. Walter de Gruyter GmbH & Co. KG, 2015.

R. MacCamy and R. Fuchs. Wave forces on piles: A diffraction theory. *U.S. Army Corps of Engineers Beach Erosion Board, Tech. Memo.*, 69, 1954.

E. Mackay, W. Shi, D. Qiao, R. Gabl, T. Davey, D. Ning, and L. Johanning. Numerical and experimental modelling of wave interaction with fixed and floating porous cylinders. *Ocean Engineering*, 242:110–118, 2021.

A. Maleki and Z. Mansour. Sloshing damping in cylindrical liquid storage tanks with baffles. *Journal of Sound and Vibration*, 311, 2008.

A. Mavrakos, D. Konispoliatis, D. Ntouras, G. Papadakis, and S. Mavrakos. Hydrodynamic coefficients in heave of a moonpool-type floater using theoretical, numerical and cfd methodologies. *Ocean Engineering*, 279, 2023.

S. Mavrakos. Wave loads on a stationary floating bottomless cylindrical body with finite wall thickness. *Applied Ocean Research*, 7:213–224, 1985.

S. Mavrakos. Added mass and damping of a vertical cylinder in finite-depth waters. *Ocean Engineering*, 15:213–229, 1988.

S. A. Mavrakos. Hydrodynamic coefficients in heave of two concentric surface-piercing truncated circular cylinders. *Applied Ocean Research*, 26, 2004.

F. Mentzoni. *Hydrodynamic Loads on Complex Structures in the Wave Zone*. Doctoral thesis, 2020.

F. Mentzoni and T. Kristiansen. A semi-analytical method for calculating the hydrodynamic force on perforated plates in oscillating flow. *International Conference on Offshore Mechanics and Arctic Engineering*, 2019.

F. Mentzoni and T. Kristiansen. Two-dimensional experimental and numerical investigations of perforated plates in oscillating flow, orbital flow and incident waves. *Applied Ocean Research*, 97, 2020.

F. Mentzoni, M. Abrahamsen-Prsic, and T. Kristiansen. Hydrodynamic coefficients of simplified subsea structures. *International Conference on Offshore Mechanics and Arctic Engineering*, 2018.

G. Mikishev and G. Churilov. Some results on experimental hydrodynamic coefficients for a cylinder with ribs. *Oscillations of Elastic Constructions with Liquid. (in Russian)*, pages 31–37, 1977.

G. Mikishev and N. Dorozhkin. An experimental investigation of free oscillations of a liquid in containers. *Izv. Akad., Nauk SSSR, Otd. Tekh., Nauk, Mekh. I Mashinostr*, 4:48–83, 1961.

J. Miles. Ring damping of free surface oscillations in a circular tank. *Journal of Applied Mechanics*, 25:274–276, 02 1958.

J. Miles and F. Gilbert. Scattering of gravity waves by a circular dock. *Journal of Fluid Mechanics*, 34:783–793, 1968.

B. Molin. On the piston and sloshing modes in moonpools. *Journal of Fluid Mechanics*, 430:27–50, 03 2001.

B. Molin and J. Legras. Hydrodynamic modelling of the roseau tower stabilizer. *Proceedings 9th International Conference on Owshore Mechanics and Arctic Engineering (OMAE), Houston, ¹X, ;.S.A. Vol I, Part B*, pages 329–336, 1990.

B. Molin, F. Remy, S. Rigaud, and C. Jouette. Lng-fpso's : frequency domain, coupled analysis of support and liquid cargo motion. *Proceedings of the IMAM conference, Rethymnon, Greece,*, 2002.

B. Molin, F. Remy, and T. Ripol. Experimental study of the heave added mass and damping of solid and perforated disks close to the free surface. *Conference: International Congress of International Maritime Association of the Mediterranean, Varna, Bulgaria*, 2007.

B. Molin, X. Zhang, H. Huang, and F. Remy. On natural modes in moonpools and gaps in finite depth. *Journal of Fluid Mechanics*, 840:530–554, 2018.

M. Moreau, T. Kristiansen, B. Ommani, and B. Molin. An upright bottomless vertical cylinder with baffles floating in waves. *Applied Ocean Research*, 119, 2022.

M. Moreau, T. Kristiansen, B. Ommani, and B. Molin. Sloshing-induced motions of a spar inside a cylindrical dock with baffles in waves. *Applied Ocean Research*, 134, 2023a.

M. Moreau, T. Kristiansen, B. Ommani, and B. Molin. Coupled sloshing and body motions of a floating circular dock with damping devices. *Proceedings of the 14th International Conference on Hydrodynamics (ICHD), Wuxi, China*, 2023b.

J. R. Morison, M. P. O Brien, J. W. Johnson, and S. A. Schaaf. The force exerted by surface waves on piles. *Journal of Petroleum Technology*, 2:149—-154, 1950.

J. N. Newman. The exciting forces on fixed bodies in waves. *Journal of Ship Research*, 1962.

J. N. Newman. *Marine Hydrodynamics*. The MIT Press, first edition edition, 1977.

M. H. Nokob and R. Yeung. Diffraction and radiation loads on open cylinders of thin and arbitrary shapes. *Journal of Fluid Mechanics*, 772:649–677, 2015.

M. H. Nokob and R. W. Yeung. Hypersingular integral-equation method for wave diffraction about arbitrary, shell-like vertical cylinders in finite-depth waters. *29th International Workshop on Water Waves and Floating Bodies, Osaka, Japan*, 2014a.

M. H. Nokob and R. W. Yeung. Computations of arbitrary thin-shell vertical cylinders in a wave field by a hypersingular integral-equation method. *ASME 33rd International Conference on Offshore Mechanics and Arctic Engineering, OMEA 2014, San Francisco*, 2014b.

F. Olver, D. Lozier, R. Boisvert, and C. Clark. Nist handbook of mathematical functions. 01 2010.

M. Ostrogradsky. Mémoire sur la propagation des ondes dans un bassin cylindrique. *Mémoires présentés par divers savans à l'académie royale des sciences de l'institut de France.*, III:23–44, 1832. (in French).

M.-S. Park and W. Koo. Mathematical modeling of partial-porous circular cylinders with water waves. *Mathematical Problems in Engineering*, 2015.

L. Ramírez, D. Fraile, and G. Brindley. *Offshore Wind in Europe, Key trends and statistics 2020*. windeurope.org [Accessed 25 September 2023], global wind energy council (gwec) edition, 2021.

S. Ravinthrakumar, T. Kristiansen, and B. Ommani. A 2D experimental and numerical study of moonpools with recess. *OMAE2018-78326*, 2018.

S. Ravinthrakumar, T. Kristiansen, B. Molin, and B. Ommani. A two-dimensional numerical and experimental study of piston and sloshing resonance in moonpools with recess. *Journal of Fluid Mechanics*, 877:142–166, 2019.

L. Reiersen, T. Kristiansen, B. Ommani, and A. Fredriksen. Investigation of moonpools as pitch motion reducing device. *Applied Ocean Research*, 108, 2021.

J. B. G. Roberts and P. D. Spanos. *Random Vibration and Statistical Linearization*. 1990.

T. Sabuncu and S. Calisal. Hydrodynamic coefficients for vertical circular cylinder at finite depth. *Ocean Engineering*, 8:25–63, 1981.

T. Sarpkaya. Force on a circular cylinder in viscous oscillatory flow at low keulegan—carpenter numbers. *Journal of Fluid Mechanics*, 165:61–71, 1986.

H. Schlichting. *Boundary Layer Theory*. McGraw-Hill, Inc., 7th edition edition, 1979.

B. Skaare. Development of the hywind concept. *Proceedings of the ASME 2017 36th International Conference on Ocean, Offshore and Arctic Engineering, Trondheim, Norway*, 2017.

A. Sommerfeld. Vorlesungen über theoretische physik. *Leipzig Akd. Verlagsgesellschaft*, 69, 1948.

A. Song and O. M. Faltinsen. An experimental and numerical study of heave added mass and damping of horizontally submerged and perforated rectangular plates. *Journal of Fluids and Structures*, 39:87–101, 2013.

E. Sorolla, M. J. R., and M. Mattes. Algorithm to calculate a large number of roots of the cross-product of bessel functions. *IEEE Transactions on Antennas and Propagation*, 61:2180—-2187, 2013.

T. Stehly and P. Duffy. *2020 Cost of Wind Energy Review*. National renewable energy lab. (nrel), golden, co (united states) edition, 2021.

D. Stephens, H. Leonard, and T. Perry. *Investigation of the Damping of Liquids in Right-Circular Cylindrical Tanks, Including the Effects of a Time-Variant Liquid Depth*. NASA TN D-1367, 1962.

H. Takahara and K. Kimura. Frequency response of sloshing in an annular cylindrical tank subjected to pitching excitation. *Journal of Sound and Vibration*, 331(13):3199–3212, 2012.

A. Timokha. The narimanov-moiseev modal equations for sloshing in an annular tank. *Proceedings of the Institute Mathematics of the NAS of Ukraine*, 12: 122–147, 2015.

J. Wang and D. Zhou. Analytical solution for liquid sloshing with small amplitude in a cylindrical tank with an annual baffle. *Journal of Vibration and Shock*, 2010.

J. Wang, S. Lo, and D. Zhou. Liquid sloshing in rigid cylindrical container with multiple rigid annular baffles: Free vibration. *Journal of Fluids and Structures*, 34:138–156, 2012.

J. Wang, S. H. Lo, D. Zhou, and Y. Dong. Nonlinear sloshing of liquid in a rigid cylindrical container with a rigid annular baffle under lateral excitation. *Shock and Vibration*, 17, 2019.

R. Yeung. Added mass and damping of a vertical cylinder in finite-depth waters. *Applied Ocean Research*, 3:63–80, 1980.

H. Yue, C. Jianyun, and Q. Xu. Sloshing characteristics of annular tuned liquid damper (atld) for applications in composite bushings. *Structural Control and Health Monitoring*, 25, 2018.

C. H. Ziener, F. T. Kurz, L. R. Buschle, and T. Kampf. Orthogonality, lommel integrals and cross product zeros of linear combinations of bessel functions. *SpringerPlus*, 4, 2015.

A | Domain decomposition: semi-analytical results

A.1 Integral from matching conditions

A.1.1 Dock without spar

The integrals established from the matching conditions of both the radiation and diffraction problems for the dock without spar detailed in Chapter 2 are given below for $(p, q) \in \mathbb{N}^2$:

$$T^{II}_{q,p} = \int_{-h}^{-(d+s)} Z_q(z) \cos\left(\frac{p\pi(z+h)}{l}\right) dz = \frac{(-1)^p l^2 \alpha_q \sin(\alpha_q l)}{(-p^2\pi^2 + \alpha_q^2 l^2) N_p^{\frac{1}{2}}}, \tag{A.1}$$

$$T^{III}_{q,p} = \int_{-d}^{0} \tilde{Z}_p(z) Z_q(z) dz = \Big[(\beta_p - \alpha_q) \sin(\beta_p d + \alpha_q h) + 2\alpha_q \sin(\alpha_q (h-d)) + (\beta_q + \alpha_q) \sin(\beta_p d - \alpha_q h) \Big] / \left(2(\beta_p^2 - \alpha_q^2) N_p^{\frac{1}{2}} \tilde{N}_p^{\frac{1}{2}} \right), \tag{A.2}$$

$$T^{III,surge}_{p} = \int_{-d}^{0} \tilde{Z}_p(z) dz = \frac{\sin(\beta_p d)}{\beta_p \tilde{N}_p^{\frac{1}{2}}}, \tag{A.3}$$

$$T^{III,pitch}_{p,1} = \int_{-d}^{0} z \tilde{Z}_p(z) dz = \frac{\cos(\beta_p d) - 1}{\beta_p^2 \tilde{N}_p^{\frac{1}{2}}}, \tag{A.4}$$

$$T^{III,pitch}_{p,2} = \int_{-d}^{0} \frac{\partial \phi^{(2),III}_{5,m}}{\partial r}(b, z) \tilde{Z}_p(z) dz = \frac{-g \sin(\beta_p d)\beta_p - \cos(\beta_p d)\omega^2 + \omega^2}{\omega^2 \beta_p^2 \tilde{N}_p^{\frac{1}{2}}}, \tag{A.5}$$

$$T^{III,heave}_{p,1} = \int_{-d}^{0} \frac{\partial \phi^{(2),III}_{3,m}}{\partial r}(b, z) \tilde{Z}_p(z) dz = 0, \tag{A.6}$$

$$T_{p,1}^{II,pitch} = \int_{-h}^{-(d+s)} \phi_{5,m}^{(2),II}(a,z)\cos\left(\frac{p\pi(z+h)}{l}\right)dz = \begin{cases} -\frac{1}{6}al^2 + \frac{1}{8}a^3 \text{ if } p = 0 \\ \frac{(-1)^{p+1}l^2a}{p^2\pi^2} \text{ if } p \geq 1 \end{cases}, \tag{A.7}$$

$$\tilde{T}_{p,1}^{II,pitch} = \int_{-h}^{-(d+s)} \phi_{5,m}^{(2),II}(c,z)\cos\left(\frac{p\pi(z+h)}{l}\right)dz = \begin{cases} -\frac{1}{6}cl^2 + \frac{1}{8}c^3 \text{ if } p = 0 \\ \frac{(-1)^{p+1}l^2c}{p^2\pi^2} \text{ if } p \geq 1 \end{cases}, \tag{A.8}$$

$$T_{p,1}^{II,heave} = \int_{-h}^{-(d+s)} \phi_{3,m}^{(2),II}(a,z)\cos\left(\frac{p\pi(z+h)}{l}\right)dz = \begin{cases} \frac{1}{6}l^2 - \frac{1}{4}a^2 \text{ if } p = 0 \\ \frac{(-1)^p l^2}{p^2\pi^2} \text{ if } p \geq 1 \end{cases}, \tag{A.9}$$

$$\tilde{T}_{p,1}^{II,heave} = \int_{-h}^{-(d+s)} \phi_{3,m}^{(2),II}(c,z)\cos\left(\frac{p\pi(z+h)}{l}\right)dz = \begin{cases} \frac{1}{6}l^2 - \frac{1}{4}c^2 \text{ if } p = 0 \\ \frac{(-1)^p l^2}{p^2\pi^2} \text{ if } p \geq 1 \end{cases}, \tag{A.10}$$

$$T_{p,3}^{III,pitch} = \int_{-d}^{0} \phi_{5,m}^{(2),III}(c,z)\tilde{Z}_p(z)dz = -c\frac{g\sin(\beta_p d)\beta_p + \omega^2(\cos(\beta_p d) - 1)}{\beta_p^2\omega^2\tilde{N}_p^{\frac{1}{2}}}, \tag{A.11}$$

$$T_{p,2}^{III,heave} = \int_{-d}^{0} \phi_{3,m}^{(2),III}(c,z)\tilde{Z}_p(z)dz = \frac{g\sin(\beta_p d)\beta_p + \omega^2(\cos(\beta_p d) - 1)}{\beta_p^2\omega^2\tilde{N}_p^{\frac{1}{2}}}, \tag{A.12}$$

$$\begin{aligned} T_{p,4}^{III,pitch} &= \int_{-d}^{0} \frac{\partial\phi_{5,m}^{(2),III}}{\partial r}(c,z)Z_p(z)dz \\ &= \frac{\alpha_p(d\omega^2 - g)\sin(\alpha_p(d-h)) - g\sin(\alpha_p h)\alpha_p - \cos(\alpha_p h)\omega^2 + \cos(\alpha_p(d-h))\omega^2}{\alpha_p^2\omega^2 N_p^{\frac{1}{2}}}, \end{aligned} \tag{A.13}$$

$$T_{p,3}^{III,heave} = \int_{-d}^{0} \frac{\partial \phi_{3,m}^{(2),III}}{\partial r}(c,z)Z_p(z)dz = 0, \tag{A.14}$$

$$T_{p,3}^{II,heave} = \int_{-h}^{-(d+s)} \frac{\partial \phi_{3,m}^{(2),II}}{\partial r}(a,z)Z_p(z)dz = -\frac{a\sin(\alpha_p l)}{2l\alpha_p N_p^{\frac{1}{2}}}, \tag{A.15}$$

$$\begin{aligned} T_{p,3}^{II,pitch} &= \int_{-h}^{-(d+s)} \frac{\partial \phi_{5,m}^{(2),II}}{\partial r}(a,z)Z_p(z)dz \\ &= \frac{-4\alpha_p^2\sin(\alpha_p l)l^2 + 3a^2\sin(\alpha_p l)\alpha_p^2 - 8\alpha_p l\cos(\alpha_p l) + 8\sin(\alpha_p l)}{8l\alpha^3 N_p^{\frac{1}{2}}}, \end{aligned} \tag{A.16}$$

$$\begin{aligned} T_{p,2}^{II,pitch} &= \int_{-h}^{-(d+s)} \frac{\partial \phi_{5,m}^{(2),II}}{\partial r}(c,z)Z_p(z)dz \\ &= \frac{-4\alpha_p^2\sin(\alpha_p l)l^2 + 3c^2\sin(\alpha_p l)\alpha_p^2 - 8\alpha_p l\cos(\alpha_p l) + 8\sin(\alpha_p l)}{8l\alpha^3 N_p^{\frac{1}{2}}}, \end{aligned} \tag{A.17}$$

$$T_{p,2}^{II,heave} = \int_{-h}^{-(d+s)} \frac{\partial \phi_{3,m}^{(2),II}}{\partial r}(c,z)Z_p(z)dz = -\frac{c\sin(\alpha_p l)}{2l\alpha_p N_p^{\frac{1}{2}}}, \tag{A.18}$$

$$\begin{vmatrix} T_{p,1}^{B,surge} \\ T_{p,1}^{B,heave} \\ T_{p,1}^{B,pitch} \end{vmatrix} = \int_{-(d+s)}^{-d} \begin{vmatrix} 1 \\ 0 \\ z \end{vmatrix} Z_p(z)dz$$

$$= \begin{vmatrix} \frac{\sin(\alpha_p(h-d)) - \sin(\alpha_p l)}{\alpha_p N_p^{\frac{1}{2}}} \\ 0 \\ \frac{\cos(\alpha_p(d-h)) + \sin(\alpha_p(d-h))\alpha_p d + \alpha_p(h-l)\sin(\alpha_p l) - \cos(\alpha_p l)}{\alpha_p^2 N_p^{\frac{1}{2}}} \end{vmatrix}, \tag{A.19}$$

$$\begin{vmatrix} T_{p,2}^{B,surge} \\ T_{p,2}^{B,heave} \\ T_{p,2}^{B,pitch} \end{vmatrix} = \int_{-(d+s)}^{0} \begin{vmatrix} 1 \\ 0 \\ z \end{vmatrix} Z_p(z)dz = \begin{vmatrix} \frac{\sin(\alpha_p h) - \sin(\alpha_p l)}{\alpha_p N_p^{\frac{1}{2}}} \\ 0 \\ \frac{\alpha_p(d+s)\sin(\alpha_p l) + \cos(\alpha_p h) - \cos(\alpha_p l)}{\alpha_p^2 N_p^{\frac{1}{2}}} \end{vmatrix}, \tag{A.20}$$

A.1.2 Dock with spar

The matching conditions between the domains I, II and III are identical either the spar is inside the dock or not. New integrals are defined from the matching conditions with either the domain IV or V:

$$T_{q,p}^{V} = \int_{-h}^{-d_0} Z_q(z) \cos\left(\frac{p\pi(z+h)}{h-d_0}\right) \mathrm{d}z$$

$$= \frac{(-1)^p \alpha_q \left(h-d_0\right)^2 \left(\cos\left(\alpha_q d_0\right)\sin\left(h\alpha_q\right) - \sin\left(\alpha_q d_0\right)\cos\left(h\alpha_q\right)\right)}{N_q^{\frac{1}{2}}\left(\left(h-d_0\right)^2 \alpha_q^2 - \pi^2 p^2\right)}, \tag{A.21}$$

$$\begin{vmatrix} T_{p,3}^{B,surge} \\ T_{p,3}^{B,pitch} \end{vmatrix} = \int_{-d_0}^{0} \begin{vmatrix} 1 \\ z \end{vmatrix} Z_p(z)dz = \begin{vmatrix} \frac{\sin(\alpha_p(d_0-h)) + \sin(\alpha_p h)}{N_p^{\frac{1}{2}}\alpha_p} \\ \frac{\alpha_p d_0 \sin(\alpha_p(h-d_0)) + \cos(\alpha_p h) - \cos(\alpha_p(h-d_0))}{\alpha_p^2 N_p^{\frac{1}{2}}} \end{vmatrix}, \tag{A.22}$$

$$\left| \begin{array}{l} T_{p,1}^{V,heave} \\ \\ T_{p,1}^{V,pitch} \end{array} \right. = \int_{-h}^{-d_0} \phi_{5,m}^{V}(a_0, z) \cos\left(\frac{p\pi(z+h)}{h-d_0}\right) dz,\ q \in \mathbb{N}, \tag{A.23}$$

$$\left| \begin{array}{l} T_{p,2}^{V,heave} \\ \\ T_{p,2}^{V,pitch} \end{array} \right. = \int_{-h}^{-d_0} \frac{\partial \phi_{j,m}^{V}}{\partial r}(a_0, z)\, Z_p(z)\, dz. \tag{A.24}$$

The expressions of the integrals (A.23) and (A.24) are:

$$T_{p,1}^{V,heave} = \begin{cases} \dfrac{(h-d_0)^2}{6} - \dfrac{1}{4}a_0^2 \text{ if } p = 0 \\ \\ \dfrac{(-1)^p (h-d_0)^2}{p^2\pi^2} \text{ if } p \geq 1 \end{cases} \tag{A.25}$$

$$T_{p,1}^{V,pitch} = \begin{cases} -\dfrac{a_0}{6}\left((h-d_0)^2 - \dfrac{3a_0^2}{4}\right) \text{ if } p = 0 \\ \\ \dfrac{(-1)^{p+1} a_0 (h-d_0)^2}{p^2\pi^2} \text{ if } p \geq 1 \end{cases} \tag{A.26}$$

$$T_{p,2}^{V,heave} = a_0 \frac{\sin(\alpha_p d_0)\cos(\alpha_p h) - \cos(\alpha_p d_0)\sin(\alpha_p h)}{2(h-d_0) N_p^{\frac{1}{2}} \alpha_p} \tag{A.27}$$

$$T_{p,2}^{V,pitch} =$$

$$\frac{\left(-2\alpha_p (h-d0)\cos(h\alpha_p) - \left(-2 + \left(h^2 - 2d0h - 3/4\left(a_0^2\right) + d0^2\right)\alpha_p^2\right)\sin(h\alpha_p)\right)\cos(\alpha_p d0)}{2N_p^{\frac{1}{2}}(h-d0)\alpha_p^3}$$

$$+ \frac{\sin(\alpha_p d0)\left(\left(-2 + \left(h^2 - 2d0h - 3/4\left(a_0^2\right) + d0^2\right)\alpha_p^2\right)\cos(h\alpha_p) - 2\alpha_p \sin(h\alpha_p)(h-d0)\right)}{2N_p^{\frac{1}{2}}(h-d0)\alpha_p^3}. \tag{A.28}$$

A.2 Matrix equations

A.2.1 Diffraction problem, dock without spar

The coefficients of the matrices $\mathbb{B}^S$ and $\boldsymbol{C}^S$ from the diffraction problem of the dock without spar are given by:

$$\mathbb{B}^S_{q,j} = \sum_{n=0}^{N_{II}} H^{(3)}_{j,n} H^{(6)}_{p,q,n} + \sum_{n=0}^{N_{III}} \left[H^{(4)}_{j,n} H^{(8)}_{p,q,n} + H^{(1)}_{p,n} H^{(4)}_{j,n} H^{(9)}_{p,q,n} \right] - \delta_{q,j},$$

$$q \in [0, (N_I - 1)], j \in [0, (N_I - 1)], \tag{A.29}$$

$$\mathbb{B}^S_{q,j} = \sum_{n=0}^{N_{II}} H^{(2)}_{j,n} H^{(7)}_{p,q,n}, \quad q \in [0, (N_I - 1)], j \in [N_I, (N_{IV} - 1)], \tag{A.30}$$

$$\mathbb{B}^S_{q,j} = \sum_{n=0}^{N_{II}} H^{(3)}_{j,n} H^{(10)}_{p,q,n}, \quad q \in [N_I, (N_{IV} - 1)], j \in [0, (N_I - 1)], \tag{A.31}$$

$$\mathbb{B}^S_{q,j} = \sum_{n=0}^{N_{II}} H^{(2)}_{j,n} H^{(11)}_{p,q,n} - \delta_{q,j}, \quad q \in [N_I, (N_{IV} - 1)], j \in [N_I, (N_{IV} - 1)], \tag{A.32}$$

$$\boldsymbol{C}^S_q = \begin{cases} -H^{(5)}_{p,q}, & q \in [0, (N_I - 1)] \\ 0 & q \in [N_I, (N_{IV} - 1)] \end{cases}, \tag{A.33}$$

for each $p \in [0, N_S]$. The coefficients H are given for $(p, q, n) \in \mathbb{N}^3$ by:

$$H^{(1)}_{p,q} = -\frac{P^{III}_{p,q,r}(b)}{Q^{III}_{p,q,r}(b)}, \tag{A.34}$$

$$H^{(2)}_{n,q} = \frac{1}{l} T^{II}_{n,q}, \tag{A.35}$$

$$H^{(3)}_{n,q} = \frac{1}{l} T^{II}_{n,q}, \tag{A.36}$$

$$H^{(4)}_{n,q} = \frac{1}{d} T^{III}_{n,q}, \tag{A.37}$$

$$H^{(6)}_{p,q,n} = \frac{K_p(\alpha_q c)}{h \alpha_q K'_p(\alpha_q c)} \epsilon_n T^{II}_{q,n} P^{II}_{p,n,r}(c), \tag{A.38}$$

$$H^{(7)}_{p,q,n} = \frac{K_p(\alpha_q c)}{h\alpha_q K'_p(\alpha_q c)} \epsilon_n T^{II}_{q,n} Q^{II}_{p,n,r}(c), \tag{A.39}$$

$$H^{(8)}_{p,q,n} = \frac{K_p(\alpha_q c)}{h\alpha_q K'_p(\alpha_q c)} T^{III}_{q,n} P^{III}_{p,n,r}(c), \tag{A.40}$$

$$H^{(9)}_{p,q,n} = \frac{K_p(\alpha_q c)}{h\alpha_q K'_p(\alpha_q c)} T^{III}_{q,n} Q^{III}_{p,n,r}(c), \tag{A.41}$$

$$H^{(10)}_{p,q,n} = \frac{I_p(\alpha_q a)}{h\alpha_q I'_p(\alpha_q a)} \epsilon_n T^{II}_{q,n} P^{II}_{p,n,r}(a), \tag{A.42}$$

$$H^{(11)}_{p,q,n} = \frac{I_p(\alpha_q a)}{h\alpha_q I'_p(\alpha_q a)} \epsilon_n T^{II}_{q,n} Q^{II}_{p,n,r}(a), \tag{A.43}$$

$$H^{(5)}_{p,q} = \begin{cases} \dfrac{K_p(\alpha_0 c)}{b\alpha_0 K'_p(\alpha_0 c) Z'_0(h)} \left[k \dfrac{J_p(kc)}{H_p(kc)} H'_p(kc) - kJ'_p(kc) \right] & \text{if } q = 0 \\ 0 \text{ if } q > 0 \end{cases} . \tag{A.44}$$

The matrix system $\mathbb{B}^S \boldsymbol{A}^S = \boldsymbol{C}^S$ is solved in python for the coefficients A^I and A^{IV}. The remaining A coefficients given by:

$$A^{II}_{1,p,q} = \sum_{n=0}^{N_I} H^{(3)}_{n,q} A^I_{p,n}, \tag{A.45}$$

$$A^{II}_{2,p,q} = \sum_{n=0}^{N_{IV}} H^{(2)}_{n,q} A^{IV}_{p,n}, \tag{A.46}$$

$$A^{III}_{1,p,q} = \sum_{n=0}^{N_I} H^{(4)}_{n,q} A^I_{p,n}, \tag{A.47}$$

$$A^{III}_{2,p,q} = H^{(1)}_{p,q} A^{III}_{1,p,q}. \tag{A.48}$$

A.2.2 Diffraction problem, dock with spar

$\boldsymbol{C}^S_q$ is unchanged from the case of the dock without spar (cf. Eq. (A.33)). For each $p \in [0, N_S]$, the coefficients of $\mathbb{B}^S$ for the dock with the spar are:

$$\mathbb{B}^S_{q,j} = \sum_{n=0}^{N_{II}} \left(H^{(3)}_{j,n} H^{(6)}_{p,q,n} + H^{(4)}_{j,n} H^{(8)}_{p,q,n} \right) + \sum_{n=0}^{N_{III}} H^{(1)}_{p,n} H^{(4)}_{j,n} H^{(9)}_{p,q,n},$$

$$q \in [0, (N_I - 1)], j \in [0, (N_I - 1)], \tag{A.49}$$

$$\mathbb{B}^S_{q,j} = \sum_{n=0}^{N_{II}} H^{(2)}_{j,n} H^{(7)}_{p,q,n}, \quad q \in [0, (N_I - 1)], j \in [N_I, (N_{IV} - 1)], \tag{A.50}$$

$$\mathbb{B}^S_{q,j} = \frac{1}{Q^{IV}_{p,q,r}(a)} \sum_{n=0}^{N_{II}} H^{(3)}_{j,n} H^{(10)}_{p,q,n}, \quad q \in [N_I, (N_{IV} - 1)], j \in [N_I, (N_{IV} - 1)], \tag{A.51}$$

$$\mathbb{B}^S_{q,j} = \frac{1}{Q^{IV}_{p,q,r}(a)} \sum_{n=0}^{N_{II}} \sum_{m=0}^{N_{IV}} \left[H^{(2)}_{m,n} H^{(11)}_{p,q,n} - \delta_{m,q} P^{IV}_{p,q,r}(a) \right] H^{(14)}_{p,m,j},$$

$$q \in [N_I, (N_{IV} - 1)], j \in [N_I, (N_{IV} - 1)], \tag{A.52}$$

where $H^{(1)}$ to $H^{(9)}$ where defined in Eqs. (A.34) to (A.41) and are unchanged from the case of the dock without spar. $H^{(10)}$ to $H^{(14)}$ are given by:

$$H^{(10)}_{p,q,n} = \frac{1}{h} \epsilon_n T^{II}_{q,n} P^{II}_{p,n,r}(a), \tag{A.53}$$

$$H^{(11)}_{p,q,n} = \frac{1}{h} \epsilon_n T^{II}_{q,n} Q^{II}_{p,n,r}(a), \tag{A.54}$$

$$H^{(12)}_{p,q,n} = \frac{1}{h - d_0} T^V_{n,q}, \tag{A.55}$$

$$H^{(13)}_{p,q,n} = \begin{cases} \dfrac{p T^V_{q,0}}{h a_0} \text{ if } n = 0 \\ \dfrac{2n\pi I'_p \left(\dfrac{n\pi a_0}{h - d_0} \right)}{h(h - d_0) I_p \left(\dfrac{n\pi a_0}{h - d_0} \right)} T^V_{q,n} \text{ if } n > 0 \end{cases}, \tag{A.56}$$

$$H^{(14)}_{p,q,n} = \frac{1}{P^{IV}_{p,q,r}(a_0)} \left[\sum_{j=0}^{N_{IV}} \left(H^{(13)}_{p,q,j} H^{(12)}_{n,j} - \delta_{q,n} Q^{IV}_{p,q,r}(a_0) \right) \right]. \tag{A.57}$$

The remaining A coefficients are then expressed as:

$$A^{II}_{1,p,q} = \sum_{n=0}^{N_I} H^{(3)}_{n,q} A^{I}_{p,n}, \tag{A.58}$$

$$A^{II}_{2,p,q} = \sum_{n=0}^{N_{IV}} H^{(2)}_{n,q} A^{IV}_{1,p,n}, \tag{A.59}$$

$$A^{III}_{1,p,q} = \sum_{n=0}^{N_I} H^{(4)}_{n,q} A^{I}_{p,n}, \tag{A.60}$$

$$A^{III}_{2,p,q} = H^{(1)}_{p,q} A^{III}_{1,p,q}, \tag{A.61}$$

$$A^{IV}_{1,p,q} = \sum_{j=0}^{N_{IV}} H^{(14)}_{p,q,j} A^{IV}_{2,p,j}, \tag{A.62}$$

$$A^{V}_{p,q} = \sum_{n=0}^{N_{IV}} H^{(5)}_{n,q} A^{IV}_{2,p,n}. \tag{A.63}$$

A.2.3 Radiation problem, dock without spar

The coefficients of the matrices $\mathbb{B}^R$ and $\boldsymbol{C}^R$ for the radiation problem of the dock without spar are expressed as:

$$\mathbb{B}^R_{q,j} = \sum_{n=0}^{N_{II}} H^{(4)}_{n,q} H^{(2)}_{j,n} + \sum_{n=0}^{N_{III}} H^{(6)}_{n,q} H^{(3)}_{j,n} - \delta_{q,j}, \quad q \in [0, (N_I - 1)], j \in [0, (N_I - 1)], \tag{A.64}$$

$$\mathbb{B}^R_{q,j} = \sum_{n=0}^{N_{II}} H^{(5)}_{n,q} H^{(1)}_{j,n}, \quad q \in [0, (N_I - 1)], j \in [N_I, (N_{IV} - 1)], \tag{A.65}$$

$$\mathbb{B}^R_{q,j} = \sum_{n=0}^{N_{II}} H^{(7)}_{n,q} H^{(2)}_{j,n}, \quad q \in [N_I, (N_{IV} - 1)], j \in [0, (N_I - 1)], \tag{A.66}$$

$$\mathbb{B}^R_{q,j} = \sum_{n=0}^{N_{II}} H^{(8)}_{n,q} H^{(1)}_{j,n} - \delta_{q,j}, \quad q \in [N_I, (N_{IV}-1)], j \in [N_I, (N_{IV}-1)], \tag{A.67}$$

$$\boldsymbol{C}^R_q = \begin{cases} -H_{d,q} - \sum_{n=0}^{N_{II}} (H^{(4)}_{n,q} H_{b,n} + H^{(5)}_{n,q} H_{a,n}) - \sum_{n=0}^{N_{III}} H^{(6)}_{n,q} H_{c,n}, & q \in [0, (N_I - 1)] \\ -H_{e,q} - \sum_{n=0}^{N_{II}} (H^{(7)}_{n,q} H_{b,n} + H^{(8)}_{n,q} H_{a,n}) & q \in [N_I, (N_{IV}-1)] \end{cases}. \tag{A.68}$$

The coefficients H are given below for the radiation problems in surge, heave or pitch. In the coefficients below $m = 0$ in heave, and $m = 1$ in surge and pitch.

In surge, pitch and heave:

$$H_{g,q} = -\frac{P^{III}_{m,q,r}(b)}{Q^{III}_{m,q,r}(b)}, \tag{A.69}$$

$$H^{(1)}_{j,q} = H^{(2)}_{j,q} = \frac{1}{l} T^{II}_{j,q}, \tag{A.70}$$

$$H^{(3)}_{j,q} = \frac{1}{d} T^{III}_{j,q}, \tag{A.71}$$

In surge and pitch:

$$H^{(4)}_{j,q} = \frac{K_1(\alpha_q c)}{\alpha_q K_1'(\alpha_q c) h} \epsilon_j P^{II}_{m,j,r}(c) T^{II}_{q,j}, \tag{A.72}$$

$$H^{(5)}_{j,q} = \frac{K_1(\alpha_q c)}{\alpha_q K_1'(\alpha_q c) h} \epsilon_j Q^{II}_{m,j,r}(c) T^{II}_{q,j}, \tag{A.73}$$

$$H^{(6)}_{j,q} = \frac{K_1(\alpha_q c)}{\alpha_q K_1'(\alpha_q c) h} \left(P^{III}_{m,j,r}(c) - \frac{P^{III}_{m,j,r}(b)}{Q^{III}_{m,j,r}(b)} Q^{III}_{m,j,r}(c) \right) T^{III}_{q,j}, \tag{A.74}$$

$$H^{(7)}_{j,q} = \frac{I_1(\alpha_q a)}{\alpha_q I_1'(\alpha_q a) h} \epsilon_j P^{II}_{m,j,r}(a) T^{II}_{q,j}, \tag{A.75}$$

$$H^{(8)}_{j,q} = \frac{I_1(\alpha_q a)}{\alpha_q I_1'(\alpha_q a) h} \epsilon_j Q^{II}_{m,j,r}(a) T^{II}_{q,j}, \tag{A.76}$$

In surge:

$$H_{a,q} = H_{b,q} = H_{c,q} = 0, \tag{A.77}$$

$$H_{d,q} = \frac{K_1(\alpha_q c)}{\alpha_q K_1'(\alpha_q c) hb} \left(T_{q,1}^{B,surge} + \frac{1}{d} \sum_{n=0}^{\infty} \frac{T_n^{III,surge} Q_{m,n,r}^{III}(c) T_{q,n}^{III}}{Q_{m,n,r}^{III}(b)} \right), \tag{A.78}$$

$$H_{e,q} = \frac{I_1(\alpha_q a)}{\alpha_q I_1'(\alpha_q a) hb} T_{q,2}^{B,surge}, \tag{A.79}$$

$$H_{f,q} = \frac{T_q^{III,surge}}{db Q_{m,q,r}^{III}(b)}, \tag{A.80}$$

In heave:

$$H_{a,q} = -\frac{T_{q,1}^{II,heave}}{bl}, \tag{A.81}$$

$$H_{b,q} = -\frac{\tilde{T}_{q,1}^{II,heave}}{bl}, \tag{A.82}$$

$$H_{c,q} = -\frac{T_{q,2}^{III,heave}}{db}, \tag{A.83}$$

$$H_{e,q} = \frac{I_1(\alpha_q a)}{\alpha_q I_1'(\alpha_q a) hb} (T_{q,2}^{B,heave} + T_{q,3}^{II,heave}), \tag{A.84}$$

$$H_{f,q} = -\frac{T_{q,1}^{III,heave}}{db Q_{m,q,r}^{III}(b)}, \tag{A.85}$$

$$H_{j,p}^{(4)} = \frac{K_0(\alpha_q c)}{\alpha_q K_0'(\alpha_q c) h} \epsilon_j P_{m,j,r}^{II}(c) T_{q,j}^{II}, \tag{A.86}$$

$$H_{j,q}^{(5)} = \frac{K_0(\alpha_q c)}{\alpha_q K_0'(\alpha_q c) h} \epsilon_j Q_{m,j,r}^{II}(c) T_{m,q}^{II}, \tag{A.87}$$

$$H_{j,q}^{(6)} = \frac{K_0(\alpha_q c)}{\alpha_q K_0'(\alpha_q c) h} \left(P_{m,j,r}^{III}(c) - \frac{P_{m,j,r}^{III}(b)}{Q_{m,j,r}^{III}(b)} Q_{m,j,r}^{III}(c) \right) T_{q,j}^{III}, \tag{A.88}$$

$$H_{j,q}^{(7)} = \frac{I_0(\alpha_q a)}{\alpha_q I_0'(\alpha_q a)h}\epsilon_j P_{m,j,r}^{II}(a)T_{q,j}^{II}, \tag{A.89}$$

$$H_{j,q}^{(8)} = \frac{I_0(\alpha_q a)}{\alpha_q I_0'(\alpha_q a)h}\epsilon_j Q_{m,j,r}^{II}(a)T_{q,j}^{II}, \tag{A.90}$$

$$H_{d,q} = \frac{K_1(\alpha_q c)}{\alpha_q K_1'(\alpha_q c)hb}\left(T_{q,2}^{II,heave} + T_{q,1}^{B,heave} + T_{q,3}^{III,heave} - \frac{1}{d}\sum_{n=0}^{\infty}\frac{T_{n,1}^{III,heave}Q_{m,n,r}^{III}(c)T_{n,j}^{III}}{Q_{m,n,r}^{III}(b)}\right), \tag{A.91}$$

In pitch:

$$H_{a,q} = -\frac{T_{q,1}^{II,pitch}}{b^2 l}, \tag{A.92}$$

$$H_{b,q} = -\frac{\tilde{T}_{q,1}^{II,pitch}}{b^2 l}, \tag{A.93}$$

$$H_{d,q} = \frac{K_1(\alpha_q c)}{\alpha_q K_1'(\alpha_q c)hb^2}\Bigg(T_{q,2}^{II,pitch} + T_{q,1}^{B,pitch} + T_{q,4}^{III,pitch} + \frac{1}{d}\sum_{n=0}^{\infty}\frac{(T_{n,1}^{III,pitch} - T_{n,2}^{III,pitch})Q_{m,n,r}^{III}(c)T_{q,n}^{III}}{Q_{m,n,r}^{III}(b)}\Bigg), \tag{A.94}$$

$$H_{c,q} = -\frac{T_{q,3}^{III,pitch}}{db^2}, \tag{A.95}$$

$$H_{e,q} = \frac{I_1(\alpha_q a)}{\alpha_q I_1'(\alpha_q a)hb^2}(T_{q,2}^{B,pitch} + T_{q,3}^{II,pitch}), \tag{A.96}$$

$$H_{f,q} = \frac{(T_{q,1}^{III,pitch} - T_{q,2}^{III,pitch})}{db^2 Q_{m,q,r}^{III}(b)}k. \tag{A.97}$$

Once the matrix system of equation $\mathbb{B}^R \boldsymbol{A}^R = \boldsymbol{C}^R$ is solved for the A^I and A^{IV} coefficients, the remaining A coefficients are given by:

$$A_{1,p}^{II} = H_{b,p} + \sum_{q=0}^{N_I} H_{q,p}^{(2)} A_q^I, \tag{A.98}$$

$$A^{II}_{2,p} = H_{a,p} + \sum_{q=0}^{N_{IV}} H^{(1)}_{q,p} A^{IV}_q, \tag{A.99}$$

$$A^{III}_{1,p} = H_{c,p} + \sum_{q=0}^{N_I} H^{(3)}_{q,p} A^{I}_q, \tag{A.100}$$

$$A^{III}_{2,p} = H_{f,p} + H_{g,p} A^{III}_{1,p}. \tag{A.101}$$

A.2.4 Radiation problem, dock with spar

The coefficients of the matrices $\mathbb{B}^R$ and $\boldsymbol{C}^R$ are now given for the six radiation problems in surge, heave and pitch for both the dock and the spar:

$$\mathbb{B}^R_{p,j} = \sum_{q=0}^{N_{II}} H^{(5)}_{q,p} H^{(2)}_{j,q} + \sum_{q=0}^{N_{III}} H^{(7)}_{q,p} H^{(3)}_{j,q}, \quad p \in [0,(N_I-1)], j \in [0,(N_I-1)], \tag{A.102}$$

$$\mathbb{B}^R_{p,j} = \sum_{q=0}^{N_{II}} H^{(6)}_{q,p} H^{(1)}_{j,q} H^{(11)}_{j,q}, \quad p \in [0,(N_I-1)], j \in [N_I,(N_{IV}-1)], \tag{A.103}$$

$$\mathbb{B}^R_{p,j} = \frac{1}{Q^{IV}_{m,p,r}(a)} \sum_{q=0}^{N_{II}} H^{(8)}_{q,p} H^{(2)}_{j,q}, \quad p \in [N_I,(N_{IV}-1)], j \in [0,(N_I-1)], \tag{A.104}$$

$$\mathbb{B}^R_{p,j} = \frac{1}{Q^{IV}_{m,p,r}(a)} \sum_{q=0}^{N_{II}} H^{(11)}_{p,j} \left(H^{(9)}_{q,p} H^{(1)}_{j,q} - P^{IV}_{m,p,r}(a) \delta_{p,j} \right),$$

$$p \in [N_I,(N_{IV}-1)], j \in [N_I,(N_{IV}-1)], \tag{A.105}$$

$$\boldsymbol{C}_q^R = \begin{cases} -H_{g,p} - \sum_{q=0}^{\infty}\left(H_{q,p}^{(5)}H_{b,q} + H_{q,p}^{(6)}H_{a,q} + H_{q,p}^{(7)}H_{c,q} + \sum_{j=0}^{\infty}\sum_{q=0}^{\infty}H_{q,p}^{(6)}H_{j,q}^{(1)}H_{j,j}\right), \\ \qquad\qquad p \in [0,(N_I-1)] \\ -\frac{1}{Q_{m,p,r}^{IV}(a)}\left(H_{h,p} + \sum_{q=0}^{\infty}\left(H_{q,p}^{(8)}H_{b,q} + H_{q,p}^{(9)}H_{a,q}\right)\right. \\ \qquad\left. + \sum_{j=0}^{\infty}\sum_{q=0}^{\infty}H_{j,j}\left(H_{q,p}^{(9)}H_{j,q}^{(1)} - P_{m,p,r}^{IV}(a)\delta_{p,j}\right)\right), \\ \qquad\qquad p \in [N_I,(N_{IV}-1)] \end{cases} . \tag{A.106}$$

Then the coefficients H, where $m = 0$ in heave and $m = 1$ in pitch, $(p,q) \in \mathbb{N}^2$:

For all DoFs:

$$H_{q,p}^{(4)} = \frac{2}{h-d_0}T_{q,p}^{V}, \tag{A.107}$$

$$H_{q,p}^{(8)} = \frac{1}{h}\epsilon_q P_{m,q,r}^{II}(a)T_{p,q}^{II}, \tag{A.108}$$

$$H_{q,p}^{(9)} = \frac{1}{h}\epsilon_q Q_{m,q,r}^{II}(a)T_{p,q}^{II}, \tag{A.109}$$

$$H_{f,p} = -\frac{P_{m,q,r}^{III}(b)}{Q_{m,q,r}^{III}(b)}, \tag{A.110}$$

$$H_{q,p}^{(1)} = H_{q,p}^{(2)} = \frac{1}{l}T_{q,p}^{II}, \tag{A.111}$$

$$H_{q,p}^{(3)} = \frac{1}{d}T_{q,p}^{III} \tag{A.112}$$

$$H_{p,q}^{(11)} = \frac{1}{P_{m,p,r}^{IV}(a_0)}\sum_{j=0}^{N_V}H_{j,p}^{(10)}H_{q,j}^{(4)}\left(1 - Q_{m,p,r}^{IV}(a_0)\delta_{q,p}\right), \tag{A.113}$$

$$H_{j,p} = \frac{1}{P_{m,p,r}^{IV}(a_0)}\left[H_{i,p} + \sum_{q=0}^{N_V}H_{q,p}^{(10)}H_{d,q}\right], \tag{A.114}$$

In surge (2): and DoFs (1):

$$H_{a,p} = H_{b,p} = H_{c,p} = 0, \tag{A.115}$$

In surge (2)

$$H_{e,p} = \frac{T_p^{III,surge}}{dbQ_{m,q,r}^{III}(b)}, \tag{A.116}$$

$$H_{g,p} = \frac{K_1(\alpha_p c)}{\alpha_p K_1'(\alpha_p c)hb}\left(T_{p,1}^{B,surge} + \frac{1}{d}\sum_{j=0}^{\infty}\frac{T_j^{III,surge}Q_{m,j,r}^{III}(c)T_{p,j}^{III}}{Q_{m,j,r}^{III}(b)}\right), \tag{A.117}$$

$$H_{h,p} = \frac{T_{p,2}^{B,surge}}{hb}, \tag{A.118}$$

In both surge and pitch (1), (2):

$$H_{q,p}^{(5)} = \frac{K_1(\alpha_p c)}{\alpha_p K_1'(\alpha_p c)h}\epsilon_q P_{m,q,r}^{II}(c)T_{p,q}^{II}, \tag{A.119}$$

$$H_{q,p}^{(6)} = \frac{K_1(\alpha_p c)}{\alpha_p K_1'(\alpha_p c)h}\epsilon_q Q_{m,q,r}^{II}(c)T_{p,q}^{II}, \tag{A.120}$$

$$H_{q,p}^{(7)} = \frac{K_1(\alpha_p c)}{\alpha_p K_1'(\alpha_p c)h}\left(P_{m,q,r}^{III}(c) - \frac{P_{m,q,r}^{III}(b)}{Q_{m,q,r}^{III}(b)}Q_{m,q,r}^{III}(c)\right)T_{p,q}^{III}, \tag{A.121}$$

$$H_{q,p}^{(10)} = \frac{2}{h}\begin{cases} \dfrac{T_{p,0}^{V}}{2a_0} \text{ if } q = 0 \\ \dfrac{q\pi}{h-d_0}\dfrac{I_1'(\frac{q\pi a_0}{h-d_0})}{I_1(\frac{q\pi a_0}{h-d_0})}T_{p,q}^{V} \text{ if } q \geq 1 \end{cases}, \tag{A.122}$$

In surge (1) and DoFs (2):

$$H_{d,p} = 0, \tag{A.123}$$

In all DoFs (1):

$$H_{e,p} = H_{g,p} = H_{h,p} = 0, \tag{A.124}$$

In all DoFs (2):

$$H_{i,p} = 0, \tag{A.125}$$

In heave (1), (2):

$$H^{(5)}_{q,p} = \frac{K_0(\alpha_p c)}{\alpha_p K_0'(\alpha_p c)h}\epsilon_q P^{II}_{m,q,r}(c) T^{II}_{p,q}, \tag{A.126}$$

$$H^{(6)}_{q,p} = \frac{K_0(\alpha_p c)}{\alpha_p K_0'(\alpha_p c)h}\epsilon_q Q^{II}_{m,q,r}(c) T^{II}_{p,q}, \tag{A.127}$$

$$H^{(7)}_{q,p} = \frac{K_0(\alpha_p c)}{\alpha_p K_0'(\alpha_p c)h}\left(P^{III}_{m,q,r}(c) - \frac{P^{III}_{m,q,r}(b)}{Q^{III}_{m,q,r}(b)} Q^{III}_{m,q,r}(c)\right) T^{III}_{p,q}, \tag{A.128}$$

$$H^{(10)}_{q,p} = \frac{2}{h}\begin{cases} 0 \text{ if } q = 0 \\ \\ \dfrac{q\pi}{h - d_0}\dfrac{I_0'(\frac{q\pi a_0}{h-d_0})}{I_0(\frac{q\pi a_0}{h-d_0})} T^V_{p,q} \text{ if } q \geq 1 \end{cases}, \tag{A.129}$$

In heave (2):

$$H_{a,p} = -\frac{T^{II,heave}_{p,1}}{bl}, \tag{A.130}$$

$$H_{b,p} = -\frac{\tilde{T}^{II,heave}_{p,1}}{bl}, \tag{A.131}$$

$$H_{c,p} = -\frac{T^{III,heave}_{p,2}}{db}, \tag{A.132}$$

$$H_{e,p} = -\frac{T^{III,heave}_{p,1}}{db Q^{III}_{m,q,r}(b)}, \tag{A.133}$$

$$H_{g,p} = \frac{K_1(\alpha_p c)}{\alpha_p K_1'(\alpha_p c) hb}\left(T^{II,heave}_{p,2} + T^{B,heave}_{p,1} + T^{III,heave}_{p,3} - \frac{1}{d}\sum_{j=0}^{\infty}\frac{T^{III,heave}_{j,1} Q^{III}_{m,j,r}(c) T^{III}_{p,j}}{Q^{III}_{m,j,r}(b)}\right), \tag{A.134}$$

$$H_{h,p} = \frac{T^{B,heave}_{p,2} + T^{II,heave}_{p,3}}{hb}, \tag{A.135}$$

In pitch (2):

$$H_{a,p} = -\frac{T_{p,1}^{II,pitch}}{b^2 l}, \tag{A.136}$$

$$H_{b,p} = -\frac{\tilde{T}_{p,1}^{II,pitch}}{b^2 l}, \tag{A.137}$$

$$H_{c,p} = -\frac{T_{p,3}^{III,pitch}}{db^2}, \tag{A.138}$$

$$H_{e,p} = \frac{\left(T_{p,1}^{III,pitch} - T_{p,2}^{III,pitch}\right)}{db^2 Q_{m,q,r}^{III}(b)} k \tag{A.139}$$

$$H_{g,p} = \frac{K_1(\alpha_p c)}{\alpha_p K_1'(\alpha_p c) h b^2} \left(T_{p,2}^{II,pitch} + T_{p,1}^{B,pitch} + T_{p,4}^{III,pitch} + \frac{1}{d} \sum_{j=0}^{\infty} \frac{\left(T_{j,1}^{III,pitch} - T_{j,2}^{III,pitch}\right) Q_{m,j,r}^{III}(c) T_{p,j}^{III}}{Q_{m,j,r}^{III}(b)} \right), \tag{A.140}$$

$$H_{h,p} = \frac{T_{p,2}^{B,pitch} + T_{p,3}^{II,pitch}}{hb^2}, \tag{A.141}$$

In surge (1):

$$H_{i,p} = \frac{T_{p,3}^{B,surge}}{bh}, \tag{A.142}$$

In heave (1):

$$H_{d,p} = -\frac{2T_{p,1}^{V,heave}}{b(h - d_0)}, \tag{A.143}$$

$$H_{i,p} = \frac{T_{p,2}^{V,heave}}{bh}, \tag{A.144}$$

In pitch (1):

$$H_{d,p} = -\frac{2T_{p,1}^{V,pitch}}{b^2(h-d_0)}k, \tag{A.145}$$

$$H_{i,p} = \frac{T_{p,2}^{V,pitch} + T_{p,3}^{B,pitch}}{b^2 h}. \tag{A.146}$$

Finally, the remaining A coefficients are given by:

$$A_{2,p}^{II} = H_{a,p} + \sum_{q=0}^{N_{IV}} H_{q,p}^{(1)} A_{1,q}^{IV}, \tag{A.147}$$

$$A_{1,p}^{II} = H_{b,p} + \sum_{q=0}^{N_I} H_{q,p}^{(2)} A_q^I, \tag{A.148}$$

$$A_{1,p}^{III} = H_{c,p} + \sum_{q=0}^{N_I} H_{q,p}^{(3)} A_q^I, \tag{A.149}$$

$$A_p^V = H_{d,p} + \sum_{q=0}^{N_{IV}} H_{q,p}^{(4)} A_{2,q}^{IV}, \tag{A.150}$$

$$A_{2,p}^{III} = H_{e,p} + H_{f,p} A_{1,p}^{III}, \tag{A.151}$$

$$A_{1,p}^{IV} = H_{j,p} + \sum_{q=0}^{N_{IV}} H_{q,p}^{(11)} A_{2,q}^{IV} \tag{A.152}$$

A.3 Exciting forces and moments

A.3.1 Dock without spar

The semi-analytical expressions of the forces in surge and heave and moment in pitch from the scattering of incident waves on the dock without spar, as derived in Sec. 2.2.2, are given by:

$$F_1^S = 2i\omega^2 b\pi\zeta_A \rho \left[a\sum_{q=0}^{\infty} A_{1,q}^{IV} T_{q,2}^{B,surge} - b\sum_{q=0}^{\infty} A_{2,1,q}^{III} T_q^{III,surge} - c\sum_{q=0}^{\infty} A_{1,q}^{I} T_{q,1}^{B,surge} \right] e^{-i\omega t}, \tag{A.153}$$

$$F_3^S = 2\pi b\omega^2\zeta_A\rho\Bigg[\sum_{q=0}^{\infty}\epsilon_q(-1)^q\left(A^{II}_{1,0,q}\int_a^c P^{II}_{0,q}(r)rdr + A^{II}_{2,0,q}\int_a^c Q^{II}_{0,q}(r)rdr\right)$$

$$-\sum_{q=0}^{\infty}\left(A^{III}_{1,0,q}\int_b^c P^{III}_{0,q}(r)rdr + A^{III}_{2,0,q}\int_b^c Q^{III}_{0,q}(r)rdr\right)\tilde{N}_q^{-\frac{1}{2}}\Bigg]e^{-i\omega t}, \tag{A.154}$$

$$F_5^S = 2i\omega^2\zeta_A\rho\Bigg[ba\pi\sum_{q=0}^{\infty}A^{IV}_{1,q}T^{B,pitch}_{q,2}$$

$$-\pi b\sum_{q=0}^{\infty}(-1)^q\epsilon_q\left(A^{II}_{1,1,q}\int_a^c P^{II}_{1,q}(r)r^2dr + A^{II}_{2,1,q}\int_a^c Q^{II}_{1,q}(r)r^2dr\right)$$

$$+\pi b\sum_{q=0}^{\infty}\left(A^{III}_{1,1,q}\int_b^c P^{III}_{1,q}(r)r^2dr + A^{III}_{2,1,q}\int_b^c Q^{III}_{1,q}(r)r^2dr\right)\tilde{N}_q^{-\frac{1}{2}}$$

$$-\pi b^2\sum_{q=0}^{\infty}A^{III}_{2,1,q}T^{III,pitch}_{q,1} - bc\pi\sum_{q=0}^{\infty}A^{I}_{1,q}T^{B,pitch}_{q,1}\Bigg]e^{-i\omega t}. \tag{A.155}$$

A.3.2 Dock with spar

The loads on the dock and spar derived in Sec. 2.2.3, are given by:

$$F_1^{(2),S} = -2i\omega^2 b\pi\zeta_A\rho\left[c\sum_{q=0}^{\infty}A^{I}_{1,q}T^{B,surge}_{q,1} + b\sum_{q=0}^{\infty}A^{III}_{2,1,q}T^{III,surge}_{q} - a\sum_{q=0}^{\infty}A^{IV}_{1,1,q}T^{B,surge}_{q,2}\right]e^{-i\omega t}, \tag{A.156}$$

$$F_1^{(1),S} = -2i\omega^2 b\pi\zeta_A\rho\left[a_0\sum_{q=0}^{\infty}A^{IV}_{2,1,q}T^{Surge}_{q,4}\right]e^{-i\omega t}, \tag{A.157}$$

$$F_3^{(2),S} = \omega^2\zeta_A\rho\Bigg[2\pi b\sum_{q=0}^{\infty}\epsilon_q(-1)^q\left(A^{II}_{1,0,q}\int_a^c P^{II}_{0,q}(r)rdr + A^{II}_{2,0,q}\int_a^c Q^{II}_{0,q}(r)rdr\right)$$

$$-2\pi b\sum_{q=0}^{\infty}\left(A^{III}_{1,0,q}\int_b^c P^{III}_{0,q}(r)rdr + A^{III}_{2,0,q}\int_b^c Q^{III}_{0,q}(r)rdr\right)\tilde{N}_q^{-\frac{1}{2}}\Bigg]e^{-i\omega t}, \tag{A.158}$$

$$F_3^{(1),S} = 2\omega^2\zeta_A\rho\pi b\left[\frac{1}{2}a_0^2A_{0,0}^V + 2\sum_{q=1}^{\infty}(-1)^q\frac{a_0(h-d_0)}{q\pi}\frac{I_1(\frac{q\pi a_0}{(h-d_0)})}{I_0(\frac{q\pi a_0}{(h-d_0)})}A_{0,q}^V\right]e^{-i\omega t}, \tag{A.159}$$

$$\begin{aligned}F_5^{(2),S} =& 2i\omega^2\zeta_A\rho\Bigg[ba\pi\sum_{q=0}^{\infty}A_{1,1,q}^{IV}T_{q,1}^{B,pitch}\\ &-\pi b\sum_{q=0}^{\infty}(-1)^q\epsilon_q\left(A_{1,1,q}^{II}\int_a^c P_{1,q}^{II}(r)r^2dr + A_{2,1,q}^{II}\int_a^c Q_{1,q}^{II}(r)r^2dr\right)\\ &+\pi b\sum_{q=0}^{\infty}\left(A_{1,1,q}^{III}\int_b^c P_{1,q}^{III}(r)r^2dr + A_{2,1,q}^{III}\int_b^c Q_{1,q}^{III}(r)r^2dr\right)\tilde{N}_q^{-\frac{1}{2}}\\ &-\pi b^2\sum_{q=0}^{\infty}A_{2,1,q}^{III}T_{q,1}^{III,pitch} - bc\pi\sum_{q=0}^{\infty}A_{1,q}^{I}T_{q,2}^{B,pitch}\Bigg]e^{-i\omega t},\end{aligned} \tag{A.160}$$

$$F_5^{(1),S} = -2i\omega^2\zeta_A\rho b\pi\left[a_0\sum_{q=0}^{\infty}A_{2,1,q}^{IV}T_{q,3}^{B,pitch} + \frac{a_0^3}{4}A_{1,0}^V + 2\sum_{q=1}^{\infty}(-1)^q\frac{\int_0^{a_0}I_1(\frac{q\pi r}{(h-d_0)})r^2dr}{I_1(\frac{q\pi a_0}{(h-d_0)})}A_{1,q}^V\right]e^{-i\omega t} \tag{A.161}$$

A.4 Added mass and damping coefficients

A.4.1 Dock without spar

The semi-analytical expressions of the added mass and damping coefficients derived in Sec. 2.3.1 for the dock without spar are:

$$\begin{aligned}a_{1,1} + i\frac{b_{1,1}}{\omega} =& -\rho\pi bc\sum_{q=0}^{\infty}T_{q,1}^{B,surge}A_q^I\\ &+\rho\pi ba\sum_{q=0}^{\infty}T_{q,2}^{B,surge}A_q^{IV} - \rho\pi b^2\sum_{q=0}^{\infty}A_{2,q}^{III}T_q^{III,surge},\end{aligned} \tag{A.162}$$

$$\begin{aligned}a_{3,3} + i\frac{b_{3,3}}{\omega} =& -\frac{\rho\pi}{8l}\left[c^4 - a^4 - 4l^2(c^2-a^2)\right]\\ &+\rho\pi\left(d - \frac{g}{\omega^2}\right)(c^2-b^2)\\ &+2\rho\pi b\sum_{q=0}^{\infty}(-1)^q\epsilon_q\left[\int_a^c P_{0,q}^{II}(r)rdrA_{1,q}^{II} + \int_a^c Q_{0,q}^{II}(r)rdrA_{2,q}^{II}\right]\end{aligned}$$

$$- 2\rho\pi b\sum_{q=0}^{\infty}\tilde{N}_q^{-\frac{1}{2}}\left[\int_b^c P_{0,q}^{III}(r)rdrA_{1,q}^{III}+\int_b^c Q_{0,q}^{III}(r)rdrA_{2,q}^{III}\right], \quad \text{(A.163)}$$

$$\begin{aligned}
a_{5,5}+i\frac{b_{5,5}}{\omega} =& -\frac{\rho\pi}{48l}(c^6-a^6-6l^2(c^4-a^4))\\
&+\frac{\rho\pi b^2d^2}{3\omega^2}\left(d\omega^2-\frac{3g}{2}\right)+\frac{\rho\pi}{4\omega^2}(c^4-b^4)(d\omega^2-g)\\
&-\rho\pi b^2c\sum_{q=0}^{\infty}A_q^I T_{q,1}^{B,pitch}+\rho\pi b^2a\sum_{q=0}^{\infty}A_q^{IV}T_{q,2}^{B,pitch}\\
&-\rho\pi b^2\sum_{q=0}^{\infty}(-1)^q\epsilon_q\left[\int_a^c P_{1,q}^{II}(r)r^2drA_{1,q}^{II}+\int_a^c Q_{1,q}^{II}(r)r^2drA_{2,q}^{II}\right]\\
&-\rho\pi b^2\sum_{q=0}^{\infty}\Bigg[-\tilde{N}_q^{-\frac{1}{2}}\int_b^c P_{1,q}^{III}(r)r^2drA_{1,q}^{III}\\
&+\left(bT_{q,1}^{III,pitch}-\tilde{N}_q^{-\frac{1}{2}}\int_b^c Q_{1,q}^{III}(r)r^2dr\right)A_{2,q}^{III}\Bigg], \quad \text{(A.164)}
\end{aligned}$$

$$\begin{aligned}
a_{1,5}+i\frac{b_{1,5}}{\omega} =&\rho\pi b^2d\left(\frac{g}{\omega^2}-\frac{d}{2}\right)-\rho\pi b^3\sum_{q=0}^{\infty}A_{2,q}^{III}T_q^{III,surge}\\
&+\rho\pi ab^2\sum_{q=0}^{\infty}T_{q,2}^{B,surge}A_q^{IV}-\rho\pi cb^2\sum_{q=0}^{\infty}T_{q,1}^{B,surge}A_q^I, \quad \text{(A.165)}
\end{aligned}$$

$$\begin{aligned}
a_{5,1}+i\frac{b_{5,1}}{\omega} =&\rho\pi ab\sum_{q=0}^{\infty}T_{q,2}^{B,pitch}A_q^{IV}-\rho\pi cb\sum_{q=0}^{\infty}T_{q,1}^{B,pitch}A_q^I\\
&-\rho\pi b\sum_{q=0}^{\infty}\epsilon_q(-1)^q\left[\int_a^c P_{1,q}^{II}(r)r^2drA_{1,q}^{II}+\int_a^c Q_{1,q}^{II}(r)r^2drA_{2,q}^{II}\right]\\
&\rho\pi b\sum_{q=0}^{\infty}\tilde{N}_q^{-\frac{1}{2}}\left[\int_a^c P_{1,q}^{III}(r)r^2drA_{1,q}^{III}+\int_a^c Q_{1,q}^{III}(r)r^2drA_{2,q}^{III}\right]\\
&-\rho\pi b^2\sum_{q=0}^{\infty}A_{2,q}^{III}T_{q,1}^{III,pitch}. \quad \text{(A.166)}
\end{aligned}$$

Newman (1962) established relationships between the radiation damping and the amplitude (but not the phase) of the exciting forces and moments for axi-symmetrical bodies, given by:

$$|F_1^S| = \zeta_A\left(\frac{4\rho^3 g}{\omega^3}b_{1,1}(\omega)\right)^{\frac{1}{2}} \quad \text{(A.167)}$$

$$|F_3^S| = \zeta_A(\frac{2\rho^3 g}{\omega^3} b_{3,3}(\omega))^{\frac{1}{2}} \tag{A.168}$$

$$|F_5^S| = \zeta_A(\frac{4\rho^3 g}{\omega^3} b_{5,5}(\omega))^{\frac{1}{2}} \tag{A.169}$$

A.4.2 Dock with spar

Added mass and damping coefficients for the dock with spar derived in Sec. 2.3.2 are:

$$a_{1,1}^{(1)} + i\frac{b_{1,1}^{(1)}}{\omega} = -\rho\pi a_0 b \sum_{q=0}^{\infty} T_{q,3}^{B,surge} A_{2,q}^{IV}, \tag{A.170}$$

$$a_{3,3}^{(1)} + i\frac{b_{3,3}^{(1)}}{\omega} = \pi\rho\frac{4(h-d_0)^2 a_0^2 - a_0^4}{8(h-d_0)} + \pi\rho b a_0^2 A_0^V + 4\pi\rho b \sum_{q=1}^{\infty} \frac{(-1)^q a_0 (h-d_0) I_1\left(\frac{q\pi a_0}{h-d_0}\right)}{q\pi I_0\left(\frac{q\pi a_0}{h-d_0}\right)} A_q^V, \tag{A.171}$$

$$\begin{aligned} a_{5,5}^{(1)} + i\frac{b_{5,5}^{(1)}}{\omega} = & -\rho\pi a_0 b^2 \sum_{q=0}^{\infty} T_{q,3}^{B,pitch} A_{2,q}^{IV} - \rho\pi\frac{a_0^4}{8}\frac{a_0^2/6 - (h-d_0)^2}{h-d0} - \rho b^2 \frac{a_0^3}{4} A_0^V \\ & - 2\rho\pi b^2 \sum_{q=1}^{\infty} \frac{(-1)^q a_0 (h-d_0)^2}{q^2\pi^2 I_1\left(\frac{q\pi a_0}{h-d_0}\right)} \left[\frac{q\pi}{h-d0} a_0 I_0\left(\frac{q\pi a_0}{h-d_0}\right) - 2I_1\left(\frac{q\pi a_0}{h-d_0}\right)\right] A_q^V, \end{aligned} \tag{A.172}$$

$$a_{1,5}^{(1)} + i\frac{b_{1,5}^{(1)}}{\omega} = -\rho\pi a_0 b^2 \sum_{q=0}^{\infty} T_{q,3}^{B,surge} A_{2,q}^{IV}, \tag{A.173}$$

$$\begin{aligned} a_{5,1}^{(1)} + i\frac{b_{5,1}^{(1)}}{\omega} = & -\rho\pi a_0^2 b \sum_{q=0}^{\infty} T_{q,3}^{B,pitch} A_{2,q}^{IV} \\ & - \rho\pi b \left[A_0^V \frac{a_0^3}{4} + 2\sum_{q=0}^{\infty} A_q^V (-1)^q \frac{a_0 (h-d_0)^2}{q^2\pi^2} \left(\frac{q\pi a_0 I_0\left(\frac{q\pi a_0}{h-d_0}\right)}{(h-d_0) I_1\left(\frac{q\pi a_0}{h-d_0}\right)} - 2 \right) \right], \end{aligned} \tag{A.174}$$

$$a_{1,1}^{(2)}+i\frac{b_{1,1}^{(2)}}{\omega}=-\rho\pi bc\sum_{q=0}^{\infty}T_{q,1}^{B,surge}A_q^I+\rho\pi ba\sum_{q=0}^{\infty}T_{q,2}^{B,surge}A_{1,q}^{IV}-\rho\pi b^2\sum_{q=0}^{\infty}A_{2,q}^{III}T_q^{III,surge}, \tag{A.175}$$

$$\begin{aligned}a_{3,3}^{(2)}+i\frac{b_{3,3}^{(2)}}{\omega}=&-\frac{\rho\pi}{8l}\left[c^4-a^4-4l^2(c^2-a^2)\right]+\rho\pi\left((d-\frac{g}{\omega^2}\right)(c^2-b^2)\\&+2\rho\pi b\sum_{q=0}^{\infty}(-1)^q\epsilon_q\left(\left[\int_a^c P_{0,q}^{II}(r)rdrA_{1,q}^{II}+\int_a^c Q_{0,q}^{II}(r)rdrA_{2,q}^{II}\right]\right.\\&-2\rho\pi b\sum_{q=0}^{\infty}\tilde{N}_q^{-\frac{1}{2}}\left(\left[\int_b^c P_{0,q}^{III}(r)rdrA_{1,q}^{III}+\int_b^c Q_{0,q}^{III}(r)rdrA_{2,q}^{III}\right],\end{aligned} \tag{A.176}$$

$$\begin{aligned}a_{5,5}^{(2)}+i\frac{b_{5,5}^{(2)}}{\omega}=&-\frac{\rho\pi}{48l}\left((c^6-a^6-6l^2(c^4-a^4)\right)+\frac{\rho\pi b^2d^2}{3\omega^2}\left((d\omega^2-\frac{3g}{2}\right)+\frac{\rho\pi}{4\omega^2}(c^4-b^4)(d\omega^2-g)\\&-\rho\pi b^2c\sum_{q=0}^{\infty}A_q^IT_{q,1}^{B,pitch}+\rho\pi b^2a\sum_{q=0}^{\infty}A_{1,q}^{IV}T_{q,2}^{B,pitch}\\&-\rho\pi b^2\sum_{q=0}^{\infty}(-1)^q\epsilon_q\left[\int_a^c P_{1,q}^{II}(r)r^2drA_{1,q}^{II}+\int_a^c Q_{1,q}^{II}(r)r^2drA_{2,q}^{II}\right]\\&-\rho\pi b^2\sum_{q=0}^{\infty}\left[-\tilde{N}_q^{-\frac{1}{2}}\int_b^c P_{1,q}^{III}(r)r^2drA_{1,q}^{III}\right.\\&+\left.\left(bT_{q,1}^{III,pitch}-\tilde{N}_q^{-\frac{1}{2}}\int_b^c Q_{1,q}^{III}(r)r^2dr\right)A_{2,q}^{III}\right],\end{aligned} \tag{A.177}$$

$$\begin{aligned}a_{1,5}^{(2)}+i\frac{b_{1,5}^{(2)}}{\omega}=&\rho\pi b^2d\left(\frac{g}{\omega^2}-\frac{d}{2}\right)-\rho\pi b^3\sum_{q=0}^{\infty}A_{2,q}^{III}T_q^{III,surge}\\&+\rho\pi ab^2\sum_{q=0}^{\infty}T_{q,2}^{B,surge}A_{1,q}^{IV}-\rho\pi cb^2\sum_{q=0}^{\infty}T_{q,1}^{B,surge}A_q^I,\end{aligned} \tag{A.178}$$

$$\begin{aligned}a_{5,1}^{(2)}+i\frac{b_{5,1}^{(2)}}{\omega}=&\rho\pi ab\sum_{q=0}^{\infty}T_{q,2}^{B,pitch}A_{1,q}^{IV}-\rho\pi cb\sum_{q=0}^{\infty}T_{q,1}^{B,pitch}A_q^I\\&-\rho\pi b\sum_{q=0}^{\infty}\epsilon_q(-1)^q\left[\int_a^c P_{1,q}^{II}(r)r^2drA_{1,q}^{II}+\int_a^c Q_{1,q}^{II}(r)r^2drA_{2,q}^{II}\right]\end{aligned}$$

$$\rho\pi b\sum_{q=0}^{\infty}\tilde{N}_q^{-\frac{1}{2}}\left[\int_a^c P_{1,q}^{III}(r)r^2drA_{1,q}^{III}+\int_a^c Q_{1,q}^{III}(r)r^2drA_{2,q}^{III}\right]$$
$$-\rho\pi b^2\sum_{q=0}^{\infty}A_{2,q}^{III}T_{q,1}^{III,pitch}. \tag{A.179}$$

$$d_{1,1}^{(1)}+i\frac{e_{1,1}^{(1)}}{\omega}=-\rho\pi a_0 b\sum_{q=0}^{\infty}T_{q,3}^{B,surge}A_{2,q}^{IV}, \tag{A.180}$$

$$d_{3,3}^{(1)}+i\frac{e_{3,3}^{(1)}}{\omega}=2\pi\rho b\frac{a_0^2}{2}A_0^V+2b\sum_{q=1}^{\infty}\frac{(-1)^q a_0(h-d_0)I_1\left(\frac{q\pi a_0}{h-d_0}\right)}{q\pi I_0\left(\frac{q\pi a_0}{h-d_0}\right)}A_q^V, \tag{A.181}$$

$$d_{5,5}^{(1)}+i\frac{e_{5,5}^{(1)}}{\omega}=-\rho\pi a_0 b^2\sum_{q=0}^{\infty}T_{q,3}^{B,pitch}A_{2,q}^{IV}-\rho b^2\frac{a_0^3}{4}A_0^V$$
$$-2\rho\pi b^2\sum_{q=1}^{\infty}\frac{(-1)^q a_0(h-d_0)^2}{q^2\pi^2 I_1\left(\frac{q\pi a_0}{h-d_0}\right)}\left[\frac{q\pi}{h-d0}a_0 I_0\left(\frac{q\pi a_0}{h-d_0}\right)-2I_1\left(\frac{q\pi a_0}{h-d_0}\right)\right]A_q^V, \tag{A.182}$$

$$d_{1,5}^{(1)}+i\frac{e_{1,5}^{(1)}}{\omega}=-\rho\pi a_0 b^2\sum_{q=0}^{\infty}T_{q,3}^{B,surge}A_{2,q}^{IV}, \tag{A.183}$$

$$d_{5,1}^{(1)}+i\frac{e_{5,1}^{(1)}}{\omega}=-\rho\pi a_0 b\sum_{q=0}^{\infty}T_{q,3}^{B,pitch}A_{2,q}^{IV}-\rho b\frac{a_0^3}{4}A_0^V$$
$$-2\rho\pi b\sum_{q=1}^{\infty}\frac{(-1)^q a_0(h-d_0)^2}{q^2\pi^2 I_1\left(\frac{q\pi a_0}{h-d_0}\right)}\left[\frac{q\pi}{h-d0}a_0 I_0\left(\frac{q\pi a_0}{h-d_0}\right)-2I_1\left(\frac{q\pi a_0}{h-d_0}\right)\right]A_q^V. \tag{A.184}$$

A.5 Convergence study

Results of a convergence study carried out for the dock without spar in WAMIT are presented in Fig. A.1 for the scattering loads and in Fig. A.2 for the added mass and damping coefficients. It includes both a mesh convergence study for the simulations in WAMIT, and a convergence study on the number of modes for the DD method. Simulations in WAMIT shows a peak in the phases of the loads or on the damping coefficients at the natural sloshing natural frequency, even for the finest mesh, and most likely due to numerical errors. On the other hand, added mass coefficients converged even for the coarsest mesh considered (see Fig. 2.4 in Sec. 2.4.1). The semi-analytical scattering loads converge for very few eigenmodes in each subdomain. For the radiation problem in heave and pitch however, a higher number of modes are required. This was expected as the choice of eigenmodes chosen in the subdomains at the bottom of the dock are not adapted for corner flows. Better eigenfunction expansions for the radiation problem in heave are for example presented by Faltinsen et al. (2007).
When the dimensions of the bilge-boxes goes to 0, the added mass and damping coefficients with the present semi-analytical method converge to the results from Mavrakos (1988) for the circular cylinder with thick walls. Comparisons between both results are shown in Figs. A.3 and A.4 for $(c-b)/a = 0.01$ and $s/a = 0.01$.

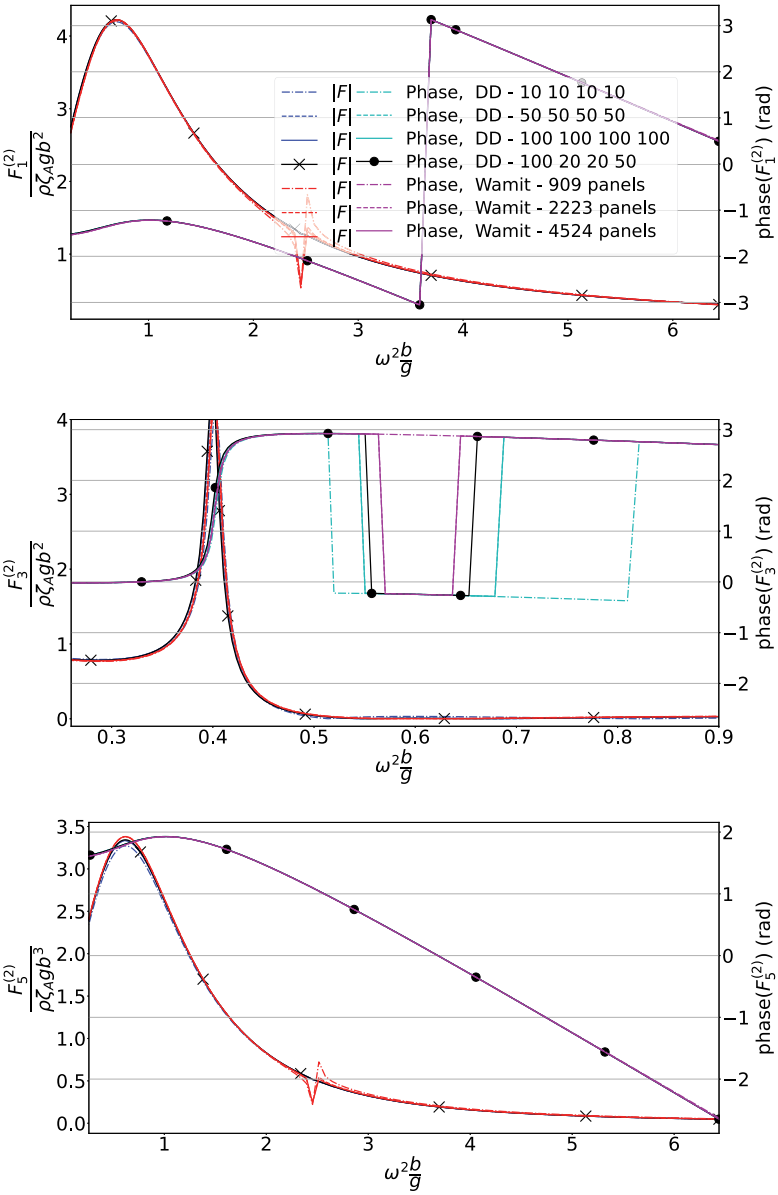

Figure A.1: *Non-dimensional amplitude of exciting forces and moments (left axis) and their phases (right axis) computed by the present DD method and the panel software WAMIT. Simulations for the dock without spar. Top: force in surge. Middle: force in heave. Bottom: moment in pitch.*

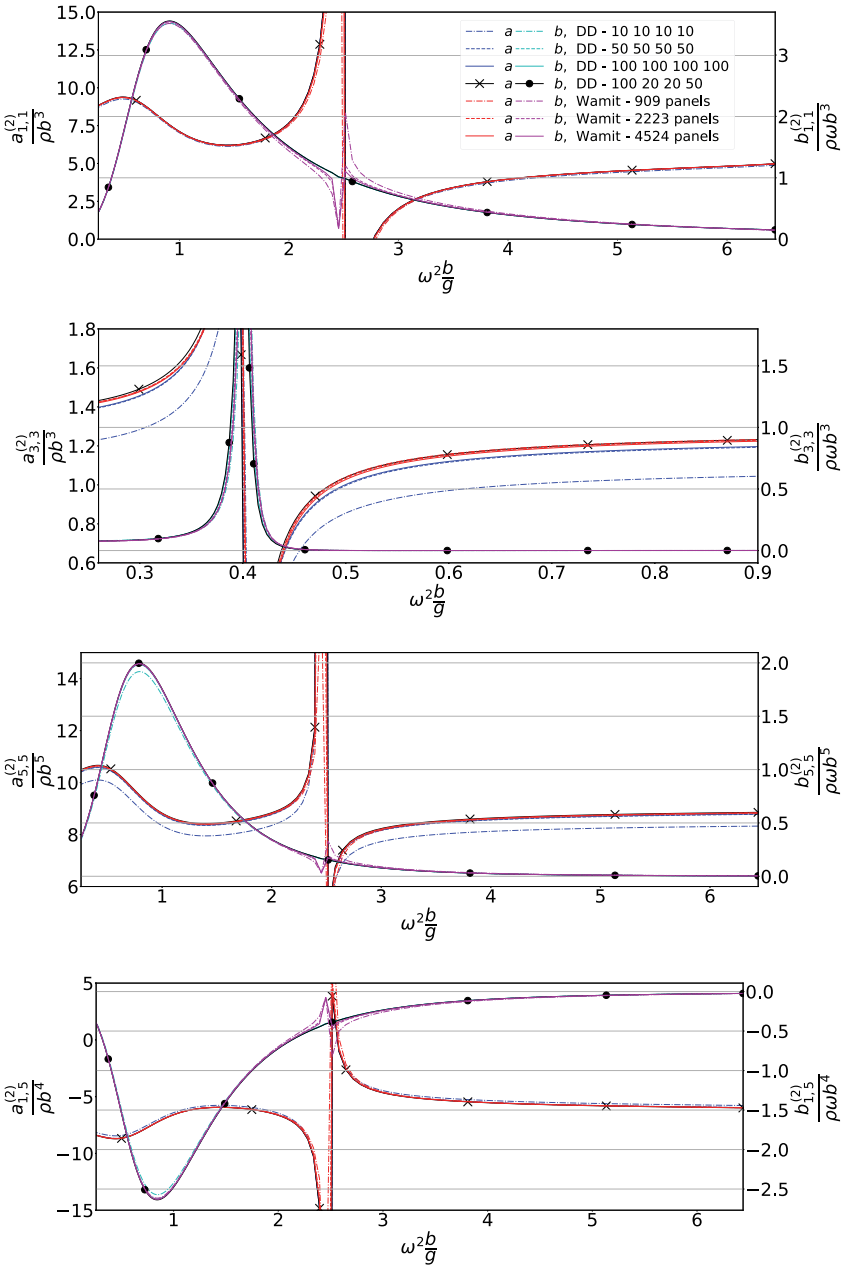

Figure A.2: *Non-dimensional added mass (left axis) and damping coefficients (right axis) computed by the present DD method and the panel software WAMIT. Simulations for the dock without spar. In the legend, a and b stand for the added mass and damping coefficients, respectively, and the number of modes associated to the domain decomposition (DD) method are given in the order from N_I to N_{IV}. From top to bottom: coefficients in surge, heave, pitch, and coupled coefficients in surge and pitch.*

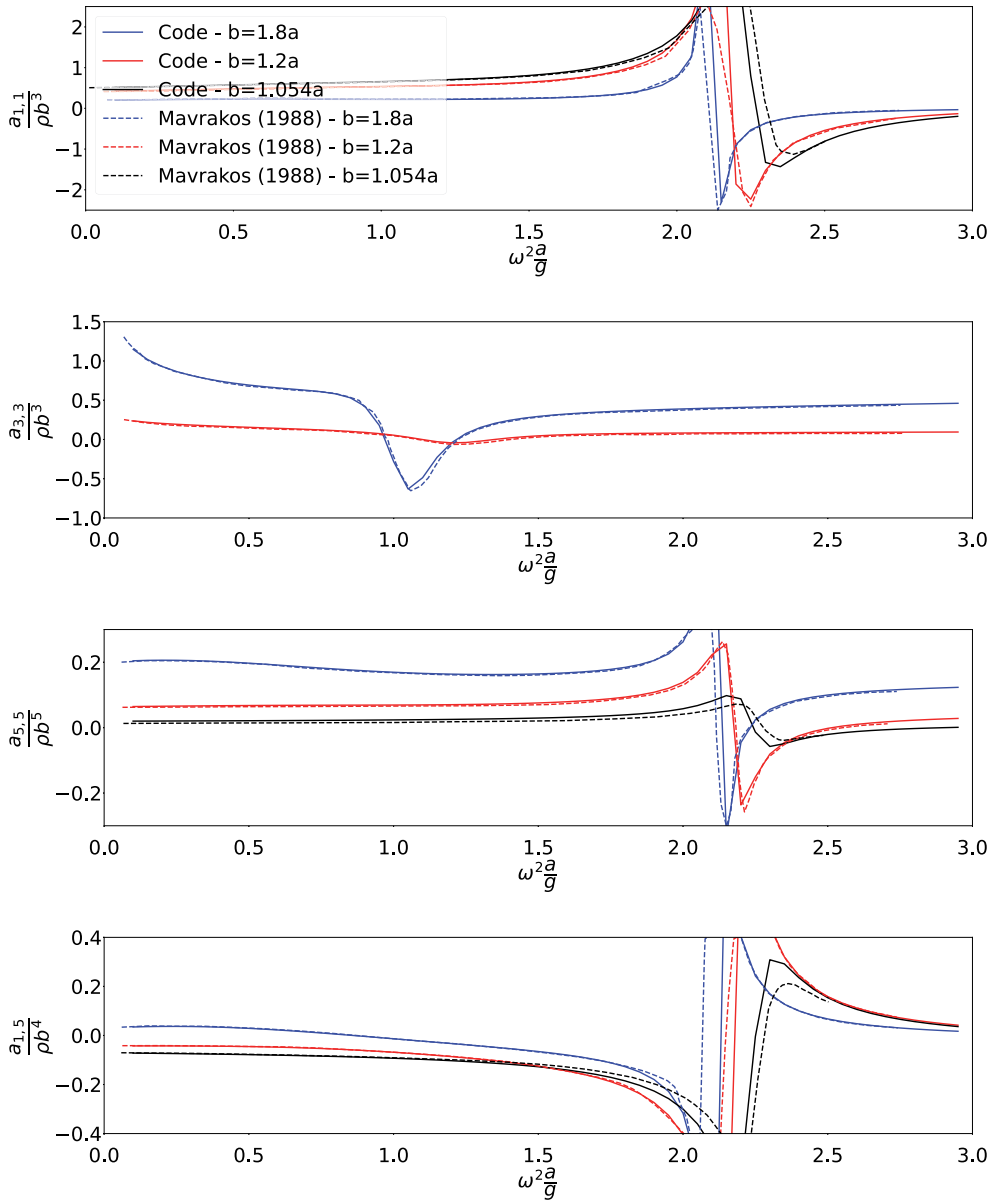

Figure A.3: *Non-dimensional added mass coefficients from Mavrakos (1985), compared with the current DD model for the case without spar and for small dimensions of the bilge boxes:* $(c-b)/a = 0.01$ *and* $s/a = 0.01$*. DD simulations were run with* $N_I = 100$*,* $N_{II} = 20$*,* $N_{III} = 20$ *and* $N_{IV} = 100$*.*

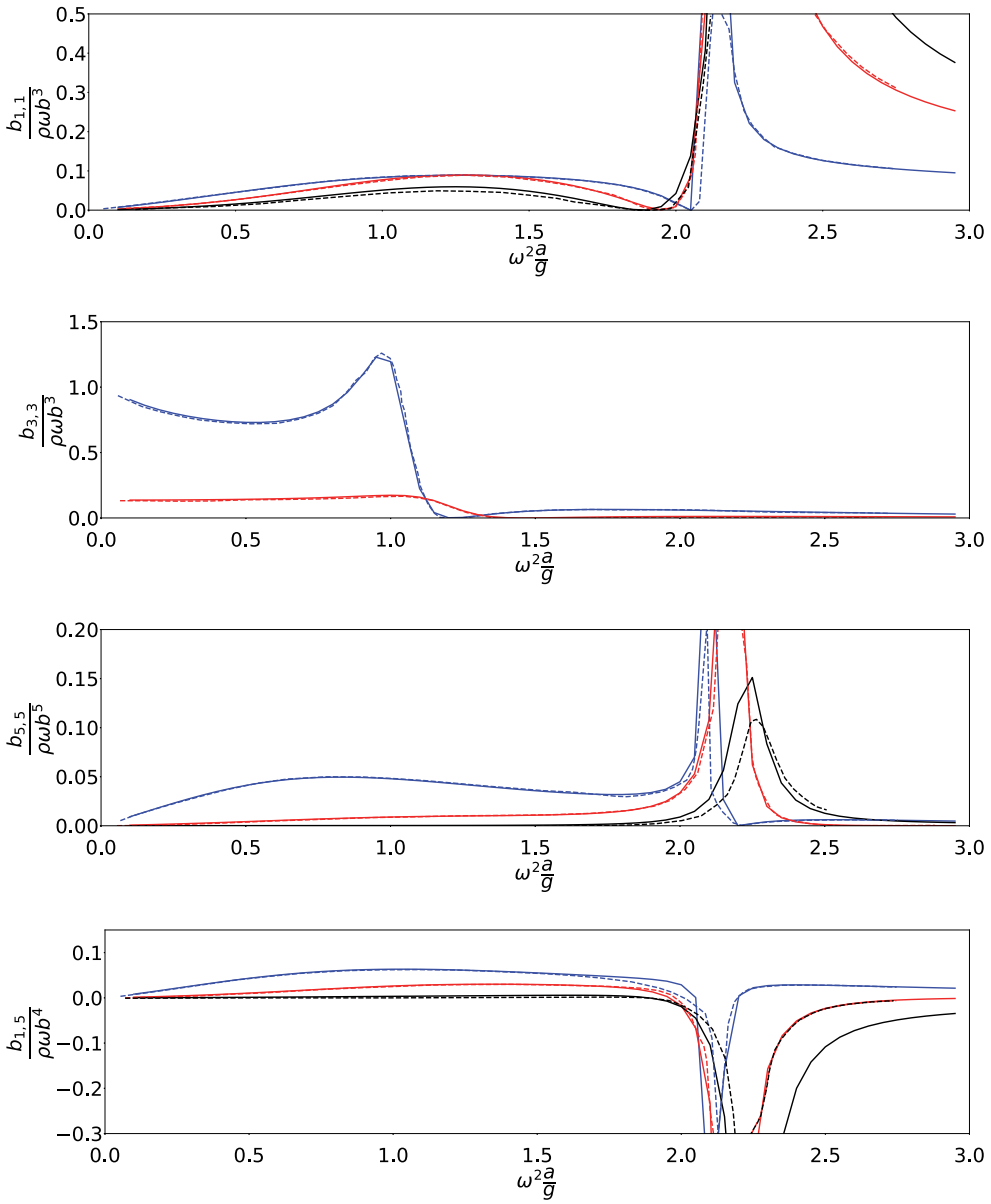

Figure A.4: *Non-dimensional damping coefficients from Mavrakos (1985), compared with the current DD model for the case without spar and for small dimensions of the bilge boxes:* $(c-b)/a = 0.01$ *and* $s/a = 0.01$. *DD simulations were run with* $N_I = 100$, $N_{II} = 20$, $N_{III} = 20$ *and* $N_{IV} = 100$.

B | Semi-analytical model - Complements

B.1 Few properties of Bessel functions

Bessel functions are the general solutions of the equation (Olver et al., 2010):

$$z^2\frac{d^2w}{dz^2} + z\frac{dw}{dz} + \left(z^2 - \nu^2\right)w = 0, \tag{B.1}$$

which in particular appears when expressing the Laplace equation in cylindrical coordinates (Faltinsen and Timokha, 2009). For real numbers z, the Bessel functions of the first and second king are the general solutions of (B.1):

$$J_\nu(z) = \left(\frac{1}{2}z\right)^\nu \sum_{k=0}^{\infty}(-1)^k \frac{\left(\frac{1}{4}z^2\right)^k}{k!\Gamma(\nu+k+1)}, \tag{B.2}$$

$$Y_\nu(z) = \frac{J_\nu(z)\cos(\nu\pi) - J_{-\nu}(z)}{\sin(\nu\pi)}, \tag{B.3}$$

where the Gamma function is defined for all strictly positive real number as:

$$\Gamma(z) = \int_0^\infty e^{-t}t^{z-1}dt. \tag{B.4}$$

If $z = n$ is an integer, then Gamma verifies $\Gamma(1) = 1$, $\Gamma(n+1) = n!$. For complex numbers z, Eq. (B.1) more generally also admit the Hankel functions of first and second kind, respectively $H_\nu^{(1)}$ and $H_\nu^{(2)}$, as solutions. These are related to the Bessel functions of first and second kind by:

$$H_\nu^{(1)}(z) = J_\nu(z) + iY_\nu(z), \tag{B.5}$$

$$H_\nu^{(2)}(z) = J_\nu(z) - iY_\nu(z). \tag{B.6}$$

When the order ν is a strictly positive integer, the following properties are verified:

$$J_{-n}(z) = (-1)^n J_n(z), \tag{B.7}$$

$$Y_{-n}(z) = (-1)^n Y_n(z). \tag{B.8}$$

The Bessel equation Eq. (B.1) becomes the modified Bessel equation when replacing z by $\pm iz$, and has for solutions the modified Bessel functions of the first and second

kinds I_ν and K_ν. Many relationships exist between the Bessel and modified Bessel functions, the following ones have in particular been used in this thesis:

$$I_\nu(z) = e^{\mp\nu\pi i/2} J_\nu\left(ze^{\pm\pi i/2}\right), \quad -\pi \leq \pm \operatorname{ph} z \leq \frac{1}{2}\pi, \tag{B.9}$$

$$K_\nu(z) = \frac{1}{2}\pi i e^{\nu\pi i/2} H_\nu^{(1)}\left(ze^{\pi i/2}\right), \quad -\pi \leq \operatorname{ph} z \leq \frac{1}{2}\pi. \tag{B.10}$$

Bessel and modified bessel functions are shown in Fig. B.1.

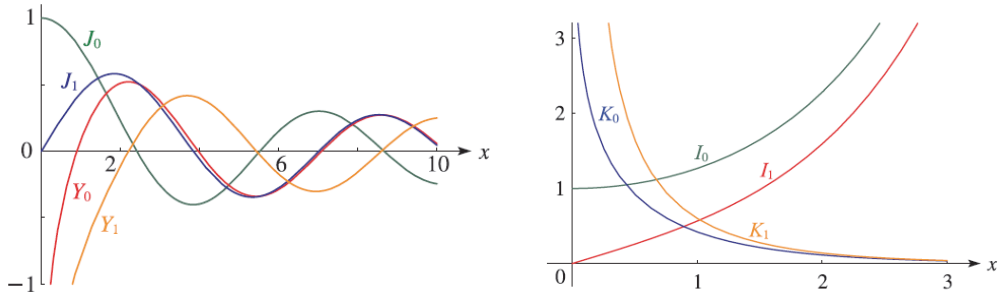

Figure B.1: *Bessel (left) and modified Bessel (right) functions of the first and second kinds for real arguments x, from the "NIST Handbook of Mathematical Functions" by Olver et al. (2010).*

Sorolla et al. (2013) use the recurrence properties of the zeros of cross products of Bessel functions for increasing orders to construct efficient numerical algorithms to estimate them. This solution has been adopted in our work to calculate the wave numbers associated to eigenmodes in the annular domain between the dock and the spar in Sec.3.1. They were coded in Python, and are given here from Listings B.1 to B.4. Analytical asymptotic formulas could alternatively be found in the literature to estimate these roots (Olver et al., 2010; Ziener et al., 2015; Yue et al., 2018).

```
from math import pi
from numpy import zeros, nan
from scipy.special import jv,yv,jvp,yvp

def Algo1(a0,a,smax):
    Eps=10**(-3)  # Accuracy criterium. Eps=10**(-3) is recomended
    # by Sorolla et al. (2013).
    imax=500      # Maximum iterations

    q=a/a0
    C0=zeros(smax)

    for s in range(1,(smax+1)):
        i=0
```

```
            err=1
            Xi=s*pi/(q-1)
            while (err>Eps) & (i<=imax):
                ## intermediate calculations
                f0=jv(0,q*Xi)*yv(0,Xi)-jv(0,Xi)*yv(0,q*Xi)

                f0p=q*jvp(0,q*Xi,1)*yv(0,Xi)+jv(0,q*Xi)*yvp(0,Xi,1)\
                -jvp(0,Xi,1)*yv(0,q*Xi)-q*jv(0,Xi)*yvp(0,q*Xi,1)

                f0pp=q**2*jvp(0,q*Xi,2)*yv(0,Xi)\
                +2*q*jvp(0,q*Xi,1)*yvp(0,Xi,1)+jv(0,q*Xi)*yvp(0,Xi,2)\
                -jvp(0,Xi,2)*yv(0,q*Xi)-2*q*jvp(0,Xi,1)*yvp(0,q*Xi,1)\
                -q**2*jv(0,Xi)*yvp(0,q*Xi,2)

                F0=f0/f0p

                F0p=(f0p**2-f0*f0pp)/(f0p**2)

                ## Iterative solution
                Xit=Xi-F0/F0p
                err=abs((Xit-Xi)/Xit)
                i=i+1
                Xi=Xit

            C0[s-1]=Xi

        C0=C0.real

        return C0
```

Listing B.1: *Algorithm 1 from Sorolla et al. (2013), calculating the roots of* $f_0(x) = J_0(qx)Y_0(x) - J_0(x)Y_0(qx)$, $q = a/a_0$.

```
def Algo2(C0,a0,a,vmax,smax):
    Eps=10**(-5)  # Accuracy criterium. Eps=10**(-3) is recomended
    # by Sorolla et al. (2013), but 10**(-5) is needed to obtain
    # the values presented in the article's table.
    imax=500      # Maximum iterations.
    nsub=10 # Number of subdomains.

    q=a/a0

    C1=zeros((vmax+1,smax))
    C1[0,:]=C0

    for v in range(1,vmax):
        for s in range(1,(smax-v)):
            i=0
            err=1
            count=0
            E=max(Eps*(C1[v-1,s]-C1[v-1,s-1]),Eps)
            delta=(C1[v-1,s]-C1[v-1,s-1])/nsub
            while (err>Eps) & (count<nsub):
```

```
                Xi=C1[v-1,s-1]+E+count*delta
                count=count+1
                while (Xi>=C1[v-1,s-1]) & (Xi<C1[v-1,s]) & (i<=imax):
                    fv=jv(v,q*Xi)*yv(v,Xi)-jv(v,Xi)*yv(v,q*Xi)
                    fvp=q*jvp(v,q*Xi,1)*yv(v,Xi)+jv(v,q*Xi)*yvp(v,Xi,1)\
                    -jvp(v,Xi,1)*yv(v,q*Xi)-q*jv(v,Xi)*yvp(v,q*Xi,1)

                    Xit=Xi-fv/fvp
                    err=abs((Xit-Xi)/Xit)
                    i=i+1
                    Xi=Xit

            C1[v,s-1]=Xi

    return C1
```

Listing B.2: *Algorithm 2 from Sorolla et al. (2013), calculating the roots of* $f_v(x) = J_v(qx)Y_v(x) - J_v(x)Y_v(qx)$, $q = a/a_0$.

```
def Algo3(C1,a0,a,vmax,smax):
    Eps=10**(-5)
    imax=500
    nsub=10
    delt=10**(-4)

    q=a/a0

    C1tild=C1[1,0:(smax-1)]

    C=zeros((vmax+1,smax))
    C[:,:]=nan
    C[0,1:]=C1tild
    C[0,0]=delt

    for v in range(1,vmax):
        for s in range(1,(smax-v)):
            i=0
            err=1
            count=0
            E=max(Eps*(C[v-1,s]-C[v-1,s-1]),Eps)
            delta=(C[v-1,s]-C[v-1,s-1])/nsub
            while (err>Eps) & (count<nsub):
                Xi=C[v-1,s-1]+E+count*delta
                count=count+1
                while (i<=imax) & (Xi<C[v-1,s]) & (Xi>=C[v-1,s-1]):
                    ftv=jvp(v,q*Xi,1)*yvp(v,Xi,1)\
                        -jvp(v,Xi,1)*yvp(v,q*Xi,1)

                    ftvp=q*jvp(v,q*Xi,2)*yvp(v,Xi,1)\
                    +jvp(v,q*Xi,1)*yvp(v,Xi,2)\
                    -jvp(v,Xi,2)*yvp(v,q*Xi,1)\
                    -q*jvp(v,Xi,1)*yvp(v,q*Xi,2)
```

```
                Xit=Xi-ftv/ftvp
                err=abs((Xit-Xi)/Xit)
                i=i+1
                Xi=Xit


            C[v,s-1]=Xi

    C[0,0]=C1tild[0]

    return C
```

Listing B.3: *Algorithm 3 from Sorolla et al. (2013), calculating the roots of* $f_\nu(x) = J'_\nu(qx)Y'_\nu(x) - J'_\nu(x)Y'_\nu(qx)$, $q = a/a_0$.

```
def RootCrossProductBessel(a0,a,Mm,Mr):
    smax=Mr+Mm # Note that smax must be strictly higher than vmax

    C0=Algo1(a0,a,smax+1)
    C1=Algo2(C0,a0,a,Mm,smax+1)
    C=Algo3(C1,a0,a,Mm,smax)

    Roots=(C[:,0:Mr]).real

    return Roots
```

Listing B.4: *Algorithms from Sorolla et al. (2013) coded in Python.* a0 *and* a *are respectively the radius of the spar and the internal radius of the dock,* Mm *is the desired number of modes, and* Mr *the desired number of roots per mode.*

Both the Bessel functions J_p and the cross product of Bessel functions $\Psi_{p,q}$ defined in Sec. 3.1 verify the following orthogonal properties (Olver et al., 2010):

$$\int_0^a J_p\left(k_{p,i}r\right) J_p\left(k_{p,j}r\right) r dr = \delta_{i,j} a^2 [\iota_{p,i}^2 - p^2] \frac{J_p^2(\iota_{p,i})}{2\iota_{p,i}^2}, \tag{B.11}$$

$$\int_{a_0}^a r\Psi_{p,i}(r)\Psi_{p,j}(r)dr = \delta_{i,j}\left[\frac{r^2}{2}\Psi_{p,i}^2(r)\right]_{a_0}^a = \delta_{i,j}\upsilon_{p,i}, \tag{B.12}$$

where $\delta_{i,j}$ is the Kronecker symbol.

B.2 Irregular frequencies

B.2.1 Circular cylinder

The irregular frequencies are found from the Spectral problem 3.1, replacing the Neumann boundary condition by the Dirichlet boundary condition $\varphi = 0$ on S_0. The solutions of the Laplace equation are once again found by separating the

variables, and the new eigen functions are determined after imposing the new body boundary conditions. After few calculations, it comes:

$$\varphi_{p,q}(r,\theta,z) = \frac{J_p\left(\tilde{\iota}_{p,q}\frac{r}{a}\right)}{J_p(\tilde{\iota}_{p,q})} \frac{\sinh\left(\frac{\tilde{\iota}_{p,q}(z+d)}{a}\right)}{\sinh\left(\frac{\tilde{\iota}_{p,q}d}{a}\right)} \times \begin{cases} \cos(p\theta) \\ \sin(p\theta) \end{cases} \tag{B.13}$$

associated with the irregular frequencies:

$$\sigma_{p,q}^{irr\,2} = \frac{g\tilde{\iota}_{p,q}}{a}\tanh^{-1}\left(\frac{\tilde{\iota}_{p,q}d}{a}\right) \tag{B.14}$$

for $(p,q) \in \mathbb{N}^2$ and where $\tilde{\iota}_{p,q}$ are now the roots by increasing order of $J_p(\tilde{\iota}_{p,q}) = 0$. The corresponding irregular periods are in Table B.1 for the closed-bottom dock with the dimensions of the experimental model. We observe that the irregular are in the range of the incoming waves tested in the tank.
Thus, a special treatment has been applied in the BEM code WAMIT to avoid any singular behaviour at these periods. This option is included in the commercial code, and consist in modelling the body by a dipole distribution on its surface, instead of the commonly used source distribution (Lee and Newman, 2006). Using the same formula with the dimensions of the spar gives much higher irregular frequencies $\sigma_{p,q}^{irr\,2} b/g \geq 33.24$.

Table B.1: *First five lowest non-dimensional irregular frequencies $\sigma_{p,q}^{irr\,2} b/g$ for a circular cylinder of radius $a/b = 0.75$ and draught $d/b = 2$.*

Modes	$\sigma^2 b/g$
$p = 0,\ q = 1$	4.54
$p = 1,\ q = 1$	7.53
$p = 2,\ q = 1$	10.26
$p = 0,\ q = 2$	11.10
$p = 3,\ q = 1$	12.86

B.2.2 Annular cylinder

For the open-bottom dock, the internal domain inside the mesh is annular. We neglect the the bilge boxes at the bottom of the dockin this analysis. The boundary value problem to be solved to find the irregular frequencies met in WAMIT is now similar to the spectral problem of the annular domain between the dock and the spar considered in Sec. 3.1.2, with the main difference that we impose now a Dirichlet body boundary condition on the body surface, which is written:

$$J_p(k_{pq}a)Y_p(k_{pq}b) - J_p(k_{pq}b)Y_p(k_{pq}a) = 0, \tag{B.15}$$

where the roots $\tilde{\iota}_{pq} = ak_{pq}$ are calculated from the second algorithm provided bySorolla et al. (2013), and ordered by increasing values. Irregular frequencies are then expressed as in Eq. (B.14). The first five lowest frequencies are given in Table B.2, the first two ones being in the range of simulated frequencies. The same treatment as in the previous section was applied in WAMIT to remove the irregular frequencies.

Table B.2: *First five lowest non-dimensional irregular frequencies* $\sigma^{irr\,2}_{p,q}b/g$ *for an annular cylinder of internal to external radii ratio* $a/b = 0.75$ *and draught* $d/b = 2$.

Modes	$\sigma^2 b/g$
$p = 0,\ q = 1$	5.33
$p = 1,\ q = 1$	5.83
$p = 2,\ q = 1$	7.04
$p = 3,\ q = 1$	8.55
$p = 4,\ q = 1$	10.13

B.3 Hydrodynamic sloshing coefficients

The hydrodynamic coefficients μ and λ presented in Eq. (3.65) for the closed-bottom dock with spar are given below:

$$\mu_{p,q} = \frac{\rho}{\kappa_{p,q}} \int_{\Sigma_0} \varphi_{p,q}(r,\theta,0)^2 r d\theta dr = \frac{\rho\pi b^2}{\kappa_{p,q}}, \tag{B.16}$$

$$\lambda_{1,1,q} = \rho \int_{\Sigma_0} \Gamma_1^{(1)}(r,\theta,0)\varphi_{1,q}(r,\theta,0) r d\theta dr = \frac{\rho\pi b}{\sqrt{\upsilon_{1,q}}} \left[-\frac{a_0^2}{a^2 - a_0^2} I_{1,q} - \frac{a^2 a_0^2}{\left(a^2 - a_0^2\right)} I_{2,q} \right], \tag{B.17}$$

$$\lambda_{2,1,q} = \rho \int_{\Sigma_0} \Gamma_1^{(2)}(r,\theta,0)\varphi_{1,q}(r,\theta,0) r d\theta dr = \frac{\rho\pi b}{\sqrt{\upsilon_{1,q}}} \left[\frac{a^2}{a^2 - a_0^2} I_{1,q} + \frac{a^2 a_0^2}{\left(a^2 - a_0^2\right)} I_{2,q} \right], \tag{B.18}$$

$$\lambda_{3,1,q} = \rho \int_{\Sigma_0} \Omega_2^{(1)}(r,\theta,0)\varphi_{1,q}(r,\theta,0) r d\theta dr = \frac{\rho\pi b}{\sqrt{\upsilon_{1,q}} k_{1,q}} \tanh(k_{1,q}\frac{d}{2}) \mathscr{G}_q^{(1)}(a, a_0), \tag{B.19}$$

$$\lambda_{4,1,q} = \rho \int_{\Sigma_0} \Omega_2^{(2)}(r,\theta,0)\varphi_{1,q}(r,\theta,0) r d\theta dr = \frac{\rho\pi b}{\sqrt{\upsilon_{1,q}} k_{1,q}} \tanh(k_{1,q}\frac{d}{2}) \mathscr{G}_q^{(2)}(a,a_0), \tag{B.20}$$

$$\lambda_{5,1,q} = \rho \int_{\Sigma_0} r\cos(\theta)\varphi_{1,q}(r,\theta,0) r d\theta dr = \frac{\rho\pi b}{\sqrt{\upsilon_{1,q}}} I_{1,q}, \tag{B.21}$$

where we defined the integrals:

$$I_{1,q} = \int_{a_0}^{a} \Psi_{1,q}(r) r^2 dr = \frac{1}{k_{1,q}^2}\Big[2r\left(Y_1'(k_{1,q}a)J_1(k_{1,q}r) - J_1'(k_{1,q}a)Y_1(k_{1,q}r)\right), \tag{B.22}$$

$$+ r^2 k_{1,q}\left(-Y_1'(k_{1,q}a)J_0(k_{1,q}r) + J_1'(k_{1,q}a)Y_0(k_{1,q}r)\right)\Big]_{r=a_0}^{r=a} \tag{B.23}$$

$$I_{2,q} = \int_{a_0}^{a} \Psi_{1,q}(r) dr = \frac{1}{k_{1,q}}\Big[- Y_1'(k_{1,q}a)J_0(k_{1,q}r) + J_1'(k_{1,q}a)Y_0(k_{1,q}r)\Big]_{r=a_0}^{r=a}. \tag{B.24}$$

We now consider the open-bottom dock with spar, similar as in Sec. 5.2.1. The radiation potentials $\phi_j^{(k),IV,\mathrm{RFS}}$ when a rigid free-surface boundary condition is imposed inside the dock are decomposed in the domain IV into a homogeneous and particular solutions $\phi_j^{(k),IV,\mathrm{RFS}} = \phi_{j,h}^{(k),IV,\mathrm{RFS}} + \phi_{j,m}^{(k),IV,\mathrm{RFS}}$. We propose the expansions:

$$\phi_{j,h}^{(k),IV,\mathrm{RFS}}(r,z) = \psi \sum_{n=0}^{\infty} \epsilon_n [A_{1,n}^{IV} P_n^{IV}(r) + A_{2,n}^{IV} Q_n^{IV}(r)] \cos(\frac{n\pi(z+h)}{h}) \tag{B.25}$$

$$\phi_{j,m}^{(k),IV,\mathrm{RFS}}(r,z) = 0, \text{ for } k = 1 \text{ or } k = 2,\ j = 1, \tag{B.26}$$

$$\phi_{5,m}^{(2),IV,\mathrm{RFS}} = -\frac{r(z+h)^2 - \frac{r^3}{4}}{2h} \tag{B.27}$$

Where we redefined the functions P_q^{IV} Q_q^{IV} similar to the domain II:

$$P_0^{IV}(r) = \frac{(\frac{r}{a_0}) - (\frac{a_0}{r})}{(\frac{a}{a_0}) - (\frac{a_0}{a})}, \tag{B.28}$$

$$Q_0^{IV}(r) = \frac{(\frac{a}{r}) - (\frac{r}{a})}{(\frac{a}{a_0}) - (\frac{a_0}{a})}, \tag{B.29}$$

$$P_n^{IV}(r) = \frac{K_1(\frac{n\pi a_0}{h})I_1(\frac{n\pi r}{h}) - I_1(\frac{n\pi a_0}{h})K_1(\frac{n\pi r}{h})}{K_1(\frac{n\pi a_0}{h})I_1(\frac{n\pi a}{h}) - I_1(\frac{n\pi a_0}{h})K_1(\frac{n\pi a}{h})},\ n \in \mathbb{N}^*, \tag{B.30}$$

$$Q_n^{IV}(r) = \frac{K_1(\frac{n\pi r}{h})I_1(\frac{n\pi a}{h}) - I_1(\frac{n\pi r}{h})K_1(\frac{n\pi a}{h})}{K_1(\frac{n\pi a_0}{h})I_1(\frac{n\pi a}{h}) - I_1(\frac{n\pi a_0}{h})K_1(\frac{n\pi a}{h})},\ n \in \mathbb{N}^*. \tag{B.31}$$

The rest of the radiation problem is solved similar as in Sec.2.3.2.
The hydrodynamic coefficients for the open-bottom dock with spar intervening in Eq. (5.25) are then given by:

$$\mu_{p,q} = \frac{\rho}{\kappa_{p,q}} \int_{\Sigma_0} \varphi_{p,q}(r,\theta,0)^2 r d\theta dr = \frac{b^2\rho\pi}{\kappa_{p,q}}, \tag{B.32}$$

$$\lambda_{1,j,q}^{(k)} = \rho \int_{\Sigma_0} \phi_{j,h}^{(k),IV,\mathrm{RFS}}(r,0)\cos(\theta)\varphi_{1,q}(r,\theta,0) r d\theta dr,$$

$$= \frac{b\rho\pi\psi}{\sqrt{\upsilon_{1,q}}} \sum_{n=0}^{\infty} (-1)^n \epsilon_n \left[A_{1,n}^{IV} \int_{a_0}^{a} r\Psi_{1,q}(r) P_n^{IV}(r) dr + A_{2,n}^{IV} \int_{a_0}^{a} r\Psi_{1,q}(r) Q_n^{IV}(r) dr \right], \tag{B.33}$$

$$\lambda_{2,1,q} = \rho \int_{\Sigma_0} \phi_{5,m}^{(2),IV,\mathrm{RFS}}(r,0)\cos(\theta)\varphi_{1,q}(r,\theta,0) r d\theta dr, \tag{B.34}$$

$$\lambda_{3,1,q} = \rho \int_{\Sigma_0} r\cos(\theta)\varphi_{1,q}(r,\theta,0) r d\theta dr = \frac{b\rho\pi}{\sqrt{\upsilon_{1,q}}} I_{1,q}, \tag{B.35}$$

and the $\tilde{P}_{q,j}^{(k)}$ coefficients:

$$\tilde{P}_{q,1}^{(1)} = -\lambda_{1,1,q}^{(1)}/\mu_{1,q}, \tag{B.36}$$

$$\tilde{P}_{q,1}^{(2)} = -\lambda_{1,1,q}^{(2)}/\mu_{1,q}, \tag{B.37}$$

$$\tilde{P}_{q,5}^{(1)} = -\lambda_{5,1,q}^{(1)}/\mu_{1,q}, \tag{B.38}$$

$$\tilde{P}_{q,5}^{(2)} = -\left(\lambda_{5,1,q}^{(2)} + \lambda_{2,1,q} + \omega^{-1}\lambda_{3,1,q} g\right)/\mu_{1,q}. \tag{B.39}$$

Analytical solutions of these integrals exist Olver et al. (2010). In particular, the following identity needs to be used to calculate the integral (B.34):

$$\int z^{\nu+3}Y_\nu(z)dz = 2(\nu+1)J_{\nu+2}(z)\cot(\pi\nu)z^{\nu+2} + \frac{\csc(\pi\nu)}{\Gamma(-\nu)}(2J_{-\nu-2}(z)\Gamma(-\nu)z^{\nu+2} + J_{-\nu-1}(z)\Gamma(-\nu)z^{\nu+3} - J_{\nu+3}(z)\cos(\pi\nu)\Gamma(-\nu)z^{\nu+3} + 2^{\nu+3} + 2^{\nu+3}\nu), \tag{B.40}$$

where csc is the cosecant function.

The relative velocity on the baffle is expressed by:

$$v_r(\theta,t) = R_{1,1}(t)\frac{\partial\varphi_{1,1}}{\partial z}\Big|_{\substack{r=a\\z=-d_B}} + \sum_{k\in\{1,2\}}\dot\eta_1^{(k)}(t)\frac{\partial\phi_1^{(k),IV,\mathrm{RFS}}}{\partial z}\Big|_{\substack{r=a\\z=-d_B}}\cos(\theta) + \dot\eta_5^{(2)}(t)\left[\frac{\partial\phi_5^{IV,\mathrm{RFS}}}{\partial z}\Big|_{\substack{r=a\\z=-d_B}} + a\cos(\theta)\right] + \dot\eta_5^{(1)}(t)\frac{\partial\phi_5^{(1),IV,\mathrm{RFS}}}{\partial z}\Big|_{\substack{r=a\\z=-d_B}}\cos(\theta). \tag{B.41}$$

B.4 Kinetic energy of the first sloshing mode

The analytical expression of the kinetic energy (3.89) in the tank without spar nor baffle can be expressed as

$$E_k = \frac{1}{2}\rho R_{1,1}^2\left[\frac{\iota_{1,1}^2\pi}{a^2J_1^2(\iota_{1,1})\cosh^2(\frac{\iota_{1,1}d}{a})}\right]\left[-\frac{a^2}{64\iota_{1,1}^2}g^{\mathrm{E}}(\iota_{1,1})\left(\frac{a}{4\iota_{1,1}}\sinh\left(\frac{2\iota_{1,1}d}{a}\right)+\frac{d}{2}\right) + \frac{a^2}{2\iota_{1,1}}f^{\mathrm{E}}(\iota_{1,1})\left(\frac{a}{4\iota_{1,1}}\sinh(\frac{2\iota_{1,1}d}{a})-\frac{d}{2}\right) + \left[\frac{\pi}{J_1^2(\iota_{1,1})\cosh^2(\frac{\iota_{1,1}d}{a})}\right]h^{\mathrm{E}}(\iota_{1,1})\left(\frac{a}{4\iota_{1,1}}\sinh(\frac{2\iota_{1,1}d}{a})+\frac{d}{2}\right)\right], \tag{B.42}$$

where $f^{\mathrm{E}}(\iota_{1,1})$, $g^{\mathrm{E}}(\iota_{1,1})$ and $h^{\mathrm{E}}(\iota_{1,1})$ are given below, both analytically and numerically for $\iota_{1,1} \simeq 1.841$:

$$\begin{cases} f^{\mathrm{E}}(\iota_{1,1}) = \iota_{1,1}J_0^2(\iota_{1,1}) + \iota_{1,1}J_1^2(\iota_{1,1}) - 2J_0(\iota_{1,1})J_1(\iota_{1,1}) \simeq 0.439, \\ g^{\mathrm{E}}(\iota_{1,1}) = \iota_{1,1}^4 {}_3F_4\left(\left[\frac{3}{2}, 2, 2\right], \left[1, 3, 3, 3\right], -\iota_{1,1}^2\right) + (-16\iota_{1,1}^2 + 32)J_1^2(\iota_{1,1}) - 16\iota_{1,1}^2 J_0^2(\iota_{1,1}) \\ \qquad\qquad \simeq -7.923, \\ h^{\mathrm{E}}(\iota_{1,1}) = \frac{1}{2}\left[- J_0(\iota_{1,1})^2 - J_1(\iota_{1,1})^2 + 1\right] \simeq 0.281. \end{cases} \tag{B.43}$$

${}_3F_4$ denotes the corresponding generalized hypergeometric function (Olver et al., 2010).

For a standing standing wave $\beta_{1,1}(t) = |\beta_{1,1}|\sin(\sigma_{1,1}t)$, $R_{1,1}$ in Eq. (B.42) is determined from the dynamic free surface boundary condition:

$$R_{1,1}(t) = |R_{1,1}|\cos(\sigma_{1,1}t) = \frac{g}{\sigma_{1,1}}|\beta_{1,1}|\cos(\sigma_{1,1}t) \tag{B.44}$$

B.5 Shift of the natural sloshing frequency due to annular baffle

The expression of the first shifted sloshing frequency in the dock with either solid or perforated baffle but without spar is calculated from Eq. (3.84):

$$\frac{\sigma_{1,1}'^2}{\sigma_{1,1}^2} = 1 - \frac{4\iota_{1,1}^3 \sinh^2\left(\iota_{1,1}\frac{d-d_b}{a}\right)}{\rho\pi a^2 \sinh\left(2\iota_{1,1}\frac{d}{a}\right)(\iota_{1,1}^2 - 1)}\left[\alpha_0 A_0^{plate}\pi + \alpha_1 C_\theta A_0^{plate}\tilde{KC}^{\frac{2}{3}}\right], \tag{B.45}$$

where we have defined $KC = \tilde{KC}\cos(\theta)$ and $C_\theta = \int_0^{2\pi} |(\cos(\theta))|^{\frac{8}{3}}\mathrm{d}\theta \simeq 2.80$. In the same way, the shifted frequency due to the baffle in the dock with the spar is given by:

$$\frac{\sigma_{1,1}'^2}{\sigma_{1,1}^2} = 1 - \frac{k_{1,1}^2 a \Psi_{1,1}^2(a)\sinh^2\left(k_{1,1}(d-d_B)\right)}{\rho\kappa_{1,1}\pi\upsilon_{1,1}\cosh^2(k_1, 1d)}\left[\alpha_0 A_0^{plate}\pi + \alpha_1 C_\theta A_0^{plate}\tilde{KC}^{\frac{2}{3}}\right]. \tag{B.46}$$

B.6 Viscous boundary layer - Empirical formulas

Both Mikishev and Dorozhkin (1961) and Stephens et al. (1962) carried out experimental work to determine the damping due to the turbulent boundary layer

flows on the wall of circular cylinders. They proposed empirical formulas based on these studies, respectively:

$$\xi = 0.79\frac{1}{\sqrt{R_e}}\left[1+\frac{0.318}{\sinh(\iota_{1,1}d/a)}\left(1+\frac{1-d/a}{\cosh(\iota_{1,1}d/a)}\right)\right] \simeq 0.79\frac{1}{\sqrt{R_e}}, \tag{B.47}$$

$$\xi = 0.83\frac{1}{\sqrt{R_e}}\left[\tanh(\iota_{1,1}d/a)\left(1+2\frac{1-d/a}{\cosh(2\iota_{1,1}d/a)}\right)\right] \simeq 0.83\frac{1}{\sqrt{R_e}}, \tag{B.48}$$

where $R_e = \dfrac{\sqrt{ga^3}}{\nu}$ is the Reynold number, and the approximations made in both cases are made assuming that $d > 2a$. These formulas have become common methodology to estimate such viscous damping, and used in several NASA projects.

B.7 From a closed- to an open-bottom dock

The contribution of the loads on the internal surface of the dock without spar to the added mass coefficients $a_{5,1}$ are shown in Fig. B.2.
Figs. B.3 and B.4 compare the added mass coefficients in the subdomain IV calculated either from the method presented in Sec. 2.3.2 for the dock with spar without baffle, or in Sec. 5.2.1 for the dock with spar with baffle. We verify that the coefficients converge when the effects of the baffle goes to 0.

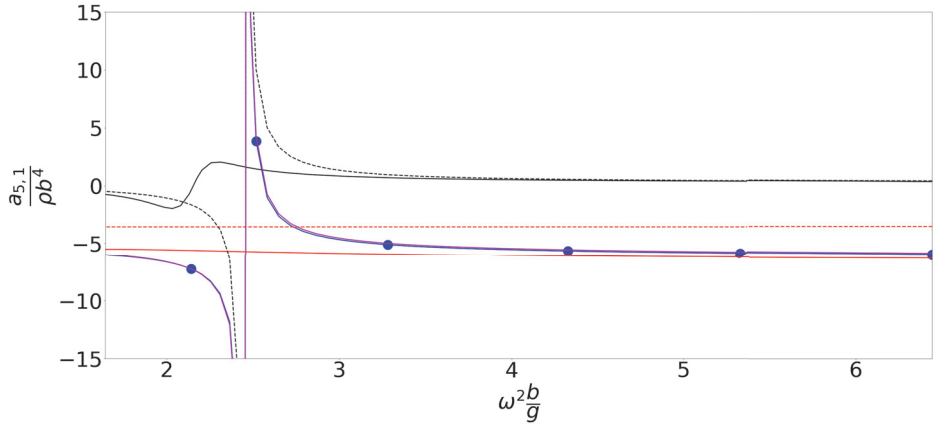

Figure B.2: *Contribution of the domain IV to the non-dimensional added mass coefficients $a_{5,1}$. Same legend as in Fig. 5.1.*

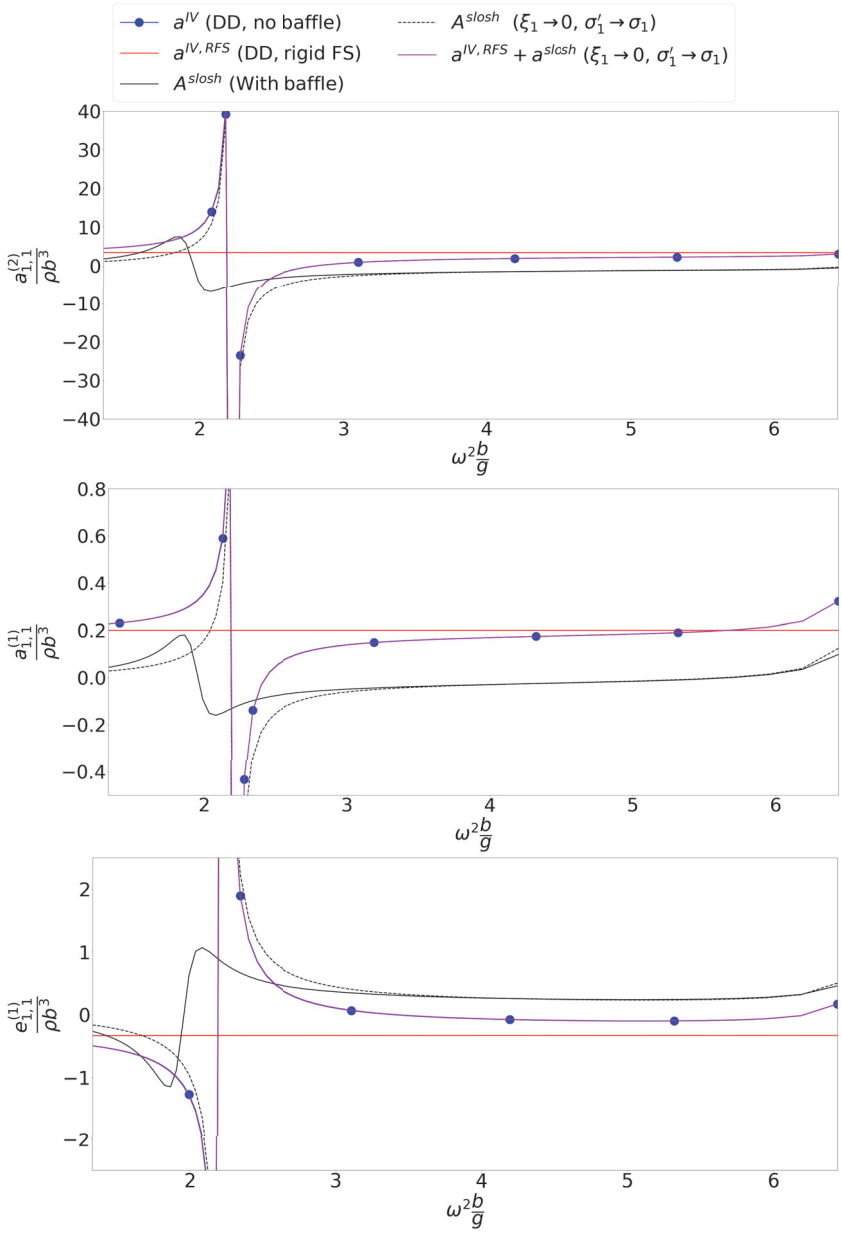

Figure B.3: *Added mass coefficients $a^{(2)}_{1,1}$ (top), $a^{(1)}_{1,1}$ (middle) and $e^{(1)}_{1,1}$ (bottom) for the dock with spar, calculated by integrating the pressure on the bodies' surface in the subdomain IV. a^{IV} is calculated with a DD method for the case without baffle (cf. Sec. 2.3.2), $a^{(k),IV,RFS}$ (or $e^{(k),IV,RFS}$) and A^{slosh} are the add mass coefficients calculated for the open-bottom dock with baffle. In that case, the equations of motions presented in the next section have been solved to estimate ξ_1 and $\sigma'_{1,1}$. When the effects of the baffles are set to 0 ($\sigma' \to \sigma$ and $\xi_1 \to 0$), we verify that this model converges to a^{IV}.*

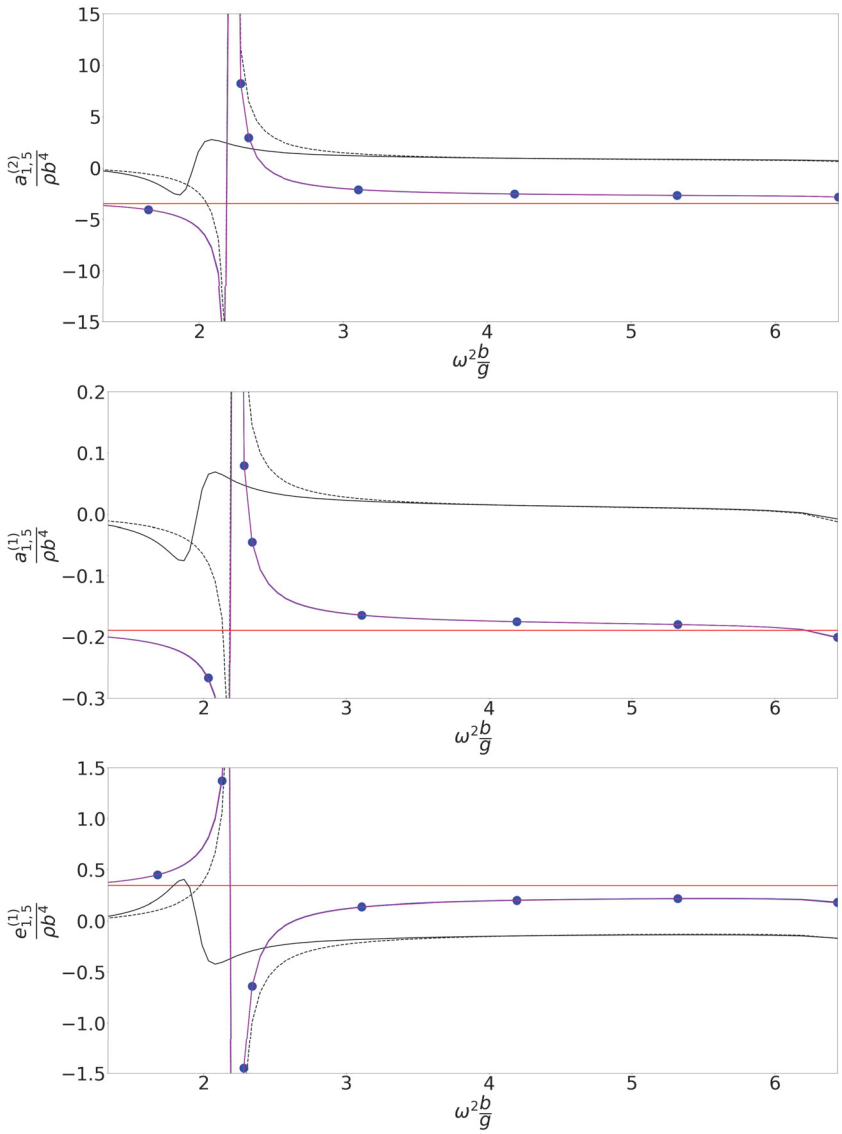

Figure B.4: *Added mass coefficients $a^{(2)}_{1,5}$ (top), $a^{(1)}_{1,5}$ (middle) and $e^{(1)}_{1,5}$ (bottom) for the dock with spar, calculated by integrating the pressure on the bodies' surface in the subdomain IV. a^{IV} is calculated with a DD method for the case without baffle (cf. Sec. 2.3.2), $a^{(k),IV,RFS}$ (or $e^{(k),IV,RFS}$) and A^{slosh} are the add mass coefficients calculated for the open-bottom dock with baffle. Same legend as in Fig. B.3.*

C | Experimental results

C.1 Decay Tests

Decay tests were also achieved for lateral motions in sway, roll and yaw. They are given for the dock alone in Table C.1.

Table C.1: *Natural periods in sway, roll and yaw of the dock estimated from the decay tests, in seconds. BB1 corresponds to the smaller bilge boxes: $H_{skm} = 0.04m$ and $B_{skm} = 0.05m$, and BB2 to the larger bilge boxes: $H_{skm} = 0.05m$ and $B_{skm} = 0.09m$.*

	$d+s = 0.5$m BB1	$d+s = 0.5$m BB2	$d+s = 0.8$m BB1	$d+s = 0.8$m BB2	$d+s = 0.5$m unmoored BB2	$d+s = 0.8$m unmoored BB2
$\eta_2^{(2)}$	7.82	8.15	10.50	10.53	/	/
$\eta_4^{(2)}$	2.40	2.51	2.10	2.20	2.93	2.34
$\eta_6^{(2)}$	2.32	2.44	2.81	2.81	/	/

Fig. C.1 shows the spectra for the dock of the time series in Fig. 4.7.

Fig. C.2 shows similar linear regression as Fig. 4.8, but for the lower draught $d+s = 0.5$m. The same method presented for surge in Sec. 4.2.2 can be applied in pitch, disregarding once again the coupling with surge motion. Linear regressions are presented in Fig. C.3, and the results are given in Table C.2. Quadratic damping in pitch is most likely caused by viscous eddies created at the sharp corners of the bilge boxes. The bilge boxes' size do seem to have an effect on $B^Q_{5,5}$ for the higher draught, even though it should be noted that motions' amplitudes are much more scattered than for surge. Because of this bad correlation, a non-physical negative linear damping was even obtained for the higher draught.

Table C.2: *Linear and quadratic damping in pitch for the dock. BB1 and BB2 are defined as in Table 4.4.*

	$d+s = 0.5$m BB1	$d+s = 0.5$m BB2	$d+s = 0.8$m BB1	$d+s = 0.8$m BB2
$B_{5,5}$ [kg.m/s]	0.78	0.02	7.98	-3.74
$B^Q_{5,5}$ [kg.m]	42.15	36.88	46.97	81.09

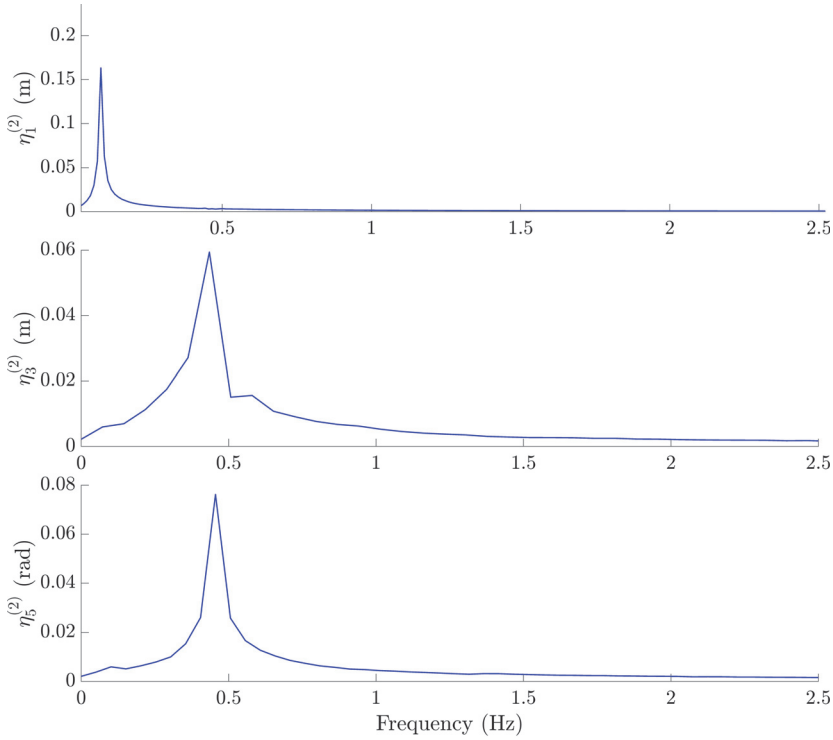

Figure C.1: *Example of spectra from decay tests for the dock's motions in surge, heave and pitch. Same case as in Fig. 4.7.*

C.2 Wave conditions

Examples of specified and measured incident wave periods and amplitudes of regular waves are presented in Fig. C.4. The amplitude of waves with higher periods were generally closer to the one specified.

C.3 Time series

Additional time series from experimental tests are presented in this section. Fig. C.5 shows results for the dock without spar, both with and without damping devices in regular and irregular waves.

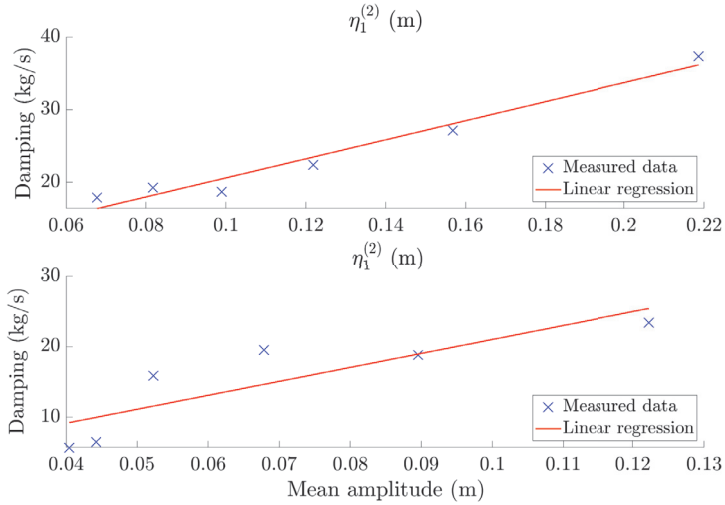

Figure C.2: *$B^E_{1,1}$ as function of $\bar{\eta}^{(2)}_{1,i}$, plotted from decay tests' time series for the dock without spar and without damping devices. Linear and quadratic damping in surge are estimated thanks to a linear regression. Draught: $d + s = 0.5m$. Top: large bilge boxes: $H_{skm} = 0.05m$ and $B_{skm} = 0.09m$. Bottom: small bilge boxes: $H_{skm} = 0.04m$ and $B_{skm} = 0.05m$.*

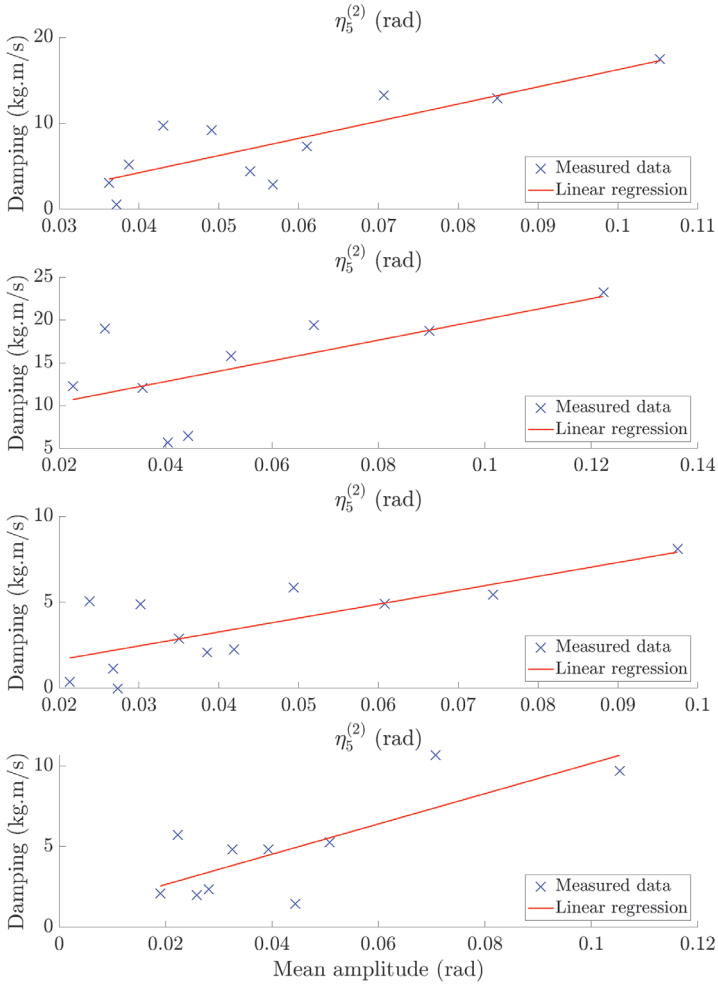

Figure C.3: *$B^E_{5,5}$ as function of $\bar{\eta}^{(2)}_{5,i}$, plotted from decay tests' time series for the dock without spar and without damping devices. Linear and quadratic damping in pitch are estimated thanks to a linear regression. First: draught: $d + s = 0.8m$, large bilge boxes: $H_{skm} = 0.05m$ and $B_{skm} = 0.09m$. Second: draught: $d + s = 0.8m$, small bilge boxes: $H_{skm} = 0.04m$ and $B_{skm} = 0.05m$. Third: draught: $d + s = 0.5m$, large bilge boxes: $H_{skm} = 0.05m$ and $B_{skm} = 0.09m$. Fourth: draught: $d + s = 0.5m$, small bilge boxes: $H_{skm} = 0.04m$ and $B_{skm} = 0.05m$.*

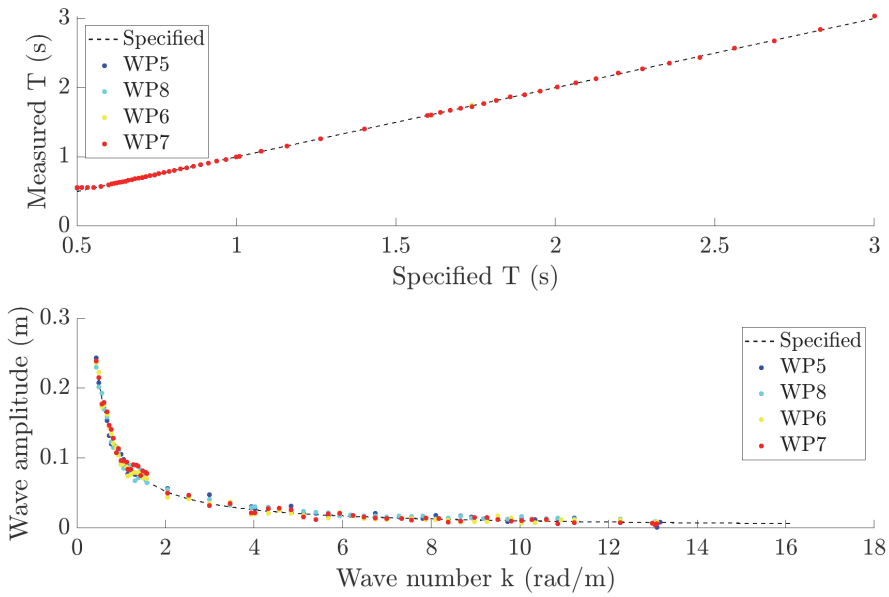

Figure C.4: *Specified and measured incident wave period and amplitudes for tests made for the dock without spar and without damping devices (2019, Set 1). Wave steepness:* $\epsilon = 1/60$.

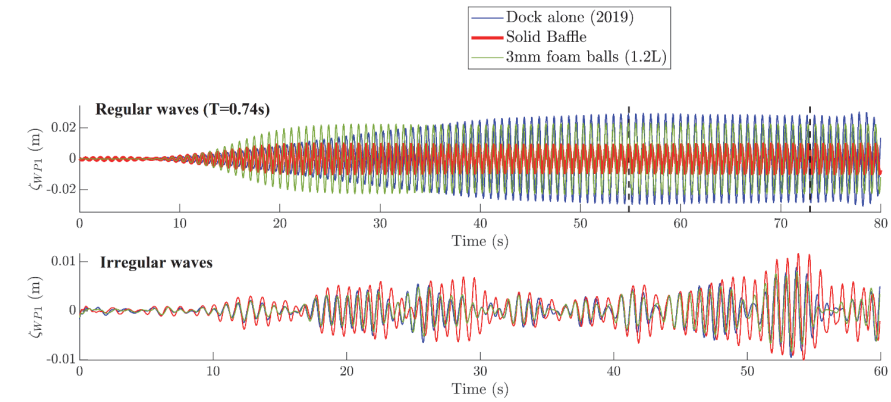

Figure C.5: *Top: time history of the free-surface elevation* ζ_{WP1} *inside the dock in regular waves for three cases, without damping devices, with foam balls (3mm, 1.2L), and with solid baffle. The incident wave period is* $T = 0.74s$ *(i.e.* $\omega^2 b/g = 2.94$*), and the wave steepness 1/60. The time window that is post-proceeded is shown for the dock alone between the cut-off delimiters. Bottom: extract of the time series of* ζ_{WP1} *in irregular waves for the same three configurations.* $H_s/b = 1/40$*, and* $T_p = 0.8s$ *(i.e.* $\omega^2 b/g = 2.52$*).*

C.4 Spar's motions in an dock-fixed coordinate system

The motions of the SPAR are initially either calculated or measured in the Earth-fixed coordinate system (ECS) $\left(O^E x^E y^E z^E\right)$. In this section, we describe how the motions of a point P fixed to the spar can also be expressed in the dock-fixed coordinate system (DCS) $\left(O^D x^D y^D z^D\right)$. The dock's motions are restrained to the three degrees of freedom in surge, heave and pitch. We denote $(\boldsymbol{e}_1^E, \boldsymbol{e}_2^E, \boldsymbol{e}_3^E)$ the orthonormal basis associated to the ECS, and $(\boldsymbol{e}_1^D, \boldsymbol{e}_2^D, \boldsymbol{e}_3^D)$ associated to the DCS. The relation between the two basis can be expressed:

$$\boldsymbol{e}_1^E = \cos\left(\eta_5^{(2)}\right)\boldsymbol{e}_1^D + \sin\left(\eta_5^{(2)}\right)\boldsymbol{e}_3^D, \tag{C.1}$$

$$\boldsymbol{e}_3^E = -\sin\left(\eta_5^{(2)}\right)\boldsymbol{e}_1^D + \cos\left(\eta_5^{(2)}\right)\boldsymbol{e}_3^D \tag{C.2}$$

.

The motions of a point P fixed to the spar are given in the ECS:

$$\boldsymbol{r}^E(P) = \left[\eta_1^{(1)} + z^S \sin\left(\eta_5^{(1)}\right) + x^S \cos\left(\eta_5^{(1)}\right)\right]\boldsymbol{e}_1^E + \left[\eta_3^{(1)} - x^S \sin\left(\eta_5^{(1)}\right) + z^S \cos\left(\eta_5^{(1)}\right)\right]\boldsymbol{e}_3^E \tag{C.3}$$

.

where the upper index S is here associated to the spar-fixed coordinate system (SCS). The motions of the same point P in the DCS is then:

$$\boldsymbol{r}^D(P) = \boldsymbol{r}^E(P) - \boldsymbol{r}^E(O^D) \tag{C.4}$$

where the position of the origin O^D of the DCS is $\boldsymbol{r}^E(O^D) = \eta_1^{(2)}\boldsymbol{e}_1^E + \eta_3^{(2)}\boldsymbol{e}_3^E$. Inserting the Eqs (C.1) to (C.3) into (C.4), we finally have:

$$\boldsymbol{r}^D(P) = x^D(P)\boldsymbol{e}_1^D + z^D(P)\boldsymbol{e}_3^D \tag{C.5}$$

with

$$\begin{aligned} x^D(P) = &\left[\eta_1^{(1)} + z^S \sin\left(\eta_5^{(1)}\right) + x^S \cos\left(\eta_5^{(1)}\right) - \eta_1^{(2)}\right]\cos\left(\eta_5^{(2)}\right) \\ &- \left[\eta_3^{(1)} - x^S \sin\left(\eta_5^{(1)}\right) + z^S \cos\left(\eta_5^{(1)}\right) - \eta_3^{(2)}\right]\sin\left(\eta_5^{(2)}\right), \end{aligned} \tag{C.6}$$

$$\begin{aligned} z^D(P) = &\left[\eta_1^{(1)} + z^S \sin\left(\eta_5^{(1)}\right) + x^S \cos\left(\eta_5^{(1)}\right) - \eta_1^{(2)}\right]\sin\left(\eta_5^{(2)}\right) \\ &+ \left[\eta_3^{(1)} - x^S \sin\left(\eta_5^{(1)}\right) + z^S \cos\left(\eta_5^{(1)}\right) - \eta_3^{(2)}\right]\cos\left(\eta_5^{(2)}\right). \end{aligned} \tag{C.7}$$

Finally, for small motions, we can linearise Eqs (C.6) and (C.7):

$$x^D(P) = \eta_1^{(1)} + z^S \eta_5^{(1)} + x^S - \eta_1^{(2)} - z^S \eta_5^{(2)}, \tag{C.8}$$

$$z^D(P) = x^S \eta_5^{(2)} + \eta_3^{(1)} - x^S \eta_5^{(1)} + z^S - \eta_3^{(2)}. \tag{C.9}$$

C.5 Repetition tests

Mean values and standard deviations of the spar's heave motions from 2019 repetition tests are given in Fig. C.6. Comparisons of the dock's RAOs in surge and pitch between 2018 and 2019 tests with the same set-up for the dock alone are presented in Fig. C.7 and C.8, showing even lower discrepancies than for the free-surface elevation ζ_{WP1}'s RAOs, already discussed in Sec. 4.5.1.

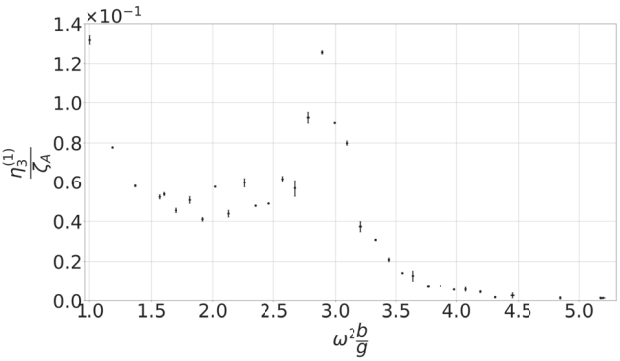

Figure C.6: *.Mean values and standard deviations of the RAOs of the spar's heave motions for the same repetitions tests as in Fig. 4.19.*

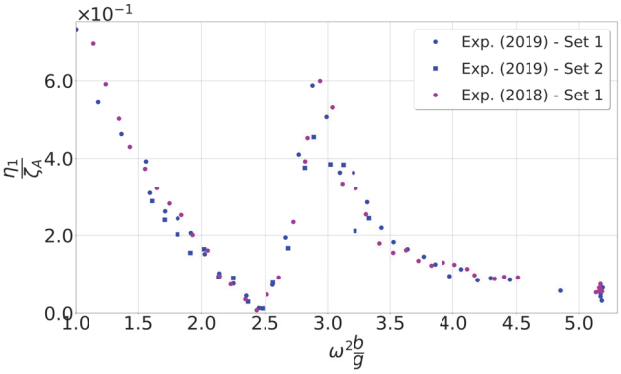

Figure C.7: *. Comparisons of $\eta_1^{(2)}$'s RAOs for several tests made between 2018 and 2019 with the same set-up for the dock alone, and in the same range of incident wave frequencies. $\epsilon = 1/60$, draught of the dock: $d + s = 0.8m$, larger bilge boxes' size (BB2).*

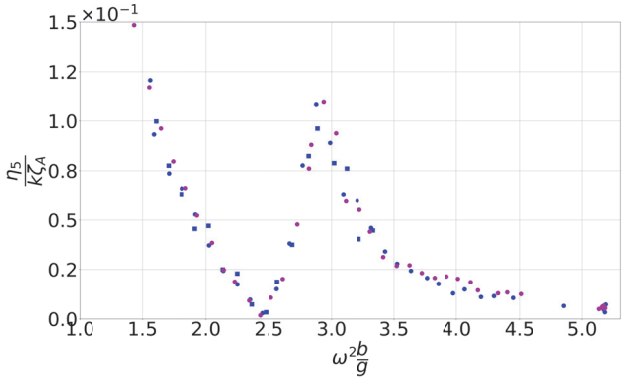

Figure C.8: *. Comparisons of $\eta_5^{(2)}$'s RAOs for several tests made between 2018 and 2019 with the same set-up for the dock alone, and in the same range of incident wave frequencies. $\epsilon = 1/60$, draught of the dock: $d + s = 0.8m$, larger bilge boxes' size (BB2).*

C.6 Irregular waves

The theoretical and measured incident waves' spectra for tests without the spar are presented in Fig. C.9 for 2018's model tests and Fig. C.10 for 2019's model tests, while Fig. C.11 shows the motions' spectra for 2018 tests with $\omega_p^2 b/g = 2.52$ and $H_s/b = 1.5/40$.

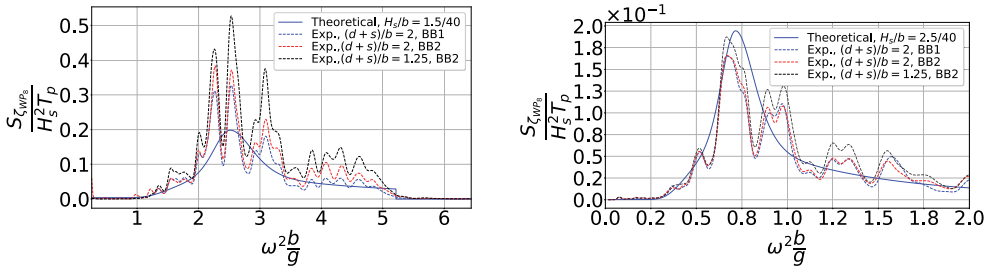

Figure C.9: *JONSWAP spectra of incident waves, as instructed to the command of the wave maker (theoretical), and measured in front of the dock without spar at the wave probe WP8 with the model in place (experimental). $\sigma_G = 0.0109$. Tests from 2019.*

Numerical and experimental results in irregular waves for the dock without spar nor damping devices are presented in Figs. C.12 and C.13 for two draughts and two BB's sizes. The agreement is good near sloshing resonance, the numerical motions are over-predicted for lower frequencies. The semi-analytical does not indeed include any viscous damping, and these observations are similar the ones made for results in regular waves (cf. Sec. 6.1.4).

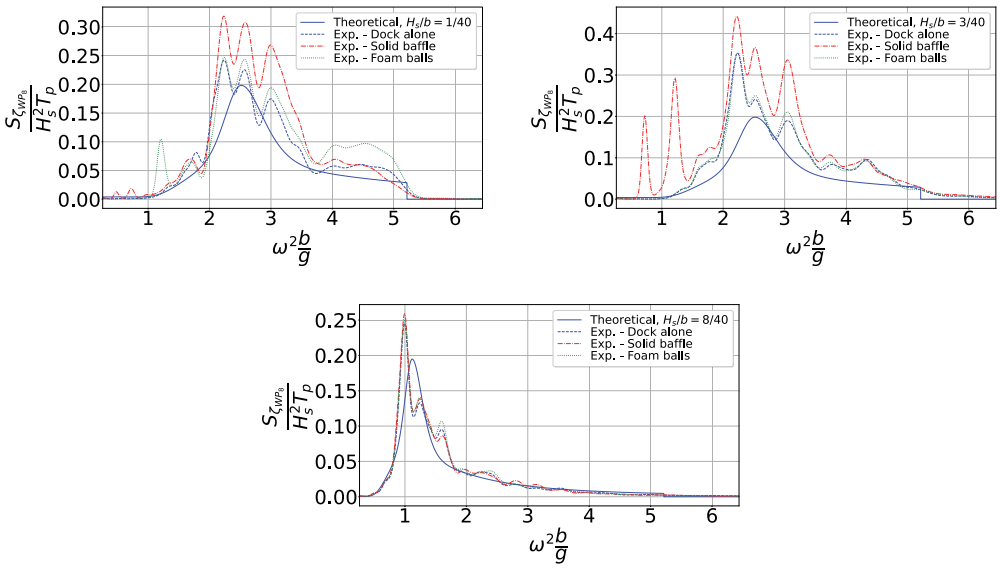

Figure C.10: *JONSWAP spectra of incident waves, as instructed to the command of the wave maker (theoretical), and measured in front of the dock without spar at the wave probe WP8 with the model in place (experimental).* $\sigma_G = 0.0208$. *Tests from 2019.*

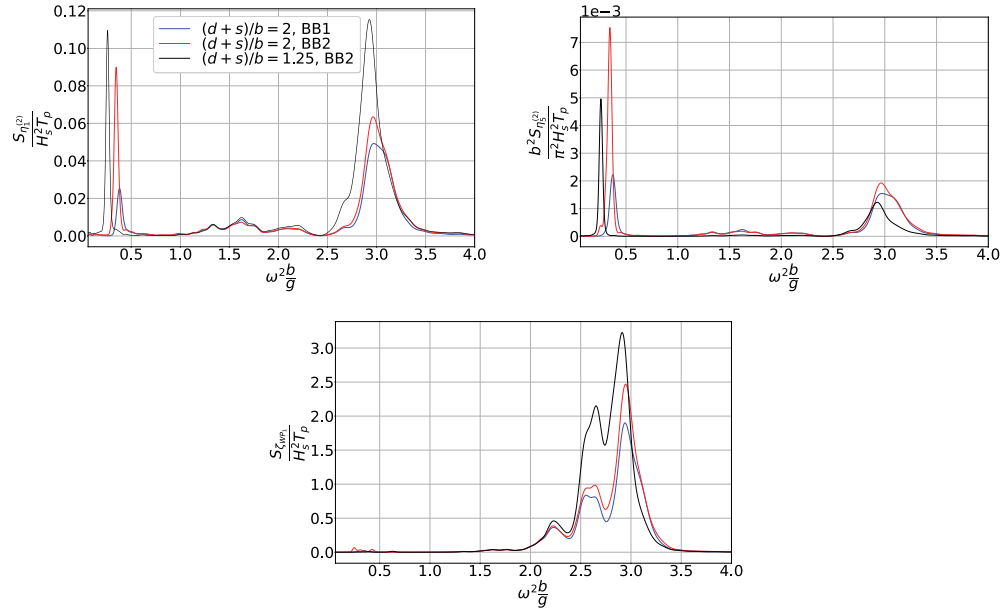

Figure C.11: *Normalised spectra of the dock's responses in surge (upper left), pitch (upper right), as well as of* ζ_{WP1} *(bottom) from the 2018 model tests without the spar with the peak frequency of incident waves* $\omega_p^2 b/g = 2.52$ *and the significant wave height* $H_s/b = 1.5/40$. $\sigma_G = 0.0109$.

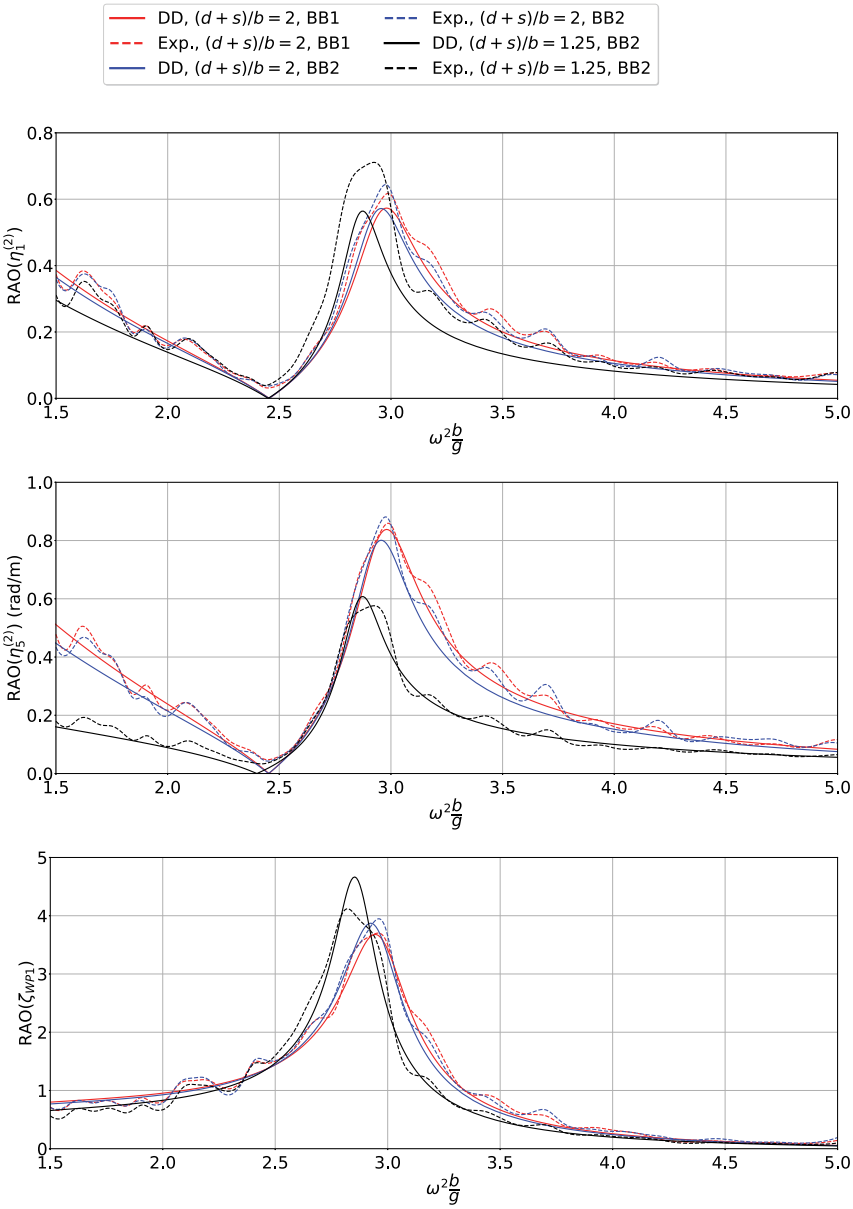

Figure C.12: *Analytical and experimental (2018 tests) RAOs for irregular waves for the dock without spar, for the two draughts and two BB's sizes. Peak frequency of the JONSWAP spectrum:* $\omega_p^2 b/g = 2.52$. $\sigma_G = 0.0109$.

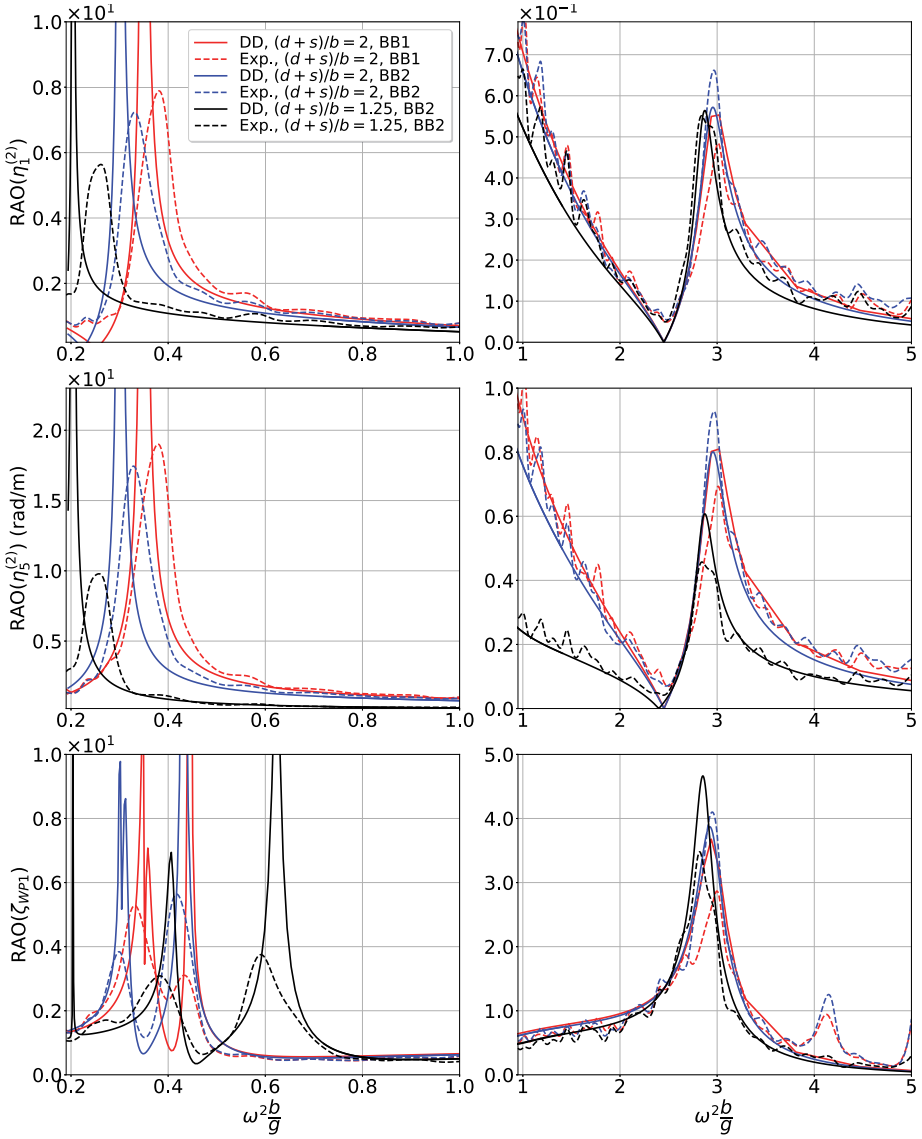

Figure C.13: *Analytical and experimental (2018 tests) RAOs for irregular waves for the dock without spar, for the two draughts and two BB's sizes. Peak frequency of the JONSWAP spectrum:* $\omega_p^2 b/g = 0.72$. $\sigma_G = 0.0109$.

D | Numerical results

D.1 Velocity profiles

Example of velocity profiles near the bilge boxes are given in Fig. D.1, decomposed in horizontal and vertical components in Fig. D.2. The complexity of the flow makes it difficult to obtain simple estimations of the damping coefficients caused by the flow separation at the sharp corners.

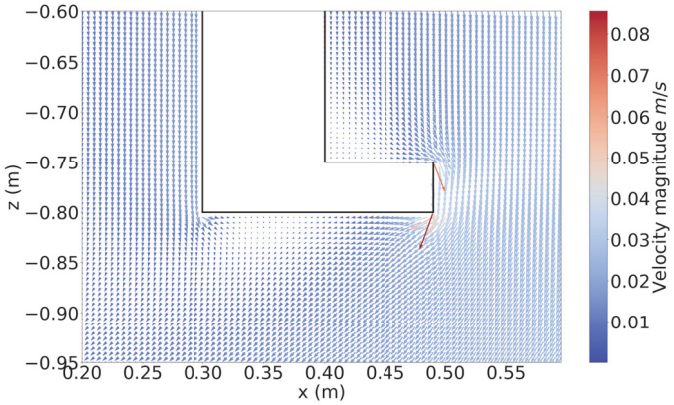

Figure D.1: *Velocity profile in $y = 0m$ in the body-fixed coordinate system near the bottom of the dock at the incident wave frequency: $\omega^2 b/g = 2.94$ (i.e. $T = 0.74s$), calculated from the DD model. Same case as for Fig. 6.2 at the time $t = 0s$. Wave steepness: $\epsilon = 1/60$.*

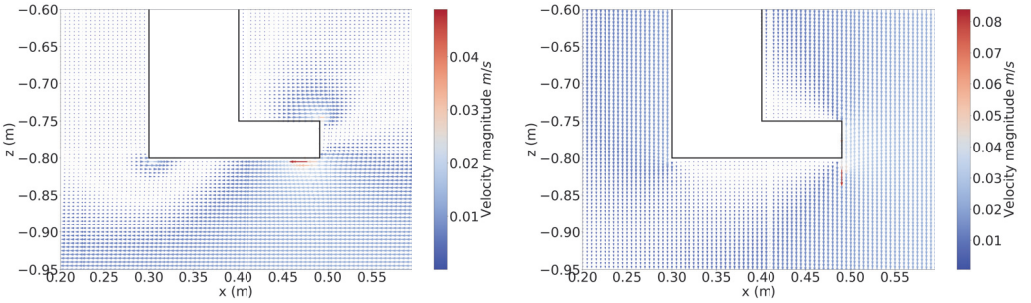

(a) *Horizontal velocities.* ***(b)*** *Vertical velocities.*

Figure D.2: *Velocity profile in $y = 0m$ in the body-fixed coordinate system at the incident wave frequency: $\omega^2 b/g = 2.94$ (i.e. $T = 0.74s$), calculated from the DD model. Same case as Fig. D.1, with a decomposition of the horizontal and vertical components of the velocity. Wave steepness: $\epsilon = 1/60$.*

D.2 Variations of the draught

Added mass and damping coefficients for the four draughts of the dock described in Sec.6.1.3 are presented from Figs. D.3 to D.6 and exciting force and moments from Figs. D.7 to D.9.. Added mass and damping coefficients in surge an pitch sharply decline with the draught, without significant shift of the natural sloshing periods. The same number of modes in the domain decomposition methods were used for the three lower draughts as for the highest one, for which a proper convergence study were carried out. Thus, the peaks observed in the damping coefficients for the two lower draughts are most likely numerical errors that should be expected to vanish for higher number of modes. The piston mode natural frequency is increased from $\omega^2 b/g = 0.4$ to $\omega^2 b/g = 1.3$ when the draughts is decreased from $(d+s)/b = 2$ to $(d+s)/b = 0.38$, also observed in the exciting force in heave.

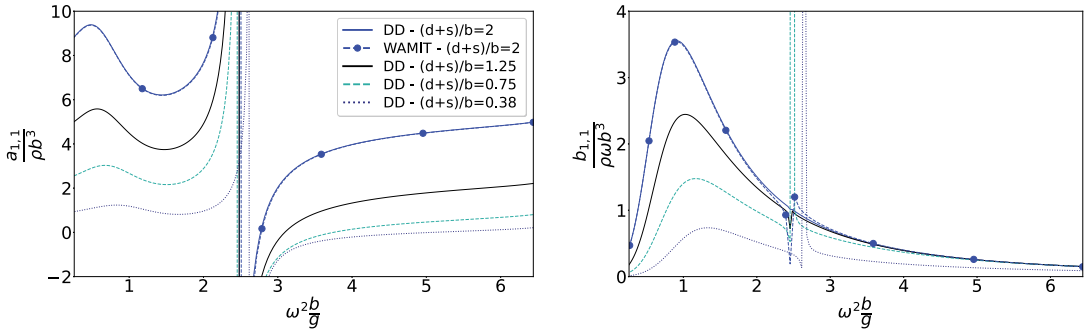

Figure D.3: *Added mass and damping coefficients in surge for different draughts of the dock without spar (BB2).*

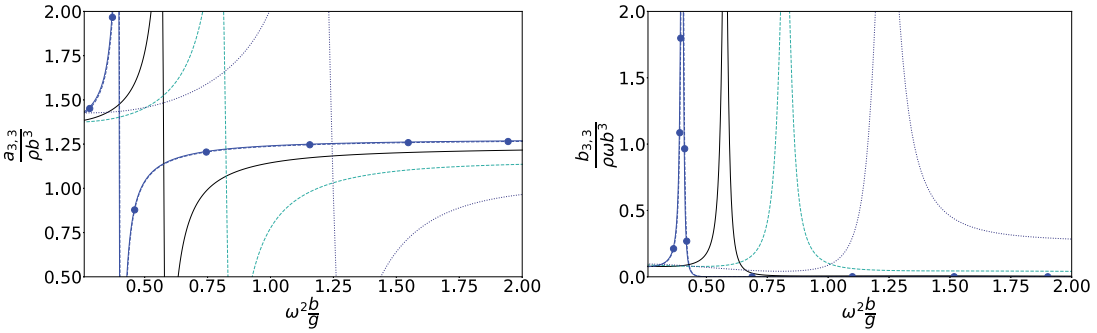

Figure D.4: *Added mass and damping coefficients in heave for different draughts of the dock without spar (BB2).*

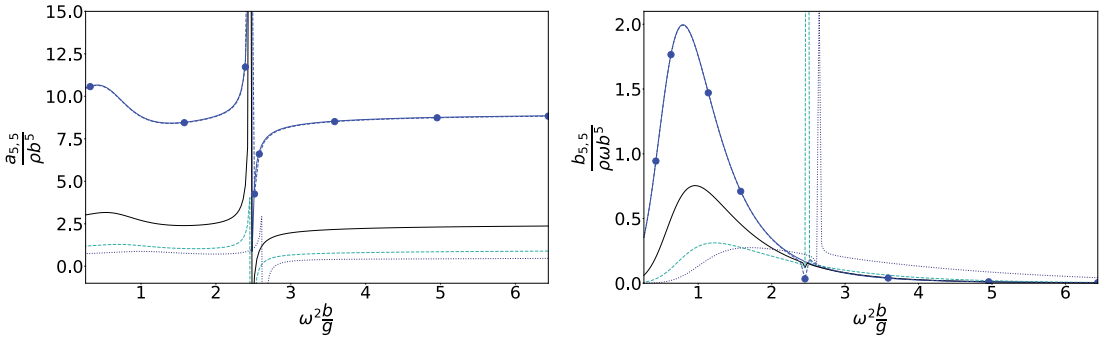

Figure D.5: *Added mass and damping coefficients in pitch for different draughts of the dock without spar (BB2).*

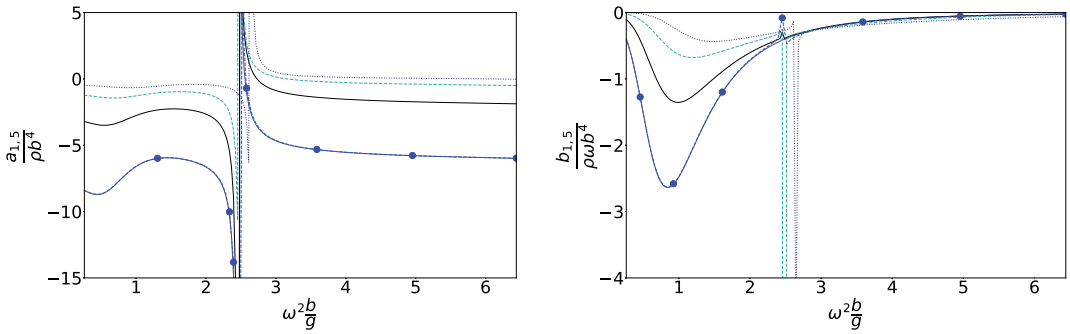

Figure D.6: *Coupled added mass and damping coefficients in surge and pitch for different draughts of the dock without spar (BB2).*

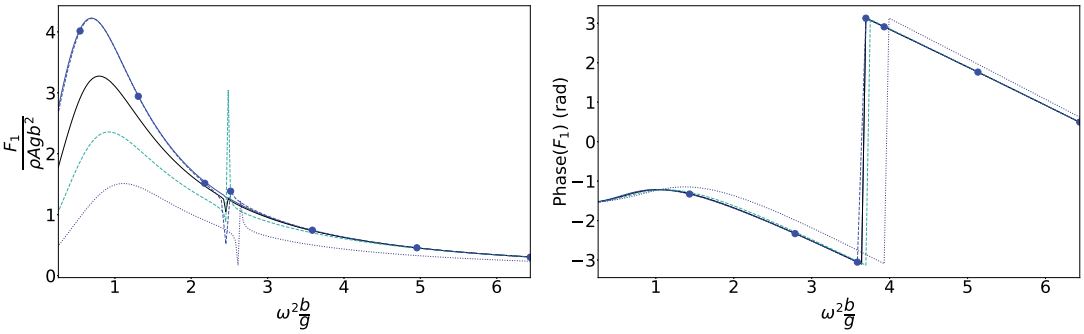

Figure D.7: *Exciting forces in surge for different draughts of the dock without spar (BB2). Amplitudes and phase.*

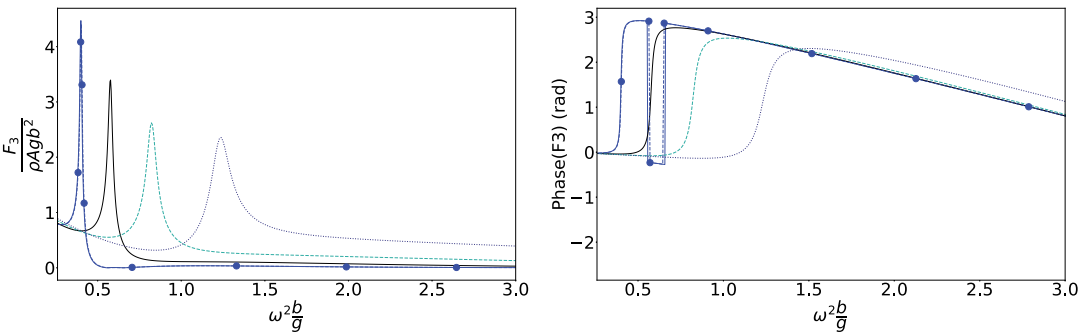

Figure D.8: *Exciting forces in heave for different draughts of the dock without spar (BB2). Amplitudes and phase.*

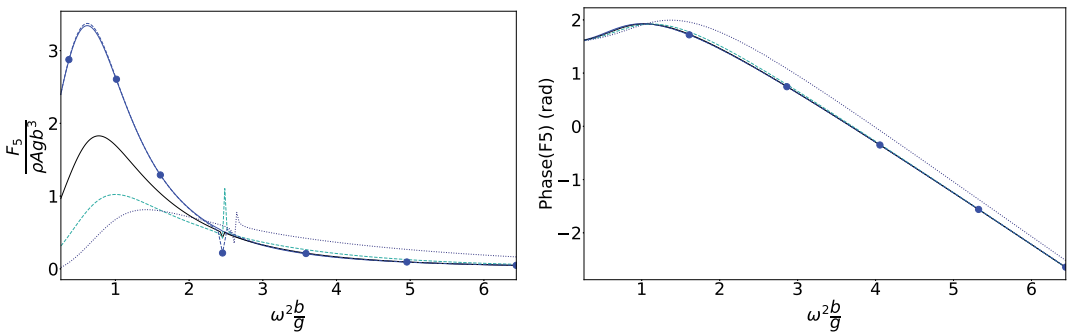

Figure D.9: *Exciting moments in pitch for different draughts of the dock without spar (BB2). Amplitudes and phase.*

D.3 Relative flow velocity

The amplitude of the relative flow velocity from the semi-analytical model on perforated baffles both due to pitching and sloshing in a dock-fixed coordinate system are given in Fig. D.10 as functions of incident wave frequencies. Contrarily to a closed-bottom dock, a vertical flow velocity is also caused by both the surge and heave motions of the dock when the internal free surface is rigid. However, their amplitudes is negligible, as shown in Fig. D.11.

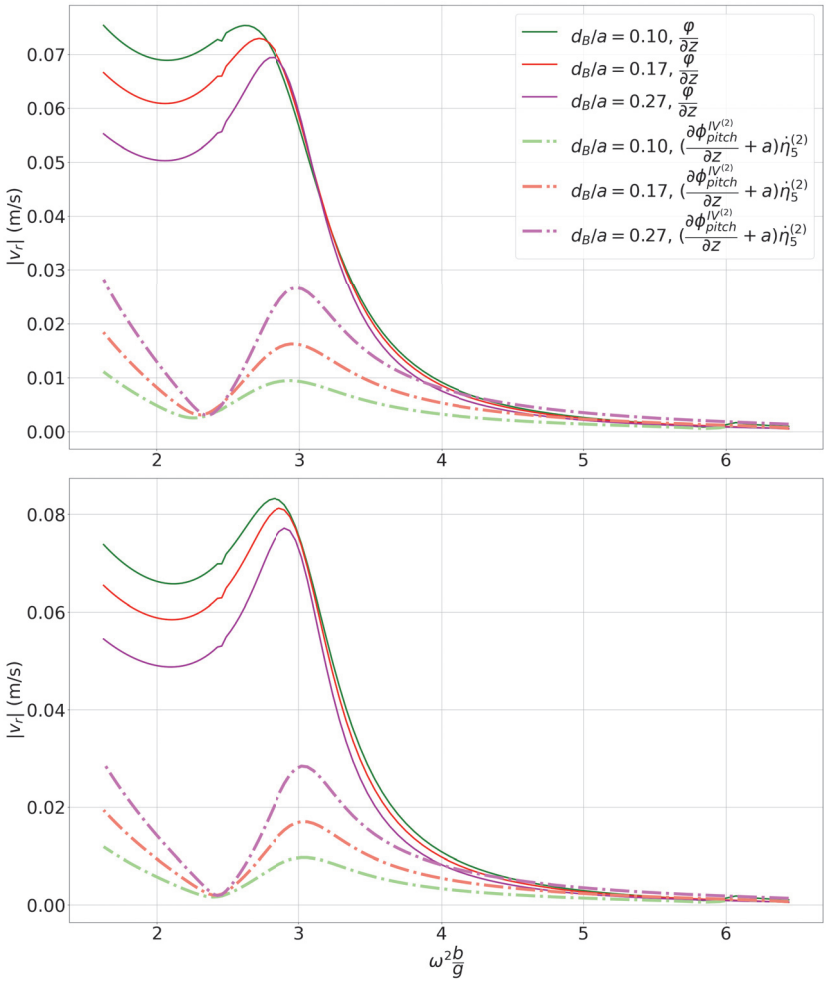

Figure D.10: *. Top:* $\tau = 0.15$*. Bottom:* $\tau = 0.30$*. Amplitude of the vertical relative flow velocity from semi-analytical simulations on the perforated baffle in* $\theta = 0°$ *in a dock-fixed coordinate system. Both the contribution of the dock's pitching (dash lines) and the sloshing waves (solid lines) are given for three values of* $\frac{d_B}{a}$*. Wave steepness:* $\epsilon = 1/60$*.*

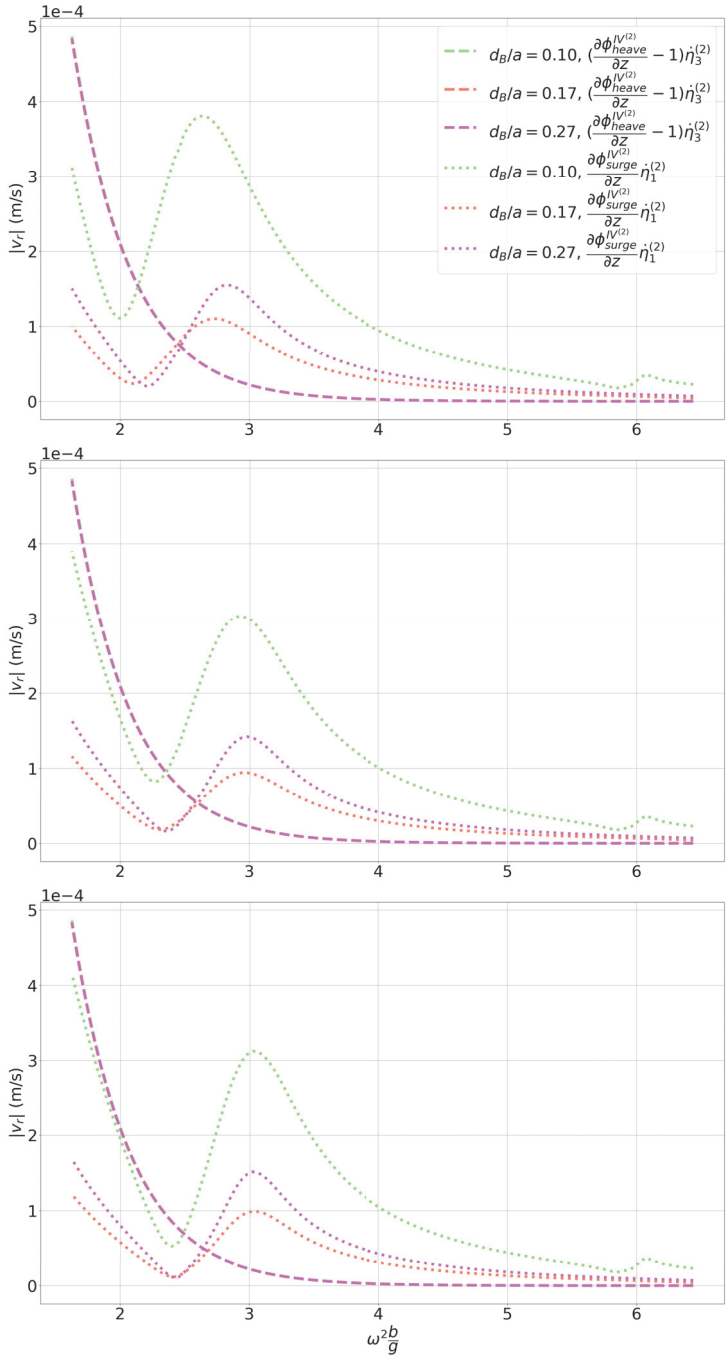

Figure D.11: *. Top: $\tau = 0$. Middle: $\tau = 0.15$.Bottom: $\tau = 0.30$. Amplitude of the vertical relative flow velocity from semi-analytical simulations on the perforated baffle in $\theta = 0°$ in a dock-fixed coordinate system. contribution of the dock's surge and heave motions when the free-surface is rigid are given for three values of d_B/a. Wave steepness: $\epsilon = 1/60$.*

D.4 Numerical simulations with annular baffles.

The number of iterations over which the equations of motion are solved until convergence of the dock's motions' RAOs when non-linear terms describing the baffles' viscous effects are included (cf. Sec. 5.1) are given in Fig. D.12.

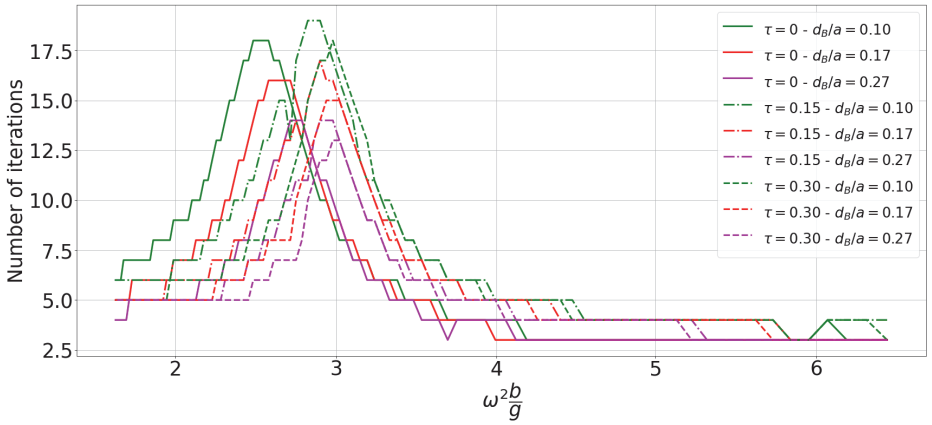

Figure D.12: *Number of iterations required for the convergence of $\eta_1^{(2)}$'s, $\eta_5^{(2)}$'s and ζ_{WP1}'s RAOs when solving the equations of motions with non-linear effects of annular baffles. Wave steepness: $\epsilon = 1/60$.*

The variations of the shifted natural sloshing frequency $\sigma'_{1,1}$ estimated from variational theory are presented in Fig. D.13 as a function of the incident wave frequency, showing little dependency of $\sigma'_{1,1}$ on $\omega^2 b/g$, which does not vary more than 2% over the range of incident wave frequencies showed on the figure.

The amplitude of the moments in pitch F_5^M on the baffles, as well as the amplitude of the vertical loads on the baffles in $\theta = 0°$, both estimated from Morison's formula (cf. Eq. (5.7)) are also presented for solid and perforated baffles in Fig. D.14 and Fig. D.15, respectively. As expected, the loads are lower for perforate baffles. For these last, the damping loads dominate compare to inertial loads.

Several parameters resulting from numerical simulation for the dock+spar system when a solid baffle is installed at $d_B/a = 0.17$ are given in Fig. D.16. These results are similar to the ones discussed for the case without spar. We can note that the relative flow velocity on the baffle is again dominated by the contributions of sloshing waves, in particularly compared to the radiated flow caused by the spar's motions.

RAOs of the spar's surge and pitch motions for the case with and without baffles are presented in both a dock-fixed (DCS) and Earth-fixed (ECS) coordinate systems

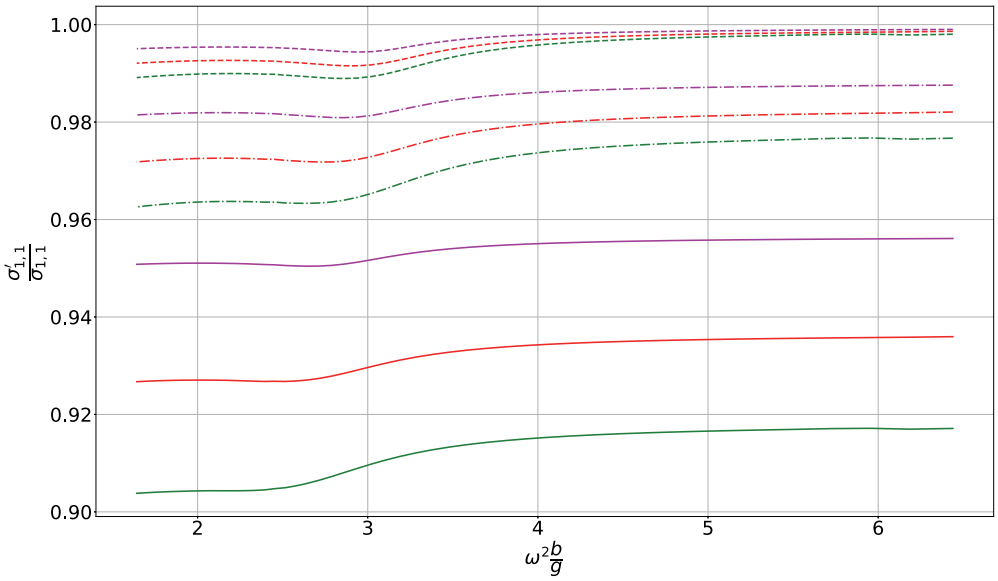

Figure D.13: *Shifted lowest natural sloshing frequency estimated from variational method (cf. Eq. (3.84)), and Mentzoni's coefficients from Table 3.2 as a function of the incident wave frequency.* $\sigma'_{1,1}/\sigma_{1,1} = 1$ *when there is no baffle. Same legend as in Fig. 6.14. Wave steepness:* $\epsilon = 1/60$.

in Fig. D.17. Because of the phase shift of the dock's motions in $\omega^2 b/g = 2.5$ (see Sec. 6.3) which become in opposition of phases with the spar's motions for higher frequency, $\eta_1^{(1)}$'s and $\eta_5^{(1)}$'s amplitudes are higher in the dock-fixed coordinate system.

D.5 Time domain solver

A time domain solver is implemented for the simplified representation of the dock without spar and with a closed bottom (see Fig. (2.3) in Sec. 2.1.2). The motions are restricted to surge in this example. The internal flow is described by the damped modal equations (cf. Eq. (3.85) in Sec. 3.5).
Added mass and damping coefficients $a_{1,1}$ and $b_{1,1}$ are calculated for the external problem only, in the way of Yeung (1980), as well as the diffraction problem to determined the exciting force F_1^S in the way of Garrett (1971), i.e. through a domain decomposition approach. $a_{1,1}$, $b_{1,1}$ and F_1^S are solved in the frequency domain. Incident irregular waves are discretised in the frequency domain from a JONSWAP spectrum, and represented as the summation of regular waves. Due to linearity of the diffraction problem, the scattering force $F_1^S(t)$ is then obtained by summing the contribution of each frequency. Assuming a non-linear damping of dock's motions by the sloshing waves, it is a priori not possible to sum the

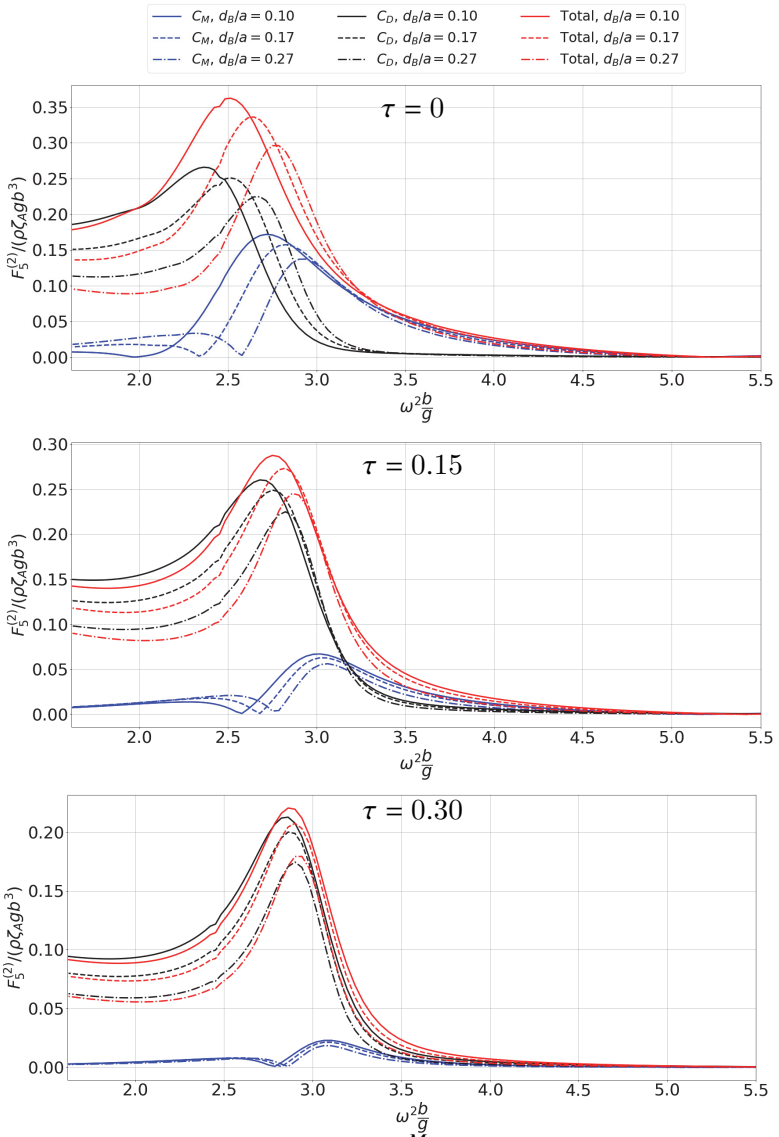

Figure D.14: *Amplitude of the moment F_5^M on the baffle estimated from Morison's formula (cf. Eq. (5.7)) for solid baffle (top) and perforated baffles with perforation ratios $\tau = 0.15$ (middle) and $\tau = 0.3$ (bottom). The amplitude of the inertial and damping terms in Morison's equations are also indicated, and referred to in the legend as C_M and C_D, respectively. The Submergence of the baffle: $d_B/a = 0.17$. Wave steepness: $\epsilon = 1/60$.*

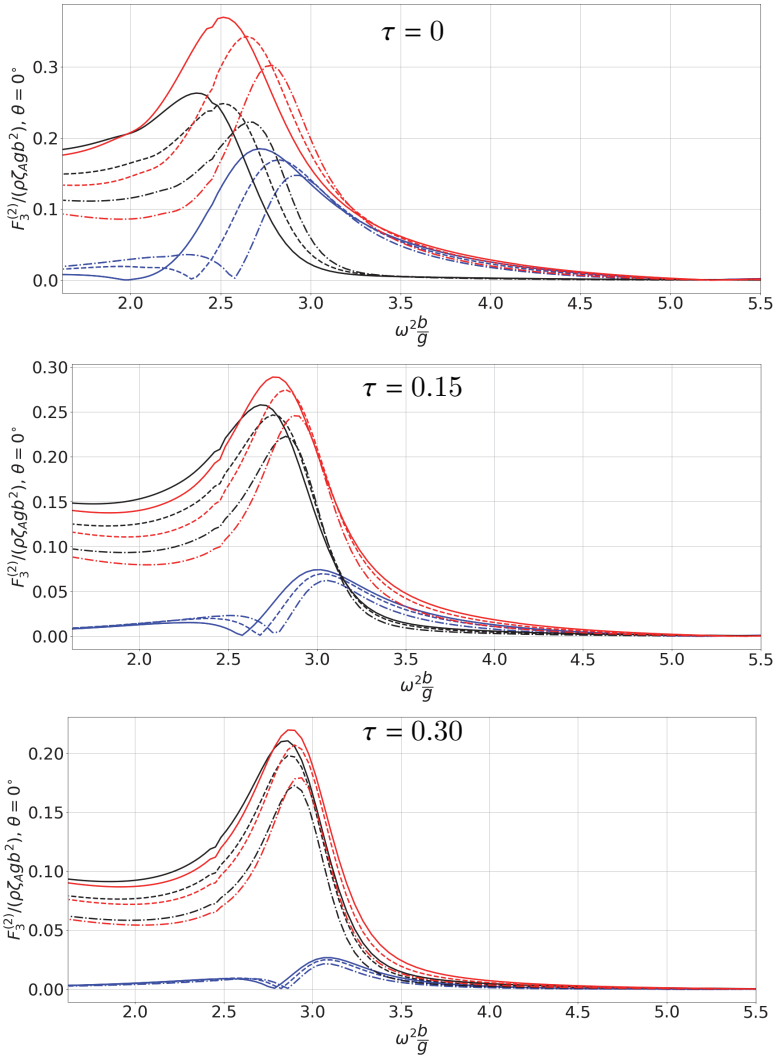

Figure D.15: *Amplitude of the vertical loads on the baffle in $\theta = 0°$ estimated from Morison's formula (cf. integrand of Eq. (5.7)) for solid baffle (top) and perforated baffles with perforation ratios $\tau = 0.15$ (middle) and $\tau = 0.3$ (bottom). The legend is the same as Fig. D.14. The Submergence of the baffle: $d_B/a = 0.17$. Wave steepness: $\epsilon = 1/60$.*

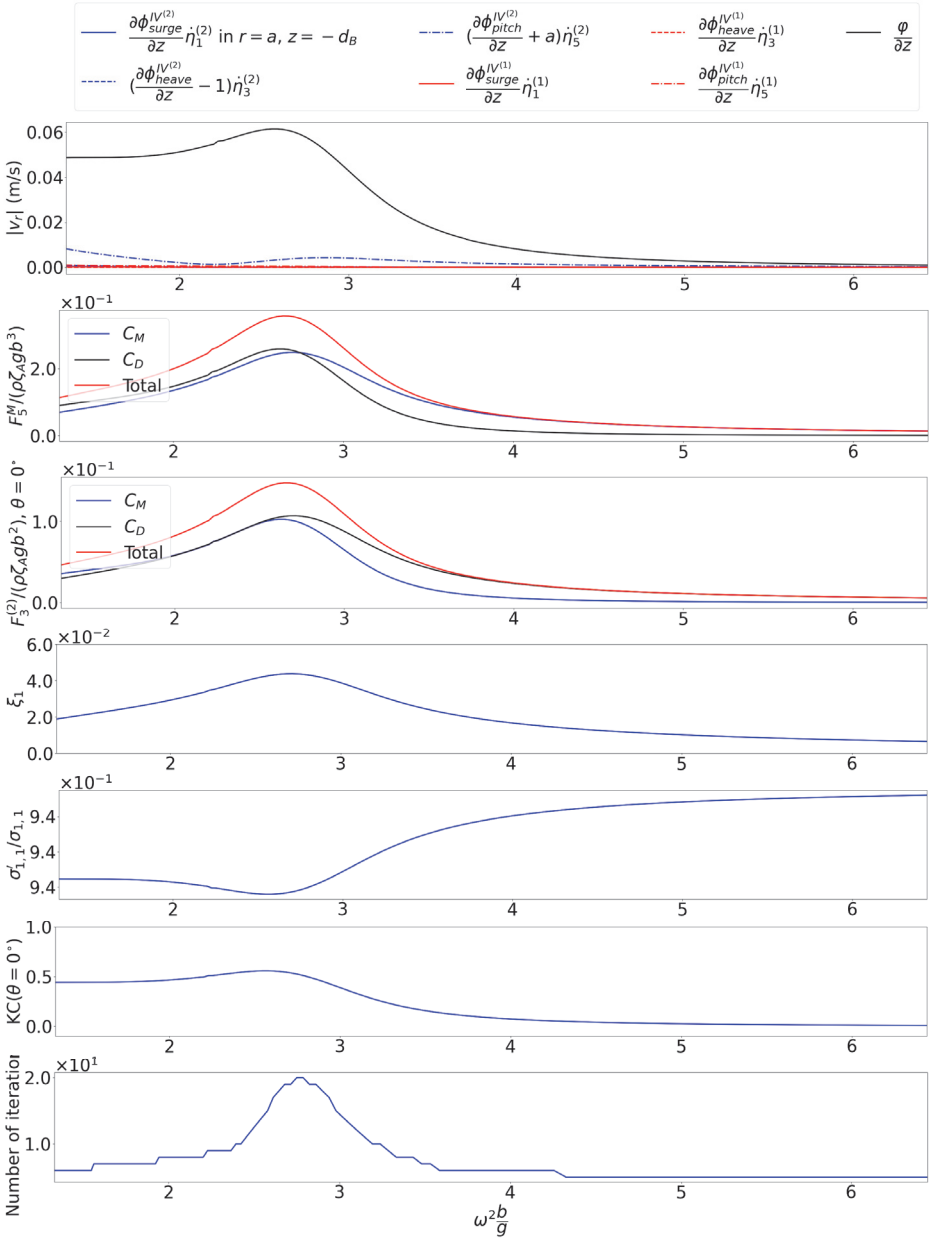

Figure D.16: *Several results from semi-analytical simulations for the dock with the spar and a solid baffle ($\tau = 0$) in regular incident waves. Wave steepness: $\epsilon = 1/60$.*

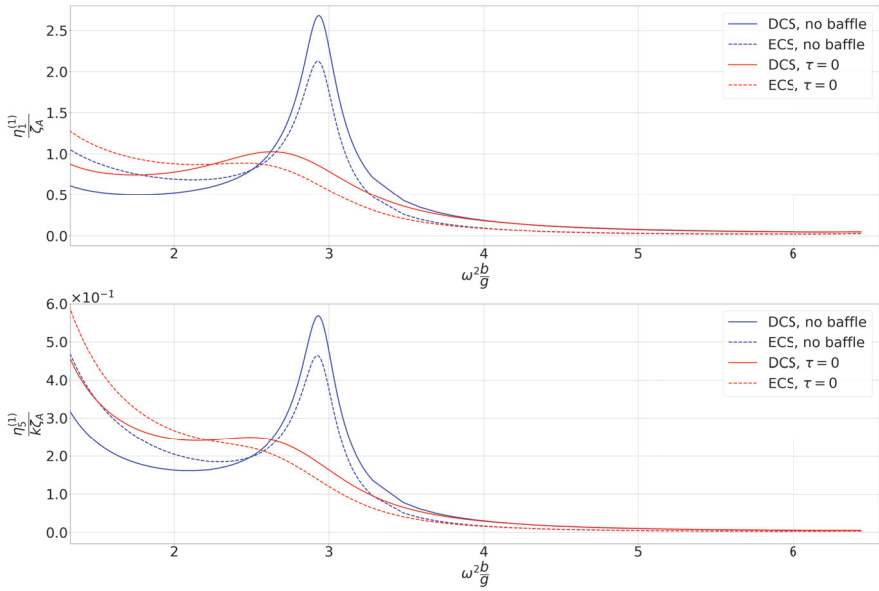

Figure D.17: *Dimensional surge and pitch motions of the spar in both an Earth-fixed (ECS) and dock-fixed (DCS) coordinate systems from the semi-analytical model. Motions in full scale. Wave steepness:* $\epsilon = 1/60$.

contribution of the loads caused by the dock's motions. The equations of motions are thus expressed in time domain (Faltinsen and Timokha, 2009):

$$\left[M + a_{1,1}(\infty)\right]\ddot{\eta}_1^{(2)}(t) + b_{1,1,}(\infty)\dot{\eta}_1^{(2)}(t) + \int_0^t h_{1,1}(\tau)\dot{\eta}_1(t-\tau)d\tau + c_{1,1}\eta_1^{(2)} = F_1^S(t) + F_1^{\text{slosh}}(t), \tag{D.1}$$

where $h_{1,1}(t)$ is the retardation function, which can be estimated either from the added mass or from the damping coefficients. The asymptotic behaviour of $a_{1,1}$ for high frequency is a priori unknown, such that the use of $b_{1,1}$, which convergences to 0 for high frequency, is preferred here:

$$h_{1,1}(t) = \frac{2}{\pi}\int_0^\infty (b_{1,1}(\omega) - \overbrace{b_{1,1,}(\infty)}^{=0})\cos(\omega t)d\omega. \tag{D.2}$$

$h_{1,1}$ is shown in Fig. D.18. $F_1^{\text{slosh}}(t)$ in Eq. (D.1) includes all the hydrodynamic loads caused by the internal fluid. Near sloshing resonance, and under first mode approximation, it is given by:

$$F_1^{\text{slosh}}(t) = \underbrace{-\rho a^2 \pi d}_{\tilde{C}_1}\ddot{\eta}_1^{(2)} \underbrace{-\rho\frac{\pi a}{k_{1,1}}\tanh(k_{1,1}d)}_{\tilde{C}_2}\dot{R}_{1,1}(t), \tag{D.3}$$

where $R_{1,1}$ also contains here the transient part of the solution of the modal equation, contrary to the solution presented in Sec. 2.1.2. For the simplified model considered here, the excitation in the right hand side of the modal equation is simply given by:

$$K_{1,1}(t) = -\frac{\lambda_{1,1}}{\mu_{1,1}}\ddot{\eta}_1^{(2)}(t), \tag{D.4}$$

with

$$\lambda_{1,1} = \frac{\rho\pi a}{\iota_{1,1}^2}, \tag{D.5}$$

$$\mu_{1,1} = \frac{\rho\pi a^3(\iota_{1,1}^2 - 1)}{2\iota_{1,1}^3 \tanh(\frac{\iota_{1,1}d}{a})}. \tag{D.6}$$

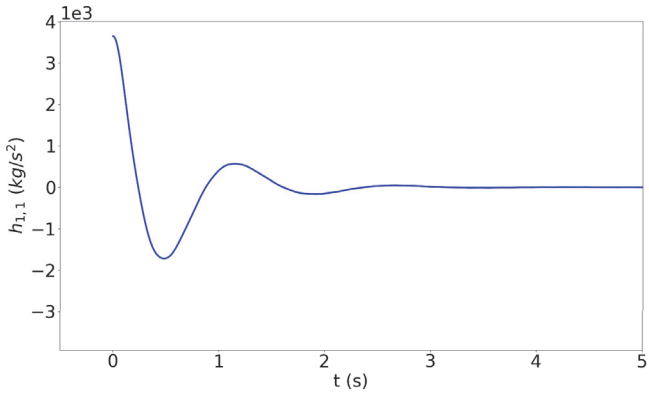

Figure D.18: *Retardation function* $h_{1,1}$ *(cf. Eq.* (D.2)

At this point, we established a system of equations constituted by the the equation of motion (D.1) for the external problem, and the damped modal equations for the internal problem (cf. Eq. (3.85) in Sec. 3.5), for which the unknown are η_1 and either $\beta_{1,1}$ or $R_{1,1}$. This system is expressed as the ordinary differential equation (ODE):

$$\dot{u} = f(u, t), \tag{D.7}$$

where the variable $u = [u_1\ u_2\ u_3\ u_4]^T$ is given by:

$$u_1 = \eta_1^{(2)}, \tag{D.8}$$

$$u_2 = \beta_1, \tag{D.9}$$

$$u_3 = \underbrace{\left[M + a_{1,1}(\infty) - \tilde{C}_1\right]}_{D_1} \ddot{\eta}_1^{(2)}(t) \underbrace{-\tilde{C}_2}_{D_2} \dot{\beta}_1, \tag{D.10}$$

$$u_4 = \dot{\beta}_1 + \underbrace{\frac{\lambda_{1,1}}{\mu 1,1}}_{D_3} \dot{\eta_1}^{(2)}, \tag{D.11}$$

and where $\tilde{C}_1$ and $\tilde{C}_2$ are defined in Eq. (D.3). The function $f(u,t) = \begin{bmatrix} f_1(u,t) \\ f_2(u,t) \\ f_3(u,t) \\ f_4(u,t) \end{bmatrix}$ is expressed as:

$$f_1(u,t) = \frac{u_3 - D_2 u_4}{D_1 - D_3 D_2}, \tag{D.12}$$

$$f_2(u,t) = \frac{D_3 u_3 - D_1 u_4}{D_2 D_3 - D_4 D_1}, \tag{D.13}$$

$$f_3(u,t) = -\int_0^t h_{1,1}(\tau) f_1(u, t-\tau) d\tau - c_{1,1} u_1 + F_1^S(t), \tag{D.14}$$

$$f_4(u,t) = -2\xi_1 \sigma_{1,1} f_2(u,t) - \sigma_{1,1}^2 u_2, \tag{D.15}$$

where the D coefficients are defined in Eqs. (D.14)-(D.15). A Runge-Kutta scheme of order 4 is implemented to solve the ODE (D.7).

The method is first verified for different incident regular waves, and compared to the frequency domain solution, determined from the equations of motions presented in Chapter 5. Fig. D.19 shows an example of result in regular waves for an incident wave period near resonance $T = 0.74$s, and with the arbitrary damping ξ_1 in the modal equations. The time domain solution includes the transient phase of the signals, as well as the natural period in surge due to mooring. Because of the damping, both solutions in time and frequency domains converge for high t.

Then, irregular waves are considered and a JONWSWAP spectrum characterised by the peak period $T_p = 0.8$s and the significant wave height $H_s/b = 1/40$ is discretised in the frequency domain (cf. Fig. D.20) in order to generate time series of incident waves. Time series are hence generated over 600s, and the power spectra of $\eta_1^{(2)}$ and ζ_{WP1} calculated and filtered from the time domain solutions. Several arbitrary values of the damping ratio ξ_1 are tested, and the results once

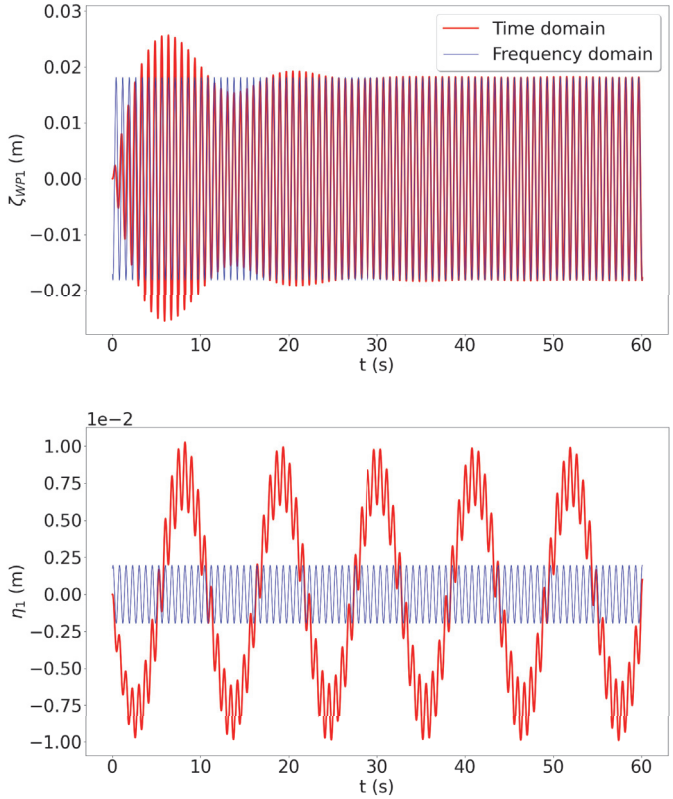

Figure D.19: *Time series of ζ_{WP1} (top) and of the dock's surge motions (bottom), both solved in the frequency and time domains for regular incident waves with a period $T = 0.74s$. Wave steepness: $\epsilon = 1/60$. The dimensions of the dock are those described in Chapter 4 with $d/b = 2$. Damping: $\xi_1 = 1\%$. The natural period in surge due to mooring is observed from the time domain solution.*

again compared to the frequency domain solutions.
RAOs are presented in Fig. D.21. The results calculated from the time solver seem to converge to the frequency domain solution, except at the peak sloshing resonance, for which the time domain solutions are lower. The difference between the amplitudes of the time and frequency domains-calculated RAOs is even higher for low damping ratios, most likely caused by longer transient phases of the signals, which are not included in the frequency domain solutions.

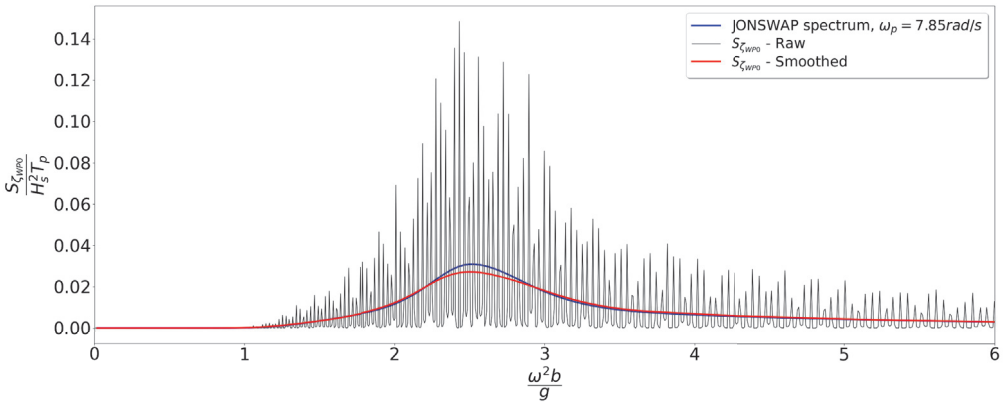

Figure D.20: *Discretisation of the JONSWAP's spectrum.* $\sigma_G = 0.0159$.

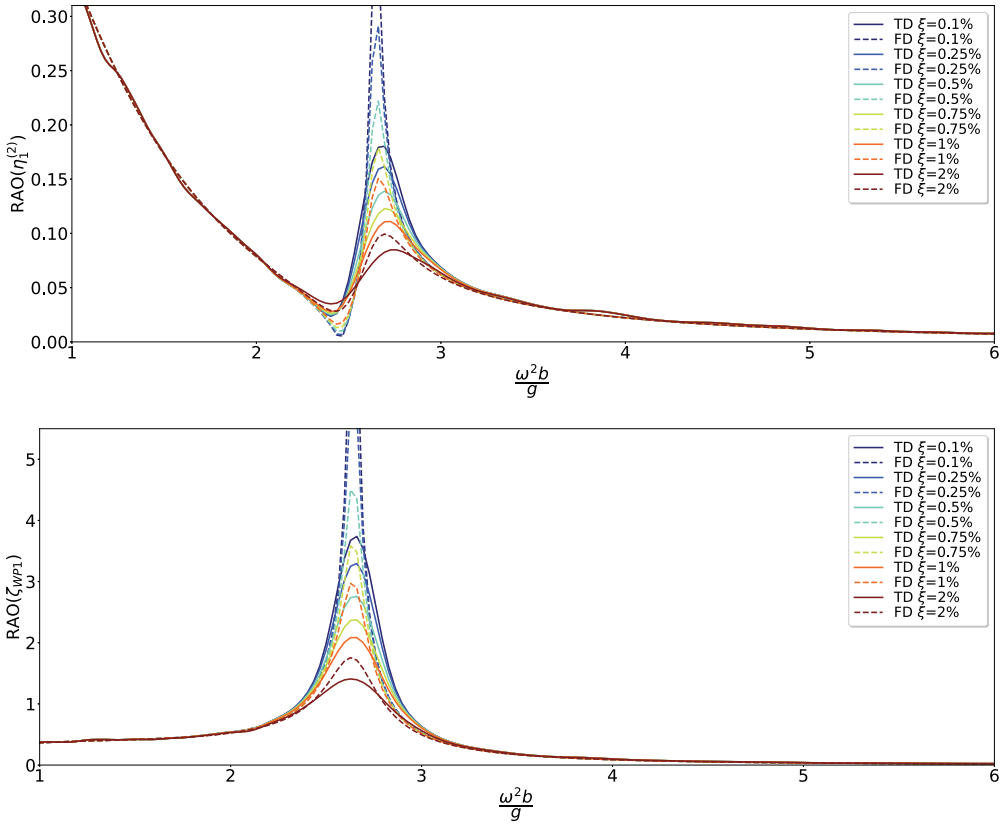

Figure D.21: *RAOs of* $\eta_1^{(2)}$ *(top) and* ζ_{WP1} *(bottom) calculated from both the time domain (TD) and frequency domain (FD) solutions. Gaussian filtering of the spectra obtained from the time domain solutions:* $\sigma_G = 0.0159$.

Previous PhD theses published at the Department of Marine Technology (earlier: Faculty of Marine Technology) NORWEGIAN UNIVERSITY OF SCIENCE AND TECHNOLOGY

Report No.	Author	Title
	Kavlie, Dag	Optimization of Plane Elastic Grillages, 1967
	Hansen, Hans R.	Man-Machine Communication and Data-Storage Methods in Ship Structural Design, 1971
	Gisvold, Kaare M.	A Method for non-linear mixed -integer programming and its Application to Design Problems, 1971
	Lund, Sverre	Tanker Frame Optimalization by means of SUMT-Transformation and Behaviour Models, 1971
	Vinje, Tor	On Vibration of Spherical Shells Interacting with Fluid, 1972
	Lorentz, Jan D.	Tank Arrangement for Crude Oil Carriers in Accordance with the new Anti-Pollution Regulations, 1975
	Carlsen, Carl A.	Computer-Aided Design of Tanker Structures, 1975
	Larsen, Carl M.	Static and Dynamic Analysis of Offshore Pipelines during Installation, 1976
UR-79-01	Brigt Hatlestad, MK	The finite element method used in a fatigue evaluation of fixed offshore platforms. (Dr.Ing. Thesis)
UR-79-02	Erik Pettersen, MK	Analysis and design of cellular structures. (Dr.Ing. Thesis)
UR-79-03	Sverre Valsgård, MK	Finite difference and finite element methods applied to nonlinear analysis of plated structures. (Dr.Ing. Thesis)
UR-79-04	Nils T. Nordsve, MK	Finite element collapse analysis of structural members considering imperfections and stresses due to fabrication. (Dr.Ing. Thesis)
UR-79-05	Ivar J. Fylling, MK	Analysis of towline forces in ocean towing systems. (Dr.Ing. Thesis)
UR-79- x	Finn Gunnar Nielsen, MH	Hydrodynamic problems related to oil barriers for offshore application
UR-80-06	Nils Sandsmark, MM	Analysis of Stationary and Transient Heat Conduction by the Use of the Finite Element Method. (Dr.Ing. Thesis)
UR-80-09	Sverre Haver, MK	Analysis of uncertainties related to the stochastic modeling of ocean waves. (Dr.Ing. Thesis)

UR-81-15	Odland, Jonas	On the Strength of welded Ring stiffened cylindrical Shells primarily subjected to axial Compression
UR-82-17	Engesvik, Knut	Analysis of Uncertainties in the fatigue Capacity of Welded Joints
UR-82-18	Rye, Henrik	Ocean wave groups
UR-83-30	Eide, Oddvar Inge	On Cumulative Fatigue Damage in Steel Welded Joints
UR-83-33	Mo, Olav	Stochastic Time Domain Analysis of Slender Offshore Structures
UR-83-34	Amdahl, Jørgen	Energy absorption in Ship-platform impacts
UR-84-37	Mørch, Morten	Motions and mooring forces of semi submersibles as determined by full-scale measurements and theoretical analysis
UR-84-38	Soares, C. Guedes	Probabilistic models for load effects in ship structures
UR-84-39	Aarsnes, Jan V.	Current forces on ships
UR-84-40	Czujko, Jerzy	Collapse Analysis of Plates subjected to Biaxial Compression and Lateral Load
UR-85-46	Alf G. Engseth, MK	Finite element collapse analysis of tubular steel offshore structures. (Dr.Ing. Thesis)
UR-86-47	Dengody Sheshappa, MP	A Computer Design Model for Optimizing Fishing Vessel Designs Based on Techno-Economic Analysis. (Dr.Ing. Thesis)
UR-86-48	Vidar Aanesland, MH	A Theoretical and Numerical Study of Ship Wave Resistance. (Dr.Ing. Thesis)
UR-86-49	Heinz-Joachim Wessel, MK	Fracture Mechanics Analysis of Crack Growth in Plate Girders. (Dr.Ing. Thesis)
UR-86-50	Jon Taby, MK	Ultimate and Post-ultimate Strength of Dented Tubular Members. (Dr.Ing. Thesis)
UR-86-51	Walter Lian, MH	A Numerical Study of Two-Dimensional Separated Flow Past Bluff Bodies at Moderate KC-Numbers. (Dr.Ing. Thesis)
UR-86-52	Bjørn Sortland, MH	Force Measurements in Oscillating Flow on Ship Sections and Circular Cylinders in a U-Tube Water Tank. (Dr.Ing. Thesis)
UR-86-53	Kurt Strand, MM	A System Dynamic Approach to One-dimensional Fluid Flow. (Dr.Ing. Thesis)
UR-86-54	Arne Edvin Løken, MH	Three Dimensional Second Order Hydrodynamic Effects on Ocean Structures in Waves. (Dr.Ing. Thesis)
UR-86-55	Sigurd Falch, MH	A Numerical Study of Slamming of Two-

		Dimensional Bodies. (Dr.Ing. Thesis)
UR-87-56	Arne Braathen, MH	Application of a Vortex Tracking Method to the Prediction of Roll Damping of a Two-Dimension Floating Body. (Dr.Ing. Thesis)
UR-87-57	Bernt Leira, MK	Gaussian Vector Processes for Reliability Analysis involving Wave-Induced Load Effects. (Dr.Ing. Thesis)
UR-87-58	Magnus Småvik, MM	Thermal Load and Process Characteristics in a Two-Stroke Diesel Engine with Thermal Barriers (in Norwegian). (Dr.Ing. Thesis)
MTA-88-59	Bernt Arild Bremdal, MP	An Investigation of Marine Installation Processes – A Knowledge - Based Planning Approach. (Dr.Ing. Thesis)
MTA-88-60	Xu Jun, MK	Non-linear Dynamic Analysis of Space-framed Offshore Structures. (Dr.Ing. Thesis)
MTA-89-61	Gang Miao, MH	Hydrodynamic Forces and Dynamic Responses of Circular Cylinders in Wave Zones. (Dr.Ing. Thesis)
MTA-89-62	Martin Greenhow, MH	Linear and Non-Linear Studies of Waves and Floating Bodies. Part I and Part II. (Dr.Techn. Thesis)
MTA-89-63	Chang Li, MH	Force Coefficients of Spheres and Cubes in Oscillatory Flow with and without Current. (Dr.Ing. Thesis
MTA-89-64	Hu Ying, MP	A Study of Marketing and Design in Development of Marine Transport Systems. (Dr.Ing. Thesis)
MTA-89-65	Arild Jæger, MH	Seakeeping, Dynamic Stability and Performance of a Wedge Shaped Planing Hull. (Dr.Ing. Thesis)
MTA-89-66	Chan Siu Hung, MM	The dynamic characteristics of tilting-pad bearings
MTA-89-67	Kim Wikstrøm, MP	Analysis av projekteringen for ett offshore projekt. (Licenciat-avhandling)
MTA-89-68	Jiao Guoyang, MK	Reliability Analysis of Crack Growth under Random Loading, considering Model Updating. (Dr.Ing. Thesis)
MTA-89-69	Arnt Olufsen, MK	Uncertainty and Reliability Analysis of Fixed Offshore Structures. (Dr.Ing. Thesis)
MTA-89-70	Wu Yu-Lin, MR	System Reliability Analyses of Offshore Structures using improved Truss and Beam Models. (Dr.Ing. Thesis)
MTA-90-71	Jan Roger Hoff, MH	Three-dimensional Green function of a vessel with forward speed in waves. (Dr.Ing. Thesis)
MTA-90-72	Rong Zhao, MH	Slow-Drift Motions of a Moored Two-Dimensional Body in Irregular Waves. (Dr.Ing. Thesis)
MTA-90-73	Atle Minsaas, MP	Economical Risk Analysis. (Dr.Ing. Thesis)

MTA-90-74	Knut-Aril Farnes, MK	Long-term Statistics of Response in Non-linear Marine Structures. (Dr.Ing. Thesis)
MTA-90-75	Torbjørn Sotberg, MK	Application of Reliability Methods for Safety Assessment of Submarine Pipelines. (Dr.Ing. Thesis)
MTA-90-76	Zeuthen, Steffen, MP	SEAMAID. A computational model of the design process in a constraint-based logic programming environment. An example from the offshore domain. (Dr.Ing. Thesis)
MTA-91-77	Haagensen, Sven, MM	Fuel Dependant Cyclic Variability in a Spark Ignition Engine - An Optical Approach. (Dr.Ing. Thesis)
MTA-91-78	Løland, Geir, MH	Current forces on and flow through fish farms. (Dr.Ing. Thesis)
MTA-91-79	Hoen, Christopher, MK	System Identification of Structures Excited by Stochastic Load Processes. (Dr.Ing. Thesis)
MTA-91-80	Haugen, Stein, MK	Probabilistic Evaluation of Frequency of Collision between Ships and Offshore Platforms. (Dr.Ing. Thesis)
MTA-91-81	Sødahl, Nils, MK	Methods for Design and Analysis of Flexible Risers. (Dr.Ing. Thesis)
MTA-91-82	Ormberg, Harald, MK	Non-linear Response Analysis of Floating Fish Farm Systems. (Dr.Ing. Thesis)
MTA-91-83	Marley, Mark J., MK	Time Variant Reliability under Fatigue Degradation. (Dr.Ing. Thesis)
MTA-91-84	Krokstad, Jørgen R., MH	Second-order Loads in Multidirectional Seas. (Dr.Ing. Thesis)
MTA-91-85	Molteberg, Gunnar A., MM	The Application of System Identification Techniques to Performance Monitoring of Four Stroke Turbocharged Diesel Engines. (Dr.Ing. Thesis)
MTA-92-86	Mørch, Hans Jørgen Bjelke, MH	Aspects of Hydrofoil Design: with Emphasis on Hydrofoil Interaction in Calm Water. (Dr.Ing. Thesis)
MTA-92-87	Chan Siu Hung, MM	Nonlinear Analysis of Rotordynamic Instabilities in Highspeed Turbomachinery. (Dr.Ing. Thesis)
MTA-92-88	Bessason, Bjarni, MK	Assessment of Earthquake Loading and Response of Seismically Isolated Bridges. (Dr.Ing. Thesis)
MTA-92-89	Langli, Geir, MP	Improving Operational Safety through exploitation of Design Knowledge - an investigation of offshore platform safety. (Dr.Ing. Thesis)
MTA-92-90	Sævik, Svein, MK	On Stresses and Fatigue in Flexible Pipes. (Dr.Ing. Thesis)
MTA-92-91	Ask, Tor Ø., MM	Ignition and Flame Growth in Lean Gas-Air Mixtures. An Experimental Study with a Schlieren

		System. (Dr.Ing. Thesis)
MTA-86-92	Hessen, Gunnar, MK	Fracture Mechanics Analysis of Stiffened Tubular Members. (Dr.Ing. Thesis)
MTA-93-93	Steinebach, Christian, MM	Knowledge Based Systems for Diagnosis of Rotating Machinery. (Dr.Ing. Thesis)
MTA-93-94	Dalane, Jan Inge, MK	System Reliability in Design and Maintenance of Fixed Offshore Structures. (Dr.Ing. Thesis)
MTA-93-95	Steen, Sverre, MH	Cobblestone Effect on SES. (Dr.Ing. Thesis)
MTA-93-96	Karunakaran, Daniel, MK	Nonlinear Dynamic Response and Reliability Analysis of Drag-dominated Offshore Platforms. (Dr.Ing. Thesis)
MTA-93-97	Hagen, Arnulf, MP	The Framework of a Design Process Language. (Dr.Ing. Thesis)
MTA-93-98	Nordrik, Rune, MM	Investigation of Spark Ignition and Autoignition in Methane and Air Using Computational Fluid Dynamics and Chemical Reaction Kinetics. A Numerical Study of Ignition Processes in Internal Combustion Engines. (Dr.Ing. Thesis)
MTA-94-99	Passano, Elizabeth, MK	Efficient Analysis of Nonlinear Slender Marine Structures. (Dr.Ing. Thesis)
MTA-94-100	Kvålsvold, Jan, MH	Hydroelastic Modelling of Wetdeck Slamming on Multihull Vessels. (Dr.Ing. Thesis)
MTA-94-102	Bech, Sidsel M., MK	Experimental and Numerical Determination of Stiffness and Strength of GRP/PVC Sandwich Structures. (Dr.Ing. Thesis)
MTA-95-103	Paulsen, Hallvard, MM	A Study of Transient Jet and Spray using a Schlieren Method and Digital Image Processing. (Dr.Ing. Thesis)
MTA-95-104	Hovde, Geir Olav, MK	Fatigue and Overload Reliability of Offshore Structural Systems, Considering the Effect of Inspection and Repair. (Dr.Ing. Thesis)
MTA-95-105	Wang, Xiaozhi, MK	Reliability Analysis of Production Ships with Emphasis on Load Combination and Ultimate Strength. (Dr.Ing. Thesis)
MTA-95-106	Ulstein, Tore, MH	Nonlinear Effects of a Flexible Stern Seal Bag on Cobblestone Oscillations of an SES. (Dr.Ing. Thesis)
MTA-95-107	Solaas, Frøydis, MH	Analytical and Numerical Studies of Sloshing in Tanks. (Dr.Ing. Thesis)
MTA-95-108	Hellan, Øyvind, MK	Nonlinear Pushover and Cyclic Analyses in Ultimate Limit State Design and Reassessment of Tubular Steel Offshore Structures. (Dr.Ing. Thesis)
MTA-95-109	Hermundstad, Ole A., MK	Theoretical and Experimental Hydroelastic Analysis of High Speed Vessels. (Dr.Ing. Thesis)

MTA-96-110	Bratland, Anne K., MH	Wave-Current Interaction Effects on Large-Volume Bodies in Water of Finite Depth. (Dr.Ing. Thesis)
MTA-96-111	Herfjord, Kjell, MH	A Study of Two-dimensional Separated Flow by a Combination of the Finite Element Method and Navier-Stokes Equations. (Dr.Ing. Thesis)
MTA-96-112	Æsøy, Vilmar, MM	Hot Surface Assisted Compression Ignition in a Direct Injection Natural Gas Engine. (Dr.Ing. Thesis)
MTA-96-113	Eknes, Monika L., MK	Escalation Scenarios Initiated by Gas Explosions on Offshore Installations. (Dr.Ing. Thesis)
MTA-96-114	Erikstad, Stein O., MP	A Decision Support Model for Preliminary Ship Design. (Dr.Ing. Thesis)
MTA-96-115	Pedersen, Egil, MH	A Nautical Study of Towed Marine Seismic Streamer Cable Configurations. (Dr.Ing. Thesis)
MTA-97-116	Moksnes, Paul O., MM	Modelling Two-Phase Thermo-Fluid Systems Using Bond Graphs. (Dr.Ing. Thesis)
MTA-97-117	Halse, Karl H., MK	On Vortex Shedding and Prediction of Vortex-Induced Vibrations of Circular Cylinders. (Dr.Ing. Thesis)
MTA-97-118	Igland, Ragnar T., MK	Reliability Analysis of Pipelines during Laying, considering Ultimate Strength under Combined Loads. (Dr.Ing. Thesis)
MTA-97-119	Pedersen, Hans-P., MP	Levendefiskteknologi for fiskefartøy. (Dr.Ing. Thesis)
MTA-98-120	Vikestad, Kyrre, MK	Multi-Frequency Response of a Cylinder Subjected to Vortex Shedding and Support Motions. (Dr.Ing. Thesis)
MTA-98-121	Azadi, Mohammad R. E., MK	Analysis of Static and Dynamic Pile-Soil-Jacket Behaviour. (Dr.Ing. Thesis)
MTA-98-122	Ulltang, Terje, MP	A Communication Model for Product Information. (Dr.Ing. Thesis)
MTA-98-123	Torbergsen, Erik, MM	Impeller/Diffuser Interaction Forces in Centrifugal Pumps. (Dr.Ing. Thesis)
MTA-98-124	Hansen, Edmond, MH	A Discrete Element Model to Study Marginal Ice Zone Dynamics and the Behaviour of Vessels Moored in Broken Ice. (Dr.Ing. Thesis)
MTA-98-125	Videiro, Paulo M., MK	Reliability Based Design of Marine Structures. (Dr.Ing. Thesis)
MTA-99-126	Mainçon, Philippe, MK	Fatigue Reliability of Long Welds Application to Titanium Risers. (Dr.Ing. Thesis)
MTA-99-127	Haugen, Elin M., MH	Hydroelastic Analysis of Slamming on Stiffened Plates with Application to Catamaran Wetdecks. (Dr.Ing. Thesis)
MTA-99-	Langhelle, Nina K., MK	Experimental Validation and Calibration of

128		Nonlinear Finite Element Models for Use in Design of Aluminium Structures Exposed to Fire. (Dr.Ing. Thesis)
MTA-99-129	Berstad, Are J., MK	Calculation of Fatigue Damage in Ship Structures. (Dr.Ing. Thesis)
MTA-99-130	Andersen, Trond M., MM	Short Term Maintenance Planning. (Dr.Ing. Thesis)
MTA-99-131	Tveiten, Bård Wathne, MK	Fatigue Assessment of Welded Aluminium Ship Details. (Dr.Ing. Thesis)
MTA-99-132	Søreide, Fredrik, MP	Applications of underwater technology in deep water archaeology. Principles and practice. (Dr.Ing. Thesis)
MTA-99-133	Tønnessen, Rune, MH	A Finite Element Method Applied to Unsteady Viscous Flow Around 2D Blunt Bodies With Sharp Corners. (Dr.Ing. Thesis)
MTA-99-134	Elvekrok, Dag R., MP	Engineering Integration in Field Development Projects in the Norwegian Oil and Gas Industry. The Supplier Management of Norne. (Dr.Ing. Thesis)
MTA-99-135	Fagerholt, Kjetil, MP	Optimeringsbaserte Metoder for Ruteplanlegging innen skipsfart. (Dr.Ing. Thesis)
MTA-99-136	Bysveen, Marie, MM	Visualization in Two Directions on a Dynamic Combustion Rig for Studies of Fuel Quality. (Dr.Ing. Thesis)
MTA-2000-137	Storteig, Eskild, MM	Dynamic characteristics and leakage performance of liquid annular seals in centrifugal pumps. (Dr.Ing. Thesis)
MTA-2000-138	Sagli, Gro, MK	Model uncertainty and simplified estimates of long term extremes of hull girder loads in ships. (Dr.Ing. Thesis)
MTA-2000-139	Tronstad, Harald, MK	Nonlinear analysis and design of cable net structures like fishing gear based on the finite element method. (Dr.Ing. Thesis)
MTA-2000-140	Kroneberg, André, MP	Innovation in shipping by using scenarios. (Dr.Ing. Thesis)
MTA-2000-141	Haslum, Herbjørn Alf, MH	Simplified methods applied to nonlinear motion of spar platforms. (Dr.Ing. Thesis)
MTA-2001-142	Samdal, Ole Johan, MM	Modelling of Degradation Mechanisms and Stressor Interaction on Static Mechanical Equipment Residual Lifetime. (Dr.Ing. Thesis)
MTA-2001-143	Baarholm, Rolf Jarle, MH	Theoretical and experimental studies of wave impact underneath decks of offshore platforms. (Dr.Ing. Thesis)
MTA-2001-144	Wang, Lihua, MK	Probabilistic Analysis of Nonlinear Wave-induced Loads on Ships. (Dr.Ing. Thesis)
MTA-2001-145	Kristensen, Odd H. Holt, MK	Ultimate Capacity of Aluminium Plates under Multiple Loads, Considering HAZ Properties.

		(Dr.Ing. Thesis)
MTA-2001-146	Greco, Marilena, MH	A Two-Dimensional Study of Green-Water Loading. (Dr.Ing. Thesis)
MTA-2001-147	Heggelund, Svein E., MK	Calculation of Global Design Loads and Load Effects in Large High Speed Catamarans. (Dr.Ing. Thesis)
MTA-2001-148	Babalola, Olusegun T., MK	Fatigue Strength of Titanium Risers – Defect Sensitivity. (Dr.Ing. Thesis)
MTA-2001-149	Mohammed, Abuu K., MK	Nonlinear Shell Finite Elements for Ultimate Strength and Collapse Analysis of Ship Structures. (Dr.Ing. Thesis)
MTA-2002-150	Holmedal, Lars E., MH	Wave-current interactions in the vicinity of the sea bed. (Dr.Ing. Thesis)
MTA-2002-151	Rognebakke, Olav F., MH	Sloshing in rectangular tanks and interaction with ship motions. (Dr.Ing. Thesis)
MTA-2002-152	Lader, Pål Furset, MH	Geometry and Kinematics of Breaking Waves. (Dr.Ing. Thesis)
MTA-2002-153	Yang, Qinzheng, MH	Wash and wave resistance of ships in finite water depth. (Dr.Ing. Thesis)
MTA-2002-154	Melhus, Øyvin, MM	Utilization of VOC in Diesel Engines. Ignition and combustion of VOC released by crude oil tankers. (Dr.Ing. Thesis)
MTA-2002-155	Ronæss, Marit, MH	Wave Induced Motions of Two Ships Advancing on Parallel Course. (Dr.Ing. Thesis)
MTA-2002-156	Økland, Ole D., MK	Numerical and experimental investigation of whipping in twin hull vessels exposed to severe wet deck slamming. (Dr.Ing. Thesis)
MTA-2002-157	Ge, Chunhua, MK	Global Hydroelastic Response of Catamarans due to Wet Deck Slamming. (Dr.Ing. Thesis)
MTA-2002-158	Byklum, Eirik, MK	Nonlinear Shell Finite Elements for Ultimate Strength and Collapse Analysis of Ship Structures. (Dr.Ing. Thesis)
IMT-2003-1	Chen, Haibo, MK	Probabilistic Evaluation of FPSO-Tanker Collision in Tandem Offloading Operation. (Dr.Ing. Thesis)
IMT-2003-2	Skaugset, Kjetil Bjørn, MK	On the Suppression of Vortex Induced Vibrations of Circular Cylinders by Radial Water Jets. (Dr.Ing. Thesis)
IMT-2003-3	Chezhian, Muthu	Three-Dimensional Analysis of Slamming. (Dr.Ing. Thesis)
IMT-2003-4	Buhaug, Øyvind	Deposit Formation on Cylinder Liner Surfaces in Medium Speed Engines. (Dr.Ing. Thesis)
IMT-2003-5	Tregde, Vidar	Aspects of Ship Design: Optimization of Aft Hull with Inverse Geometry Design. (Dr.Ing. Thesis)

IMT-2003-6	Wist, Hanne Therese	Statistical Properties of Successive Ocean Wave Parameters. (Dr.Ing. Thesis)
IMT-2004-7	Ransau, Samuel	Numerical Methods for Flows with Evolving Interfaces. (Dr.Ing. Thesis)
IMT-2004-8	Soma, Torkel	Blue-Chip or Sub-Standard. A data interrogation approach of identity safety characteristics of shipping organization. (Dr.Ing. Thesis)
IMT-2004-9	Ersdal, Svein	An experimental study of hydrodynamic forces on cylinders and cables in near axial flow. (Dr.Ing. Thesis)
IMT-2005-10	Brodtkorb, Per Andreas	The Probability of Occurrence of Dangerous Wave Situations at Sea. (Dr.Ing. Thesis)
IMT-2005-11	Yttervik, Rune	Ocean current variability in relation to offshore engineering. (Dr.Ing. Thesis)
IMT-2005-12	Fredheim, Arne	Current Forces on Net-Structures. (Dr.Ing. Thesis)
IMT-2005-13	Heggernes, Kjetil	Flow around marine structures. (Dr.Ing. Thesis
IMT-2005-14	Fouques, Sebastien	Lagrangian Modelling of Ocean Surface Waves and Synthetic Aperture Radar Wave Measurements. (Dr.Ing. Thesis)
IMT-2006-15	Holm, Håvard	Numerical calculation of viscous free surface flow around marine structures. (Dr.Ing. Thesis)
IMT-2006-16	Bjørheim, Lars G.	Failure Assessment of Long Through Thickness Fatigue Cracks in Ship Hulls. (Dr.Ing. Thesis)
IMT-2006-17	Hansson, Lisbeth	Safety Management for Prevention of Occupational Accidents. (Dr.Ing. Thesis)
IMT-2006-18	Zhu, Xinying	Application of the CIP Method to Strongly Nonlinear Wave-Body Interaction Problems. (Dr.Ing. Thesis)
IMT-2006-19	Reite, Karl Johan	Modelling and Control of Trawl Systems. (Dr.Ing. Thesis)
IMT-2006-20	Smogeli, Øyvind Notland	Control of Marine Propellers. From Normal to Extreme Conditions. (Dr.Ing. Thesis)
IMT-2007-21	Storhaug, Gaute	Experimental Investigation of Wave Induced Vibrations and Their Effect on the Fatigue Loading of Ships. (Dr.Ing. Thesis)
IMT-2007-22	Sun, Hui	A Boundary Element Method Applied to Strongly Nonlinear Wave-Body Interaction Problems. (PhD Thesis, CeSOS)
IMT-2007-23	Rustad, Anne Marthine	Modelling and Control of Top Tensioned Risers. (PhD Thesis, CeSOS)
IMT-2007-24	Johansen, Vegar	Modelling flexible slender system for real-time

		simulations and control applications
IMT-2007-25	Wroldsen, Anders Sunde	Modelling and control of tensegrity structures. (PhD Thesis, CeSOS)
IMT-2007-26	Aronsen, Kristoffer Høye	An experimental investigation of in-line and combined inline and cross flow vortex induced vibrations. (Dr. avhandling, IMT)
IMT-2007-27	Gao, Zhen	Stochastic Response Analysis of Mooring Systems with Emphasis on Frequency-domain Analysis of Fatigue due to Wide-band Response Processes (PhD Thesis, CeSOS)
IMT-2007-28	Thorstensen, Tom Anders	Lifetime Profit Modelling of Ageing Systems Utilizing Information about Technical Condition. (Dr.ing. thesis, IMT)
IMT-2008-29	Refsnes, Jon Erling Gorset	Nonlinear Model-Based Control of Slender Body AUVs (PhD Thesis, IMT)
IMT-2008-30	Berntsen, Per Ivar B.	Structural Reliability Based Position Mooring. (PhD-Thesis, IMT)
IMT-2008-31	Ye, Naiquan	Fatigue Assessment of Aluminium Welded Box-stiffener Joints in Ships (Dr.ing. thesis, IMT)
IMT-2008-32	Radan, Damir	Integrated Control of Marine Electrical Power Systems. (PhD-Thesis, IMT)
IMT-2008-33	Thomassen, Paul	Methods for Dynamic Response Analysis and Fatigue Life Estimation of Floating Fish Cages. (Dr.ing. thesis, IMT)
IMT-2008-34	Pákozdi, Csaba	A Smoothed Particle Hydrodynamics Study of Two-dimensional Nonlinear Sloshing in Rectangular Tanks. (Dr.ing.thesis, IMT/ CeSOS)
IMT-2007-35	Grytøyr, Guttorm	A Higher-Order Boundary Element Method and Applications to Marine Hydrodynamics. (Dr.ing.thesis, IMT)
IMT-2008-36	Drummen, Ingo	Experimental and Numerical Investigation of Nonlinear Wave-Induced Load Effects in Containerships considering Hydroelasticity. (PhD thesis, CeSOS)
IMT-2008-37	Skejic, Renato	Maneuvering and Seakeeping of a Singel Ship and of Two Ships in Interaction. (PhD-Thesis, CeSOS)
IMT-2008-38	Harlem, Alf	An Age-Based Replacement Model for Repairable Systems with Attention to High-Speed Marine Diesel Engines. (PhD-Thesis, IMT)
IMT-2008-39	Alsos, Hagbart S.	Ship Grounding. Analysis of Ductile Fracture, Bottom Damage and Hull Girder Response. (PhD-thesis, IMT)
IMT-2008-40	Graczyk, Mateusz	Experimental Investigation of Sloshing Loading and Load Effects in Membrane LNG Tanks Subjected to Random Excitation. (PhD-thesis, CeSOS)

IMT-2008-41	Taghipour, Reza	Efficient Prediction of Dynamic Response for Flexible amd Multi-body Marine Structures. (PhD-thesis, CeSOS)
IMT-2008-42	Ruth, Eivind	Propulsion control and thrust allocation on marine vessels. (PhD thesis, CeSOS)
IMT-2008-43	Nystad, Bent Helge	Technical Condition Indexes and Remaining Useful Life of Aggregated Systems. PhD thesis, IMT
IMT-2008-44	Soni, Prashant Kumar	Hydrodynamic Coefficients for Vortex Induced Vibrations of Flexible Beams, PhD thesis, CeSOS
IMT-2009-45	Amlashi, Hadi K.K.	Ultimate Strength and Reliability-based Design of Ship Hulls with Emphasis on Combined Global and Local Loads. PhD Thesis, IMT
IMT-2009-46	Pedersen, Tom Arne	Bond Graph Modelling of Marine Power Systems. PhD Thesis, IMT
IMT-2009-47	Kristiansen, Trygve	Two-Dimensional Numerical and Experimental Studies of Piston-Mode Resonance. PhD-Thesis, CeSOS
IMT-2009-48	Ong, Muk Chen	Applications of a Standard High Reynolds Number Model and a Stochastic Scour Prediction Model for Marine Structures. PhD-thesis, IMT
IMT-2009-49	Hong, Lin	Simplified Analysis and Design of Ships subjected to Collision and Grounding. PhD-thesis, IMT
IMT-2009-50	Koushan, Kamran	Vortex Induced Vibrations of Free Span Pipelines, PhD thesis, IMT
IMT-2009-51	Korsvik, Jarl Eirik	Heuristic Methods for Ship Routing and Scheduling. PhD-thesis, IMT
IMT-2009-52	Lee, Jihoon	Experimental Investigation and Numerical in Analyzing the Ocean Current Displacement of Longlines. Ph.d.-Thesis, IMT.
IMT-2009-53	Vestbøstad, Tone Gran	A Numerical Study of Wave-in-Deck Impact usin a Two-Dimensional Constrained Interpolation Profile Method, Ph.d.thesis, CeSOS.
IMT-2009-54	Bruun, Kristine	Bond Graph Modelling of Fuel Cells for Marine Power Plants. Ph.d.-thesis, IMT
IMT 2009-55	Holstad, Anders	Numerical Investigation of Turbulence in a Sekwed Three-Dimensional Channel Flow, Ph.d.-thesis, IMT.
IMT 2009-56	Ayala-Uraga, Efren	Reliability-Based Assessment of Deteriorating Ship-shaped Offshore Structures, Ph.d.-thesis, IMT
IMT 2009-57	Kong, Xiangjun	A Numerical Study of a Damaged Ship in Beam Sea Waves. Ph.d.-thesis, IMT/CeSOS.
IMT 2010-58	Kristiansen, David	Wave Induced Effects on Floaters of Aquaculture Plants, Ph.d.-thesis, CeSOS.

IMT 2010-59	Ludvigsen, Martin	An ROV-Toolbox for Optical and Acoustic Scientific Seabed Investigation. Ph.d.-thesis IMT.
IMT 2010-60	Hals, Jørgen	Modelling and Phase Control of Wave-Energy Converters. Ph.d.thesis, CeSOS.
IMT 2010- 61	Shu, Zhi	Uncertainty Assessment of Wave Loads and Ultimate Strength of Tankers and Bulk Carriers in a Reliability Framework. Ph.d. Thesis, IMT/ CeSOS
IMT 2010-62	Shao, Yanlin	Numerical Potential-Flow Studies on Weakly-Nonlinear Wave-Body Interactions with/without Small Forward Speed, Ph.d.thesis,CeSOS.
IMT 2010-63	Califano, Andrea	Dynamic Loads on Marine Propellers due to Intermittent Ventilation. Ph.d.thesis, IMT.
IMT 2010-64	El Khoury, George	Numerical Simulations of Massively Separated Turbulent Flows, Ph.d.-thesis, IMT
IMT 2010-65	Seim, Knut Sponheim	Mixing Process in Dense Overflows with Emphasis on the Faroe Bank Channel Overflow. Ph.d.thesis, IMT
IMT 2010-66	Jia, Huirong	Structural Analysis of Intect and Damaged Ships in a Collission Risk Analysis Perspective. Ph.d.thesis CeSoS.
IMT 2010-67	Jiao, Linlin	Wave-Induced Effects on a Pontoon-type Very Large Floating Structures (VLFS). Ph.D.-thesis, CeSOS.
IMT 2010-68	Abrahamsen, Bjørn Christian	Sloshing Induced Tank Roof with Entrapped Air Pocket. Ph.d.thesis, CeSOS.
IMT 2011-69	Karimirad, Madjid	Stochastic Dynamic Response Analysis of Spar-Type Wind Turbines with Catenary or Taut Mooring Systems. Ph.d.-thesis, CeSOS.
IMT - 2011-70	Erlend Meland	Condition Monitoring of Safety Critical Valves. Ph.d.-thesis, IMT.
IMT – 2011-71	Yang, Limin	Stochastic Dynamic System Analysis of Wave Energy Converter with Hydraulic Power Take-Off, with Particular Reference to Wear Damage Analysis, Ph.d. Thesis, CeSOS.
IMT – 2011-72	Visscher, Jan	Application of Particla Image Velocimetry on Turbulent Marine Flows, Ph.d.Thesis, IMT.
IMT – 2011-73	Su, Biao	Numerical Predictions of Global and Local Ice Loads on Ships. Ph.d.Thesis, CeSOS.
IMT – 2011-74	Liu, Zhenhui	Analytical and Numerical Analysis of Iceberg Collision with Ship Structures. Ph.d.Thesis, IMT.
IMT – 2011-75	Aarsæther, Karl Gunnar	Modeling and Analysis of Ship Traffic by Observation and Numerical Simulation. Ph.d.Thesis, IMT.

Imt – 2011-76	Wu, Jie	Hydrodynamic Force Identification from Stochastic Vortex Induced Vibration Experiments with Slender Beams. Ph.d.Thesis, IMT.
Imt – 2011-77	Amini, Hamid	Azimuth Propulsors in Off-design Conditions. Ph.d.Thesis, IMT.
IMT – 2011-78	Nguyen, Tan-Hoi	Toward a System of Real-Time Prediction and Monitoring of Bottom Damage Conditions During Ship Grounding. Ph.d.thesis, IMT.
IMT- 2011-79	Tavakoli, Mohammad T.	Assessment of Oil Spill in Ship Collision and Grounding, Ph.d.thesis, IMT.
IMT- 2011-80	Guo, Bingjie	Numerical and Experimental Investigation of Added Resistance in Waves. Ph.d.Thesis, IMT.
IMT- 2011-81	Chen, Qiaofeng	Ultimate Strength of Aluminium Panels, considering HAZ Effects, IMT
IMT- 2012-82	Kota, Ravikiran S.	Wave Loads on Decks of Offshore Structures in Random Seas, CeSOS.
IMT- 2012-83	Sten, Ronny	Dynamic Simulation of Deep Water Drilling Risers with Heave Compensating System, IMT.
IMT- 2012-84	Berle, Øyvind	Risk and resilience in global maritime supply chains, IMT.
IMT- 2012-85	Fang, Shaoji	Fault Tolerant Position Mooring Control Based on Structural Reliability, CeSOS.
IMT- 2012-86	You, Jikun	Numerical studies on wave forces and moored ship motions in intermediate and shallow water, CeSOS.
IMT- 2012-87	Xiang ,Xu	Maneuvering of two interacting ships in waves, CeSOS
IMT- 2012-88	Dong, Wenbin	Time-domain fatigue response and reliability analysis of offshore wind turbines with emphasis on welded tubular joints and gear components, CeSOS
IMT- 2012-89	Zhu, Suji	Investigation of Wave-Induced Nonlinear Load Effects in Open Ships considering Hull Girder Vibrations in Bending and Torsion, CeSOS
IMT- 2012-90	Zhou, Li	Numerical and Experimental Investigation of Station-keeping in Level Ice, CeSOS
IMT- 2012-91	Ushakov, Sergey	Particulate matter emission characteristics from diesel enignes operating on conventional and alternative marine fuels, IMT
IMT- 2013-1	Yin, Decao	Experimental and Numerical Analysis of Combined In-line and Cross-flow Vortex Induced Vibrations, CeSOS

IMT-2013-2	Kurniawan, Adi	Modelling and geometry optimisation of wave energy converters, CeSOS
IMT-2013-3	Al Ryati, Nabil	Technical condition indexes doe auxiliary marine diesel engines, IMT
IMT-2013-4	Firoozkoohi, Reza	Experimental, numerical and analytical investigation of the effect of screens on sloshing, CeSOS
IMT-2013-5	Ommani, Babak	Potential-Flow Predictions of a Semi-Displacement Vessel Including Applications to Calm Water Broaching, CeSOS
IMT-2013-6	Xing, Yihan	Modelling and analysis of the gearbox in a floating spar-type wind turbine, CeSOS
IMT-7-2013	Balland, Océane	Optimization models for reducing air emissions from ships, IMT
IMT-8-2013	Yang, Dan	Transitional wake flow behind an inclined flat plate-----Computation and analysis, IMT
IMT-9-2013	Abdillah, Suyuthi	Prediction of Extreme Loads and Fatigue Damage for a Ship Hull due to Ice Action, IMT
IMT-10-2013	Ramìrez, Pedro Agustìn Pèrez	Ageing management and life extension of technical systems- Concepts and methods applied to oil and gas facilities, IMT
IMT-11-2013	Chuang, Zhenju	Experimental and Numerical Investigation of Speed Loss due to Seakeeping and Maneuvering. IMT
IMT-12-2013	Etemaddar, Mahmoud	Load and Response Analysis of Wind Turbines under Atmospheric Icing and Controller System Faults with Emphasis on Spar Type Floating Wind Turbines, IMT
IMT-13-2013	Lindstad, Haakon	Strategies and measures for reducing maritime CO2 emissons, IMT
IMT-14-2013	Haris, Sabril	Damage interaction analysis of ship collisions, IMT
IMT-15-2013	Shainee, Mohamed	Conceptual Design, Numerical and Experimental Investigation of a SPM Cage Concept for Offshore Mariculture, IMT
IMT-16-2013	Gansel, Lars	Flow past porous cylinders and effects of biofouling and fish behavior on the flow in and around Atlantic salmon net cages, IMT
IMT-17-2013	Gaspar, Henrique	Handling Aspects of Complexity in Conceptual Ship Design, IMT
IMT-18-2013	Thys, Maxime	Theoretical and Experimental Investigation of a Free Running Fishing Vessel at Small Frequency of Encounter, CeSOS
IMT-19-2013	Aglen, Ida	VIV in Free Spanning Pipelines, CeSOS

IMT-1-2014	Song, An	Theoretical and experimental studies of wave diffraction and radiation loads on a horizontally submerged perforated plate, CeSOS
IMT-2-2014	Rogne, Øyvind Ygre	Numerical and Experimental Investigation of a Hinged 5-body Wave Energy Converter, CeSOS
IMT-3-2014	Dai, Lijuan	Safe and efficient operation and maintenance of offshore wind farms ,IMT
IMT-4-2014	Bachynski, Erin Elizabeth	Design and Dynamic Analysis of Tension Leg Platform Wind Turbines, CeSOS
IMT-5-2014	Wang, Jingbo	Water Entry of Freefall Wedged – Wedge motions and Cavity Dynamics, CeSOS
IMT-6-2014	Kim, Ekaterina	Experimental and numerical studies related to the coupled behavior of ice mass and steel structures during accidental collisions, IMT
IMT-7-2014	Tan, Xiang	Numerical investigation of ship's continuous- mode icebreaking in leverl ice, CeSOS
IMT-8-2014	Muliawan, Made Jaya	Design and Analysis of Combined Floating Wave and Wind Power Facilities, with Emphasis on Extreme Load Effects of the Mooring System, CeSOS
IMT-9-2014	Jiang, Zhiyu	Long-term response analysis of wind turbines with an emphasis on fault and shutdown conditions, IMT
IMT-10-2014	Dukan, Fredrik	ROV Motion Control Systems, IMT
IMT-11-2014	Grimsmo, Nils I.	Dynamic simulations of hydraulic cylinder for heave compensation of deep water drilling risers, IMT
IMT-12-2014	Kvittem, Marit I.	Modelling and response analysis for fatigue design of a semisubmersible wind turbine, CeSOS
IMT-13-2014	Akhtar, Juned	The Effects of Human Fatigue on Risk at Sea, IMT
IMT-14-2014	Syahroni, Nur	Fatigue Assessment of Welded Joints Taking into Account Effects of Residual Stress, IMT
IMT-1-2015	Bøckmann, Eirik	Wave Propulsion of ships, IMT
IMT-2-2015	Wang, Kai	Modelling and dynamic analysis of a semi-submersible floating vertical axis wind turbine, CeSOS
IMT-3-2015	Fredriksen, Arnt Gunvald	A numerical and experimental study of a two-dimensional body with moonpool in waves and current, CeSOS
IMT-4-2015	Jose Patricio Gallardo Canabes	Numerical studies of viscous flow around bluff bodies, IMT

IMT-5-2015	Vegard Longva	Formulation and application of finite element techniques for slender marine structures subjected to contact interactions, IMT
IMT-6-2015	Jacobus De Vaal	Aerodynamic modelling of floating wind turbines, CeSOS
IMT-7-2015	Fachri Nasution	Fatigue Performance of Copper Power Conductors, IMT
IMT-8-2015	Oleh I Karpa	Development of bivariate extreme value distributions for applications in marine technology,CeSOS
IMT-9-2015	Daniel de Almeida Fernandes	An output feedback motion control system for ROVs, AMOS
IMT-10-2015	Bo Zhao	Particle Filter for Fault Diagnosis: Application to Dynamic Positioning Vessel and Underwater Robotics, CeSOS
IMT-11-2015	Wenting Zhu	Impact of emission allocation in maritime transportation, IMT
IMT-12-2015	Amir Rasekhi Nejad	Dynamic Analysis and Design of Gearboxes in Offshore Wind Turbines in a Structural Reliability Perspective, CeSOS
IMT-13-2015	Arturo Jesùs Ortega Malca	Dynamic Response of Flexibles Risers due to Unsteady Slug Flow, CeSOS
IMT-14-2015	Dagfinn Husjord	Guidance and decision-support system for safe navigation of ships operating in close proximity, IMT
IMT-15-2015	Anirban Bhattacharyya	Ducted Propellers: Behaviour in Waves and Scale Effects, IMT
IMT-16-2015	Qin Zhang	Image Processing for Ice Parameter Identification in Ice Management, IMT
IMT-1-2016	Vincentius Rumawas	Human Factors in Ship Design and Operation: An Experiential Learning, IMT
IMT-2-2016	Martin Storheim	Structural response in ship-platform and ship-ice collisions, IMT
IMT-3-2016	Mia Abrahamsen Prsic	Numerical Simulations of the Flow around single and Tandem Circular Cylinders Close to a Plane Wall, IMT
IMT-4-2016	Tufan Arslan	Large-eddy simulations of cross-flow around ship sections, IMT

IMT-5-2016	Pierre Yves-Henry	Parametrisation of aquatic vegetation in hydraulic and coastal research,IMT
IMT-6-2016	Lin Li	Dynamic Analysis of the Instalation of Monopiles for Offshore Wind Turbines, CeSOS
IMT-7-2016	Øivind Kåre Kjerstad	Dynamic Positioning of Marine Vessels in Ice, IMT
IMT-8-2016	Xiaopeng Wu	Numerical Analysis of Anchor Handling and Fish Trawling Operations in a Safety Perspective, CeSOS
IMT-9-2016	Zhengshun Cheng	Integrated Dynamic Analysis of Floating Vertical Axis Wind Turbines, CeSOS
IMT-10-2016	Ling Wan	Experimental and Numerical Study of a Combined Offshore Wind and Wave Energy Converter Concept
IMT-11-2016	Wei Chai	Stochastic dynamic analysis and reliability evaluation of the roll motion for ships in random seas, CeSOS
IMT-12-2016	Øyvind Selnes Patricksson	Decision support for conceptual ship design with focus on a changing life cycle and future uncertainty, IMT
IMT-13-2016	Mats Jørgen Thorsen	Time domain analysis of vortex-induced vibrations, IMT
IMT-14-2016	Edgar McGuinness	Safety in the Norwegian Fishing Fleet – Analysis and measures for improvement, IMT
IMT-15-2016	Sepideh Jafarzadeh	Energy effiency and emission abatement in the fishing fleet, IMT
IMT-16-2016	Wilson Ivan Guachamin Acero	Assessment of marine operations for offshore wind turbine installation with emphasis on response-based operational limits, IMT
IMT-17-2016	Mauro Candeloro	Tools and Methods for Autonomous Operations on Seabed and Water Coumn using Underwater Vehicles, IMT
IMT-18-2016	Valentin Chabaud	Real-Time Hybrid Model Testing of Floating Wind Tubines, IMT
IMT-1-2017	Mohammad Saud Afzal	Three-dimensional streaming in a sea bed boundary layer
IMT-2-2017	Peng Li	A Theoretical and Experimental Study of Wave-induced Hydroelastic Response of a Circular Floating Collar
IMT-3-2017	Martin Bergström	A simulation-based design method for arctic maritime transport systems

IMT-4-2017	Bhushan Taskar	The effect of waves on marine propellers and propulsion
IMT-5-2017	Mohsen Bardestani	A two-dimensional numerical and experimental study of a floater with net and sinker tube in waves and current
IMT-6-2017	Fatemeh Hoseini Dadmarzi	Direct Numerical Simualtion of turbulent wakes behind different plate configurations
IMT-7-2017	Michel R. Miyazaki	Modeling and control of hybrid marine power plants
IMT-8-2017	Giri Rajasekhar Gunnu	Safety and effiency enhancement of anchor handling operations with particular emphasis on the stability of anchor handling vessels
IMT-9-2017	Kevin Koosup Yum	Transient Performance and Emissions of a Turbocharged Diesel Engine for Marine Power Plants
IMT-10-2017	Zhaolong Yu	Hydrodynamic and structural aspects of ship collisions
IMT-11-2017	Martin Hassel	Risk Analysis and Modelling of Allisions between Passing Vessels and Offshore Installations
IMT-12-2017	Astrid H. Brodtkorb	Hybrid Control of Marine Vessels – Dynamic Positioning in Varying Conditions
IMT-13-2017	Kjersti Bruserud	Simultaneous stochastic model of waves and current for prediction of structural design loads
IMT-14-2017	Finn-Idar Grøtta Giske	Long-Term Extreme Response Analysis of Marine Structures Using Inverse Reliability Methods
IMT-15-2017	Stian Skjong	Modeling and Simulation of Maritime Systems and Operations for Virtual Prototyping using co-Simulations
IMT-1-2018	Yingguang Chu	Virtual Prototyping for Marine Crane Design and Operations
IMT-2-2018	Sergey Gavrilin	Validation of ship manoeuvring simulation models
IMT-3-2018	Jeevith Hegde	Tools and methods to manage risk in autonomous subsea inspection,maintenance and repair operations
IMT-4-2018	Ida M. Strand	Sea Loads on Closed Flexible Fish Cages
IMT-5-2018	Erlend Kvinge Jørgensen	Navigation and Control of Underwater Robotic Vehicles

IMT-6-2018	Bård Stovner	Aided Intertial Navigation of Underwater Vehicles
IMT-7-2018	Erlend Liavåg Grotle	Thermodynamic Response Enhanced by Sloshing in Marine LNG Fuel Tanks
IMT-8-2018	Børge Rokseth	Safety and Verification of Advanced Maritime Vessels
IMT-9-2018	Jan Vidar Ulveseter	Advances in Semi-Empirical Time Domain Modelling of Vortex-Induced Vibrations
IMT-10-2018	Chenyu Luan	Design and analysis for a steel braceless semi-submersible hull for supporting a 5-MW horizontal axis wind turbine
IMT-11-2018	Carl Fredrik Rehn	Ship Design under Uncertainty
IMT-12-2018	Øyvind Ødegård	Towards Autonomous Operations and Systems in Marine Archaeology
IMT-13-2018	Stein Melvær Nornes	Guidance and Control of Marine Robotics for Ocean Mapping and Monitoring
IMT-14-2018	Petter Norgren	Autonomous Underwater Vehicles in Arctic Marine Operations: Arctic marine research and ice monitoring
IMT-15-2018	Minjoo Choi	Modular Adaptable Ship Design for Handling Uncertainty in the Future Operating Context
MT-16-2018	Ole Alexander Eidsvik	Dynamics of Remotely Operated Underwater Vehicle Systems
IMT-17-2018	Mahdi Ghane	Fault Diagnosis of Floating Wind Turbine Drivetrain- Methodologies and Applications
IMT-18-2018	Christoph Alexander Thieme	Risk Analysis and Modelling of Autonomous Marine Systems
IMT-19-2018	Yugao Shen	Operational limits for floating-collar fish farms in waves and current, without and with well-boat presence
IMT-20-2018	Tianjiao Dai	Investigations of Shear Interaction and Stresses in Flexible Pipes and Umbilicals
IMT-21-2018	Sigurd Solheim Pettersen	Resilience by Latent Capabilities in Marine Systems
IMT-22-2018	Thomas Sauder	Fidelity of Cyber-physical Empirical Methods. Application to the Active Truncation of Slender Marine Structures
IMT-23-2018	Jan-Tore Horn	Statistical and Modelling Uncertainties in the Design of Offshore Wind Turbines

IMT-24-2018	Anna Swider	Data Mining Methods for the Analysis of Power Systems of Vessels
IMT-1-2019	Zhao He	Hydrodynamic study of a moored fish farming cage with fish influence
IMT-2-2019	Isar Ghamari	Numerical and Experimental Study on the Ship Parametric Roll Resonance and the Effect of Anti-Roll Tank
IMT-3-2019	Håkon Strandenes	Turbulent Flow Simulations at Higher Reynolds Numbers
IMT-4-2019	Siri Mariane Holen	Safety in Norwegian Fish Farming – Concepts and Methods for Improvement
IMT-5-2019	Ping Fu	Reliability Analysis of Wake-Induced Riser Collision
IMT-6-2019	Vladimir Krivopolianskii	Experimental Investigation of Injection and Combustion Processes in Marine Gas Engines using Constant Volume Rig
IMT-7-2019	Anna Maria Kozlowska	Hydrodynamic Loads on Marine Propellers Subject to Ventilation and out of Water Condition.
IMT-8-2019	Hans-Martin Heyn	Motion Sensing on Vessels Operating in Sea Ice: A Local Ice Monitoring System for Transit and Stationkeeping Operations under the Influence of Sea Ice
IMT-9-2019|	Stefan Vilsen	Method for Real-Time Hybrid Model Testing of Ocean Structures – Case on Slender Marine Systems
IMT-10-2019	Finn-Christian W. Hanssen	Non-Linear Wave-Body Interaction in Severe Waves
IMT-11-2019	Trygve Olav Fossum	Adaptive Sampling for Marine Robotics
IMT-12-2019	Jørgen Bremnes Nielsen	Modeling and Simulation for Design Evaluation
IMT-13-2019	Yuna Zhao	Numerical modelling and dyncamic analysis of offshore wind turbine blade installation
IMT-14-2019	Daniela Myland	Experimental and Theoretical Investigations on the Ship Resistance in Level Ice
IMT-15-2019	Zhengru Ren	Advanced control algorithms to support automated offshore wind turbine installation
IMT-16-2019	Drazen Polic	Ice-propeller impact analysis using an inverse propulsion machinery simulation approach
IMT-17-2019	Endre Sandvik	Sea passage scenario simulation for ship system performance evaluation

IMT-18-2019	Loup Suja-Thauvin	Response of Monopile Wind Turbines to Higher Order Wave Loads
IMT-19-2019	Emil Smilden	Structural control of offshore wind turbines – Increasing the role of control design in offshore wind farm development
IMT-20-2019	Aleksandar-Sasa Milakovic	On equivalent ice thickness and machine learning in ship ice transit simulations
IMT-1-2020	Amrit Shankar Verma	Modelling, Analysis and Response-based Operability Assessment of Offshore Wind Turbine Blade Installation with Emphasis on Impact Damages
IMT-2-2020	Bent Oddvar Arnesen Haugaløkken	Autonomous Technology for Inspection, Maintenance and Repair Operations in the Norwegian Aquaculture
IMT-3-2020	Seongpil Cho	Model-based fault detection and diagnosis of a blade pitch system in floating wind turbines
IMT-4-2020	Jose Jorge Garcia Agis	Effectiveness in Decision-Making in Ship Design under Uncertainty
IMT-5-2020	Thomas H. Viuff	Uncertainty Assessment of Wave-and Current-induced Global Response of Floating Bridges
IMT-6-2020	Fredrik Mentzoni	Hydrodynamic Loads on Complex Structures in the Wave Zone
IMT-7-2020	Senthuran Ravinthrakumar	Numerical and Experimental Studies of Resonant Flow in Moonpools in Operational Conditions
IMT-8-2020	Stian Skaalvik Sandøy	Acoustic-based Probabilistic Localization and Mapping using Unmanned Underwater Vehicles for Aquaculture Operations
IMT-9-2020	Kun Xu	Design and Analysis of Mooring System for Semi-submersible Floating Wind Turbine in Shallow Water
IMT-10-2020	Jianxun Zhu	Cavity Flows and Wake Behind an Elliptic Cylinder Translating Above the Wall
IMT-11-2020	Sandra Hogenboom	Decision-making within Dynamic Positioning Operations in the Offshore Industry – A Human Factors based Approach
IMT-12-2020	Woongshik Nam	Structural Resistance of Ship and Offshore Structures Exposed to the Risk of Brittle Failure
IMT-13-2020	Svenn Are Tutturen Værnø	Transient Performance in Dynamic Positioning of Ships: Investigation of Residual Load Models and Control Methods for Effective Compensation
IMT-14-2020	Mohd Atif Siddiqui	Experimental and Numerical Hydrodynamic Analysis of a Damaged Ship in Waves
IMT-15-2020	John Marius Hegseth	Efficient Modelling and Design Optimization of Large Floating Wind Turbines

IMT-16-2020	Asle Natskår	Reliability-based Assessment of Marine Operations with Emphasis on Sea Transport on Barges
IMT-17-2020	Shi Deng	Experimental and Numerical Study of Hydrodynamic Responses of a Twin-Tube Submerged Floating Tunnel Considering Vortex-Induced Vibration
IMT-18-2020	Jone Torsvik	Dynamic Analysis in Design and Operation of Large Floating Offshore Wind Turbine Drivetrains
IMT-1-2021	Ali Ebrahimi	Handling Complexity to Improve Ship Design Competitiveness
IMT-2-2021	Davide Proserpio	Isogeometric Phase-Field Methods for Modeling Fracture in Shell Structures
IMT-3-2021	Cai Tian	Numerical Studies of Viscous Flow Around Step Cylinders
IMT-4-2021	Farid Khazaeli Moghadam	Vibration-based Condition Monitoring of Large Offshore Wind Turbines in a Digital Twin Perspective
IMT-5-2021	Shuaishuai Wang	Design and Dynamic Analysis of a 10-MW Medium-Speed Drivetrain in Offshore Wind Turbines
IMT-6-2021	Sadi Tavakoli	Ship Propulsion Dynamics and Emissions
IMT-7-2021	Haoran Li	Nonlinear wave loads, and resulting global response statistics of a semi-submersible wind turbine platform with heave plates
IMT-8-2021	Einar Skiftestad Ueland	Load Control for Real-Time Hybrid Model Testing using Cable-Driven Parallel Robots
IMT-9-2021	Mengning Wu	Uncertainty of machine learning-based methods for wave forecast and its effect on installation of offshore wind turbines
IMT-10-2021	Xu Han	Onboard Tuning and Uncertainty Estimation of Vessel Seakeeping Model Parameters
IMT-01-2022	Ingunn Marie Holmen	Safety in Exposed Aquacultrue Operations
IMT-02-2022	Prateek Gupta	Ship Performance Monitoring using In-service Measurements and Big Data Analysis Methods
IMT-03-2022	Sangwoo Kim	Non-linear time domain analysis of deepwater riser vortex-induced vibrations
IMT-04-2022	Jarle Vinje Kramer	Hydrodynamic Aspects of Sail-Assisted Merchant Vessels
IMT-05-2022	Øyvind Rabliås	Numerical and Expermental Studies of Maneuvering in Regular and Irregular Waves

IMT-06-2022	Pramod Ghimire	Simulation-Based Ship Hybrid Power System Conspet Studies and Performance Analyses
IMT-07-2022	Carlos Eduardo Silva de Souza	Structural modelling, coupled dynamics, and design of large floating wind turbines
IMT-08-2022	Lorenzo Balestra	Design of hybrid fuel cell & battery systems for maritime vessels
IMT-09-2022	Sharmin Sultana	Process safety and risk management using system perspectives – A contribution to the chemical process and petroleum industry
IMT-10-2022	Øystein Sture	Autonomous Exploration for Marine Minerals
IMT-11-2022	Tiantian Zhu	Information and Decision-making for Major Accident Prevention – A concept of information-based strategies for accident prevention
IMT-12-2022	Siamak Karimi	Shore-to-Ship Charging Systems for Battery-Electric Ships
IMT-01-2023	Huili Xu	Fish-inspired Propulsion Study: Numerical Hydrodynamics of Rigid/Flexible/Morphing Foils and Observations on Real Fish
IMT-02-2023	Chana Sinsabvarodom	Probabilistic Modelling of Ice-drift and Ice Loading on Fixed and Floating Offshore Structures
IMT-03-2023	Martin Skaldebø	Intelligent low-cost solutions for underwater intervention using computer vision and machine learning
IMT-04-2023	Hans Tobias Slette	Vessel operations in exposed aquaculture – Achieving safe and efficient operation of vessel fleets in fish farm systems experiencing challenging metocean conditions
IMT-05-2023	Ruochen Yang	Methods and models for analyzing and controlling the safety in operations of autonomous marine systems
IMT-06-2023	Tobias Rye Torben	Formal Approaches to Design and Verification of Safe Control Systems for Autonomous Vessels
IMT-07-2023	YoungRong Kim	Modeling Operational Performance for the Global Fleet & Application of an Energy Saving Measure
IMT-08-2023	Henrik Schmidt-Didlaukies	Modeling and Hybrid Feedback Control of Underwater Vehicles
IMT-09-2023	Ehsan Esmailian	Optimal Ship Design for Operating in Real Sea States
IMT-10-2023	Astrid Vamråk Solheim	Exploring the performance of conceptual offshore production systems for deep-sea mining
IMT-11-2023	Benjamin Lagemann	Conceptual design of low-emission ships

IMT-12-2023	Erling Neerland Lone	Fatigue reliability of offshore Mooring chains under influence of mean load and corrosion
IMT-13-2023	Kamyar Malekibagherabadi	Simulator Approach to Concept Analysis and Optimization of Marine Power Plants
IMT-14-2023	Håvard Snefjellås Løvås	Optical Techniques for Hyperspectral Imaging of the Seafloor
IMT-15-2023	Stian Høegh Sørum	Uncertainties in the Design of Monopile Offshore Wind Turbines
IMT-16-2023	Nathalie Ramos	Mechanical and thermal simulations of 3D printed structures and the 3D printing process
IMT-17-2023	Daeseong Park	Model-Based Design of Marine Hybrid Power Systems
IMT-18-2023	Chuanqi Guo	Analysis and modeling of risk of an autonomous ferry for safer design and operation
IMT-01-2024	Dennis David Langer	Hyperspectral Push-broom Systems: Operations, Software Development, and Spatial Resolution
IMT-02-2024	Jens Einar Bremnes	Safe Autonomy in Marine Robotics
IMT-03-2024	George Katsikogiannis	Estimation of Long-Term Fatigue and Extreme Responses of Large-Diameter Monopiles for Offshore Wind Turbines
IMT-04-2024	Alexandre Cardaillac	Towards autonomous underwater navigation and perception for end-to-end ship hull inspection
IMT-05-2024	Tale Egeberg Aasland	Numerical studies of viscous flow around straight and curved tandem cylinders
IMT-06-2024	Felix Mehlan	Digital Twins for Fault Prognosis in Offshore Wind Turbine Drivetrains
IMT-07-2024	Thomas Johansen	Risk-Based Control of Autonomous Surface Ships
IMT-08-2024	Sheng Xu	Shipping safety in the Arctic Contributions to the understanding of shipping risk during escort and convoy operations
IMT-09-2024	Maël Moreau	Numerical and experimental hydrodynamic study of a vertical circular floating dock in waves